FLOW AND PRESSURE DROP ON THE SHELLSIDE OF CYLINDRICAL HEAT EXCHANGERS

PAUL WILLIAM MURRAY
Doctor of Philosophy

THE UNIVERSITY OF ASTON IN BIRMINGHAM

April 1988

THE UNIVERSITY OF ASTON IN BIRMINGHAM

FLOW AND PRESSURE DROP ON THE SHELLSIDE OF CYLINDRICAL HEAT EXCHANGERS

PAUL WILLIAM MURRAY
Doctor of Philosophy

APRIL 1988

Summary

This work presents pressure distributions and fluid flow patterns on the shellside of a cylindrical shell-and-tube heat exchanger. The apparatus used was constructed from glass enabling direct observation of the flow using a dye release technique and had ten traversable pressure instrumented tubes permitting detailed pressure distributions to be obtained. The 'exchanger' had a large tube bundle (278 tubes) and main flow areas typical of practical designs. Six geometries were studied: three baffle spacings both with and without baffle leakage. Results are also presented of three-dimensional modelling of shellside flows using the Harwell Laboratory's FLOW3D code.

Flow visualisation provided flow patterns in the central plane of the bundle and adjacent to the shell wall. Comparison of these highlighted significant radial flow variations. In particular, separated regions, originating from the baffle tips, were observed. The size of these regions was small in the bundle central plane but large adjacent to the shell wall and extended into the bypass lane. This appeared to reduce the bypass flow area and hence the bypass flow fraction.

The three-dimensional flow modelling results were presented as velocity vector and isobar maps. The vector maps illustrated regions of high and low velocity which could be prone to tube vibration and fouling. Separated regions were also in evidence. A non-uniform crossflow was discovered with, in general, higher velocities in the central plane of the bundle than near the shell wall. The form of the isobar maps calculated by FLOW3D was in good agreement with experimental results. In particular, larger pressure drops occurred across the inlet than outlet of a crossflow region and were higher near the upstream than downstream baffle face.

The effect of baffle spacing and baffle leakage on crossflow and window pressure drop measurements was identified.

Agreement between the current measurements, previously obtained data and commonly used design correlations/models was, in general, poor. This was explained in terms of the increased understanding of shellside flow. The bulk of previous data, which derives from small-scale rigs with few tubes, have been shown to be unrepresentative of typical commercial units.

The Heat Transfer and Fluid Flow Service design program TASC provided the best predictions of the current pressure drop results. However, a number of simple one-dimensional models in TASC are, individually, questionable. Some revised models have been proposed.

KEY WORDS: HEAT EXCHANGER, SHELLSIDE, PRESSURE DROP, FLOW DISTRIBUTION, MATHEMATICAL MODELS, VISUALISATION

To Rachel

A Blade of Grass

You ask for a poem
I offer you a blade of grass.
You say it is not good enough.
You ask for a poem.

I say this blade of grass will do.
It has dressed itself in frost,
It is more immediate
Than any image of my making.

You say it is not a poem,
It is a blade of grass and grass
Is not quite good enough.
I offer you a blade of grass.

You are indignant.
You say it is too easy to offer grass.
It is absurd.
Anyone can offer a blade of grass.

You ask for a poem.
And so I write you a tragedy about
How a blade of grass
Becomes more and more difficult to offer,

And about how as you grow older
A blade of grass
Becomes more difficult to accept.

Brian Patten

ACKNOWLEDGEMENTS

I would like to express my gratitude to the following:

Dr L E Haseler and Dr J D Jenkins for their supervision.

Dr B A Splawski for his discussions on the three-dimensional flow modelling.

Messrs. K Matthews, L Ward and other members of the divisional workshop for their help with construction and subsequent modifications of the experimental apparatus.

Miss J Moore for her patience and care in typing this thesis.

The Science and Engineering Research Council for their financial support.

The Heat Transfer and Fluid Flow Service for financing the work through member companies and the Department of Trade and Industry.

Finally, I would like to especially thank my parents, Maureen and David, for their support and encouragement.

CONTENTS

LIST OF TABLES

Page No

LIST OF FIGURES

NOMENCLATURE

A_b	Bypass flow area	(m^2)
A_c	Minimum crossflow area, measured at or near the shell centre-line	(m^2)
$\overline{A}_c^m$	Minimum average crossflow area as defined by Equation (2.22), Moore (1974)	(m^2)
A_c^s	Superficial crossflow area	(m^2)
A_{cb}^m	Minimum crossflow area in the plane described by the baffle tips	(m^2)
A_{ct}^m	Total minimum area for crossflow including bypass area, based on total shellside mass flowrate	(m^2)
$\overline{A}_{ct}^m$	Total minimum average area for crossflow including bypass area, based on total shellside mass flowrate	(m^2)
A_e	Effective leakage area as defined by Equation (2.86), Wills (1984)	(m^2)
A_{eff}	Effective crossflow area as defined by Equation (2.27), Emmerson (1963)	(m^2)
A_L	Total leakage area of a segmentally cut baffle	(m^2)
$A_{\ell o}$	Leakage area of a baffle in the crossflow or overlap region	(m^2)
$A_{\ell w}$	Leakage area of a baffle in the window region	(m^2)
A_r	Minimum crossflow area in the r^{th} row of a tube bundle, Emmerson (1963)	(m^2)
A_T	Total minimum area for crossflow including bypass area	(m^2)
A_w	Window flow area measured in the plane of the baffle	(m^2)
a	Constant in Equation (E.8)	
a'	Parameters used in Equation (2.71), Wills (1984)	(-)
a_{Gc}	Coefficient in Grant and Murray's (1972) crossflow friction factor correlation, Equation (2.11)	(-)
$a_{G\ell}$	Coefficient in Grant and Murray's (1972) baffle leakage friction factor correlation, Equation (2.28)	(-)
a_{Mb}	Coefficient in Moore's (1974) crossflow bypass friction factor correlation, Equation (2.20)	(-)
$a_{M\ell}$	Coefficient in Moore's (1974) baffle leakage friction factor correlation, Equation (2.20)	(-)
a_W, a_W'	Coefficient in Wills' (1984) window flow model, Equation (2.40)	(-)

B	Extent of crossflow from the shell centre-line	(m)
B_c	Baffle cut as a fraction of the shell inside diameter	(-)
B_f	Fractional distance across the width of a baffle space, measured from the upstream baffle face	(-)
B_s	Baffle spacing	(m)
b_{Gc}	Exponent in Grant and Murray's (1972) crossflow friction factor correlation, Equation (2.11)	(-)
$b_{G\ell}$	Exponent in Grant and Murray's (1972) baffle leakage friction factor correlation, Equation (2.28)	(-)
b_{Mb}	Exponent in Moore's (1974) crossflow bypass friction factor correlation, Equation (2.20)	(-)
$b_{M\ell}$	Exponent in Moore's (1974) baffle leakage friction factor correlation, Equation (2.29)	(-)
b_W, b_W'	Constant in Wills' (1984) window flow model, Equation (2.40)	(-)
C_w	Average crossflow width in a circular tube bundle as defined by Equation (2.28), Moore (1974)	(m)
C_d	Coefficient of discharge for flow through an annular orifice	(-)
c	Tube-baffle (c_{tb}) and/or shell-baffle (c_{sb}) diametral clearance	(m)
$c_{M\ell}$	Constant in Macbeth's (1983) baffle leakage pressure drop correlation, Equation (2.31)	(-)
D_g	Minimum gap between tubes in a tube bundle	(m)
D_h	Hydraulic diameter for the window region, defined as for D_v	(m)
D_{ot}	Outer-tube limit diameter of a tube bundle within a cylindrical shell (Moore, 1974). Defined as the diameter to the outer tube plus P_t-D_t	
D_t	Tube outside diameter	(m)
D_v	Volumetric hydraulic diameter defined as $D_t[g(P_t/D_t)^2-1]$, where $g = 4/\pi$ for square and $4\sin(\pi/3)/\pi$ for triangular layouts	(m)

D_w	Volumetric hydraulic diameter for the window region. Defined as for D_v	(m)
D_z	Volumetric hydraulic diameter for longitudinal shellside flow. Defined as for D_v	(m)
$d_{M\ell}$	Coefficient in Macbeth's (1983) baffle leakage pressure drop correlation, Equation (2.31)	(-)
Eu	Euler number defined as $\Delta p/\frac{1}{2}\rho u^2$	(-)
e	Parameter defined by Equation (8.10)	(-)
F_b	Fraction of the total minimum flow area occupied by a bypass lane, Equation (2.19)	(-)
$F_{c\ell}$	Crossflow leakage interaction factor defined by Equation (2.68), Wills (1984)	(-)
F_r	Empirical correction factor used in Palen and Taborek's (1969) window model, Equation (2.34)	(-)
f_b	Bypass friction factor	(-)
f_c^B	Crossflow friction factor as defined by Butterworth (1979)	(-)
f_c^{GS}	Crossflow friction factor defined by Equations (2.8) and (2.9), Gunter and Shaw (1945)	(-)
f_c^m	Crossflow friction factor based on the minimum flow area, Equation (2.1)	(-)
$\bar{f}_c^m$	Crossflow friction factor based on the average minimum flow area in circular bundles. Defined by Equation (2.23), Moore (1974)	(-)
f_c^s	Crossflow friction factor based on the superficial flow area	(-)
f_ℓ^G	Baffle leakage friction factor used in Grant and Murray's (1972) correlation, Equation (2.28)	(-)
f_ℓ^M	Baffle leakage friction factor used in Moore's (1974) correlation, Equation (2.29)	(-)
fn	A function of	(-)
f_p	Fractional penetration distance of crossflow into the window region	(-)
f_w	Window flow friction factor	(-)
h	Height of window measured from the baffle tip to the shell wall	(m)

K	Surface permeability, the fraction of free flow area to the total area	(-)
k_B	Flow conductivity or permeability coefficient in Equation (2.15), Butterworth (1979)	(m^2)
k_{bp}	Bypass pressure loss coefficient	(-)
k_p	Crossflow pressure loss coefficient based on the total minimum flow area including bypass lanes	(-)
k_p'	Reference crossflow loss coefficient defined through Equation (2.14b), ESDU (1984)	(-)
k_2	Geometry factor used in Equation (2.12), Zukauskus (1983)	(-)
L_c	Crossflow path length	(m)
$\dot{M}_b$	Bypass mass flowrate	(kg/s)
$\dot{M}_c$	Crossflow mass flowrate	(kg/s)
$\dot{M}_\ell$	Shell-baffle plus tube-baffle leakage mass flowrate	(kg/s)
$\dot{M}_{\ell o}$	Total baffle leakage mass flowrate in the crossflow or overlap region	(kg/s)
$\dot{M}_{\ell w}$	Total baffle leakage mass flowrate in the window region	(kg/s)
$\dot{M}_s$	Total shell-baffle leakage mass flowrate	(kg/s)
$\dot{M}_{so}$	Shell-baffle leakage mass flowrate in the overlap region	(kg/s)
$\dot{M}_{sw}$	Shell-baffle leakage mass flowrate in the window region	(kg/s)
$\dot{M}_T$	Total shellside mass flowrate	(kg/s)
$\dot{M}_t$	Total tube-baffle leakage mass flowrate	(kg/s)
$\dot{M}_{to}$	Tube-baffle leakage mass flowrate in the overlap region	(kg/s)
$\dot{M}_{tw}$	Tube-baffle leakage mass flowrate in the window region	(kg/s)
$\dot{M}_w$	Window mass flowrate	(kg/s)
m	Normalised crossflow mass flowrate as defined by Equation (8.3)	(-)
$\dot{m}_m$	Crossflow mass flux based on the minimum crossflow area	$(\frac{kg}{sm^2})$
$\dot{m}_T$	Crossflow mass flux based on the total minimum crossflow area including any bypass lanes	$(\frac{kg}{sm^2})$

N_b	Number of major restrictions to flow in a bypass lane	(-)
N_c	Number of major restrictions to flow in a crossflow region	(-)
N_s	Number of sealing strips employed in a bypass lane	(-)
N_w^B	Number of major restrictions to flow for crossflow in the window region, as defined by Bergelin et al. (1954), Equation (2.33)	(-)
N_w^P	Number of major restrictions to flow for crossflow in the window region, as defined by Palen and Taborek (1969), Equation (2.34)	(-)
n_b	Number of velocity heads lost for flow through a bypass lane	(-)
n_c	Number of velocity heads lost per row for flow over a crossflow region	(-)
$\bar{n}_c$	The number of velocity heads lost per row for flow over a crossflow region based on the average minimum crossflow area (Equation (2.22)).	(-)
n_{cn}	Number of velocity heads lost due to a sudden contraction	(-)
$\bar{n}_{ct}$	The number of velocity heads lost per row for flow over a crossflow region based on the average minimum crossflow area plus bypass area and total shellside mass flowrate	(-)
n_e	Number of velocity heads lost due to a sudden expansion	(-)
n_f	Number of frictional velocity heads lost for crossflow in the window	(-)
n_L	Number of velocity heads lost for leakage flow through a baffle	(-)
$n_{\ell o}$	Number of velocity heads lost for baffle leakage flows in the overlap region	(-)
$n_{\ell w}$	Number of velocity heads lost for baffle leakage flows in the window region	(-)

n_{tn}	Number of velocity heads lost due to turning through the window region	(-)
n_w	Number of velocity heads lost for flow through a window region	(-)
n_θ	Perimetric pressure coefficient or number of velocity heads between the forward stagnation point and an angular position, θ, around a tube in a bundle, Equation (9.10)	(-)
P_t	Diagonal tube pitch between centres of tubes	(m)
P_x	Longitudinal tube pitch between centres of tube	(m)
P_y	Transverse tube pitch between centres of tubes in the same row	(m)
p	Local pressure	(N/m^2)
Q	Volume flowrate	(m^3/hr)
R	Resistance coefficient in the equation for flow through a porous medium, Equation (7.1)	(1/m)
Re_b	Bypass Reynolds number	(-)
Re_c^m	Crossflow Reynolds number based on the minimum crossflow area and the minimum gap between tubes as the characteristic length	(-)
$\overline{Re}_c^{\,m}$	Crossflow Reynolds numbers based on the average minimum crossflow area and the minimum gap between tubes as the characteristic length	(-)
Re_c^{mt}	Crossflow Reynolds number based on the minimum crossflow flow area and the tube diameter as the characteristic length	(-)
Re_c^{mv}	Crossflow Reynolds number based on the minimum crossflow area and the volumetric hydraulic diameter as the characteristic length	(-)
Re_c^{st}	Crossflow Reynolds number based on the superficial crossflow area and the tube diameter as the characteristic length	(-)
$\overline{Re}_{ct}^{m}$	Crossflow Reynolds number based on the average minimum crossflow area plus bypass area and the total shellside mass flowrate (Equation (9.2))	(-)

Re_ℓ	Baffle leakage Reynolds number	(-)
Re_w	Window flow for Reynolds number	(-)
$\bar{R}_y$	Crossflow mean flow resistance coefficient	($1/m^2$)
$\bar{R}_z$	Longitudinal mean flow resistance coefficient	($1/m^2$)
r	Transverse pitch divided by tube diameter	(-)
s	Longitudinal pitch divided by tube diameter	(-)
t	Diagonal pitch divided by tube diameter	(-)
t_b	Baffle thickness	(m)
u_c	Crossflow velocity based on the minimum flow area at or near the centre-line of the shell	(m/s)
u_{cb}	Crossflow velocity based on the minimum flow area at the plane described by the baffle tips	(m/s)
u_w	Window flow velocity	(m/s)
u_y	Local crossflow velocity	(m/s)
u_z	Local longitudinal shellside velocity	(m/s)
v	Superficial local crossflow velocity	(m/s)
$\bar{v}$	Mean superficial crossflow velocity	(m/s)
W	Minimum flow gap per transverse tube pitch	(m)
w	Superficial local longitudinal velocity	(m/s)
x	Normalised crossflow distance as defined by Equation (8.3)	(-)
x_c	Fraction of flow in crossflow	(-)
Y	Parameter defined by Equation (8.2)	(m)
y	Crossflow distance into the window region	
y^*	Normalised minimum gap between tubes	(-)
y_θ	Minimum gap between tubes at angle θ	(m)
Z	The shape factor used in baffle leakage correlations, defined as the baffle thickness divided by the radial clearance between tube and orifice	(-)
z	Longitudinal distance	(m)

Greek Symbols

α	Assumed turning angle for fluid flowing around a window region (Moore, 1974), Equation (2.37)	(rad)
β_i (i=1,4)	Correction factors to account for property variation, bypassing, flow inclination and tube roughness. ESDU (1974)	(-)
γ	Volume porosity or void fraction	(-)
η	Dynamic viscosity	(Ns/m^2)
θ	The angle around the circumference of a tube, measured from the forward stagnation point (θ=0)	(deg)
Δp_b	Bypass flow pressure drop	(N/m^2)
Δp_c	Crossflow pressure drop	(N/m^2)
$\Delta p_{c\ell}$	Crossflow pressure drop obtained with baffle leakage flows present	(N/m^2)
Δp_{cw}	Pressure drop associated with crossflow in the window region	(N/m^2)
Δp_{cn}	Pressure drop suffered for flow through an abrupt contraction	(N/m^2)
Δp_{ex}	Pressure drop suffered for flow through an abrupt expansion	(N/m^2)
Δp_f	Frictional presure drop	(N/m^2)
Δp_ℓ	Baffle leakage pressure drop	(N/m^2)
$\Delta p_{\ell o}$	Baffle leakage pressure drop in the overlap region	(N/m^2)
$\Delta p_{\ell w}$	Baffle leakage pressure drop in the window region	(N/m^2)
Δp_{so}	Shell-baffle leakage pressure drop in the overlap region	(N/m^2)
Δp_{sw}	Shell-baffle leakage pressure drop in the window region	(N/m^2)
Δp_T	Total baffle space pressure drop	(N/m^2)
Δp_{to}	Tube-baffle leakage pressure drop in the overlap region	(N/m^2)
Δp_{tw}	Tube-baffle leakage pressure drop in the window region	(N/m^2)
Δp_{tn}	Pressure drop due to fluid turning into and out of the window region (Wills, 1974), Equation (2.39)	(N/m^2)
Δp_w	Window flow pressure drop	(N/m^2)
Δp_θ	Pressure drop between the forward stagnation point and a point $\theta°$ around the tube circumference	(N/m^2)

ν_e	Effective turbulent diffusivity, which is the sum of the laminar and turbulent components	(m^2/s)
ρ	Fluid density	(kg/m^3)
ξ	Coefficient defined in Equation (B.8)	(-)
ϕ	Coefficient defined in Equation (B.8)	(-)
ζ	Crossflow pressure drop in the window region as a fraction of the total crossflow pressure drop	(-)

CHAPTER 1

1. INTRODUCTION

Shell and tube heat exchangers are the most widely used of all unfired process heat exchange equipment. They remain popular despite their low heat transfer surface area to volume ratios, as compared to compact designs, simply because of their versatility. They represent the larger proportion of all exchangers used in industry.

1.1 Features of a Shell and Tube Heat Exchanger

The main features of a shell-and-tube heat exchanger are shown in Figure 1.1 . These include an outer shell, which acts as a containment and/or pressure vessel for the shellside fluid, surrounding a longitudinal array of tubes held in place by a rigid framework. This framework consists of a number of baffles held together by tie rods which are either bolted or welded to the tube sheets. One process stream flows inside the tubes (tubeside flow) and the other stream flows in the gaps outside the tubes enclosed by the shell (shellside flow). Heat is transferred through the tube walls.

Figure 1.1 depicts an E-type shell with a single pass on both the tubeside and the shellside. This shell type is the most commonly used since it is the simplest and least expensive design. Other combinations of passes and shell types are used and these variations are described in Standards of Tubular Exchanger Manufacturers Association (TEMA) (1978).

The baffles serve two purposes:

1) They act as supports for the tube bundle, preventing the tubes from sagging and also reduce the risk of damaging vibrations.

2) They deflect the shellside fluid to flow along the length of the shell via a number of crossflow passes. This is desirable as flow normal to tube bundles is a very efficient means of heat transfer; the alternate expansion and contraction in the tube bundle flow area produces a highly turbulent flow.

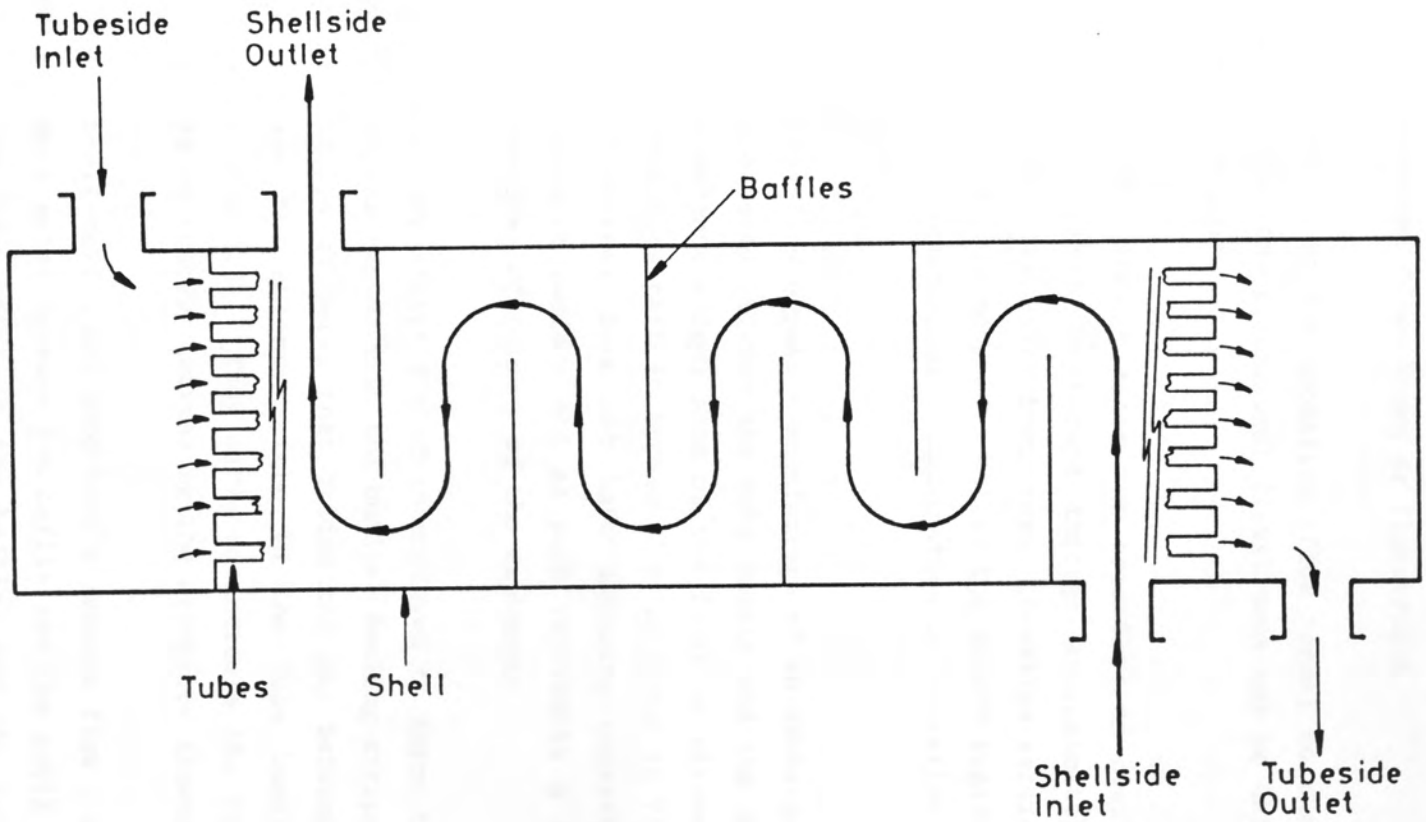

Figure 1.1 : The Main Features of a Baffled Shell-and-Tube Heat Exchanger

1.2 Flow Distribution

Shellside flow is a complicated three dimensional process. The flow distribution, however, may be conveniently represented by a number of one-dimensional flows known as flowstreams.

In addition to the crossflow (flow normal to the tube bundle), a number of other one-dimensional flowstreams may be defined to describe the shellside flow:

(1) Window flow - after one crossflow or overlap section, the fluid must be turned through approximately 180° to flow across the next, downstream, crossflow section. The region in which this occurs is called the window region, and the window flow experiences a combination of crossflow and longitudinal flow.

(2) Crossflow bypass - manufacture of an exchanger necessitates a clearance between the tube bundle and the shell wall. This clearance allows some of the fluid to circumvent the desired crossflow path in bypass flow as shown in Figure 1.2a. This flowstream does not have intimate contact with the heat transfer surface and as such represents a loss in the heat transfer efficiency of the exchanger.

Sealing strips are often employed to force the flow from the bypass region into the bundle. Sealing strips are essentially strips of metal that bridge the gap between the shell wall and the outermost tube in the tube bundle, as shown in Figure 1.2b. They serve to increase the bypass lane resistance thereby increasing the crossflow flowrate.

(3) Shell-baffle and tube-baffle leakage flow - again, tolerances must exist between the baffle and the shell wall and between the tube holes in the baffles and the tubes. These flow areas allow some of the fluid to 'short circuit' the bundle in what are known as shell-baffle and tube-baffle leakage as shown in Figure 1.2c. Shell-baffle leakage, as with

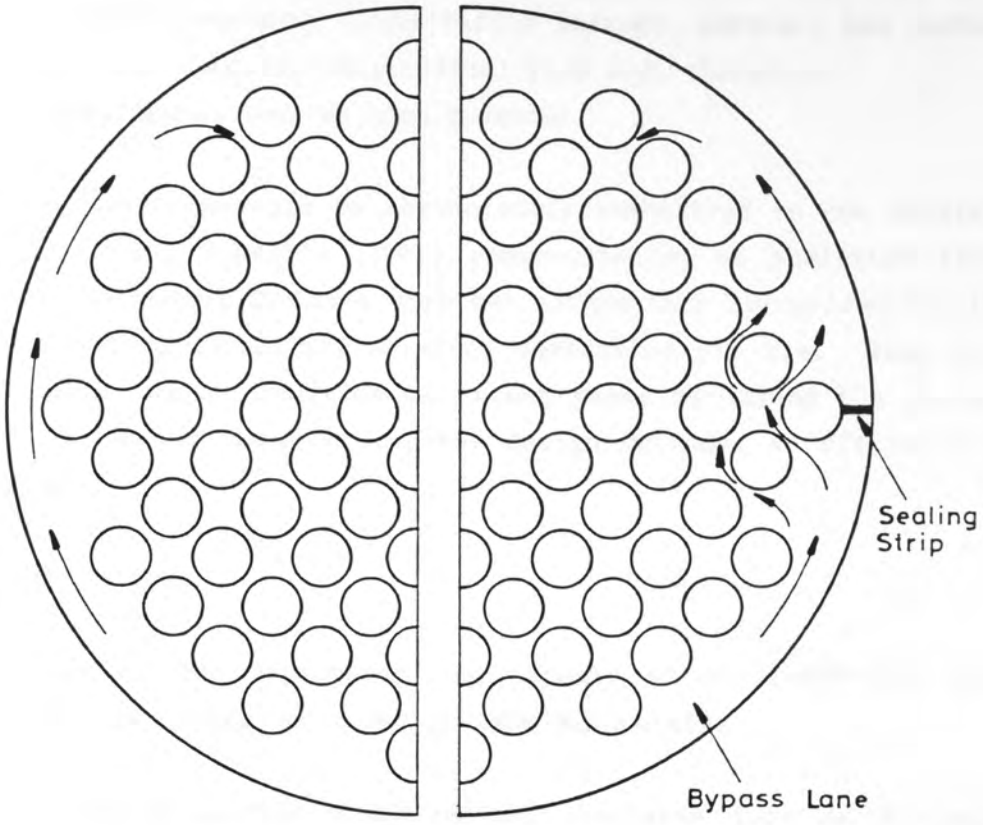

Figure 1·2 a Crossflow Bypass b: Effect of Sealing Strips on the Bypass Flow

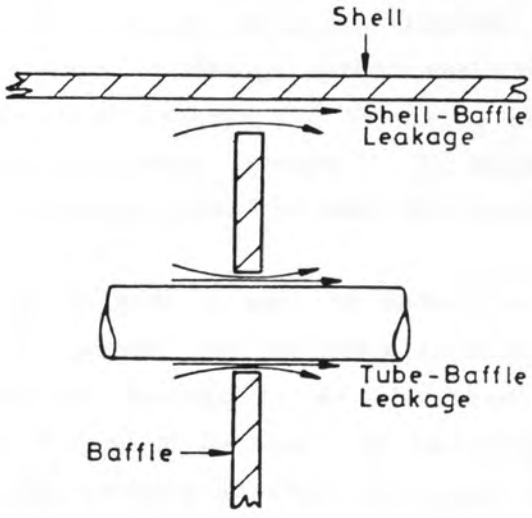

Figure 1·2 c : Tube - Baffle and Shell - Baffle Leakage

bypassing, does not have intimate contact with the heat transfer surface. Tube-baffle leakage, however, has contact in high velocity longitudinal flow and, therefore, contributes towards heat transfer.

These flowstreams can be conveniently summarised on one diagram, Figure 1.3, using Tinker's (1947) representation of shellside flow. The seminal nature of Tinker's work has always been recognised but the lack of computing capability severely restricted its use. This work has, however, come to fruition in recent years by laying the foundations of the modern network computer design methods, as discussed in Section 2.6.

1.3 Design Methods

In view of the importance and expense of shell-and-tube heat exchangers it is desirable to design them accurately.

Early design methods modelled the shellside flow as a single flowstream, known as single stream methods, which did not directly account for leakage and bypassing. These methods calculated the pressure drop and heat transfer assuming that only crossflow and window flow existed, then design or 'experience' factors were used to correct the calculated values to account for the effects of leakage and bypassing. This type of design method was rather unreliable since little was known about leakage and bypassing and the effect of each upon pressure drop and heat transfer. In extreme cases, exchangers designed in such a manner failed to meet their process requirements.

Modern design methods attempt to model the flow distribution in the form of a flow network and are known as multi-stream methods. The flow network uses an analogy to an electrical circuit, where each flowstream (as described in Section 1.3) is designated a resistance to flow. One possible network is shown in Figure 1.4, but it should be stressed that this is only one example; there are a number of other possibilities. In general the more complicated the network the more realistically the shellside flow can be modelled.

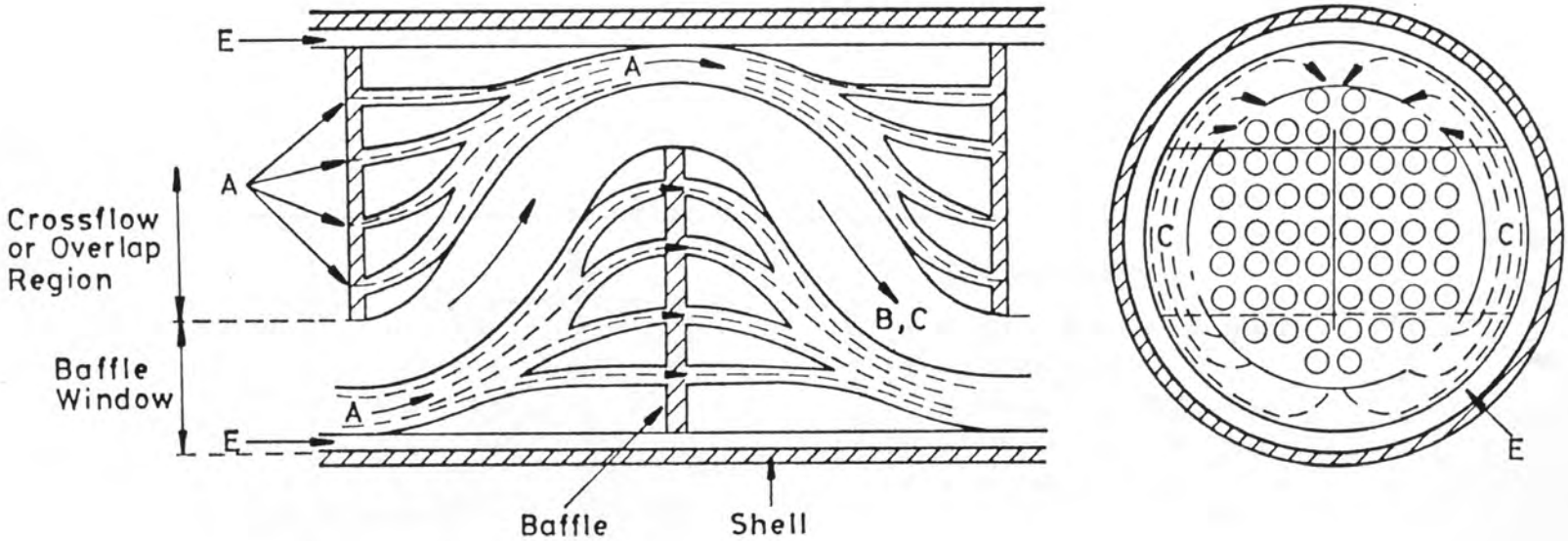

Flowstreams

A = Tube Baffle Leakage
B = Crossflow
C = Crossflow Bypass
E = Shell Baffle Leakage
W = A+B+C+E
= Window Flow in Baffle Window

Figure 1·3: Tinker's (1947) Representation of Shellside Flow

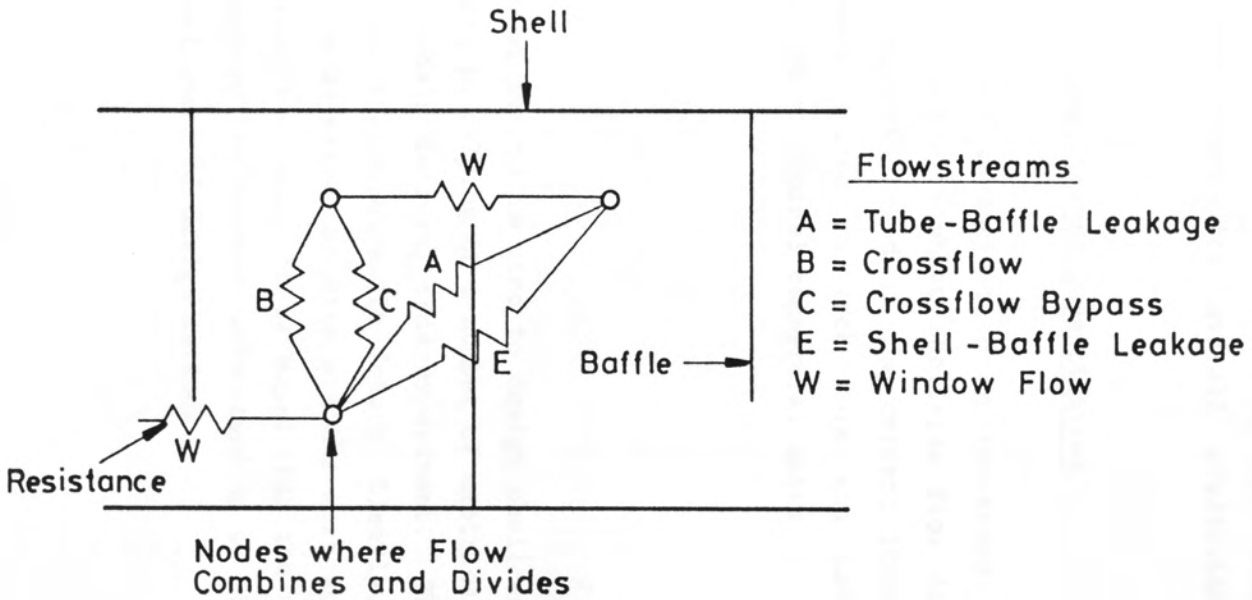

Figure 1·4: A Simple Flow Network Depicting Shellside Flow

One such computer design method is the TASC program, produced by the Heat Transfer and Fluid Flow Service (HTFS)*. This program has had considerable success in predicting overall pressure drops and heat transfer in straightforward cases, but it will become evident that (Chapter 2) there is virtually no data available which permits the detail of the models to be assessed. Only if the detail is reasonably correct can programs like TASC be used with confidence in regions beyond those where its overall predictions have been directly verified.

1.4 Scope of the Current Investigation

The present investigation is concerned with obtaining detailed information on single-phase shellside flow distribution and pressure drop. The apparatus used in the current investigation is one of the largest models used in such work and has a shellside geometry representative of typical commercial units.

Whatever method is used to design shell-and-tube heat exchangers, the engineer is relying on a number of empirical correlations and semi-empirical models deriving from experiment. This is likely to remain the case for the foreseeable future. Clearly, the more detailed and reliable the experimental data are the more accurate and reliable the design method will be. It is hoped that the work presented here will help to improve the current understanding of shellside flow and assist in the development of design methods.

---

* HTFS is a subscription based service with about 200 member companies worldwide. It provides to members authoritative computer programs, contract research, test facilities and consultancy for designers, manufacturers and users of heat transfer equipment.

CHAPTER 2

THE LITERATURE - A CRITICAL REVIEW

2. THE LITERATURE - A CRITICAL REVIEW

The following is a review of the literature concerning turbulent fluid flow and pressure drop on the shellside of shell-and-tube heat exchangers.

Shellside flow can be conveniently represented by a number of flowstreams, as discussed in Chapter 1. Pressure drop investigations of these flowstreams are generally carried out in isolation from all others. However, each flowstream can be expected to have an influence on all others in a practical exchanger. For these reasons, investigations into isolated flow phenomena are reviewed first, then the plausibility of applying the results of such investigations to the design of practical exchangers is discussed. Finally, the methods used for designing heat exchangers, in particular prediction of the shellside flow distribution and pressure drop, are presented and discussed.

2.1 Flow Across Tube Bundles

Flow across tube bundles is an important aspect of shellside flow. It is conveniently studied in rectangular tube bundles, with and without bypassing. Work in this area is critically reviewed and its application to commercial designs discussed.

2.1.1 Flow Across Tube Bundles - No Bypassing

Of all the flow phenomena relating to shell-and-tube heat exchangers, flow across tube bundles (crossflow) has been studied most. These studies have related almost exclusively to flow across rectangular banks of tubes with no bypass lanes; usually termed as ideal or homogeneous tube bundles. Bypass lanes are commonly eliminated, for rotated layouts, by half tubes fixed to the test section walls and, for in-line arrangements, by maintaining half the minimum tube spacing between outer-most tubes and test section walls as shown in Figure 2.1. Both methods also help to maintain bundle symmetry.

Crossflow pressure drop measurements can be expressed in terms of a friction factor and Reynolds number, similar to pipe flow. The purpose of this section is to present and discuss various proposals for correlating crossflow pressure drop data from ideal tube bundles.

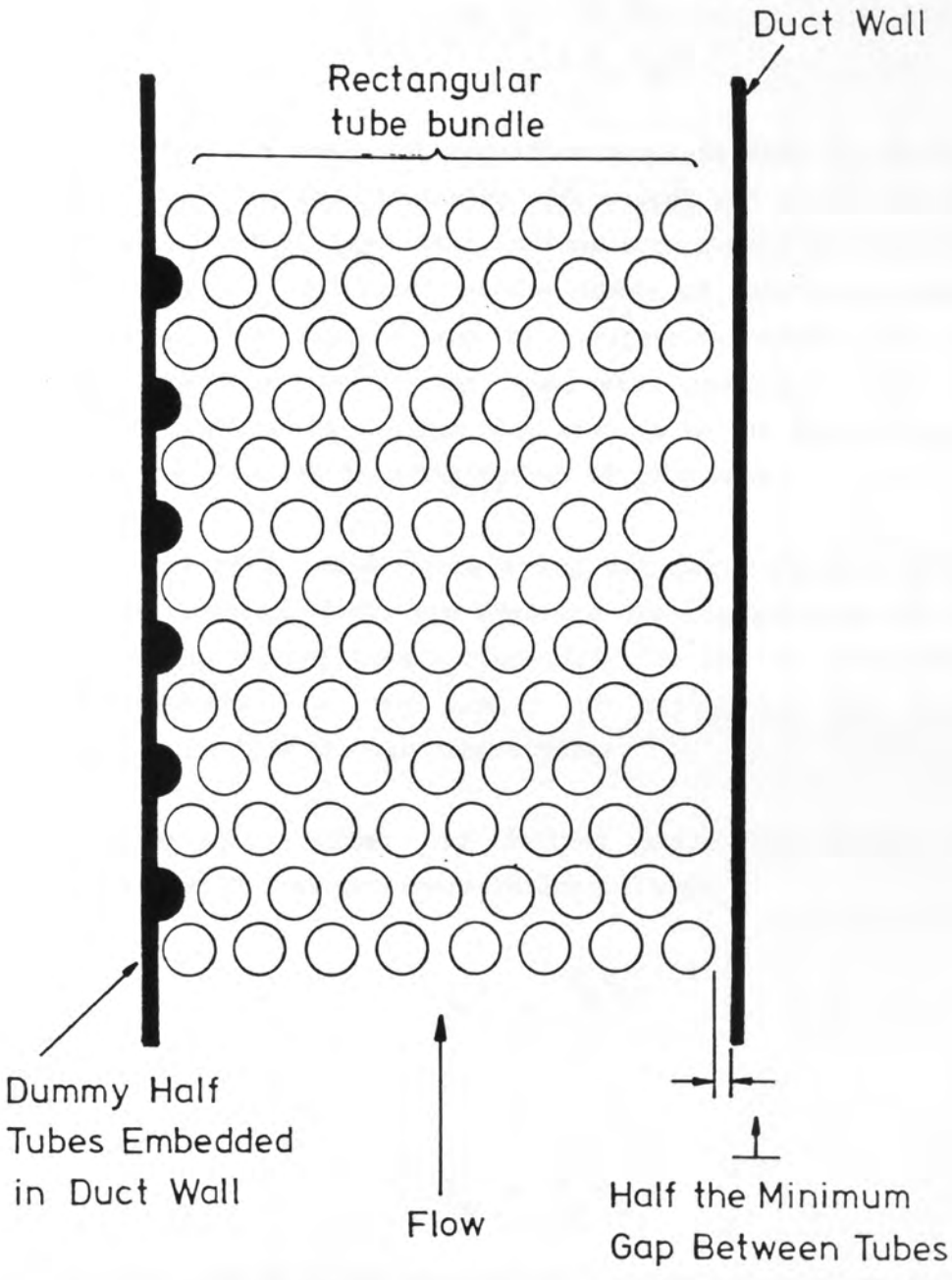

Figure 2.1: 'Ideal' Rectangular Tube Bundle Showing Methods of Eliminating Bypass Flow.

Chilton and Genereaux (1933) collected together the available published pressure drop data and attempted to produce an empirical relationship suitable for design purposes. They defined the friction factor as

$$f_c^m = \frac{2 \rho \Delta p_c}{4 N_c \dot{m}_m^2} \qquad (2.1)$$

where Δp_c is the measured crossflow pressure drop, $\dot{m}_m$ is the maximum mass flux based on the minimum crossflow area and ρ, the fluid density. N_c is the number of major restrictions encountered in flow through the bundle. This is equivalent to the number of tube rows normal to the flow for in-line layouts and for staggered layouts for which the minimum flow area is in the transverse openings. For staggered arrangements where the minimum flow area is in the diagonal gap between tubes, N_c is one less than the number of tube rows.

The use of N_c as a correlating parameter appears to be logical since, in turbulent flow, the pressure loss is governed by changes in kinetic energy rather than surface friction and is, therefore, fundamentally related to the number of expansions and contractions experienced in flow through tube bundles.

The Reynolds number was defined using the minimum clearance between tubes (D_g) as the characteristic length:

$$Re_c^m = \frac{D_g \dot{m}_m}{\eta} \qquad (2.2)$$

where

$$D_g = P_y - D_t \qquad (2.3)$$

for in-line and staggered arrangements where the minimum flow area is in the transverse gaps, or

$$D_g = P_t - D_t \qquad (2.4)$$

for staggered arrangements in which the minimum flow area relates to the diagonal gaps between tubes. P_t is the diagonal pitch between centres of tubes in successive longitudinal rows.

Two straight lines were proposed as good approximations to the limited data available at that time, one each for in-line and staggered arrangements. The relationships were

$$f_c^m = 0.314\ (Re_c^{mg})^{-0.2} \tag{2.5}$$

for in-line arrangements and

$$f_c^m = 0.751\ (Re_c^{mg})^{-0.2} \tag{2.6}$$

for staggered arrangements.

Grimison (1937) correlated the pressure data of Pierson (1937) and Huge (1937), covering a large range of longitudinal and transverse pitches, both for in-line and staggered arrangements. He defined the friction factor in an identical fashion to Chilton and Genereaux (Equation (2.1)) but did not attempt to fit the data from in-line and staggered banks with just two empirical correlations. Instead, both longitudinal and transverse pitch-diameter ratios were incorporated as parameters on a number of plots of friction factor against Reynolds number. The tube diameter was used as the characteristic length in the Reynolds number:

$$Re_c^{mt} = \frac{D_t \dot{m}_m}{\eta} \tag{2.7}$$

Interestingly, most of the combinations of longitudinal and transverse pitch-diameter ratios studied by Pierson and Huge would not generally be used in modern equipment. Commercial shell-and-tube exchangers are generally designed to the Tubular Exchanger Manufacturers Association Standards (TEMA, 1978), in which four arrangements are recommended: in-line and staggered square, equilateral triangular and rotated equilateral triangular. These four tube layouts and

relationships between various pitches for each are shown in Figure 2.2. Since the odd combinations of transverse and longitudinal pitches are not generally used, only one pitch-diameter ratio would need to be specified on a friction factor plot.

Gunter and Shaw (1945), using a selection of pressure data from the literature, represented the data for all tube arrangements and pitches on a single line. They suggested plotting a standard friction factor, modified by empirical ratios to account for tube pitch:

$$f_c^{GS} = \frac{2\rho\Delta p_c}{\dot{m}_m^2} \left(\frac{D_v}{L_c}\right) \left(\frac{P_y}{D_v}\right)^{0.4} \left(\frac{P_y}{P_t}\right)^{0.6} \qquad (2.8)$$

where, for turbulent flow

$$f_c^{GS} = 1.82 \left(Re_c^{mv}\right)^{-0.146} \qquad (2.9)$$

and

$$Re_c^{mv} = \frac{D_v \dot{m}_m}{\eta} \qquad (2.10)$$

D_v is the volumetric hydraulic diameter and L_c is the crossflow path length. They concluded that the single line was a satisfactory fit, with all the data falling within + 60% and -30% of the proposed line.

Boucher and Lapple (1948) reviewed the work of, amongst others, Chilton and Genereaux, Grimison, Gunter and Shaw. They compared each method with a comprehensive review of pressure measurements and showed that the data scattered by as much as fourfold from the proposed plots of both Chilton and Genereaux and Gunter and Shaw. The authors argued that this was because neither method was a correlation but merely an empirical representation of the data. Furthermore when correlating crossflow data in terms of a friction factor-Reynolds number relationship, an additional variable is introduced, namely tube spacing, which

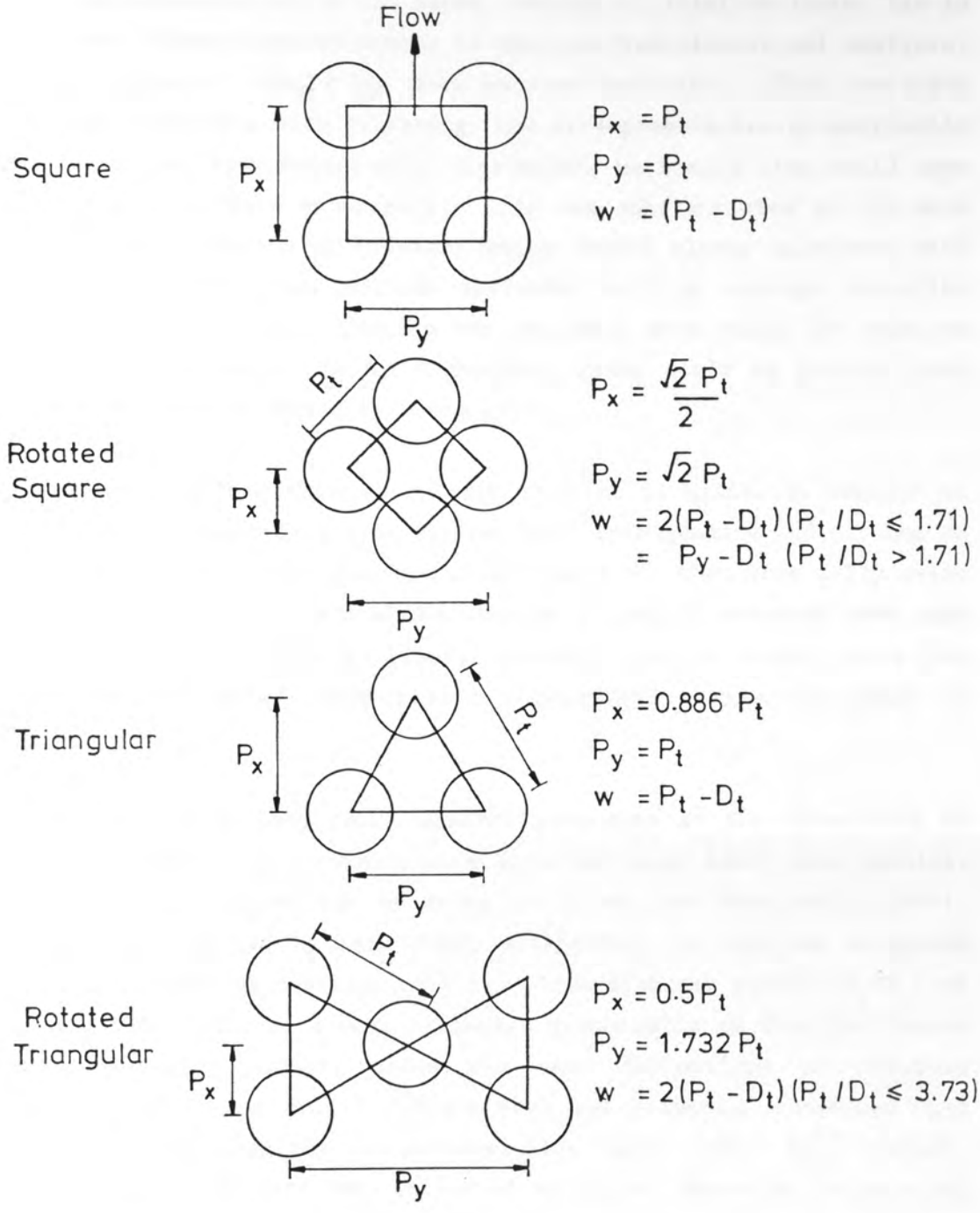

For All Arrangements $r = P_y / D_t$, $s = P_x / D_t$, $t = P_t / D_t$

Figure 2.2: Four Commonly Used Tube Layouts Showing The Definitions of The Transverse, Longitudinal and Diagonal Tube Pitches.

cannot be accounted for in the normal concept of friction factor (as in pipe flow). Since Reynolds number is derived from dimensional analysis, the principles of similarity must be complied with. They concluded that because bundles with differing tube arrangements are geometrically and, therefore, hydrodynamically dissimilar, no single line could hope to correlate the data accurately. This was substantiated by the more comprehensive approach of Grimison which showed closer agreement with the data than the other methods reviewed, with an average deviation from the data of ± 15%. Caution was expressed when using the Grimison curve since the deviation for individual cases could be greater than 15%, but no maximum deviations were given.

It appears from this early work that it is basically unsound to attempt to represent data from various tube arrangements and pitches on one or two curves. In Gunter and Shaw's defence, they were fully aware that their single line method resulted in a loss of accuracy over some existing methods. They realised, however, that a single curve had advantages over other methods from a practical engineering point of view.

As part of a long term research programme at the University of Delaware, pressure measurements were obtained using ideal tube bundles. These data were summarised by Bergelin, Brown and Doberstein (1954). The work was limited to equilateral triangular, in-line and staggered square arrangements covering only two pitch-diameter ratios (P_t/D_t) of 1.25 and 1.50. The data were presented graphically as friction factor against Reynolds number, using the same definitions as Grimison (Equations (2.1) and (2.7)). Their work was primarily concerned with what they defined as the transitional flow region ($100 < Re_c^{mt} < 4000$). A small amount of data was collected at higher Reynolds numbers and these were reported to agree well with previous data and could be predicted well by the Grimison correlation.

Grant and Murray (1972) fitted the pressure drop data of Bergelin et al. (1952) and data taken from Grimison's plots to give convenient relationships for use in the HTFS design program STEP. They defined both friction factor and Reynolds number identically to Grimison and presented a friction factor in the form of a Blasius equation:

$$f_c^m = a_{Gc}(Re_c^{mt})^{-b_{Gc}} \qquad (2.11)$$

giving coefficients (a_{Gc}) and exponents (b_{Gc}) in tabular form as functions of both Re_c^{mt} and P_t/D_t for each of the four commonly used arrangements. They stressed that their relationships were not correlations but empirical representations of the data; a number of simplifications were made in order to avoid computational problems and it was pointed out that in some cases it had been necessary to overestimate the experimental data. In exceptional cases this overprediction was as high as 100%.

Moore (1974) also used the data of Bergelin et al (1952) along with the data of Pearce (1973) to produce relationships for use in the HTFS design program TASC. The friction factor and Reynolds number were defined in an identical fashion to Chilton and Genereaux (Equations (2.1) and (2.2)). Moore argued that since crossflow is essentially flow through a series of contractions and expansions, the use of the gap between tubes in the Reynolds number was more appropriate than the tube diameter. He did not attempt to fit all the data by two curves as Chilton and Genereaux did but derived relationships for each of the four commonly used tube arrangements: in-line and staggered square, equilateral and rotated equilateral triangular. Moore plotted his relationships along with the data they represented and compared these with a selection of data from Grimison (1937), Zukauskas (1972) and Jakob (1938). All the data fell within ± 30% of the straight line relationships. While this result does not refute the arguments put forward by Boucher and Lapple on dimensional analysis, it does imply that the gap between tubes rather than the tube diameter is the important correlating parameter.

Zukauskas obtained a large amount of pressure data for flow of gases across ideal tube bundles. He summarised this work in the Heat Exchangers Design Handbook (HEDH, 1983) along with correlations to his and a selection of data from other sources. Relationships for both in-line and staggered arrangements were presented in the form of inverse power series, each covering a small range of Reynolds number (Re_c^{mt}) so that an accurate fit could be obtained:

$$\frac{Eu}{k_2} = fn\ (Re_c^{mt}) \qquad (2.12)$$

where k_2 is a geometry factor accounting for both transverse and longitudinal pitch-diameter ratios. The Euler number (Eu) is related to the more commonly used friction factor by

$$Eu = 4\ f_c^{\ m} \qquad (2.13)$$

These relationships were recommended for tube bundles with at least ten rows, correction factors were given for fewer rows.

The Engineering Science Data Unit (ESDU, 1974) presented a selection of pressure drop data based on a wide review of investigations relating to flow across ideal tube bundles. The data were correlated using an overall pressure loss coefficient, k_p:

$$k_p = \frac{2\ \rho\ \Delta p_c}{N_c\ \dot{m}_m^2} \qquad (2.14a)$$

where

$$k_p = k'_p\ \beta_i \quad (i = 1,4) \qquad (2.14b)$$

and the coefficients, β_i, are correction factors accounting for fluid property variations, bypassing, flow inclination and tube roughness respectively. k'_p is a reference loss coefficient for the case when none of the effects relating to β_i are significant and there are ten or

more tube rows. As with Zukauskas, the reference pressure loss coefficient is four times the more commonly used friction factor. Charts of k'_p against Reynolds number (Re_c^{mt}) were presented for both staggered and in-line tube arrangements, one each for a particular pitch-diameter ratio.

Butterworth (1979) proposed a novel method for correlating crossflow pressure drop using a porous media analogy. The pressure drop through a porous medium, for one-dimensional flow, can be expressed as

$$\Delta p_c = \frac{\eta L_c u_s}{k_B} \qquad (2.15)$$

which is Darcy's equation for viscous flow, where u_s is the superficial velocity and k_B is termed the flow conductivity or more usually the permeability coefficient.

In developing his correlations Butterworth assumed that a tube bundle could be treated as an isotropic porous medium, that is k_B for a square in-line layout is the same as that for a rotated square layout, likewise for triangular and rotated triangular arrangements. Data points were taken from the charts of ESDU (1974) and correlated in the form

$$k_B = fn\ (Re_c^{st},\ (P_t - D_t)\ ,\ 1/D_v) \qquad (2.16)$$

one equation each for square and triangular arrangements, where D_v is the volumetric hydraulic diameter and Re_c^{st} is the Reynolds number based on the superficial area and tube diameter.

Butterworth discovered that while the triangular and rotated triangular data were well correlated, there was some scatter shown between the square and rotated square data. However, the observed scatter was of the same order as variations in data obtained in different investigations. Lee (1981) argued that rotated square

arrangements have resistance properties more closely related to triangular layouts, since they are all staggered arrays, so the original assumption of isotropy might not be strictly correct. EDSU (1979), in a similar approach to correlating pressure data, found it necessary to distinguish between in-line and rotated square arrangements, substantiating further the point raised by Lee.

Butterworth went on to show that the relationships in terms of k_B could be converted to the more commonly used friction factor. The resulting equations were, for square and rotated square

$$f_c^s = 0.061 \frac{D_t^2 D_v}{(P_t - D_t)^3} Re_c^{st^{-0.088}} \qquad (2.17)$$

and for triangular and rotated triangular

$$f_c^s = 0.45 \frac{D_t^2 D_v}{(P_t - D_t)^3} Re_c^{st^{-0.267}} \qquad (2.18)$$

2.1.2 Comparison Between Crossflow Correlations

A relative assessment can be made of the proposed crossflow relationships by plotting each on the same basis. For convenience Grimison's definitions of friction factor and Reynolds number are used as the standard, since the majority of relationships are defined in this way. The friction factor correlations chosen for comparison are Grimison, Grant and Murray, Moore, Zukauskas, Butterworth and ESDU. Chilton and Genereaux (1933) and Gunter and Shaw's (1945) relationships are not considered further as these were shown, by Boucher and Lapple (1948), to be inferior to Grimison's correlation.

Since the definitions of Moore and Butterworth differ from Grimison's, they must be related to the standard form to give a consistent basis for comparison. This procedure is shown in Appendix A.

Figure 2.3 shows a comparison of the various friction factor relationships for rotated square tube layouts and diagonal pitch-diameter ratios of 1.25, 1.50 and 1.75. Only rotated square is considered since this is the layout used in the current experimental

work. The data of ESDU are used as a 'benchmark' against which other correlations are judged, since these data are believed to be compiled from the most thorough search of the literature. The key features shown by the three plots are:

1) The points taken from Grimison and Zukauskas's correlations agree to within + 30% to -20% of the ESDU data (apart from Zukauskas, Re = 10^3, P_t/D_t = 1.5, which is 60% above ESDU).

2) In general, Grant and Murray represent ESDU least well, consistently overpredicting the friction factor. This overprediction is most significant at the largest pitch-diameter ratio. Furthermore, it predicts Grimison very poorly despite being loosely based on this correlation; Grant and Murray had indicated, however, that their relationships were not correlations but conservative empirical representations of the data.

3) Butterworth's relationship based on an isotropic porous medium generally agrees poorly with ESDU. The agreement is only reasonable at low Reynolds numbers; the shallow gradient of the curve results in a progressively larger overprediction with increasing Reynolds number. Although the ESDU curves form the basis of Butterworth's correlation, accuracy is lost since both in-line and rotated square layouts are represented by the same relationship. In the light of this, the assumptions of isotropy between in-line and rotated square layouts appears to be unfounded.

4) Moore's method represents the data taken from the ESDU curves as well as Grimison and Zukauskas. This is rather surprising since the correlation was based on a diagonal pitch-diameter ratio (P_t/D_t) of 1.25 for a substantial proportion of the Reynolds number range.

In conclusion, ESDU, Grimison, Zukauskas and Moore all agree well with each other over the range studied. Moore's correlation has a

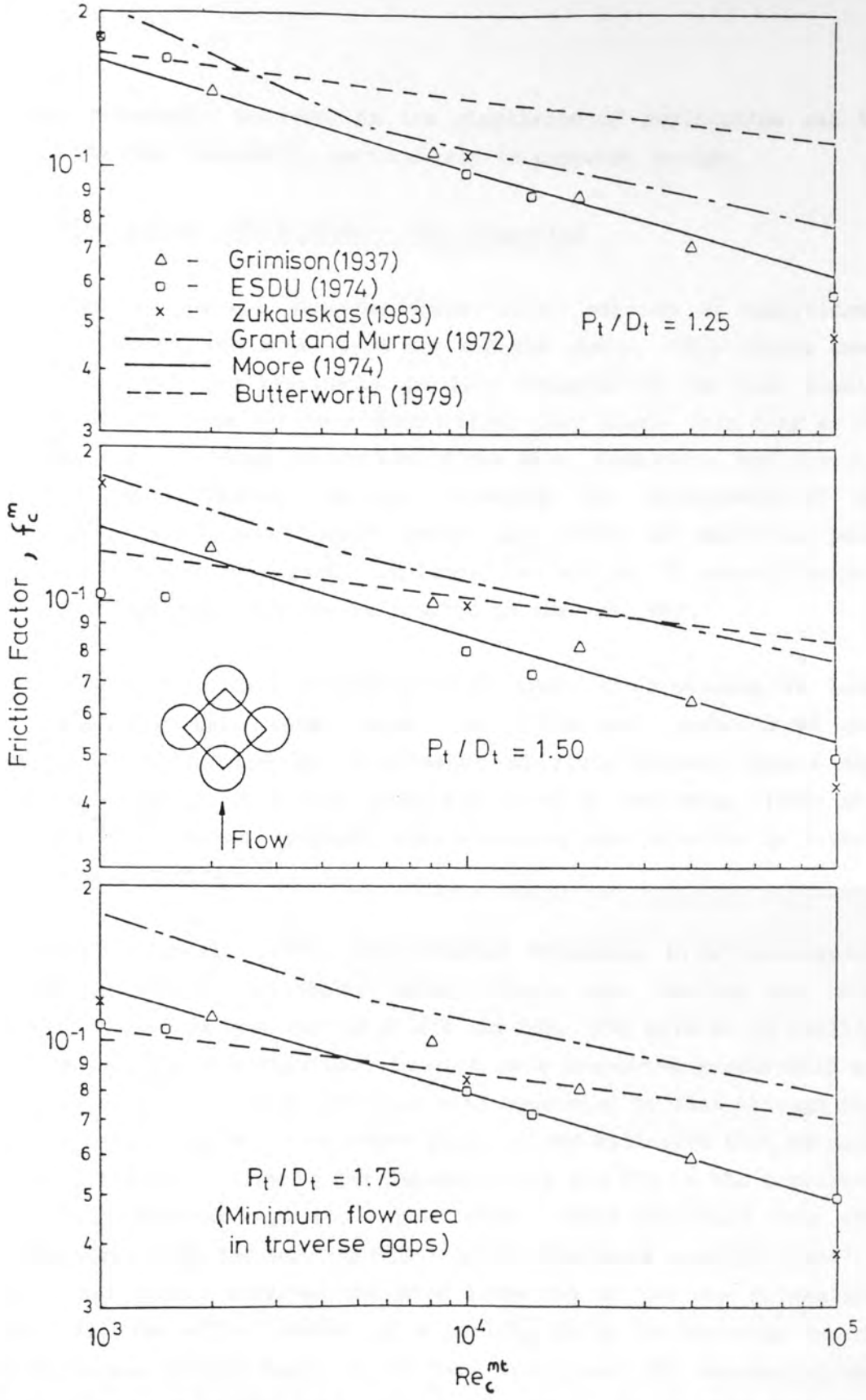

Figure 2.3: Comparison Of Various 'Ideal' Crossflow Correlations Over A Range of Re No. And Diagonal Pitch–Diameter Ratios.

distinct advantage, however, in its simplicity of application and is clearly the most desirable, particularly in computer design.

2.1.3 Flow Across Tube Bundles - With Bypassing

Mechanical design considerations often require a significant clearance between the outer tube row and the shell. This bypass lane has a relatively low resistance to flow compared to the tube bundle because the wall does not have obstructions that create form drag as in a tube bundle. A large proportion of the flow, therefore, may circumvent the heat transfer surface, lowering the efficiency of an exchanger. Additional bypass lanes may arise in multiple pass exchangers (in-line pass partition lanes) but are not discussed further since, in principle, they may be treated in the same way.

Cernik (1955) made a photographic study of bypassing in both rectangular and cylindrical geometries. His work established the existence of a substantial interchange of fluid between bypass and crossflow streams. From this study and those of Destremps (1956) and Bryce (1957) it became apparent that bypassing was potentially a very significant flowstream.

Bergelin et al. (1959) also studied bypassing in a rectangular tube bundle with a triangular layout. Tests were carried out with bypass to crossflow area ratios of 21% and 30%. The effects of sealing strips were also investigated. Results were presented graphically as the ratio of pressure drop for flow with bypassing to that through the ideal crossflow bundle. From these plots it was estimated that as much as 75% of the total flow in the laminar limit and 50% in the turbulent limit could flow through the bypass lane. They concluded that the limited work conducted was insufficient to draw more specific conclusions. Two global observations were presented on the use of sealing strips: (a) the effectiveness of a sealing strip in blocking bypass flow decreases as the depth of the bank increases; (b) increasing the number of sealing strips leads to a performance more closely approaching a tube bundle with no bypass lanes.

Bell (1960) subsequently presented a simple empirical relationship, based on the data of Bergelin et al. (1959), for pressure drop with bypassing:

$$\frac{\Delta p_b}{\Delta p_c} = \exp\left[-3.8\, F_b \left\{1-(2N_s/N_c)^{1/3}\right\}\right] \qquad (2.19)$$

where Δp_b is the pressure drop with bypassing, Δp_c is the ideal crossflow pressure drop, F_b is the fraction of the minimum total flow area that is occupied by the bypass lane and N_s is the number of sealing strips. The bypass area is based on the minimum gap between duct (or shell) wall and outermost tube in the bundle. Bell expressed some reservations about this empirical relationship since it was based on a limited investigation. He concluded that whenever possible bypass lanes should be avoided or blocked with sealing strips. It was also suggested that a tube bundle with a minimum gap between outermost tube and wall less than one half the minimum clearance between adjacent tube corresponds closely to an ideal tube bundle. In a further article (Bell, 1963) the coefficient 3.8 was altered to 4.0 in keeping with a change in the bypass flow area definition; the new area was defined as the original flow area, less the area associated with half the minimum gap between tubes (for each bypass lane).

Interestingly, Equation (2.19) is used in a recent update of the Bell commercial exchanger design method (HEDH, 1983), despite Bell's earlier comments. It will become apparent that this is a reflection on the lack of bypassing data rather than the ability of Equation (2.19) to predict accurately the effect of bypass lanes and sealing strips on crossflow pressure drop. This most recent article returned to the original definition of bypass area.

Moore (1974) derived a bypass friction factor relationship using the data of Bergelin. Unlike the 'integral' approach of Bell, Moore required a separate bypass friction factor relationship to apply in the flow network model used in the HTFS program TASC (see Section 1.4 or 2.6.2). In order to develop a practical relationship Moore used a simple parallel flow concept: the pressure drop through the bypass equals that through the ideal portion of the bundle, implicitly this assumes that the presence of bypassing does not affect the crossflow pressure drop other than reducing the mass flowrate through the ideal portion. Once this assumption is accepted, it is a simple matter to calculate the bypass flowrate using the measured pressure drop combined with a pressure drop relationship from ideal bundles. The bypass

flowrate can then be related to the overall measured pressure drop (since bypass pressure drop is assumed to equal the crossflow) using a friction factor-Reynolds number relationship. Moore derived one bypass correlation for turbulent flow, presented in a Blasius form:

$$f_b = a_{Mb} \, Re_b^{-b_{Mb}} \qquad (2.20)$$

The bypass area was defined in the same manner as Bell (1963) and the characteristic length in the Reynolds number was defined as the minimum gap between outer-tube and shell/duct wall less one half the minimum gap between tubes. The bypass correlation should only strictly be used in conjunction with Moore's ideal crossflow relationships since they are implicitly linked through the parallel flow analysis.

ESDU (1974) derived bypass loss coefficients (four times a friction factor) directly from the ideal crossflow curves by relating bypass geometry with ideal bundle geometry. This approach, however, proved unsatisfactory because the resulting bypass loss coefficients were 'lower by a factor than those found in practice ...'. The coefficients were, therefore, 'suitably factored' to bring them in line with unspecified data; no further details were given. The ESDU method was presented as a simple hand calculation for pressure drop across rectangular tube bundles with bypassing. To avoid an involved iterative procedure a bypass correction factor (β_2) was defined, which adjusted the pressure coefficient from the ideal crossflow curves (based on total flow and total minimum flow area) to represent crossflow with bypassing.

Bypass correction factors were given graphically as a function of transverse pitch to diameter ratio, bypass width to diameter ratio and Reynolds number based on the total mass flux. In this manner the need to calculate the bypass flow fraction was avoided. As with Moore's method, ESDU's bypass correction factors are only strictly applicable when used in conjunction with their ideal crossflow curves.

Currie (1983) measured local velocities in a rectangular tube bundle with and without bypassing using Laser Doppler Anemometry (LDA). The apparatus he used was similar to previous workers, except that pyrex glass was used for both the bundle and the test sections walls, to enable refractive index matching with a suitable fluid. Local velocities were measured, in 3-dimensions, and overall pressure drops, for the cases of no bypassing, bypassing with no sealing strip, and bypassing with sealing strips. He concluded that the flow in each case was two dimensional, which would be expected in a rectangular model, and that sealing strips tended to restore the velocity distribution measured in the case of a full bundle with no bypassing.

Lee et al. (1983) studied bypassing using a rectangular tube bundle with a bypass lane between the bundle and test section wall, similarly to earlier workers such as Bergelin et al. (1959). Lee, however, partitioned the flow at the exit of the test section into bypass and crossflow by placing a thin sheet of metal up against the tube in the final row next to the bypass lane. Using this arrangement the flowrates and pressure drops for each stream could be recorded. Results were presented graphically as pressure coefficient against Reynolds number, Re_c^{mt}, and bypass mass flow fraction against Re_c^{mt}. The bypass mass flow fraction was shown to be highly dependent on the ratio of bypass lane width to transverse width of the bundle, but relatively independent of Reynolds number. Lee also discovered that the Bell (1960) method significantly overpredicted his measured bypass flow fractions.

Russell and Wills (1983) correlated Lee's data using the same crossflow and bypass friction factor definitions as Moore (1974). Unlike Moore, however, Wills was able to use the measured crossflow and bypass flowrates for his correlation instead of resorting to a parallel flow model. In addition they checked the validity of the assumption used by all previous workers concerned with bypassing: the bypass stream does not influence the crossflow stream, other than reducing the crossflow flowrate. Lee (1981) had previously measured pressure drops over rectangular tube bundles with no bypassing. Russell and Wills correlated this data in the same manner as Lee's bypassing measurements

and compared the two crossflow data sets by plotting friction factor with bypassing divided by friction factor with no bypassing against Reynolds number, as shown in Figure 2.4. In this manner they showed that the greatest deviation from the non-bypassing friction factor was exhibited at the highest bypass/crossflow flowrate ratio but they did not expand on this. The trend shown by the data, however, is due to the establishment of the flow distribution; initially a uniform flow profile exists in the duct upstream of the bundle, as the flow enters the bundle some of the flow will migrate towards the lower resistance bypass lane. Fluid migration would continue throughout the length of the test section unless it were sufficiently long to create an equilibrium between forces acting on both bypass and crossflow, thereafter the ratio of crossflow to bypass flowrates would remain constant. Clearly, from the foregoing argument, Lee's bypass flow measurements, at exit from the test section, are higher than the average flow in the bypass lane and vice versa for crossflow. This would be more pronounced with large bypass areas since more fluid 'percolates' from bundle to bypass. This effect manifests itself as an increased crossflow friction factor, when a bypass lane is present, simply because these friction factors are based on the minimum crossflow flowrate (that measured at exit from the bundle). This is clearly shown to be the case in Figure 2.4. Conversely, the bypass friction factors will err on the low side since the maximum bypass flowrates were used in Russell's correlation.

Martin et al. (1987) measured pressure drops for isothermal air flow over rectangular tube bundles with and without a bypass lane, using a triangular layout and diagonal pitch to diameter ratio of 1.25. A similar set-up to Lee et al. (1983) was employed so that bypass and crossflow flowrates could be measured at exit from the test section. The results were presented as a bundle pressure loss coefficient (four times a friction factor) against Reynolds number (Re_c^{mc}) and these were compared with the correlations of Bell (1960), ESDU (1974) and Zukauskas (HEDH, 1983). Zukauskas was shown to give the best fit to the data for no bypassing. The Bell method for bypassing underestimated, while ESDU overestimated, the pressure loss coefficient derived from the experimental data. These results can be interpreted as an overestimation and underestimation of bypass flow fractions

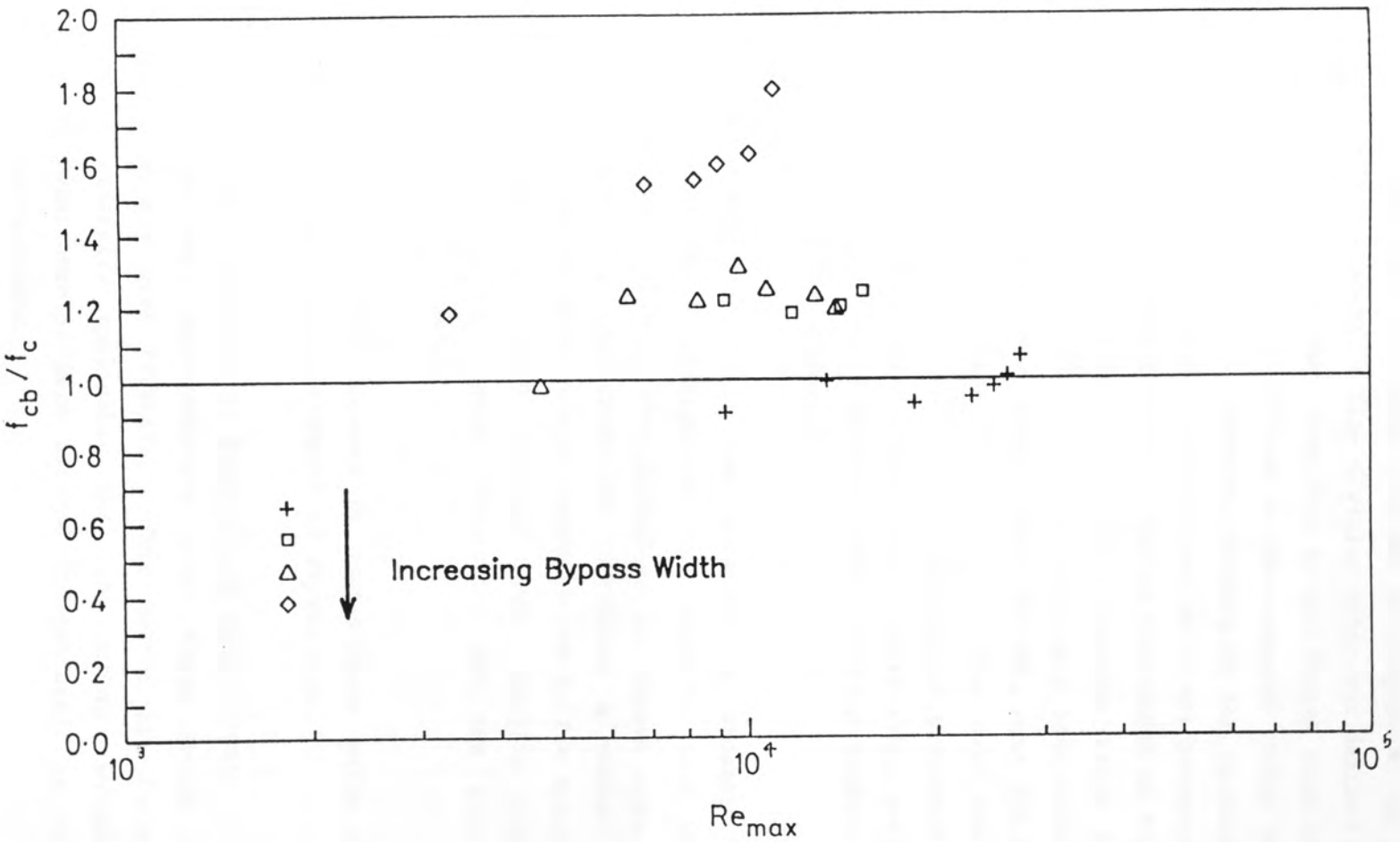

Figure 2.4: Comparison of 'Ideal' Crossflow Friction Factors and Friction Factors Derived from Measured Crossflow Flow Rates with a Bypass Lane Present (Lee et al., 1983). [after Russell and Wills, 1983]

respectively. Martin also investigated the interchange of fluid between bundle and bypass lane. By assuming that the bypass and tube bundle inlet mass flow rates divided in proportion to the respective cross-sectional areas, a flow division ratio was defined reflecting the proportion of fluid that transfers to the bypass from the bundle. The flow division ratio was defined as the measured outlet bypass flowrate minus the assumed inlet flowrate, divided by the assumed inlet cross-flow flowrate. The mass flow division ratio was presented graphically as a function of Reynolds number, and is reproduced in Figure 2.5. The key feature shown is that the flow division ratio increases with increasing bypass flow area but is relatively independent of Reynolds number. For the largest bypass width (30 mm), over 60% of the assumed inlet crossflow transfers to the bypass lane over the test section length. This result confirms the hypothesis presented earlier that using the maximum bypass flowrate for correlating purposes (as did Russell and Wills) would produce lower friction factors than using a more representative average.

Unfortunately, it is not possible to present the bypassing relationships in a generalised form akin to that for the ideal crossflow correlations; the definition of bypass area and the link between bypassing and crossflow introduces a number of unrelated variables such as bundle-shell clearance and baffle spacing as well as tube diameter and pitch. However, some specific comparisons were presented in the preceeding discussion and the following general conclusions can be made:

1) Bell's method appears to overestimate while ESDU tends to underestimate the degree of bypass flow.

2) The correlation of Russell and Wills (1983) is likely to be the most representative since these derive from measured bypass mass flowrate. This method is, in a sense, more generally applicable than the others reviewed since the relationships were derived independently of ideal crossflow correlations.

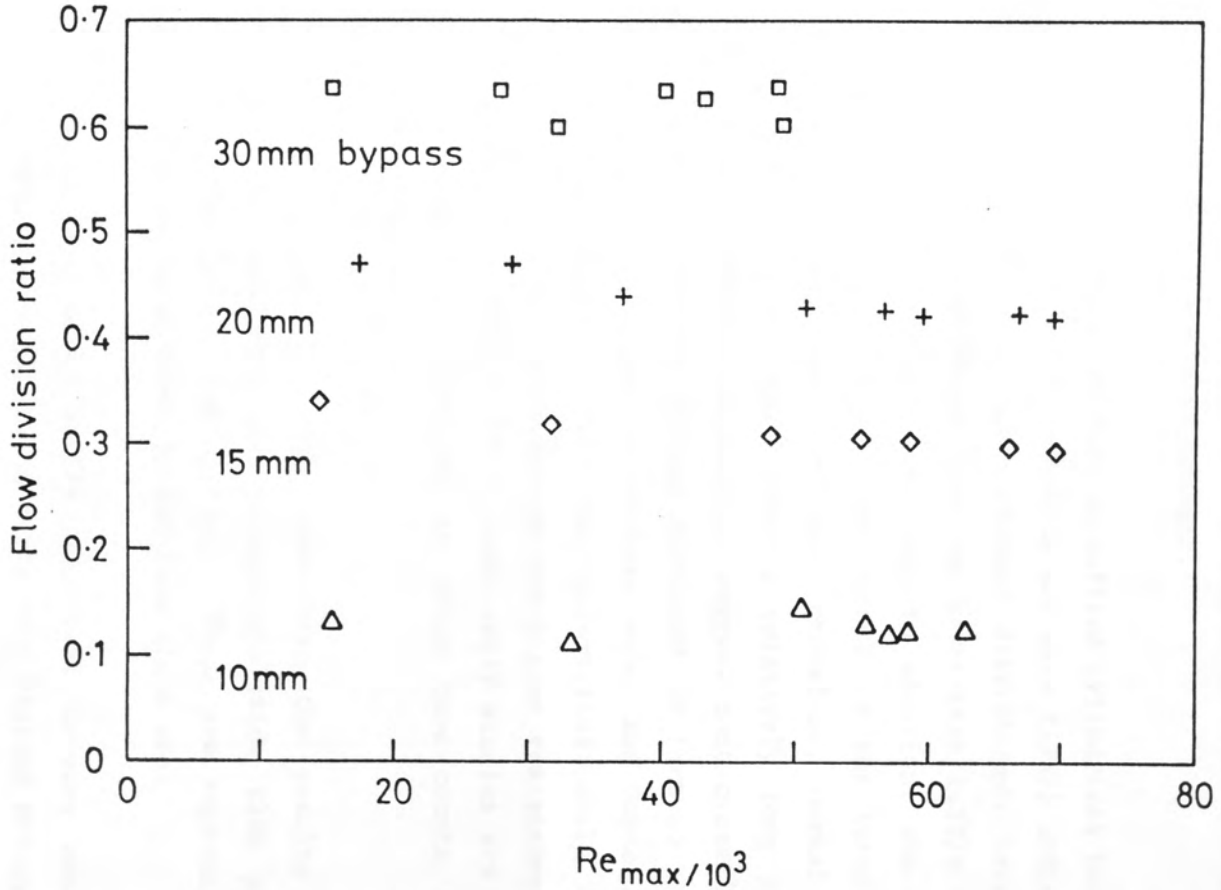

Figure 2.5: Variation of Flow Division Ratio with Reynolds Number for a Range of Bypass Widths. [after Martin et al., 1987]

2.1.4 Application to Practical Exchangers - Crossflow and Bypassing

The majority of ideal crossflow and bypassing pressure drop correlations are used in the design of commercial cylindrical exchangers. It is not immediately apparent, because of geometric dissimilarities between rectangular and baffled cylindrical units, that these correlations remain valid. This section attempts to establish the validity of applying these to commercial designs.

Early photographic studies in baffled cylindrical bundles by Kopp, Sennstrom and Gupta (1947) and Gupta and Katz (1957) indicated that the shellside flow was very non-uniformly distributed; large wakes were shown to exist, originating from the downstream baffle tip and penetrating into the crossflow zone and, in addition, the crossflow was inclined at an angle rather than normal to the tubes as in ideal bundles. They concluded that pure crossflow, normal to the tube bundles was approached only after a relatively long baffle overlap section. These studies immediately suggest that crossflow in cylindrical baffled geometries is very different in form to the ideal case. However, Kopp et al. used a tubeless model and Gupta and Katz used relatively few tubes. Such non-uniformities would diminish with increasing numbers of tubes due to the higher resistance to flow. It could be argued, therefore, that these early studies are not representative of commercial practice, in which tube counts are generally larger than those studied.

Palen and Taborek (1969) summarised the results of Gupta in annotated form depicting generalised shellside flow patterns as a function of baffle cut and spacing. These are reproduced in Figure 2.6. The key features shown by the flow plots are:

1) Large and small baffle cuts lead to very non-uniform flow conditions, with low velocity eddy regions occupying a significant proportion of the baffle compartment. This type of distribution leads to inefficient conversion of pressure drop to heat transfer.

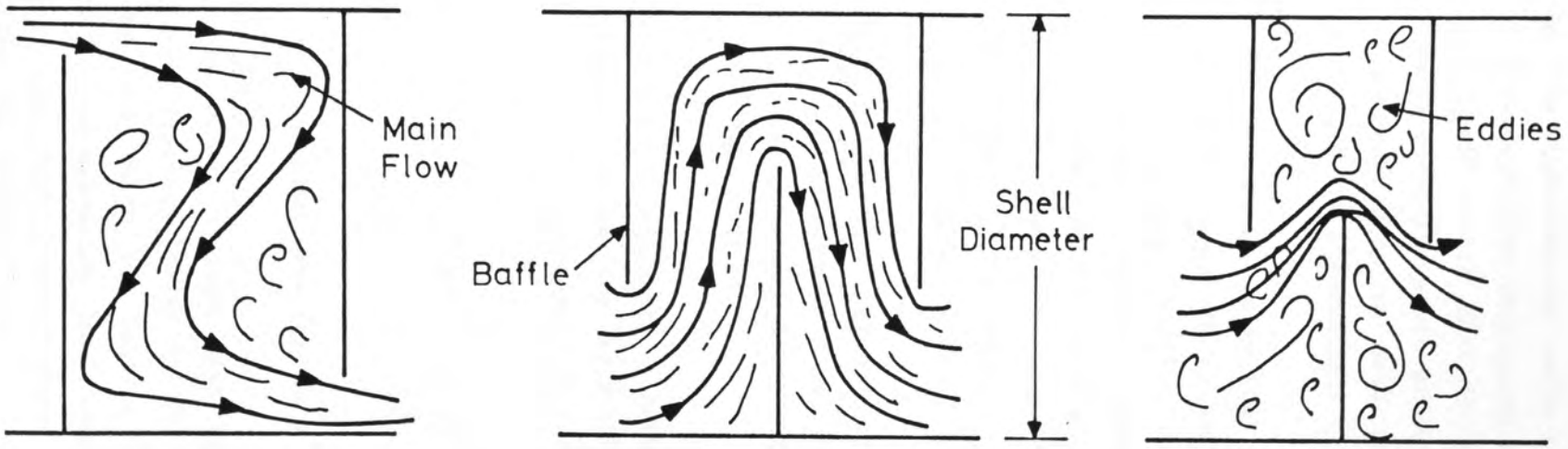

a. Small baffle cut, large baffle spacing.

b. Medium baffle cut and spacing.

c. Large baffle cut, small baffle spacing.

Figure 2.6: Generalised Shellside Flow Patterns as a Function of Baffle Cut and Spacing. [after Palen and Taborek, 1969]

2) At some 'intermediate' value of baffle cut and spacing reasonably uniform flow conditions are created, in which the crossflow tends toward that in ideal arrangements. This intermediate condition would produce the most efficient conversion of pressure drop to heat transfer (no details were given concerning the intermediate geometry).

Palen and Taborek indicated that they were able to determine the necessary corrections required to relate ideal bundle pressure drop correlations to non-ideal baffled arrangements. The data of Brown (1956) was used which cover a limited range of baffle cuts and spacings. No further details were given since their work is proprietary to Heat Transfer Research Incorporated (HTRI), a similar organisation to HTFS, based in the USA. It is likely, however, that these corrections were purely empirical.

In addition to flow pattern effects due to the presence of baffles, the varying cross-sectional area in a cylindrical arrangement imposes an acceleration and decceleration on the crossflow which is absent in ideal tube bundles.

Emmerson (1963) suggested a method of calculating an effective crossflow area. Since the effective velocity is proportional to $(1/A_{eff})^2$ (assuming a constant friction factor), he showed that

$$A_{eff} = \sqrt{\left[\frac{N_c}{\sum_{1}^{N_c} (A_r)^{-2}}\right]} \qquad (2.21)$$

where A_r is the minimum area for the r^{th} row.

The use of an average area does not account for the added accelerational pressure losses due to the changing cross-sectional flow area. However, Palen and Taborek (1969) indicated that they had accounted for acceleration loss from theoretical considerations and established that such losses, under typical conditions, were small compared with the friction loss.

Moore (1974) also derived a relationship for the mean crossflow area. He defined this area as

$$\bar{A}_c^m = C_w \frac{W}{P_y} B_s \qquad (2.22)$$

where W is the minimum gap per transverse pitch (see Figure 2.2), C_w is the average superficial crossflow width over the crossflow path length L_c. The value of C_w is equal to the cross-sectional area swept parallel to the crossflow stream, divided by the crossflow path length. The use of C_w implicitly assumes that the outer tubes of the bundle form a perfect circle, such that the outer tube limit diameter is constant around the circumference. This relationship is only strictly applicable to large bundles where non-uniformities in the outer tube limit diameter have little effect on the total crossflow area.

Moore considered further the effect of variations in velocity over the crossflow region on pressure drop. By integrating the pressure drop relationship, Equation (2.1), over the crossflow length, using a variable crossflow area and constant friction factor, Moore showed that

$$\bar{f}_c^m = f_c^m \; 0.5 \left(\frac{D_{ot}}{L_c}\right)\left(\frac{C_w}{D_{ot}}\right)^2 \ln\left[\frac{\frac{D_{ot}}{2} + \frac{L_c}{2}}{\frac{D_{ot}}{2} - \frac{L_c}{2}}\right] \qquad (2.23)$$

where $\bar{f}_c^m$ is the friction factor for a circular bundle, D_{ot} is the tube bundle diameter and L_c is the crossflow path length.

To assess the significance of this correction to the ideal bundle friction factor, Equation (2.23) has been manipulated (as shown in Appendix B) to express $\bar{f}_c^m$ as a function f_c^m and B_c (baffle cut expressed as a fraction of shell diameter) only. The resulting function is shown in Figure 2.7 as a plot of the ratio $\bar{f}_c^m$ to f_c^m against $(1-1.2B_c)$. Interestingly, the plot shows that for usual design practice ($.58 \leq 1-1.2B_c \leq 0.76$, Taborek, 1979) the corrected friction

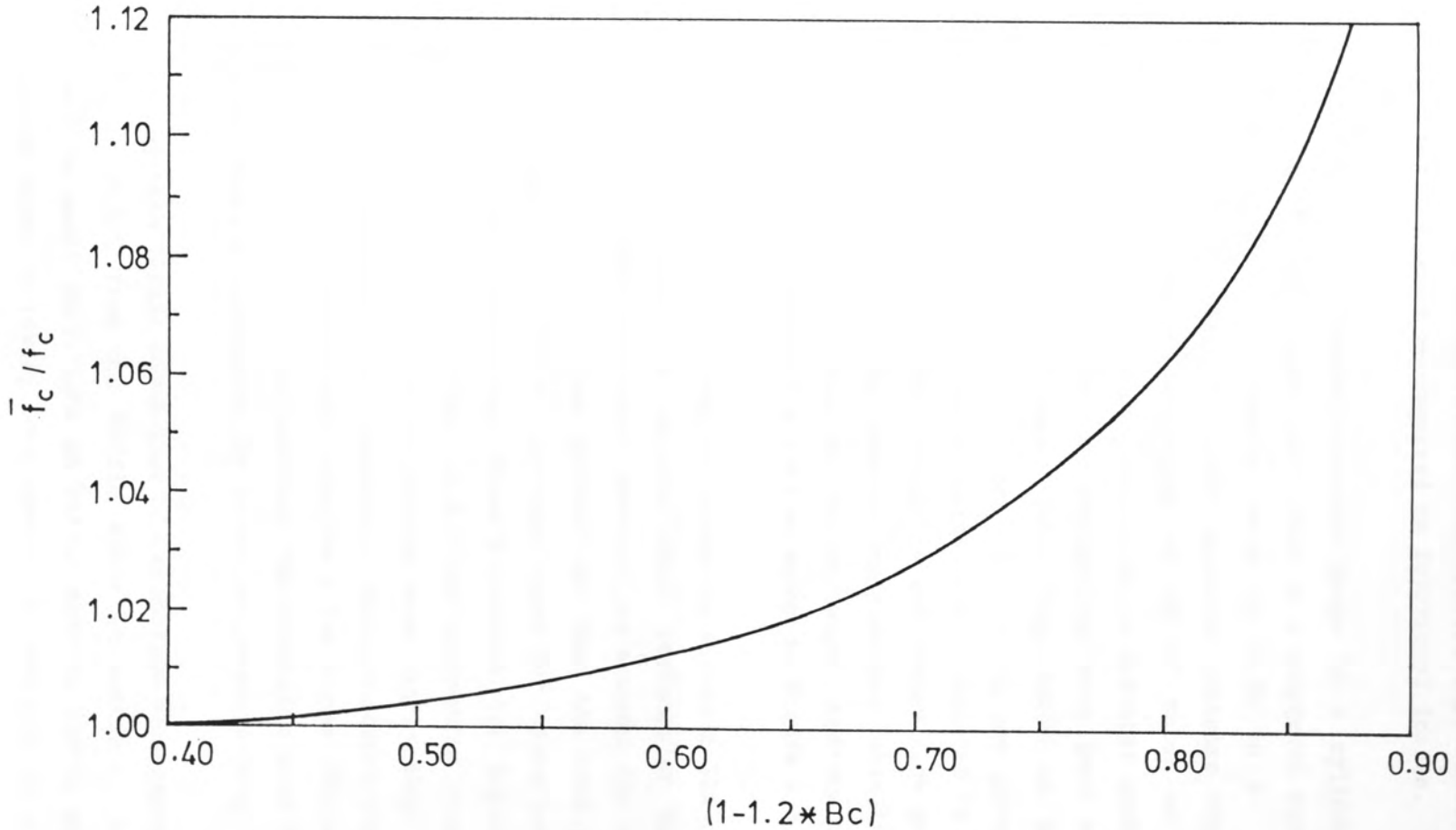

Figure 2.7: Ratio of Moore's (1974) Corrected Crossflow Friction Factor (Cylindrical Bundles) with the Ideal Friction Factor (Rectangular Bundles) as a Function of Baffle Cut.

factor is less than 5% greater than for the ideal bundle. This result concurs with the qualitative remarks made by Palen and Taborek (1969): from theoretical considerations they stated that accelerational losses were typically small as compared to frictional losses.

Brown (1956) studied pressure drops in a cylindrical exchanger consisting of eighty tubes (3/8" O.D) in a staggered square layout with a diagonal pitch to diameter ratio of 1.25 in a 5.25" internal diameter shell. Leighton (1955) measured pressure drops in a larger cylindrical exchanger consisting of 470 ¼" tubes on an equilateral triangular layout with a diagonal pitch to diameter ratio of 1.33 in an 8 3/8" O.D. shell. Both investigations were part of the Delaware University Research Programme using rigs known as Model 9 and 10 respectively. The main dimensions of each rig are given in Tables 2.1 and 2.2. In both cases leakage paths were eliminated by sticking sheets of neoprene on the baffles. Crossflow and window flow pressure measurements were obtained using pressure instrumented tubes inserted into the bundle on the central axis of the exchanger, mid-way between baffles, and in line with the baffle cuts as shown in Figure 2.8.

Brown's crossflow results agreed to within ± 30% of the turbulent flow results from the earlier ideal rectangular bundle crossflow studies. He made no attempt, however, to account for bypassing of the bundle even though he had pointed out that the area for bypass flow ranged from 15 to 25% of the total area for crossflow. Bell (1963) used this fact to correct Brown's results for bypassing using the method discussed in Section 2.1.2. The correction raised Brown's data by 43% so that the friction factors were higher than the rectangular bundle correlation for no bypassing. Bell concluded that this would be expected from a bundle with relatively few tubes (80) where separation from the baffle tip would contract the crossflow area to a significant degree, thereby increasing the crossflow pressure drop.

Leighton (1955) found that his crossflow measurements varied by as much as ± 10% from one baffle space to another. He ascribed this effect to small variations in baffle spacing and/or detachment of the neoprene sheet narrowing some spaces, in addition to allowing a degree of leakage flows.

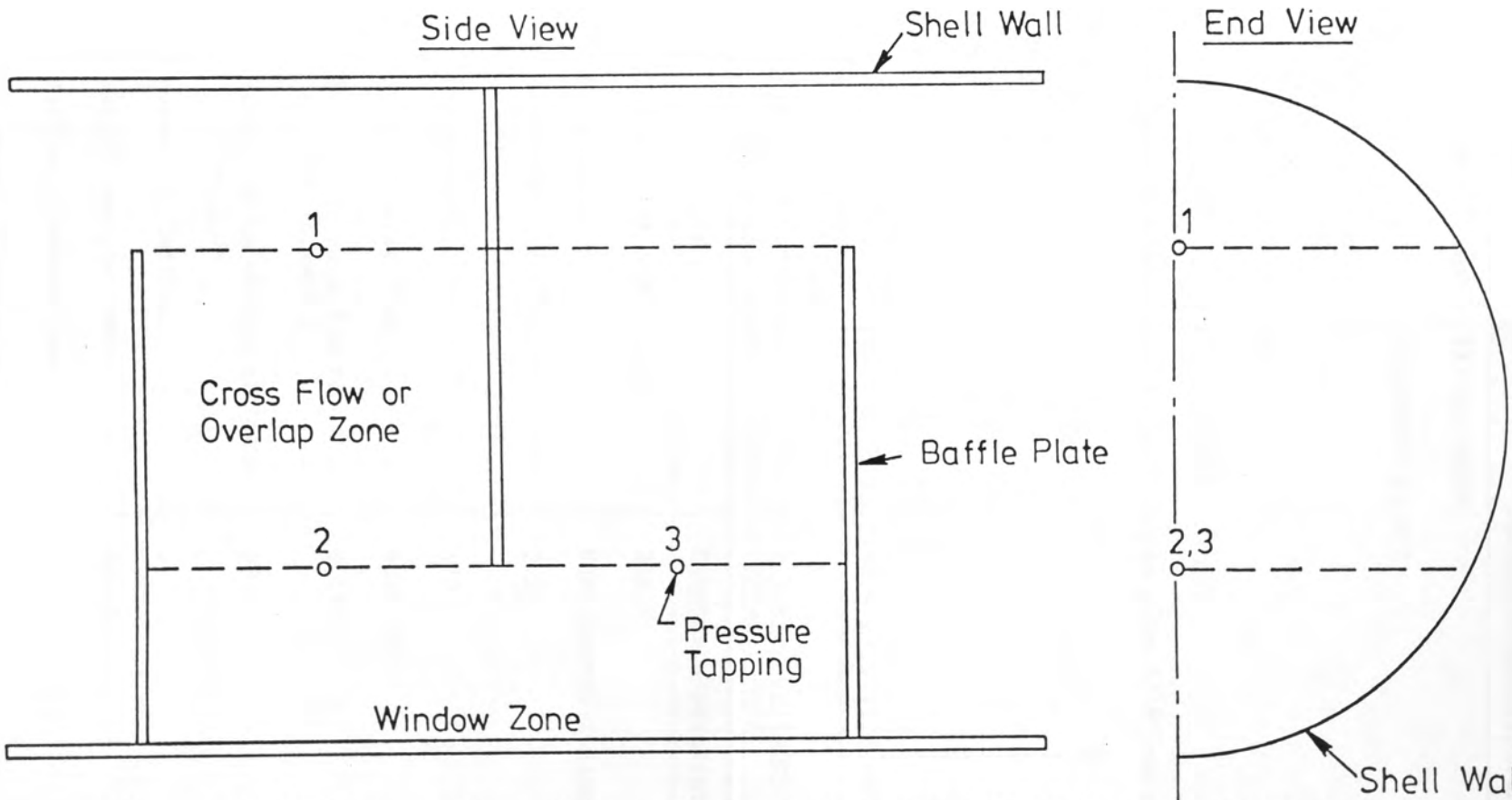

Figure 2.8: Conventional Location of Pressure Tappings to Measure Crossflow and Window Flow Pressure Drops.

Table 2.1: Main Dimensions of Brown's (1956) Cylindrical Baffled Model Exchanger (Delaware University Model 9)

Item	Dimension/Description								
Diameter of shell (mm)	133.35 (5¼")								
Tube layout	Staggered square								
Diagonal pitch/tube diameter	1.26								
Number of tubes	80								
Tube diameter (mm)	9.53 (3/8")								
Baffle thickness (mm)	3.18 (1/16" brass plus 1/16" neoprene)								
Baffle cut as a fraction of shell diameter	0.184			0.310			0.437		
Number of major restrictions to crossflow	10			6			2		
Number of baffles	7	13	25	7	13	25	7	13	25
Baffle spacing (mm)	48.4	24.8	12.7	48.4	23.8	12.7	48.4	24.8	12.7

Table 2.2: Main Dimensions of Leighton's (1955) Cylindrical Baffled Model Exchanger (Delaware University Model 10)

Item	Dimension/Description
Diameter of shell (mm)	212.7
Tube layout	Equilateral triangle
Diagonal pitch/tube diameter	1.33
Number of tubes	470
Tube diameter (mm)	6.35 (¼")
Baffle cut as a fraction of shell diameter	0.187
Number of major restrictions to crossflow	18
Number of baffles	5
Baffle spacing (mm)	65.53
Baffle thickness (mm)	1.59 (1/16")
Thickness of neoprene gaskets on baffles (mm)	1.59 (1/16")

No comparable results for a diagonal pitch-diameter ratio of 1.33 were recorded in the ideal rectangular bundle studies of Bergelin et al. (1959). Leighton interpolated between the curves of friction factor for pitch-diameter ratios (P_t/D_t) of 1.25 and 1.50. The data agreed to within ± 10% of the resultant curve. As with Brown, however, no account was made for bypassing. Bell (1963) showed that, if corrected for bypassing, all of Leighton's data were raised by 22.5%. Thus both cylindrical exchanger data fell significantly above the ideal bundle results. Bell concluded that since Leighton's data agreed more closely with the (interpolated) ideal curve, the validity of rectangular, single pass, correlations increases with larger bundles.

Macbeth (1973) obtained pressure data in a cylindrical exchanger identical in dimensions to Brown (1956). A number of baffle cuts and spacings were studied, but only one data set is comparable with Brown: an 18.4% baffle cut and 48.5 mm baffle spacing. Comparisons between the two sets of data are shown in Figure 2.9, corrected for bypassing using Moore's method gives 15% of the total flow as bypassing. The agreement is good. Bell, using his method (Equation (2.19)), reported an increase in friction factor of 43% implying a bypass flow fraction of about 20%, higher than predicted by Moore. This result is consistent with Lee et al. (1983) who found that Bell overpredicted his measured bypass flow fractions.

The evidence so far suggests that ideal crossflow correlations underpredict the crossflow pressure drop in a cylindrical baffled exchanger. Furthermore, the corrections to the ideal friction factor that have been proposed only account for a fraction of the increased pressure drop measured. However, since bypass lanes were present in all the cylindrical bundle investigations, no definite conclusions can be drawn without prior discussion of bypass correlations.

Bypass correlations are undoubtedly the most suspect of all used in practical designs for two reasons:

1) There is a very limited amount of data, most of which derive from the parallel flow concept which requires simplifying assumptions to calculate friction factors.

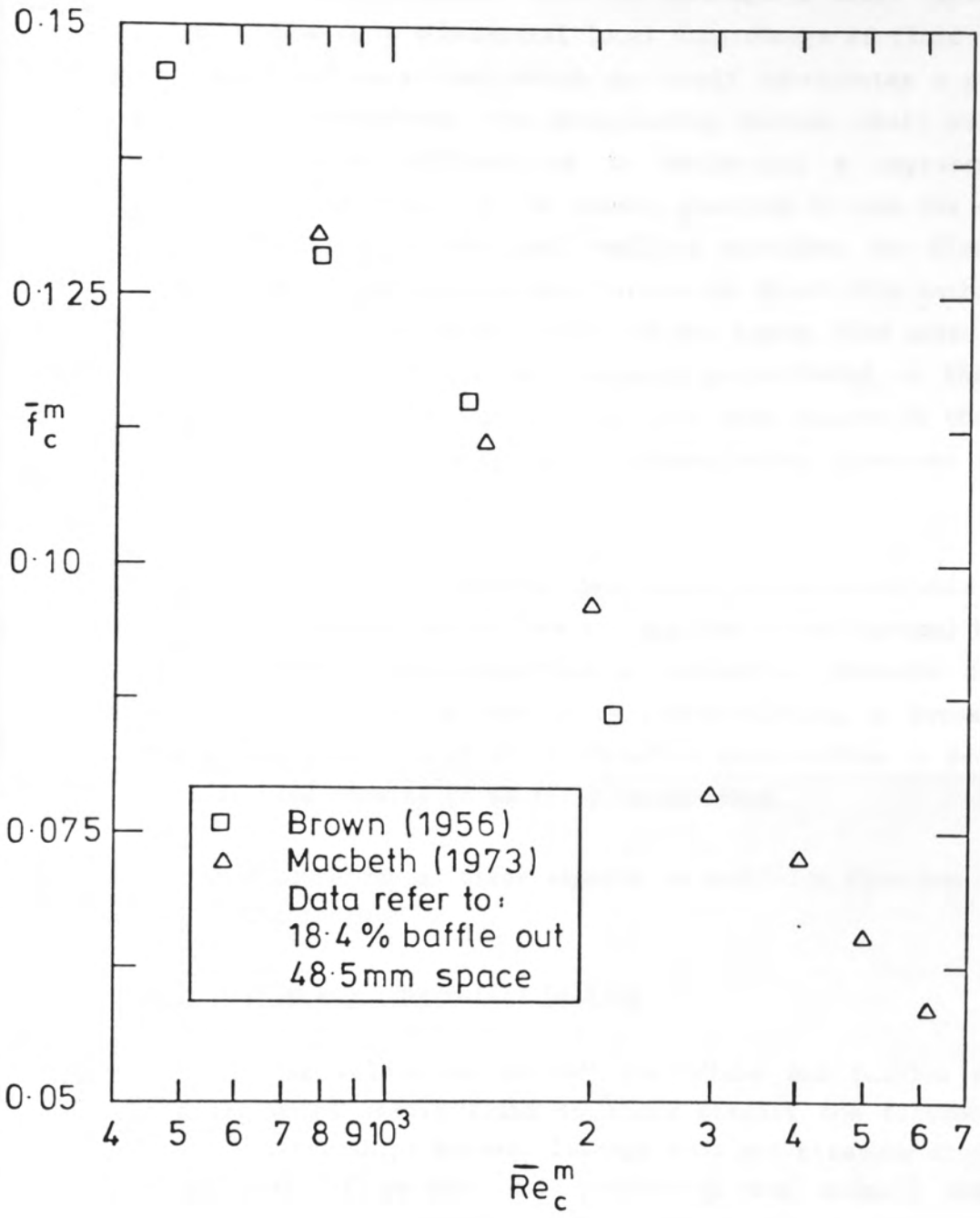

Figure 2.9: Comparison of Friction Factors Derived from the Pressure Measurements of Brown (1956) and Macbeth (1973).

2) In practical exchangers the bypass lane is curved and the flow area irregular (due to irregularities in the outer tube limit), very different from the rectangular case. This would give rise to a substantial local interchange of fluid between bypass and crossflow, which in itself constitutes a pressure loss. Furthermore, the irregularity between shell and outer tube creates difficulties in estimating a representative bypass flow area. It is common practice to use the closest tube approach to the shell wall to calculate the flow area, but clearly situations could arise for which this method does not give a true representation of the bypass flow area. Since bypass pressure drop is inversely proportional to the local flow area squared, the inverse root mean square of the local flow areas is perhaps most representative (Emmerson (1963), see Equation (2.21)).

Finally, the following general conclusion can be made: when correlations from rectangular geometries are applied to cylindrical baffled units a significant underprediction of crossflow pressure drop is observed. Whether this is due to an overprediction of bypass flow fractions or the inability of ideal crossflow correlations to deal with the practical case remains to be fully established.

Further discussions of these aspects of shellside flow are presented in Chapter 9.

2.2 Shell-Baffle and Tube-Baffle Leakage

Manufacturing tolerances between shell/tube and baffles provide leakage areas which enable fluid to short circuit the tortuous main flow path. Relationships between leakage flow and pressure drop are a fundamental part of methods for predicting the overall shellside pressure drop and heat transfer. The purpose of this section is to discuss experimental work on leakage, present some proposed pressure drop-mass flowrate relationships and, finally, to discuss their validity when applied to commercial designs.

In shell-and-tube heat exchangers the clearances between tube and baffle and shell and baffle form annular orifices. Bell and Bergelin (1957) performed a comprehensive series of experiments on flow through a single annular orifice formed between a disc and the cylindrical

shell in which it was situated. The apparatus comprised a 133 mm shell with discs of various diameter and thickness. The experiments covered a range of Reynolds numbers (based on diametral clearance and orifice cross-sectional flow area) between 5 and 25000 and 'shape factors', Z (orifice length divided by radial clearance), of between 0.118 and 33.3. The experimental pressure drops measured over the orifice were presented, for both concentric and tangent orifice cases, as smoothed plots of discharge coefficient (C_d) against shape factor (Z). Each curve related to a specific Reynolds number, spanning the full range studied. The tangent orifice case is generally accepted to apply in shell-and-tube heat exchangers. The discharge coefficient can be related to the velocity head loss coefficient by

$$n_\ell = C_d^{-2} \tag{2.24}$$

which is simply four times a friction factor.

The Reynolds number was based on the diametral clearance, c, and the annulus cross-sectional area, A_ℓ,

$$Re_\ell = \frac{\dot{M}_\ell \, c}{A_\ell \, \eta} \tag{2.25}$$

and the 'shape factor', by

$$Z = \frac{2 \, t_b}{c} \tag{2.26}$$

where t_b is the annulus length or baffle thickness.

The pressure drop for flow length through a single baffle or annular orifice was defined as

$$\Delta p_\ell = \frac{1}{2\rho} \left(\frac{\dot{M}_\ell}{C_d A_\ell}\right)^2 \tag{2.27}$$

$$= \frac{n_\ell}{2\rho} \left(\frac{\dot{M}_\ell}{A_\ell}\right)^2$$

Bell et al. implied that the curves were applicable to both shell-baffle and tube-baffle leakage. They also developed a theoretical model for leakage flows which was claimed to be in good agreement with the data. The model was very complex, partly empirical, and generally unsuitable for design purposes where the components of shellside pressure drop are often evaluated within an iterative loop. This model does not appear to present any advantages over the smoothed data plots given.

Grant and Murray (1972) correlated the smoothed curves of Bell and Bergelin for use in the HTFS design program STEP (also known as the 'Divided Flow' method, see Section 2.7.2). One relationship was derived for shell-baffle and tube-baffle leakage and took the form

$$f_\ell^G = a_{G\ell} \, Re_\ell^{b_{G\ell}} \qquad (2.28)$$

where values of $a_{G\ell}$ and $b_{G\ell}$ were chosen from a table according to the Reynolds number range and the value of the shape factor, Z. The Reynolds number definition was identical to that of Bell and Bergelin (1957) and the friction factor may be related to Bell's discharge coefficient through Equation (2.24). No indication was given about how well Equation (2.28) fitted the original data.

Moore (1974) also correlated the data of Bell and Bergelin for use in the HTFS program TASC. The resulting relationship, applicable for both shell-baffle and tube-baffle leakage, was

$$n_\ell = 2 \, f_\ell^M \, Z + a_{M\ell} \, (Z)^{-b_{M\ell}} \qquad (2.29)$$

where the first term represents frictional losses and the second geometric loses. For the frictional term, a standard in-pipe friction factor-Reynolds number relationship was used (Wilson et al. (1922)),

the same correlation used for the axial flow pressure drop in Moore's window model (see Sectin 2.3):

$$f_{\ell}^{M} = 0.0035 + 0.264\ Re_{\ell}^{-0.42} \qquad (2.30)$$

Moore calculated the total number of velocity heads from Bell's smoothed data plots and subtracted the number of velocity heads lost due to friction (Equation (2.30)), the remaining values were correlated as a geometric loss giving the second term in Equation (2.29). As with Grant and Murray, no indication of how well this correlation fitted the data was given.

In the course of the Heat Transfer and Fluid Flow Service (HTFS) experimental programme at Winfrith, a considerable number of pressure drop measurements were taken in axial flow exchangers with orifice baffles (zero cut), so that tube-baffle and/or shell-baffle leakage dominated. Macbeth published three experimental papers concerned with leakage:

1) Macbeth (1975) which presented data on a 300-tube exchanger, orifice baffled with both tube-baffle and shell-baffle leakage present.

2) Macbeth and Neilson (1977) which presented data from a 7-tube exchanger with tube-baffle leakage only, covering a range of clearances, tube layouts and baffle spacings.

3) Macbeth and Anderson (1983) which presented data from single tube experiments with either tube-baffle or shell-baffle leakage type configurations.

In a paper published in 1984, Macbeth compared his single tube measurements (1983) with the data of Bell and Bergelin. The agreement was very good (within 6%). In particular, the shell-baffle data were in as good agreement with Bell and Bergelin's data as were the tube-baffle data, implying that only one correlation was needed for both geometric configurations. Macbeth also compared his 7-tube measurements

(Macbeth, 1977) with Bell's data and found considerable discrepancies between the two. He concluded that the discrepancies were due to the fact that the 7-tube data derived from a bundle environment as opposed to a single orifice in which the upstream and downstream areas are comparatively large. It was suggested that the 7-tube bundle tests were likely to be more representative of heat exchanger conditions, in which upstream and downstream flow areas are comparatively small. Macbeth went on to derive a correlation based on the 7-tube data in terms of the number of velocity heads (n_ℓ) lost:

$$n_\ell = (c_{M\ell} + d_{M\ell} \, Re_\ell^{-2/3}) \, Z^{2/3} \qquad (2.31)$$

with all other definitions in keeping with Bell and Bergelin (1957). (Macbeth had reported an equivalent formulation of Equation (2.31) in his 1983 paper but involving tube diameter rather than baffle thickness).

To test the hypothesis that the 7-tube correlation was more applicable to large tube bundles than the single orifice data, Macbeth compared pressure drops based on Equation (2.31) and Bell's single orifice data with the 300-tube bundle measurements, Macbeth (1975). The 7-tube correlation agreed only marginally better than Bell's data with the 300-tube measurements (Macbeth, 1975). Nevertheless, Macbeth was satisfied that his hypothesis regarding differences between single tubes and bundles had been borne out by the comparison. However, there was still a significant and systematic scatter in the 300-tube data, as compared to the 7-tube correlation, a problem that was not addressed.

Haseler and Murray (1985), in a review of baffle leakage, discovered that neither the correlations of Grant and Murray nor Moore adequately fitted the data of Bell. This prompted them to derive a new fit to the original data, in the form

$$n_\ell = fn \, (Re_\ell, \, Z) \qquad (2.32)$$

A table was presented showing a comparison of how well Moore (Equation (2.29)), Macbeth (Equation (2.31)) and the new correlation

agreed with Bell's data. This is reproduced in Table 2.3 and clearly shows that the new correlation was a significant improvement over the others. It also extended into the region of low Z (very thin, very loose baffles) which Moore did not try to cover accurately since such values are unlikely to be found in commercial design. Macbeth's correlation, derived from his 7-tube bundle experiments, showed a very poor fit to Bell's data, in contrast to his single tube data which showed good agreement.

Table 2:3 RMS Error in Number of Velocity Heads Predicted by Various Leakage Correlations

	Equation (2.32)	Moore (1974)	Macbeth (1984)
R.M.S. Error (%) Z = Full Range Re = Full Range	6.86	24.51	65.72
R.M.S. Error (%) $Z \geq 1$ $50 \leq Re \leq 5000$	5.52	9.17	63.87
R.M.S. Error (%) $Z \geq 1$ Re = Full Range	5.49	18.20	58.83
R.M.S. Error (%) $Z < 1$ Re = Full Range	8.37	31.12	74.11

They went on to address the discrepancies shown between the single orifice data of Bell and Macbeth's multi-tube results. Macbeth's 7-tube bundle results were plotted, for one value of Z, together with the 7-tube correlation and the improved fit to Bell's data (Equation (2.32)). This plot is reproduced in Figure 2.10. Two striking features were shown by the data:

1) There was a systematic reduction in pressure drop with decreasing baffle spacing.

2) At Reynolds number above 1000 all the data fell significantly below the single orifice data, as exemplified by Equation (2.32) in Figure 2.10.

Haseler and Murray explained the baffle spacing dependency as a leakage jetting effect: after leaving one baffle the flow does not fully diverge to give a uniform flux across the bundle before it converges towards the next tube-baffle orifices. Curiously, Macbeth (1984) stated that no effect of baffle spacing had been detected. The second of the above observations was explained in terms of a 'finite area contraction' effect. They pointed out that in single orifice experiments the area contraction ratio (area inside orifice divided by area outside) tended to zero (that is a severe contraction), whilst in Macbeth's work the area contraction ratio was finite (0.357). The reduced pressure loss due to the finite area contraction was estimated, from a simple model of flow contraction followed by expansion in pipe flow, as a reduction in velocity heads lost of 0.65. This was clearly in the correct order of magnitude to explain the discrepancies between multi-tube and single orifice tests (see Figure 2.10). No explanation was given for the discrepancies shown between Macbeth's 7 and 300-tube data except that some systematic experimental error may have occurred.

2.2.1 Application to Practical Exchangers - Leakage

Two pertinent questions arise regarding the application of work on leakage, in isolation to other flows, to the case of practical exchanger design:

1) Is it valid to apply empirical relationships derived from leakage flows alone, to segmentally baffled heat exchangers which have a number of other flowstreams present?

2) Which leakage data are most applicable to segmentally baffled exchangers, Macbeth's multi-tube measurements or Bell and Bergelin's single orifice data?

Firstly, all the leakage experiments reviewed were conducted with axial flow conditions (normal to the orifice) both upstream and downstream of the orifice. In a practical segmentally baffled exchanger, the crossflow stream might force the leakage to flow at an inclined angle to the baffle. It is plausible that this 'interaction' between crossflow and leakage might alter the resistance characteristics of the

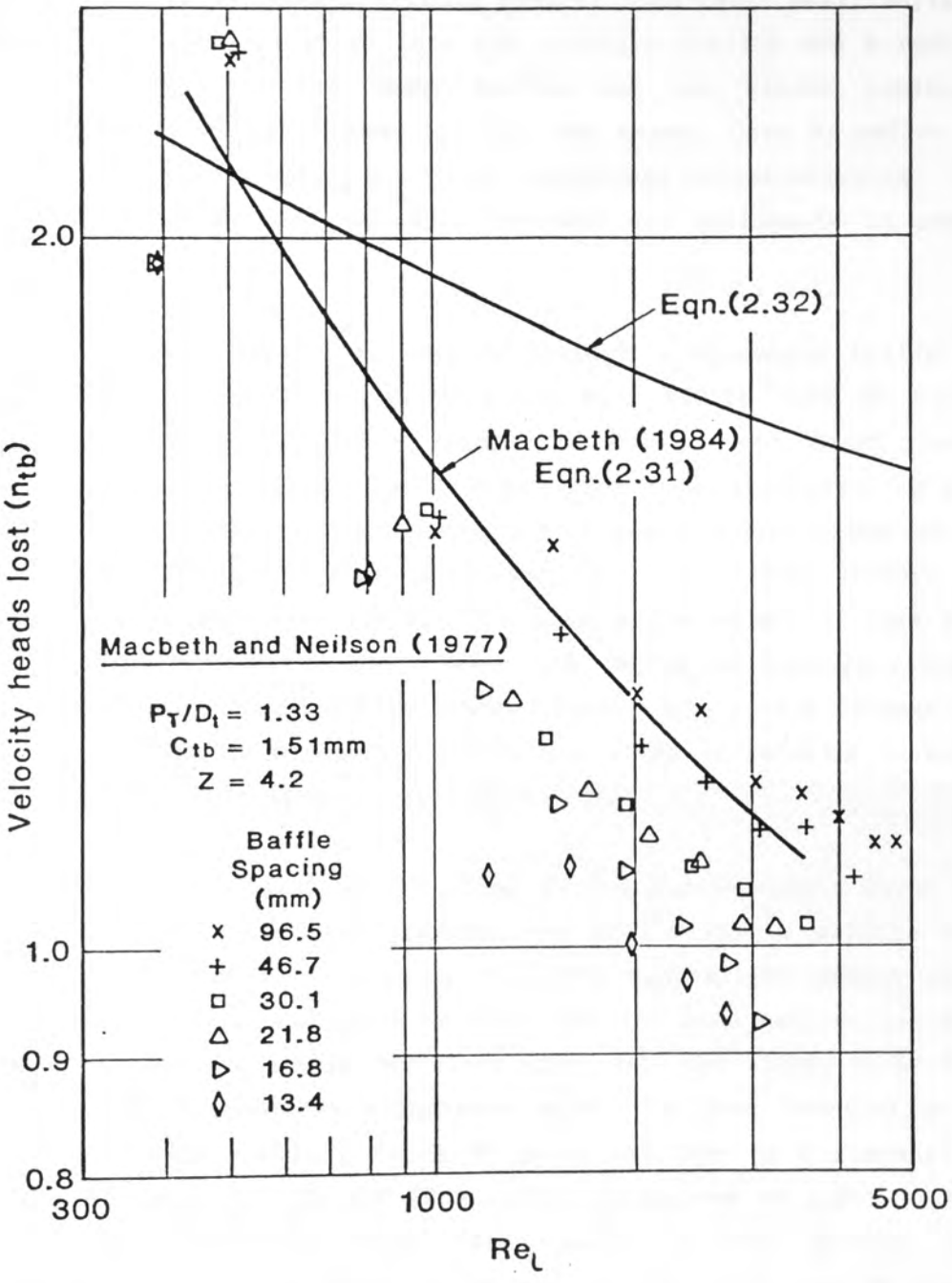

Figure 2.10: Comparison of the Leakage Pressure Drop Correlations of Haseler and Murray (1985) and Macbeth (1984) with the Leakage data of Macbeth and Neilson (1977).

leakage annuli. Early work by Briskin (1950), however, showed this not to be the case; he studied pure longitudinal flow through a baffle and leakage in the presence of a crossflow stream and showed that either pressure drop correlations could predict both cases well. Sullivan and Bergelin (1956) presented data for a single orifice and a rectangular tube bundle with one leaky baffle and one window region. They concluded, from comparisons of the two cases, that crossflow had no measurable effect upon the orifice resistance characteristics. In this respect it seems that the data reviewed are applicable to commercial design.

A further aspect of leakage through a segmental baffle is the variation in pressure driving force from baffle root to tip. The larger pressure difference across the baffle root would force more leakage flow through the baffle there than close to the baffle tip. It is assumed, however, when applying leakage correlations in modern exchanger design methods (See Section 2.7), that leakage occurs uniformly through the baffle. The qualitative effect of this would be for design methods to overpredict the degree of leakage since these methods use the total baffle space pressure drop as the leakage driving force. A further discussion of leakage flows in relation to exchanger design methods is given in Section 2.7.2.

The second question, relating to the discrepancies shown between Macbeth's multi-tube measurements and Bell's single orifice results, can be answered by addressing the area contraction effect discussed earlier. Haseler and Murray argued that the area contraction effects, shown to be important in Macbeth's work, were not likely to be significant in shell-and-tube exchangers since the area contraction ratios were typically smaller: for a ¼" (6.35 mm) tube on a diagonal pitch-diameter ratio of 1.25 and TEMA (1978) clearances of 1/64" (0.397 mm), the area contraction ratio (area inside orifice divided by area outside) is 0.041, a factor of ten smaller than that used by Macbeth.

In conclusion, the evidence suggests that Bell and Bergelin's (1957) data may be applied with reasonable confidence to segmentally baffle exchangers designed to TEMA standards. Some overprediction in leakage flow fractions might occur when correlations of Bell's data are

used in flowstream models such as TASC (Sections 2.7.1. and 2.7.2), but this is due to simplification used in such models and not a limitation of the data.

2.3 Flow in the Window Region

Flow in a shell-and-tube heat exchanger is generally separated into two regions: crossflow in the baffle overlap zone and the window or turn-around zone. This distinction is not made on a phenomenological basis since the fluid continues to flow in crossflow into the window region (see Section 2.6.2 and Chapter 8). It is, however, a convenient distinction to make when studying shellside flow and pressure drop. This section discusses window pressure drop data and presents the various ways in which pressure drop relationships were formulated for design purposes.

As part of the programme at the University of Delaware, Bergelin, Brown and Colburn (1954) published results of crossflow and window flow measurements, obtained and subsequently published by Brown (1956), from a small exchanger known as Model 9, the dimensions of which are shown in Table 2.1. Model 9 was used under non-leakage conditions; leakage flows were eliminated using neoprene gaskets as discussed earlier. Bypassing was reduced to a minimum by using a full tube bundle which extended close to the shell wall. Combinations of three baffle cuts and three baffle spacings were studied. The window results were presented as pressure drop against window velocity based on the free flow area in the plane of the window. The key feature highlighted by the data was the considerable scatter; it was established that the largest ratios of crossflow to window velocities gave the highest pressure drops. To include this effect they used the geometric mean of the crossflow and window flow velocities, $\sqrt{u_c.u_w}$, as a correlating parameter. This improved the fit considerably, but a systematic spread remained for various baffle configurations. In conclusion, Bergelin stated that the current understanding of window flow did not permit further interpretation of the data. Nevertheless, Bergelin went on to propose a pressure drop relationship based on Brown's rather limited data. It was suggested that crossflow persists in the window region

and that this should be accounted for in the window pressure drop relationship. A difficulty arose in deciding how far, on average, the crossflow penetrated into the window region. Due to lack of quantitative data they arbitrarily set this to the number tube rows in the window, neglecting any row with less than half the tubes of the centreline. The window pressure drop was assumed to be the sum of crossflow-in-the-window and a 180° change in direction. The resultant semi-analytical equation was

$$\Delta p_w = (2 + 0.6N_w^B) \frac{1}{2} \rho u_z^2 \qquad (2.33)$$

where u_z is the geometric mean velocity and N_w^B is the assumed number of major restrictions to crossflow in the window. The coefficient 2 represents velocity heads lost for two 90° bends and the coefficient 0.6 represents the number of velocity heads lost per crossflow restriction, backed out of Brown's (1956) window data. When Equation (2.33) was applied to Brown's data the predictions varied from the window measurements by -30 to +20%. Bergelin concluded that the agreement was satisfactory considering the complicated flow conditions in the window region and suggested that Equation (2.33) might prove useful as an estimate of window pressure drop.

Bell (1960) subsequently reported these results and the window model in a paper on exchanger design based on the Delaware University experimental programme. Interestingly, despite Bergelin's reservations about Equation (2.33), it appears in the most recent update of the Bell design method (HEDH, 1983).

Leighton (1955) measured window pressure drops within a cylindrical baffled exchanger in the absence of leakage. This rig was known as Model 10 in the Delaware University research programme and the main dimensions are given in Table 2.2. As with Leighton's crossflow measurements (see Section 2.1.3) a significant variation between baffle space measurements under the same conditions were observed. Again, Leighton attributed this to poor sealing from the neoprene gaskets. On closer examination of his results, however, a definite trend can be established; in the majority of his experiments window pressure drop

are alternately large and small in successive baffle spaces. The larger measurement almost always occurs in a top window compartment and smaller measurements in a bottom window compartment. It is plausible that air entrained during start-up of the rig collected at the top of the exchanger towards the downstream baffle. As leakage had been eliminated this region would experience low velocities. If the seals were effective this air would remain trapped for the duration of an experiment. Leighton's rig (Model 10) had a metallic shell with apparently no means of monitoring the existence of trapped air. He gave no indication concerning the need to purge and this is a plausible explanation for the trend his data exhibit. Correspondingly, this could account for the variations also shown by the crossflow measurements (see Section 2.1.3).

Macbeth (1973) also studied non-leakage conditions in a cylindrical baffle exchanger identical in dimensions to that of Brown (1956). Macbeth's results showed good agreement with the data of Brown, as did his crossflow measurements (Figure 2.9).

Palen and Taborek (1969) produced a semi-analytical model, based on Brown's (1956) data, for a computer design program, known as the 'Stream Analysis' method (Section 2.6.1), under the auspices of Heat Transfer Research Incorporated (HTRI). This model is proprietary to HTRI but its general form was published:

$$\Delta p_w = (4\, f_w N_w^P F_r + 2\,\theta)\, \frac{1}{2}\, \rho\, u_w^2 \qquad (2.34)$$

where f_w is the window friction factor, N_w^P is the assumed number of tube rows crossed in the window, and F_r is an empirical correction factor.

The first term accounts for frictional losses and the second term accounts for turning losses. The form of the first term implies that the axial frictional losses are neglected (typically very small) and that this term represents crossflow-in-the-window losses. Details of

the second term were never disclosed except that θ varies from 0 to 1 as the baffle space varies from large to small as compared to the shell diameter.

Grant and Murray (1974) correlated the data of Brown (1956) and Macbeth (1973) using the ratio of the window flow area to the crossflow area as the correlating parameter. They checked their resultant equation against the data of Sullivan and Bergelin (1956), which had previously been correlated by Parker and Mok (1968). The agreement was good and this equation took the commonly used form

$$\Delta p_w = n_w \frac{1}{2\rho} \left(\frac{\dot{M}_w}{A_w}\right)^2 \qquad (2.35)$$

where A_w is the window flow area and the number of velocity heads lost was given as a function of the window to minimum crossflow area ratio by

$$n_w = fn \left(\frac{A_w}{A_c{}^m}\right) \qquad (2.36)$$

where $A_c{}^m$ is the minimum crossflow area at the shell centre line. This correlation implicitly accounts for longitudinal and crossflow-in-the-window frictional losses. A questionable feature of this correlation is the lack of dependency on the number of tube rows crossed in the window.

Moore (1974) produced a semi-analytical window model, also based on Brown's (1956) data, for the original version of the HTFS program TASC. His model did not include crossflow-in-the-window losses. These were accounted for in the TASC program by the crossflow correlation, assuming that the crossflow extended to the centre of gravity of the window region. Moore, unlike Palen and Taborek, did account for longitudinal frictional losses but did not use exchanger data. Instead Moore used a standard in-pipe friction factor-Reynolds number relationship (Wilson et al. 1922) with an appropriate hydraulic diameter. The

resultant equation was essentially a combined version of both the Bergelin et al.(1954) method, Equation (2.33), and the Palen and Taborek (1969) method, Equation (2.34):

$$\Delta p_w = \left(\frac{4f_w L_b}{D_w} + 2 \sin(\alpha)\right)\frac{A_w}{A_c^m}.\frac{1}{2}\rho u_w^2 \qquad (2.37)$$

where the first term accounts for longitudinal frictional losses and the second term accounts for the turning losses. The angle in the second term is that subtended by the intersection of the line drawn between the centre of gravity of two adjacent window regions and a line parallel to the tube bundle axis as shown in Figure 2.11. This angle, α, is likely to be identical to the angle used within Palen and Taborek's (1969) model, Equation (2.34). Multiplying the window velocity by A_w/A_c^m results in a geometric mean velocity similar to that used in the original model of Bergelin et al. (1954), Equation (2.33).

In all the equations discussed no account was taken of any contraction and expansion effects (apart from Grant and Murray (1974) where such effects were included implicitly) for cases in which the crossflow area does not equal the window flow area. Wills (1984) highlighted this fact and went on to develop a window model that accounted for contraction and expansion effects. He neglected longitudinal flow pressure losses, modelling the window purely on kinetic energy losses and crossflow-in-the-window frictional losses:

$$\Delta p_w = \Delta p_{tn} + \Delta p_e + \Delta p_{cn} + \Delta p_f \qquad (2.38)$$

where subscripts w, tn, e, cn and f denote window, turning, expansion, contraction and frictional.

Wills modelled the turning losses by an analogy to pipe bends, in a similar manner to his predecessors. His turning losses did not, however, include an angle term accounting for the decreasing magnitude of the flow vector undergoing reversal as the baffle spacing increases. Another significant difference was in the velocity used. Prior to Wills' work the geometric mean of the crossflow and window flow areas

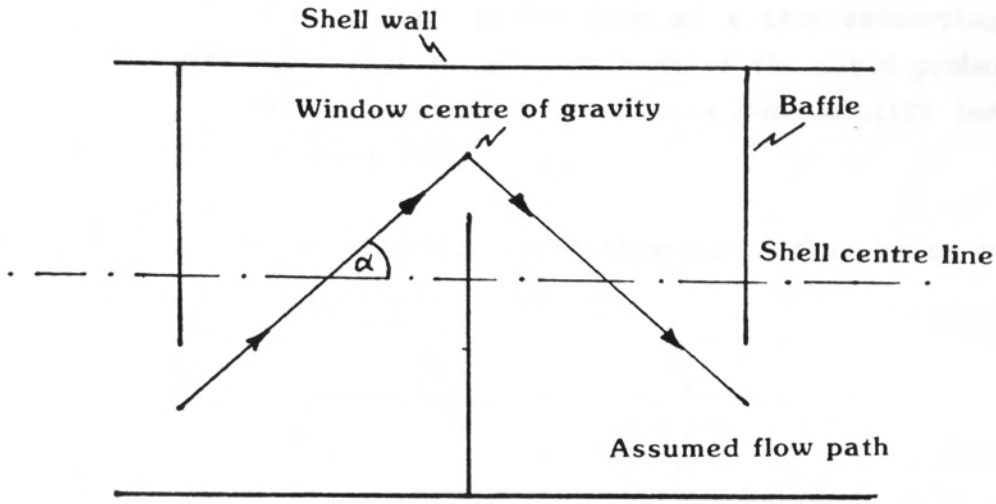

Figure 2.11: Assumed Flow Path of Crossflow and Window Flow. [after Moore, 1974].

was used. Wills argued that for the first window bend, that is outlet from the crossflow region to inlet of the window region, the crossflow velocity should be used and for the second bend the window velocity should be used. This reasoning resulted in

$$\Delta p_{tn} = \rho \frac{u_c^2}{2} + \rho \frac{u_w^2}{2} \qquad (2.39)$$

This assumes one velocity head lost per 90° bend ($\frac{1}{2}\rho u^2$). A valid criticism of this approach is the lack of a term accounting for the fact that with large baffle spacings much of the fluid probably turns prior to the window region, in which case two velocity heads would overpredict the turning loss.

Wills modelled expansion and contraction losses by an analogy to pipe flow (Holland, 1973):

$$\Delta p_e = \left(1 - \frac{A_w}{A^m_{cb}}\right)^2 \rho \frac{u_w^2}{2} \qquad (2.40a)$$

$$\Delta p_{cn} = a_w \left(b_w - \frac{A_w}{A^m_{cb}}\right) \rho \frac{u_w^2}{2} \qquad (A_w < A^m_{cb}) \qquad (2.40b)$$

$$\Delta p_{cn} = a'_w \left(b'_w \left(\frac{A_w}{A^m_{cb}}\right)^2 - \frac{A_w}{A^m_{cb}}\right) \rho \frac{u_w^2}{2} \qquad (A^m_{cb} < A_w) \qquad (2.40c)$$

where the coefficients are selected from a table depending on the values of A_w/A^m_{cb}, where A^m_{cb} is the minimum crossflow area at the baffle tip.

Wills compared his model with the relationship derived by Grant and Murray and Moore with the non-leakage window pressure drop data of Macbeth (1973). These comparisons are reproduced in Figure 2.12 and the general conclusions drawn were as follows:

1) all methods showed reasonable agreement with Macbeth's data when $A_w/A^m_{cb} = 1$;

2) both Bell and Moore severely underpredicted Macbeth's data when $A_w/A^m_{cb} < 1$ (by as much as 70%);

3) Grant and Murray's method agreed very well with the data, consistently predicting on the conservative side (over-prediction); Wills argued that this would be expected since the correlation was based on Macbeth's data and quoted a mean ratio of predicted to experimental pressure drop of $1.17 \pm .17$;

4) Wills' model also gave good predictions, underpredicting when $A_w/A^m_{cb}<1$ and overpredicting when $A_w/A^m_{cb}\geq 1$; the mean ratio of predicted to experimental values was 0.97 ± 0.15.

Wills concluded that his was better than all other models known in detail. Furthermore, it was flexible and more widely applicable than other methods since it was not based on any correlation of window pressure drop data. Whilst Wills' model undoubtedly predicts the data well, some reservations are held regarding his conclusions since the model was tested on a very limited amount of data. Further discussions on this model are given in chapter 9, in relation to the current experimental results.

2.3.1 Application to Commercial Designs - Window Flow

All of the window correlations and semi-analytical models reviewed apply strictly to the case of no baffle leakage. Furthermore, these models can only be tested independently against non-leakage window data since the window flowrate must be known. In a practical exchanger leakage flows are always present. A point worth discussing, therefore, is whether and to what extent leakage flows affect the window flow distribution and pressure drop.

As already noted, the leakage flowrate through a segmental baffle varies from a maximum at the baffle root to a minimum at the baffle tip

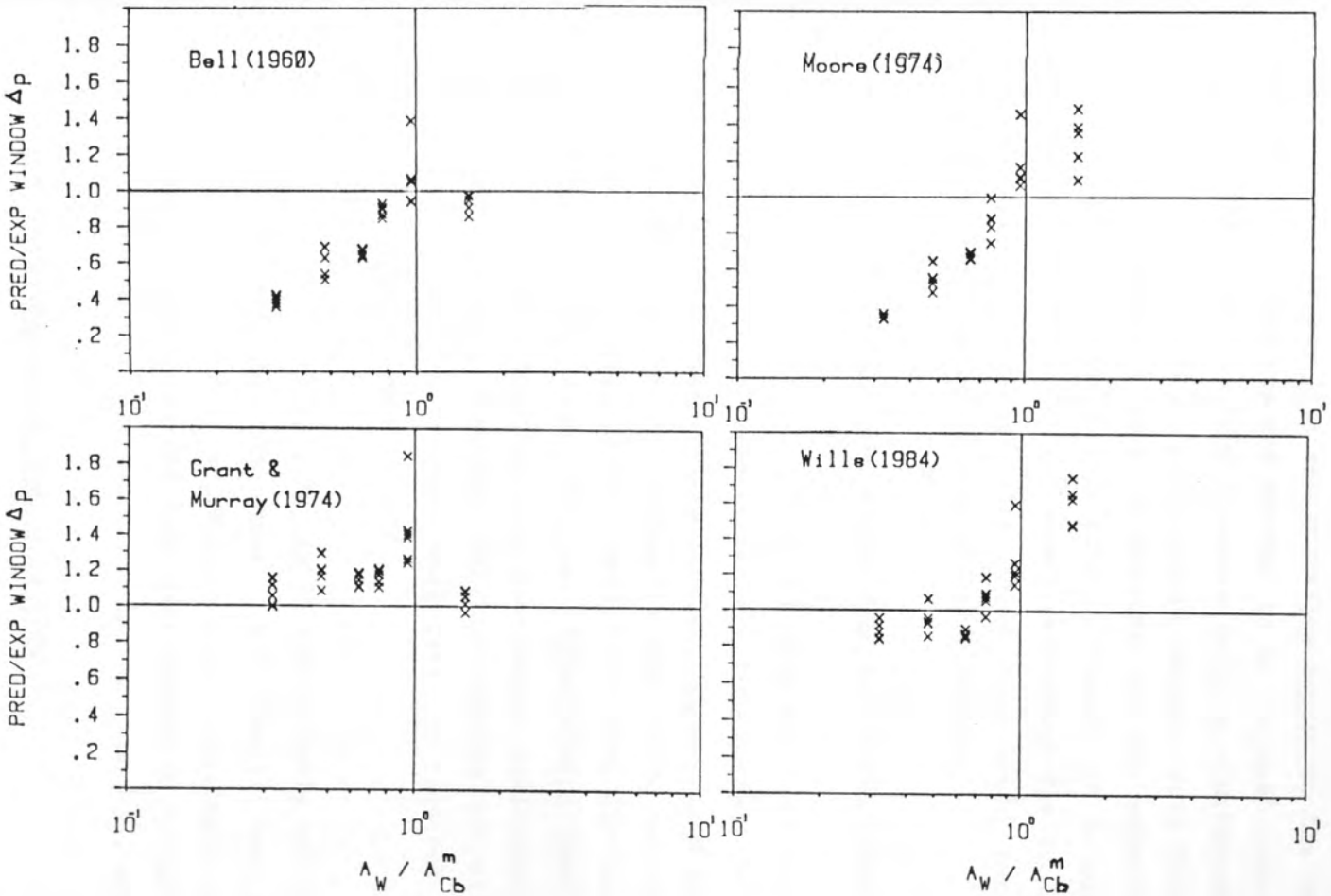

Figure 2.12: Comparison of Experimental Window Pressure Drops Obtained by Macbeth (1973) and those Predicted by Four Commonly Used Design Methods. [after Wills, 1984].

because of the variation in pressure driving force. This leakage profile would plausibly have the effect of forcing the crossflow stream to flow at an inclined angle to the bundle. The net result of this on the window flow would be to reduce the angle through which the fluid must turn in flowing from one crossflow region to the next. Since the turning pressure losses are assumed to be the most significant proportion of the overall window pressure drop, a considerable overprediction, using the models reviewed, could result. Both Palen and Taborek, and Moore included a term to account for the reduction in turning losses with increasing baffle pitch; however, it is plausible that a further term is required for added reductions due to the presence of leakage flows. Clearly, this added term would necessarily be a function of both leakage and crossflow flowrates.

2.4 Cylindrical Baffled Exchangers With All Flows Present

A comparatively small amount of work has been conducted using a cylindrical baffled exchangers with all flow streams present. Work in this area, as with other baffle studies, concentrated on measuring one crossflow and one window flow pressure drop on the vertical centre line of the shell. In view of the complicated flow distribution when all flows are present, such data are considerably more difficult to interpret than data obtained in a non-leakage configuration. This type of work is, however, essential for the verification of pressure drop design methods and, at present, more data are required from full size commercial units to meet this end.

Macbeth (1973, 1974, 1975, 1979) has probably contributed more to this area of work than any other. His results form a particularly comprehensive set of data which have proved invaluable to HTFS in the improvement of two shell-and-tube heat exchanger design methods, TASC and STEP, both methods are discussed in Sections 2.6.2 and 2.7.

2.5 Flow Visualisation of Shellside Flow

A comparatively small amount of work on flow visualisation has appeared in the literature. The difficulties in obtaining qualitative, let alone quantitative results, when applying flow visualisation to complex geometries is undoubtedly a significant factor.

One of the earliest shellside flow visualisation studies were made by Gupta and Katz (1957) using a small glass cylindrical exchanger. They visualised the flow by introducing tracer particles. Their flow pattern studies revealed that the flow on the shellside could be divided into three distinct zones, each exhibiting different flow characteristics: (i) longitudinal flow, (ii) true crossflow, and (iii) recirculating eddy zones. Gupta and Katz went on to estimate the proportion of each zone from photographs and ciné film and related these results to heat transfer. The rig they used had only 26 tubes in a 6" shell, so that for half of their experiments only one tube row was situated in the window region which is totally unrepresentative of commercial designs. It is, therefore, difficult to relate these results to practical exchangers.

Since the studies of Gupta and Katz (1957) no significant work on flow visualisation appeared in the literature until Berner el al. (1984) and Perez (1984).

Berner et al. (1984) studied flow in a plexiglass rectangular baffled shell of cross-section 30 cm x 6 cm. No tubes were used in their work, they concentrated on the effect that baffle pitch and cut had on the flow distribution, under conditions of no baffle leakage. The flow was visualised by dye injection and aluminium tracer particles. Typical results were comparable with those presented by Kopp et al. (1947) and Gupta and Katz (1957) (depicted diagrammatically by Palen and Taborek (1969) as Figure 2.6) and are reproduced in Figure 2.13. These photographic sequences show global flow patterns with various baffle cuts, of which the most striking features are the large wakes shed from the baffle tips, a feature consistent when few or no tubes are present. Berner et al. observed that the wakes were smaller and considerably more chaotic at the higher Reynolds numbers studied. Although the effect of a tube bundle was not studied, they assumed that this would improve the large scale uniformity of flow and reduce flow phenomena such as separation and recirculation.

The most recent and comprehensive shellside flow visualisation study was conducted by Perez (1984). He used a 4" cylindrical shell

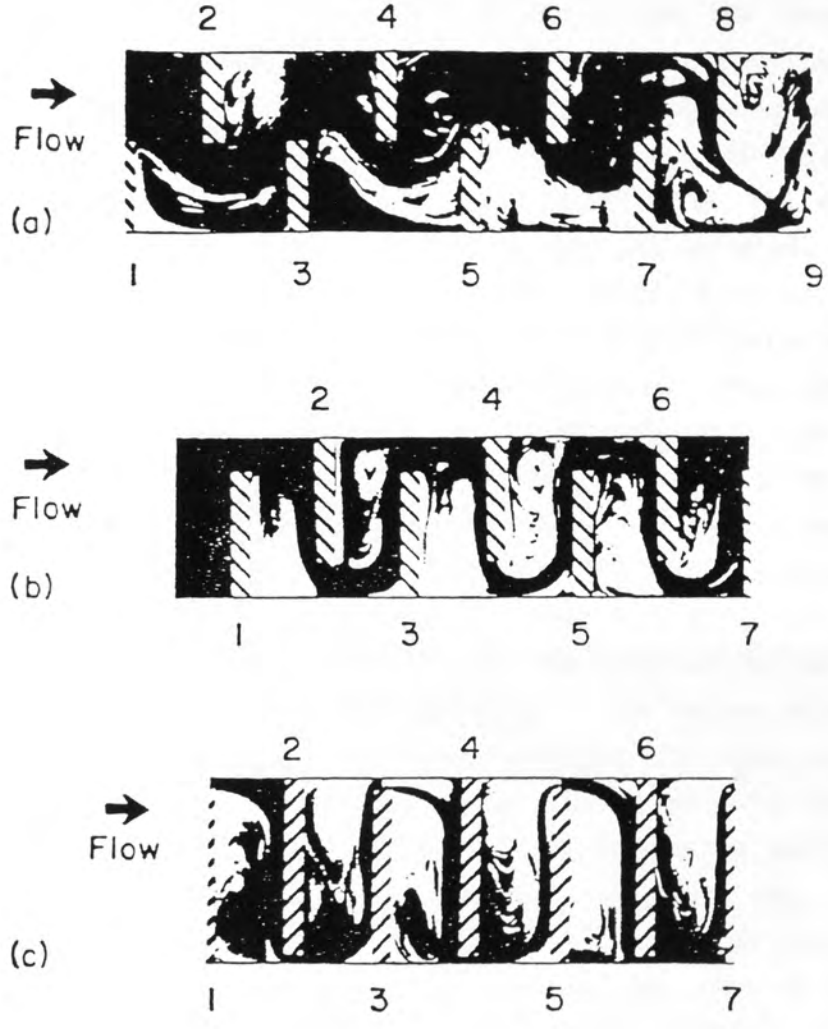

Figure 2.13: Flow Visualisation of Shellside Flow by Dye Injection: Non-Leakage, No Tubes. [after Berner et al., 1984].

with 92, ¼" tubes, on an equilateral triangular layout of diagonal pitch-diameter ratio of 1.5. Both shell-baffle and tube-baffle leakage were eliminated through careful design and fabrication of the model. Crossflow bypassing was minimised by using a tube bundle that extended close to the shell wall. An oil-lampblack visualisation technique was employed. All surfaces within the model were covered with plasticised contact paper to which a mixture of oil and lampblack powder was applied. When the shellside fluid (air) flowed over the coated surfaces the mixture moved under the action of shear stresses, following the paths of the fluid adjacent to the surface. In regions of high velocity the mixture was completely removed from the surface, in regions of very low velocity the mixture remained stationary. At the end of each experiment the contact paper was removed and photographed. Photographs were presented, for three baffle cuts corresponding to 22, 30 and 46% of the shell diameter. Typical results of flow patterns adjacent to the shell wall and around the circumference of tubes are shown in Figure 2.14. Flow patterns adjacent to the shell wall indicated three regions of low flow (I, II, III), which may be located using the bundle layout and the schematic flow diagram shown in Figure 2.14a. The most noteworthy feature was the very large separated region originating from the baffle tip and shown as zone II. Interestingly, this separated region does not appear to reattach on the upstream baffle face, but continues into the stagnant zone observed in the corner between baffle and shell wall (zone III). It is worth noting that Perez used a small bundle with a large pitch-diameter ratio, in larger more dense bundles the separated and stagnant zone would be significantly smaller. Figure 2.14b shows the perimetric flow patterns of tubes just inside the crossflow region, the precise position of which can be located on the bundle cross-section. The upper tier of the two sets of photographs corresponds to the view seen by an observer upstream of the tube looking in the direction of flow, whilst the lower tier corresponds to the view seen downstream of the tube facing the oncoming flow. The photographs clearly show the forward stagnation point and the rear separated region with a pair of eddies (shown by the streak lines within the separated region). Furthermore, the upper reaches of each photograph show evidence of the large separated region, originating from the baffle tip and penetrating into the crossflow zone, exemplified by the lack of streak lines in Figure 2.14b. Each of the above

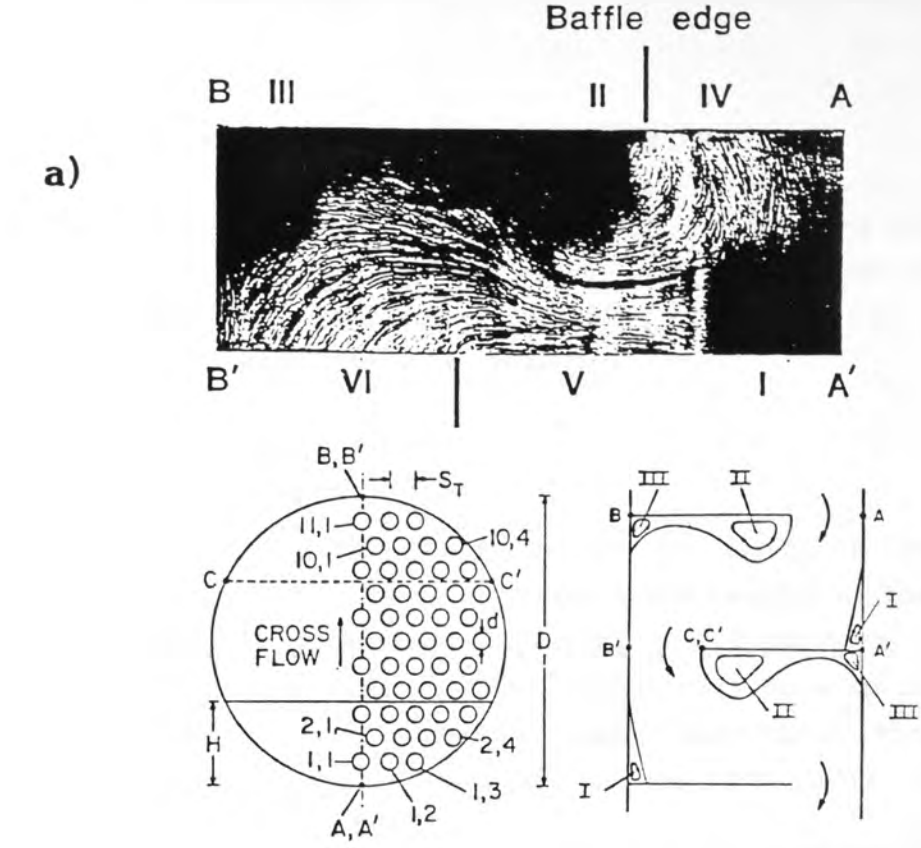

Figure 2.14: Flow Patterns Adjacent to the Shell Wall (a), and Adjacent to Tubes (b).
[after Perez, 1984].

points were discussed fully by Perez along with their implications on shellside heat transfer. However, as with the investigations of Gupta and Katz (1957), these results might be misleading because of the small scale model used.

2.6 Shellside Pressure Drop Prediction Methods

There are essentially two methods used to estimate shellside pressure drop for design purposes: single and multi-stream methods. Space does not permit a detailed presentation of each method, but the salient features of each will be discussed.

2.6.1 Single-stream Methods

The importance of single-stream methods for design of shell-and-tube heat exchangers has declined in recent years because of the advent of readily available computing facilities and production of more reliable multi-stream methods. However, since they form an important link in the 'evolution' of exchanger design techniques, three well known methods are discussed. These are due to Kern (1950), Williams and Katz (1952) and Bell (1960).

Kern (1950) treated shellside flow as analogous to pipe flow. He used overall pressure drop data from a commercial unit, in service, to produce a simple correlation. This correlation relates to 25% baffle cuts only and makes no account of bypassing and leakage flows. Despite this rather crude approach, Kern's method soon became an industrial standard simply because it was convenient to use.

Williams and Katz (1952) used a window pressure drop correlation published by Donohue (1949) to back out crossflow pressure drops from their own overall baffle space data. The resulting crossflow pressure drops were presented in chart form as friction factor against Reynolds number. Whilst this method distinguishes between crossflow and window flow, it is, as with Kern's method, based on a very limited amount of data. Furthermore, no account is made of bypassing or leakage and as such presents no real advantage over Kern's method.

Bell (1960) presented a method for prediction of shellside pressure drop based on the comprehensive Delaware University data, as summarised by Bergelin et al. (1958). This methods treats the exchanger as a number of ideal crossflow sections connected by window regions. The pressure drop is firstly estimated for both crossflow and window flow, then empirical correction factors are applied to account for bundle bypassing and baffle leakage, avoiding the need for an iterative procedure. Bell's method has been periodically updated and is presented, in its most up-to-date form, in the Heat Exchanger Design Handbook (HEDH, 1983). The basic method, however, remains essentially as Bell originally presented it.

Of all the single-stream methods only Bell's remains popular. This is simply because it recognises, in principle, all the flowstreams of Tinker's original model. Whitley (1961) showed that of the three methods briefly discussed, Bell's was the most reliable in predicting his field measurements. The other two methods gave very unreliable results with an overprediction in overall pressure drop of up to ten times the measured value.

One major disadvantage shared by all single-stream methods is their inability to resolve the shellside flow distribution. Only if the flow distribution is calculated can local heat transfer coefficients be estimated with reasonable accuracy. In this respect multi-stream type models are more desirable.

2.6.2 Multi-stream Methods

Multi-stream methods attempt to model the shellside flow distribution in the form of a series/parallel network. The flow network is analogous to an electrical resistance circuit, in which hydraulic resistance and mass flow replace electrical resistance and current respectively. The flow network may be defined in a number of ways and is a function of the assumptions made about the shellside flow. Generally the more complicated the network the closer the true shellside flow will be approximated. Space does not permit a comprehensive discussion of all multi-stream methods, but since each method in principle uses similar networks and solution techniques only the

salient features will be discussed. Firstly, to establish the basic principles, a simple flowstream method will be described along with a possible solution technique. Consider a model consisting of five flowstreams:

1) Crossflow ($\dot{M}_c$)
2) Bypass ($\dot{M}_b$)
3) Window flow ($\dot{M}_w$)
4) Shell-baffle leakage ($\dot{M}_s$)
5) Tube-baffle leakage ($\dot{M}_t$)

which is shown in network form in Figure 1.4. From mass continuity the following equations can be derived relating the flow in various streams:

$$\dot{M}_T = \dot{M}_c + \dot{M}_b + \dot{M}_s + \dot{M}_t \qquad (2.41)$$

$$\dot{M}_w = \dot{M}_c + \dot{M}_b$$

$$= \dot{M}_T - \dot{M}_\ell \qquad (2.42)$$

where $\dot{M}$ is the mass flowrate and subscript T refers to total baffle space. Assuming that the pressure drops suffered across parallel flow paths are equal, the following pressure drop relationships can be obtained:

$$\Delta p_c = \Delta p_b \qquad (2.43)$$

$$\Delta p_t = \Delta p_\ell = \Delta p_c + \Delta p_w \qquad (2.44)$$

The final equations required are the relationships between pressure drop and flowrate for each stream:

$$\Delta p_i = f_n (\dot{M}_i, f_i, A_i) \quad (i = 1,5) \qquad (2.45)$$

These relationships are mainly derived from experiment, some proposed relationships were reviewed in Sections 2.1 to 2.5. Once the representative cross-sectional flow areas (A_i) are defined, Equations (2.41) to (2.44) can be solved by balancing pressure drops across parallel flowpaths. The solution is clearly iterative since the friction factors, f_i, are functions of mass flowrate. One possible iterative solution for this example is given in Appendix C.

Tinker (1948) was the first to introduce the concept of shellside flowstreams, that is the division of the flow into a number of distinct components (see Figure 1.3). Despite the lack of data available to Tinker, his knowledge of shell-and-tube heat exchangers coupled with a degree of intuition, enabled him to develop his pioneering method. Unfortunately for Tinker, the lack of computing facilities coupled with sparse experimental data made it impossible for him to establish a rigorous solution procedure. Instead, a number of simplifying assumptions were necessary, but the method still remained very lengthy and complicated. As a result engineers tended not to use this method, even after a further simplified adaptation was published in 1958 which was non-iterative.

It appears that Tinker's ideas were well before his time and ironically gave justification to the development of single-stream methods. It was inevitable, however, that the full implications of his work would be realised with the development and availability of digital computers.

Twenty-one years on from Tinker's first publication, Palen and Taborek (1969) 're-discovered' the multi-stream concept and were in the position to exploit fully those original ideas. Their method is known as the 'Stream Analysis' method and is proprietary to HTRI. As a result only the qualitative form of the correlations, physical models and solution technique used have been published. However, the results of a comparison between the stream analysis, Tinker's and Bell's method with a limited but typical range of operation conditions were given. The conclusions drawn were that Bell's single-stream method was the least accurate, predicting the selection of data to within -50% to +100%. For a multi-stream method, Tinker's faired rather poorly, consistently

underpredicting (by over 60% in some cases). Their own 'Stream Analysis' method showed closest agreement with the data, predicting the shellside pressure drop to within -30% to +50%. This method, however, incorporated a number of unspecified empirical correction factors which undoubtedly derived from the data they considered in this comparison. The good agreement shown is, therefore, quite possibly misleading.

Both Grant and Murray (1972) and Moore (1974) produced multi-stream models under the auspices of HTFS, known as the Divided Flow and the original release of TASC respectively. A fundamental difference in approach exists between the two models. The Divided Flow model is based exclusively on empirical correlations of experimental data derived from laboratory models of shell-and-tube heat exchangers. The TASC model, however, incorporates simple one-dimensional physical models and correlations of a more general nature. In addition, the two models differ in the detail of how flowstreams, hydraulic diameters and flow areas are defined. The basic network defined by Moore is given in Figure 1.4 and the relationships defining the model are given in Equations (2.41) to (2.44). The Divided Flow model uses a slightly more complicated network shown in Figure 2.15, in which baffle leakage streams are subdivided into equal halves. The defining pressure drop and continuity relations are, however, identical to Moore for a mid-baffle space. The net result, other things being equal, would be for both models to give the same flow fractions, despite the more complicated network. This is because the driving pressure force for leakage in both models is the sum of the crossflow and window components.

The exact definition of leakage flows in baffle space methods is clearly a problem. In the models described, the leakage from one node to the next appears to flow counter to the main flow at some stage. Clearly, leakage flows in the window region of a baffle are likely to be confined to the window region throughout consecutive adjacent baffle spaces. The implications of this weakness in baffle space multi-stream methods will be discussed further in Section 2.7.2.

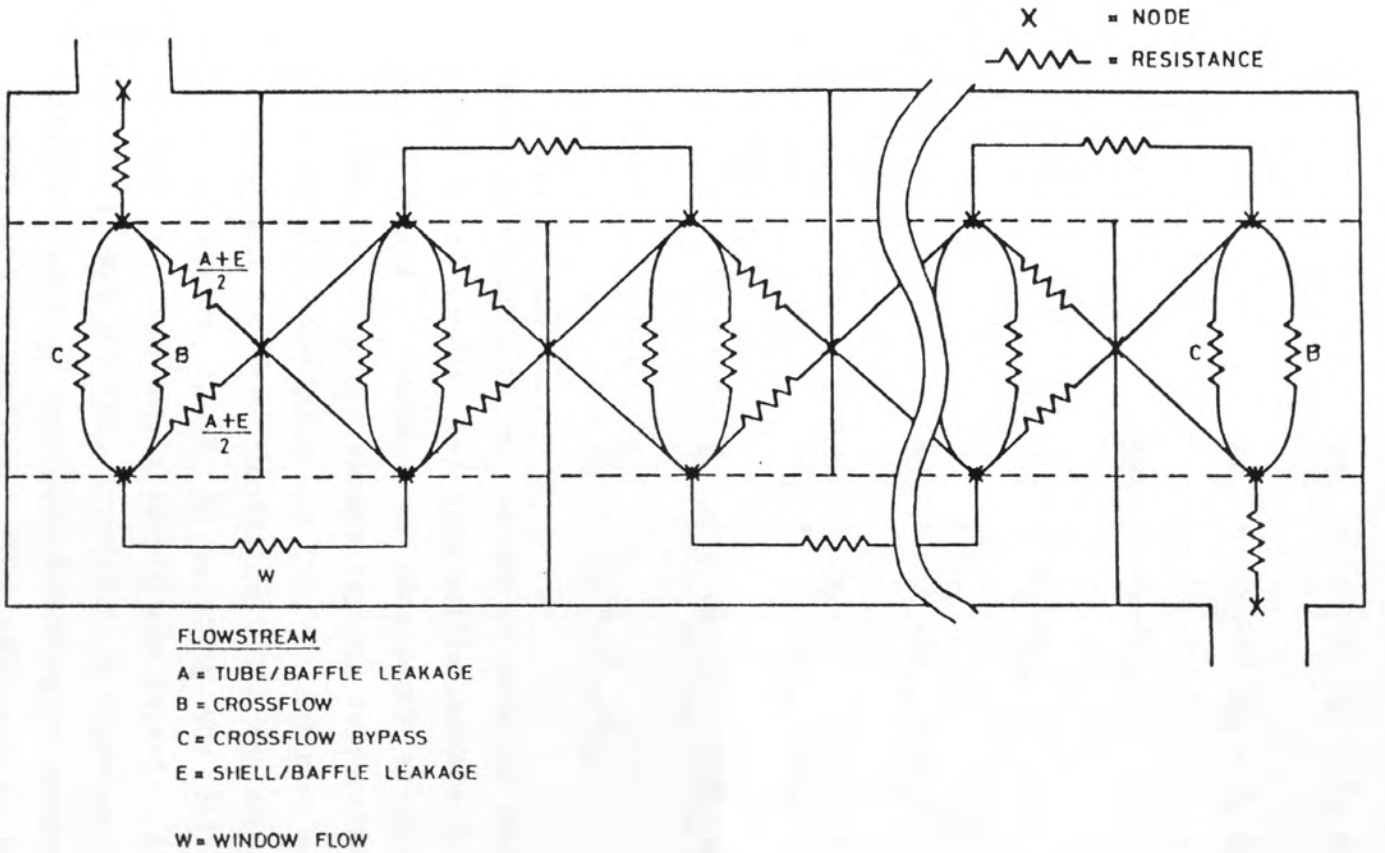

Figure 2.15: Flow Network Used in the 'Divided Flow' Heat Exchanger Design Method (Grant and Murray(1972)).

Parker and Mok (1968) adopted a different approach to modelling shellside flow by devising a scheme to solve over the whole length of a given exchanger, known as an overall multi-stream method. The following relationships, for an exchanger with N_B baffles, were given for pressure drop and mass flowrate:

$$\Delta p_T = (N_B+1)\ \Delta p_c + N_B\ \Delta p_w \tag{2.46}$$

$$\Delta p_T = (N_B+1)\ \Delta p_b + N_B\ \Delta p_w \tag{2.47}$$

$$\Delta p_T = N_B\ \Delta p_{so} \tag{2.48}$$

$$\Delta p_T = N_B\ \Delta p_{to} \tag{2.49}$$

$$\Delta p_T = \frac{N_B}{2}\ (\Delta p_{tw} + \Delta p_w) \tag{2.50}$$

$$\Delta p_T = \frac{N_B}{2}\ (\Delta p_{sw} + \Delta p_w) \tag{2.51}$$

$$\dot{M}_T = \dot{M}_w+\dot{M}_{so}+\dot{M}_{to}+ 2(\dot{M}_{sw}+\dot{M}_{tw}) \tag{2.52}$$

$$\dot{M}_w = \dot{M}_c+\dot{M}_b+\dot{M}_{sw}+\dot{M}_{tw} \tag{2.53}$$

where subscripts so, sw, to and tw refer to shell-baffle leakage in the overlap and window, and tube-baffle leakage in the overlap and window respectively. Leakage is considered as parallel streams spanning adjacent overlap and window regions respectively. No details of the flow network were given but from the defining equations its form can be deduced and is shown in Figure 2.16a and in a simpler diagrammatical form in Figure 2.16b. By relating the defining equations to this network two interesting points are raised. Firstly, Equations (2.48) to (2.51) are strictly incorrect, a rigorous analysis would yield two different sets of equations depending on whether an odd or even number of baffles were employed. With reference to Figure 2.17 the two cases are as follows:

1) Even N_B - Equations (2.48) to (2.51) require an additional end space crossflow pressure drop.

2) Odd N_b - Equations (2.48) and (2.49) require an additional end space crossflow pressure drop. A further equation is necessary to define the leakage in the window regions furthest from the nozzles since there the total pressure drop is actually

$$\Delta p_T = \frac{N_B}{2} \Delta p_{tw} + 2 \Delta p_c \qquad (2.54)$$

and similarly for the shell-baffle leakage.

These errors in the original model would only be significant if the number of baffle spaces were small.

Secondly, when an odd number of baffles are employed the leakage in the window regions, closest to the nozzles, is greater than that through the windows furthest from the nozzles. This is due to differences in pressure driving forces. Again, this effect would only be significant when relatively few baffle compartments are present.

Despite the small inaccuracies in Parker and Mok's original model, leakage is dealt with in a more realistic manner than the baffle space methods. However, whilst this type of approach is likely to give a good representation of the shellside flow, it has one major disadvantage as pointed out by Wills (1984). Commercial design methods require values of local pressures since heat transfer calculations need to be performed in increments along the shell. Furthermore, since pressure drop and heat transfer are linked through variations in physical properties, a substantial iterative procedure would be required between the two. Such procedures are minimised when solving for one baffle space only, this is an important facet of the baffle space methods.

Wills (1984) reviewed many of the single and multi-stream methods to establish which offered most potential for developing an improved model. Single-stream methods were discounted because of their inability to account for leakage and bypassing in a rational manner. Parker and Mok's overall multi-stream method was also discounted because it was not in a practical form for commercial design purposes. Wills concluded that the baffle space multi-stream methods, despite

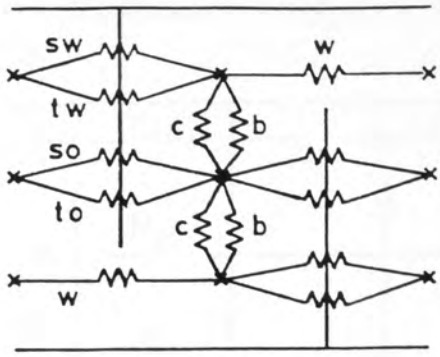

c - Crossflow
b - Bypassing
w - Window flow
sw - Shell-baffle leakage in window overlap
so - " " " " " "
tw - Tube-baffle leakage in window overlap
to - " " " " " "

Figure 2.16 a: Flow Network Used in Parker and Mok's Shellside Pressure Drop Design Method.

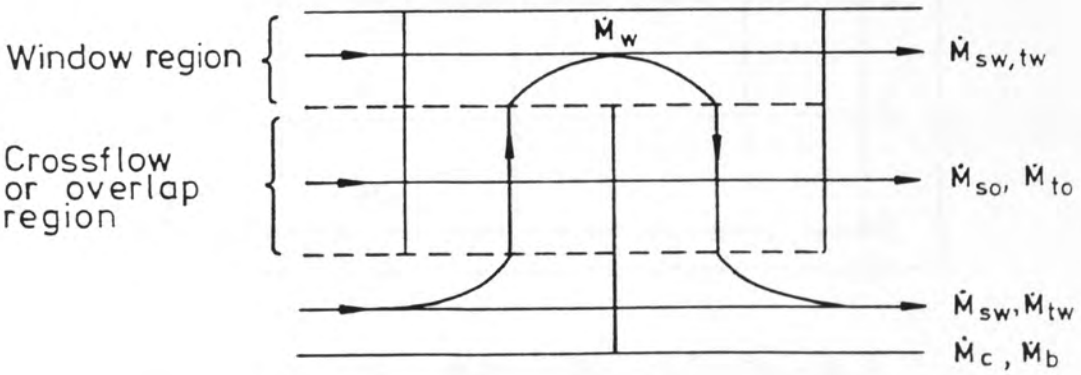

$$\dot{M}_T = \dot{M}_c + \dot{M}_b + 2\dot{M}_{tw} + 2\dot{M}_{sw} + \dot{M}_{to} + \dot{M}_{so}$$

Figure 2.16 b: Schematic of the Assumed Flow Distribution Used in Parker and Mok's Method.

Even N_B

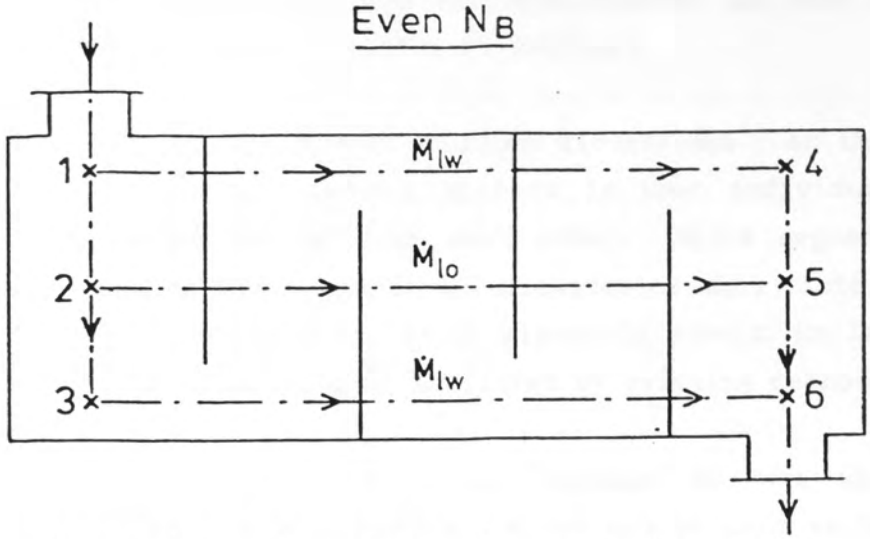

$$\Delta p_T = (p_1 - p_6), \quad \Delta p_c = (p_1 - p_3) = (p_4 - p_6)$$

$$\therefore \Delta p_{lo} = \Delta p_T - \Delta p_c, \quad \Delta p_{lw} = \Delta p_T - \Delta p_c$$

Odd N_B

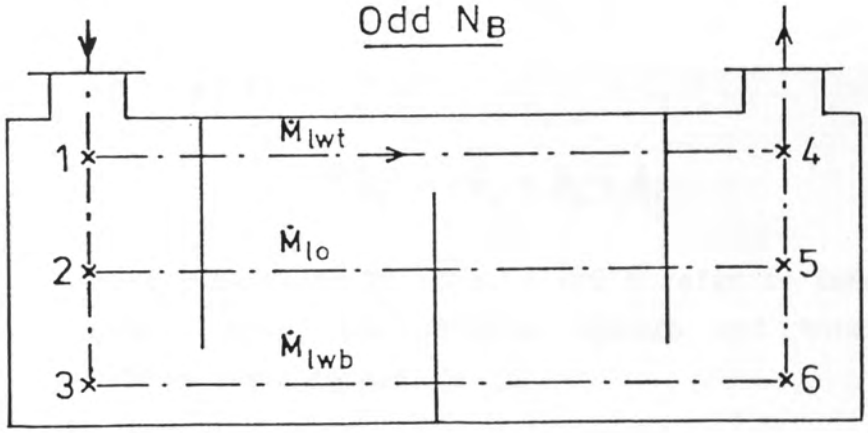

$$\Delta p_T = (p_1 - p_4), \quad \Delta p_c = (p_1 - p_3) = (p_6 - p_4)$$

$$\therefore \Delta p_{lo} = \Delta p_T - \Delta p_c, \quad \Delta p_{lwt} = \Delta p_T$$

$$\Delta p_{lwb} = \Delta p_T - 2\Delta p_c$$

Figure 2.17: Corrected Pressure Drop Equations for Parker and Mok's (1968) Design Method.

their simplifications, offered the best scope for development. In order to build on the foundations of the multi-stream method, Wills investigated further the weak features inherent in this type of model. These may be summarised briefly as follows:

1) Interactions between various flowstreams - an implicit assumption in all network methods is that individual flowstreams have no influence on each other. Wills argued that in such complex flow situations, flowstreams must 'interact' and that such interactions would plausibly result in larger pressure drops than could be predicted by existing methods.

2) Baffle leakage - baffle leakage in the window was not correctly accounted for. Wills showed this to be the case by comparing Parker and Mok's continuity equations with those for the baffle space methods. Baffle space methods assume that the crossflow and window flowrates are equal:

$$\dot{M}_w = \dot{M}_c + \dot{M}_b \qquad (2.55)$$

and total flow

$$\dot{M}_T = \dot{M}_w + \dot{M}_s + \dot{M}_t \qquad (2.56)$$

where subscripts T, c, b, s and t refer to total, crossflow, bypass, total shell-baffle leakage and total tube-baffle leakage respectively.

Parker and Mok define the following corresponding relationships

$$\dot{M}_w = \dot{M}_c + \dot{M}_w + \dot{M}_{sw} + \dot{M}_{tw} \qquad (2.57)$$

and

$$\dot{M}_T = \dot{M}_w + 2(\dot{M}_{sw} + \dot{M}_{tw}) + \dot{M}_{so} + \dot{M}_{to} \qquad (2.58)$$

where subscripts so, sw, to and tw refer to shell-baffle leakage in the overlap and the window, and tube-baffle leakage in overlap and window respectively. Comparison of Equations (2.55) and (2.56) with Equations (2.57) and (2.58) clearly shows that the baffle space methods assume that leakage in the window is a single-stream, neglecting the additional parallel stream, of equal magnitude, accounted for in Parker and Mok's method. The net result of this weakness would be an underprediction of total leakage flowrate in the window and subsequent overprediction of the crossflow flowrate.

3) Crossflow in the window region - since crossflow persists into the window region a rational method was required to establish, for various geometric configurations, how far on average crossflow penetrates into the window. Hitherto, this distance has been chosen on a rather arbitrary basis, for example Bell (1960) used half the number of tube rows in the window while Moore (1974) chose the centre of gravity of the window region (Section 2.3).

Wills went on to propose models to account for each of the three major weaknesses inherent in existing methods. These models were imposed onto the basic framework and solution procedure of Moore (original release of TASC) and is known collectively as the 'Stream Interaction' model incorporated in the current version of TASC. Since one of the purposes of this work is to assess the Stream Interaction method in the light of new experimental data, the component models will be discussed in some detail in the following section.

2.7 The Stream Interaction Method

The purpose of this section is to describe and discuss the models, proposed by Wills, that constitute the Stream Interaction method.

2.7.1 Flow Interactions

An assumption implicit in all multi-stream methods is that pressure drop in a particular flowstream is a function of hydraulic

resistance and flowrate in that stream only, that is there are no added pressure losses due to stream interactions. Since friction factor - Reynolds number relationships derive from isolated flow phenomena (described in Sections 2.1 to 2.5), it is plausible that the shellside pressure drop in a practical exchanger is larger than the sum of the individual components. Wills questioned the non-interaction assumption and argued further that the most significant effect was likely to be shown by the baffle leakage mixing with the crossflow stream. To check this hypothesis Wills compared pressure drop data obtained by Macbeth (1973) for both leakages and non-leakage conditions. By correlating both crossflow and window flow pressure drops ($\Delta p = fn(\dot{M})$) from the non-leakage case Wills was able to derive the flow fractions associated with the window for the leakage case. In the non-leakage case clearly all the flow passes through the window. The crossflow and window flow fractions were assumed equal enabling a comparison to be made between crossflow pressure drop, with (measured) and without leakage (calculated) for the same absolute flowrate. By assuming that the crossflow and window flowrates are equal in the leakage case, the effects of leakage into the window zone were neglected. The added pressure drop due to this leakage stream was, however, estimated and shown to be insignificant. Wills chose only one of the three corresponding leakage/non-leakage data sets that were available from Macbeth's investigations. This derived from an 18% baffle cut and 48.5 mm baffle spacing. It was argued that geometries with small baffle cuts, which have a comparatively large proportion of leakage area in the overlap, would exhibit the most significant effects of 'crossflow-leakage interaction'. Comparisons of crossflow pressure drop with and without leakage are reproduced in Figure 2.18. It appears that the presence of baffle leakage significantly increases the crossflow pressure drop (up to a factor of two above the non-leakage case). Wills concluded that crossflow-leakage interaction was a very significant effect and should be accounted for. A further data set from Macbeth's work deriving from a 25% baffle cut has also been analysed in the way described and included in Figure 2.18. Following Will's logic a 25% baffle cut with an identical baffle spacing would exhibit significantly less enhancement in crossflow pressure drop, simply because there is less leakage in the overlap. Interestingly, the opposite is shown to be the case, contradicting the original hypothesis. Further investigations into the

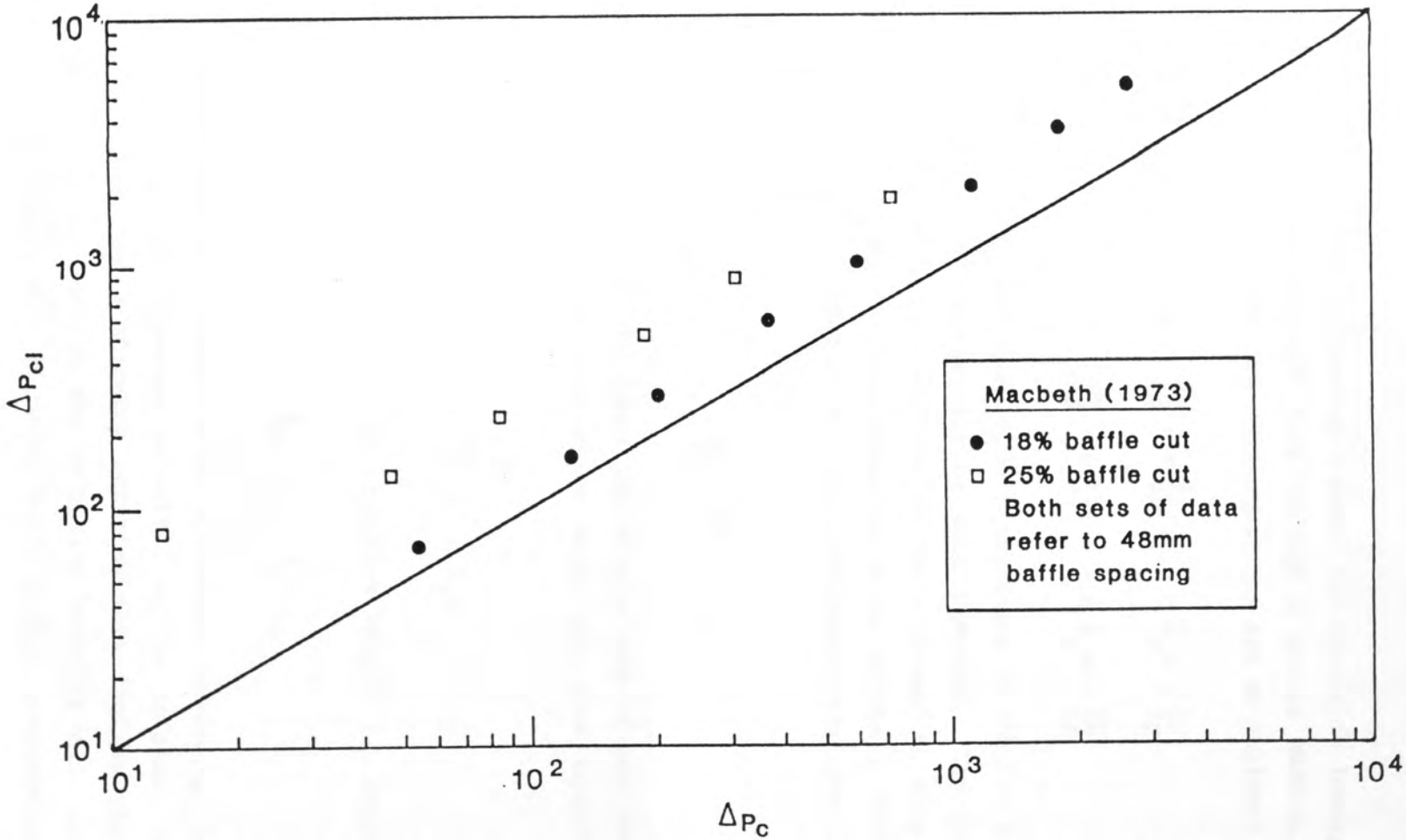

Figure 2.18: Comparison of Measured Crossflow Pressure Drops with Leakage(Macbeth, 1973) and Derived Non-Leakage Crossflow Pressure Drops. [after Wills, 1984].

crossflow-leakage interaction phenomenon are discussed, in the light of the current experimental results, in Chapter 9.

Wills went on to develop a model for crossflow leakage interaction based on two-dimensional flow through a porous medium, as shown in Figure 2.19, for which the flow equations are as follows:

$$\frac{\rho}{\gamma}\left(v\frac{\partial v}{\partial y} + w\frac{\partial v}{\partial z}\right) = -\eta\,\bar{R}_y v - \frac{\partial p}{\partial y} \qquad (2.59a)$$

$$\frac{\rho}{\gamma}\left(v\frac{\partial w}{\partial y} + w\frac{\partial w}{\partial z}\right) = -\eta\,\bar{R}_z w - \frac{\partial p}{\partial z} \qquad (2.59b)$$

where $\bar{R}_y$ and $\bar{R}_z$ are mean flow resistances in the two flow directions and γ is the volume porosity or void fraction. The leakage flow is assumed to be purely axial flow, in the z-direction, with a superficial velocity component w. The crossflow flows in the y direction, superficial velocity component v. The continuity equation for this model is

$$\frac{\partial v}{\partial y} + \frac{\partial w}{\partial z} = 0 \qquad (2.60)$$

Firstly, Wills considers the simple case of non-leakage giving a uniform flow in the y-direction only, the flow equations therefore reduce to

$$\frac{dp}{dy} = \eta\,\bar{R}_y v \qquad (2.61)$$

which when integrated over the crossflow length, L_c, becomes

$$\Delta p_c = \eta\,\bar{R}_y v\,L_c \qquad (2.62)$$

For the more complicated situation involving leakage, Wills assumed that the leakage velocity, w, is constant throughout the region. From the continuity equation this implies that v is not a function of y, that is the crossflow velocity does not vary in the crossflow direction. Allowing for a uniform pressure gradient in the

y-direction, the flow equations (Equation (2.59)) reduce to

$$\frac{\rho}{\gamma} w \frac{dv}{dz} = - \eta \bar{R}_y v - \frac{\Delta p_c}{L_c} \qquad (2.63)$$

Wills solution for this is

$$v = \frac{\Delta p_c}{\eta \bar{R}_y L_c} \{1 - \exp(-[\frac{\bar{R}_y \eta \gamma}{\rho w}] z)\} \qquad (2.64)$$

Wills did not state what boundary conditions apply at the crossflow inlet, but simply assumed that the solution applies in the range $z = 0$ to $z = B_s$. This implies that the crossflow velocity is zero along the downstream baffle, rising gradually to a maximum along the upstream baffle face.

Since an analytical solution over the full crossflow length was required (for convenience within a flowstream method) Wills defined an average crossflow velocity, $\bar{v}$, as

$$\bar{v} = \frac{1}{B_s} \int_0^{B_s} v \, dz \qquad (2.65)$$

Combining Equations (2.64) and (2.65), integrating between $z = 0$ to B_s and rearranging gives

$$\Delta p_c = \frac{\eta \bar{v} \bar{R}_y L_c}{1 - \frac{1}{\Omega}(1-\exp(-\Omega))} \qquad (2.66)$$

where

$$\Omega = \frac{\gamma \eta \bar{R}_y B_s}{\rho w}$$

By comparing Equation (2.66) with (2.62) for the non-leakage case ($\bar{v} = v$ since $v \neq$ fn (z)), Wills was able to express the crossflow pressure drop in the leakage case as a function of crossflow pressure drop in the non-leakage case:

$$\Delta p_{c\ell} = \Delta p_c F_{c\ell} \qquad (2.67)$$

where $F_{c\ell}$ is the crossflow-leakage interaction factor defined as

$$F_{c\ell} = 1/\{1 - \frac{1}{\Omega}(1-\exp(-\Omega))\} \tag{2.68}$$

In calculating the mean crossflow superficial velocity, $\bar{v}$, Wills assumes that this stream occupies the total space between baffles:

$$\bar{v} = \frac{\dot{M}_c}{\rho A_c^s} \tag{2.69}$$

where A_c^s is the superficial crossflow area. However, Wills' solution implies a crossflow velocity profile inclined at an angle to the baffle in which the crossflow occupies only part of the baffle overlap region; the remainder being occupied by the leakage stream as shown in Figure 2.20. If this hypothesis is correct the average crossflow velocity can be expressed as

$$\bar{v} = \frac{\dot{M}_c}{\rho A_c^s} \quad \frac{1}{[\dot{M}_c/(\dot{M}_c+\dot{M}_{\ell o}/2)]}$$

$$= \frac{\dot{M}_c + \dot{M}_{\ell o}/2}{\rho A_c^s} \tag{2.70}$$

implying an enhancement in crossflow pressure drop for the simpler reason that the crossflow velocity is higher due to the presence of leakage.

Wills went on to propose an interaction pressure drop relationship for bypassing and shell-baffle leakage, similarly to the crossflow case. This model was not supported by any experimental data.

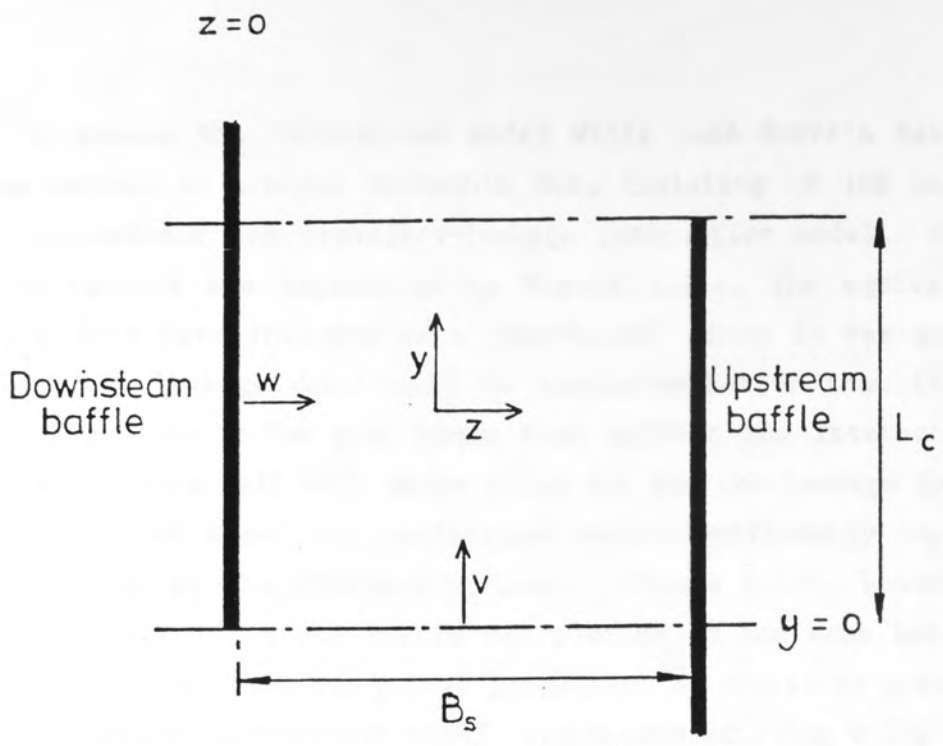

Figure 2.19: Geometry Used in the Derivation of Wills' (1984) Crossflow–Leakage Interaction Model.

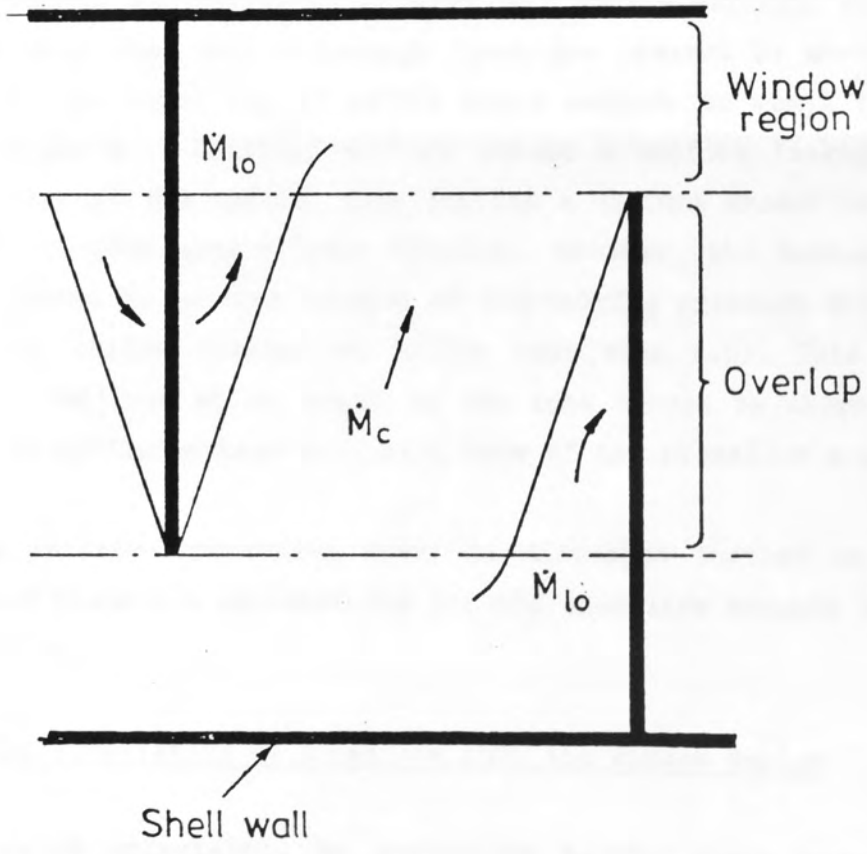

Figure 2.20: The Effect of Baffle Leakage in the Overlap on the Crossflow.

To assess the interaction model Wills used Moore's basic multi-stream method to predict Macbeth's data (relating to 18% baffle cut) with and without the crossflow-leakage interaction model. Comparison of the results are reproduced in Figure 2.21a. The equivalent non-leakage data were included as a 'benchmark' since it was argued that none of the leakage data could be predicted better than the simpler non-leakage case. The plot shows that without the interaction model the leakage data fell well below those for the non-leakage case. With the interaction model the predictions were significantly improved and were as good as the non-leakage case. Figure 2.21b, however, shows Macbeth's data for a 25% baffle cut plotted on the same basis. This plot shows a significantly poorer prediction of crossflow pressure drop with the leakage interaction model, again contradicting Wills' original hypothesis.

In conclusion, there is little evidence to suggest that leakage interaction is a significant phenomenon. Poor prediction of crossflow pressure drop when baffle leakage flows are present is more likely to be due to the inability of baffle space methods to model the leakage stream properly. Existing methods assume a uniform leakage velocity profile through the baffle, this implies a uniform crossflow occupying the complete flow area between baffles. However, the leakage velocity profile cannot be uniform because of the varying pressure driving force across the baffle (larger at baffle root than tip). This implies a crossflow inclined at an angle to the tube bundle as shown in Figure 2.20, with baffle leakage occupying some of the crossflow area.

The leakage-interaction model is discussed further in Chapter 9 along with plausible explanations for the anomalies brought to light in this section.

2.7.2 The Penetration of Crossflow into the Window Region

A major uncertainty in predicting baffle space pressure drops using component models/correlations is establishing how far, on average, crossflow penetrates into the window region. Bell (1960) suggested half the number of tube rows in the window, Moore (1974) suggested that the crossflow penetrated to the centroid of the window

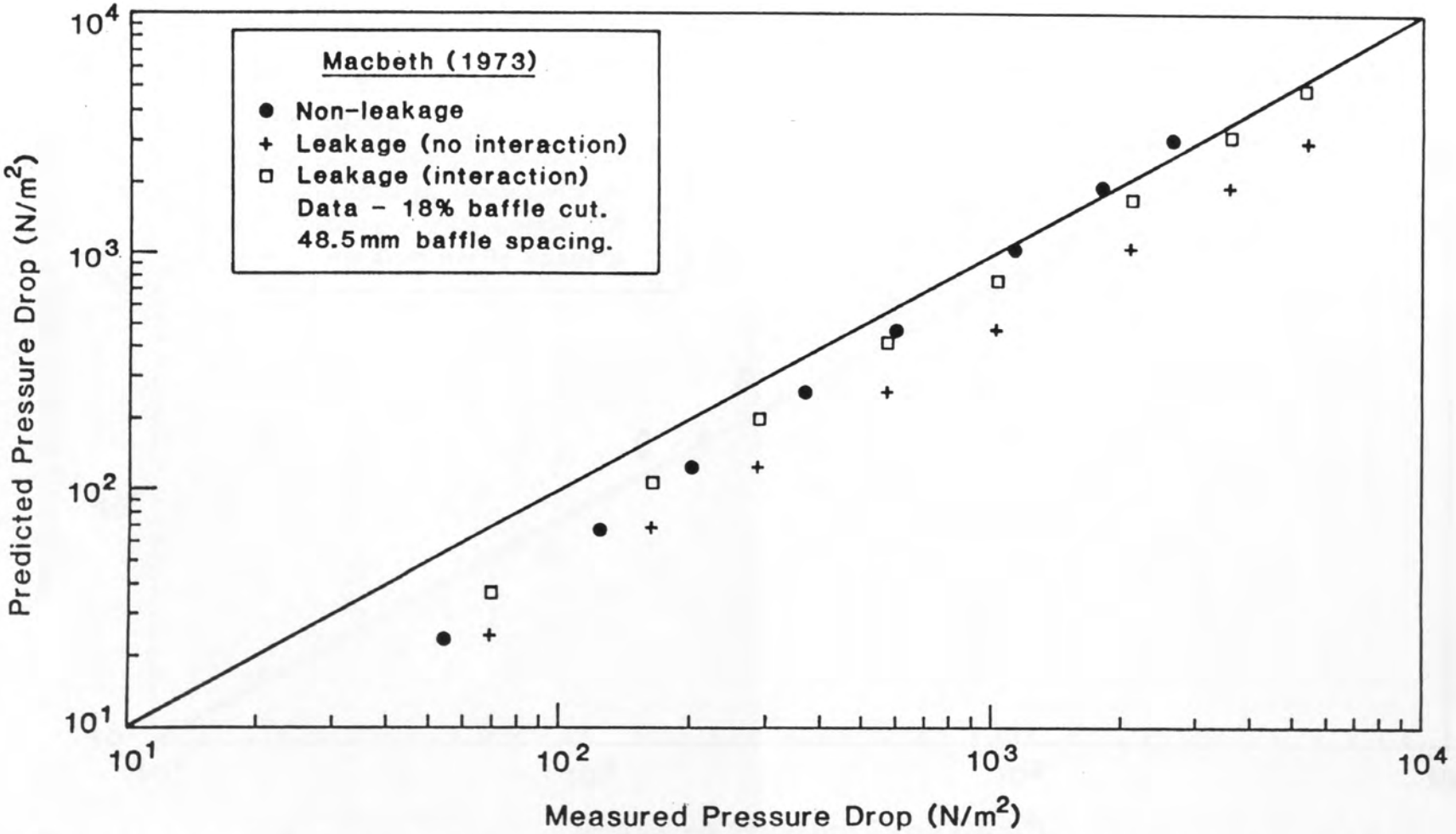

Figure 2.21 a: Prediction of Macbeth's (1973) Crossflow Measurements Using Moore's (1974) Method, with and without Will's (1984) Crossflow – Leakage Interaction Model. Baffle Cut = 18 %.

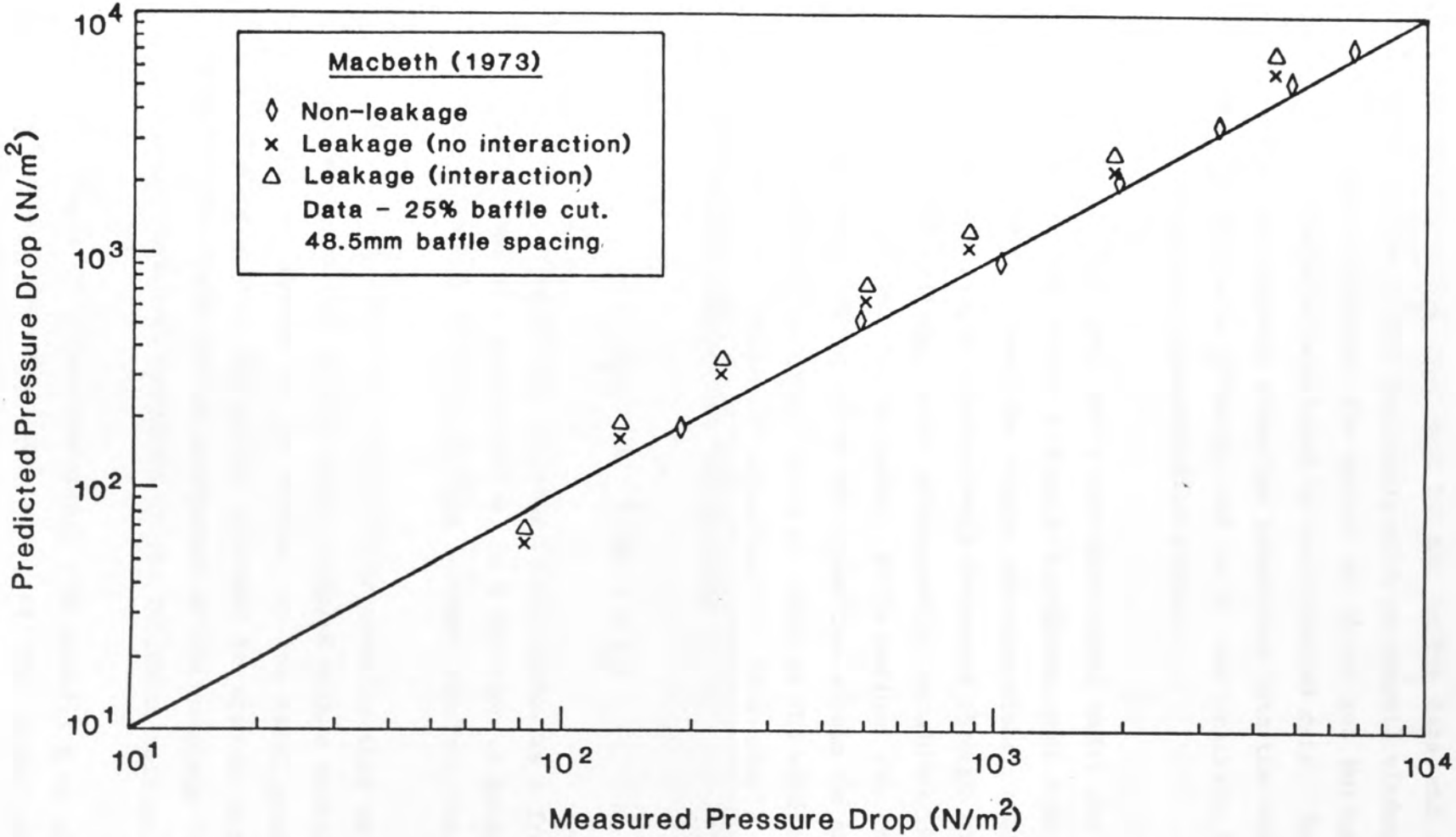

Figure 2.21 b: Prediction of Macbeth's (1973) Crossflow Measurements Using Moore's (1974) Method, with and without Will's (1984) Crossflow – Leakage Interaction Model. Baffle Cut = 25 %.

regions. Grant and Murray (1972), however, avoided the need to consider such effects; they defined the boundary between crossflow and window region as the plane described by the baffle tips and accounted for crossflow in the window implicitly with an overall window correlation. Wills did not recommend the method of Grant and Murray since their empirical correlation was based on very limited data. Furthermore, he argued that the distance crossflow penetrates into the window must be a function of shellside geometry and so it was unlikely that Bell and Moore's methods were representative either.

Instead, Wills proposed a one-dimensional model for crossflow in the window by considering a simple two-dimensional representation of the window flow. Here the single one-dimensional crossflow stream flowing into the window progressively decreases through losses in axial flow along the window, which subsequently recombines into a single crossflow in the next baffle space. Wills defined the crossflow penetration as the point at which the crossflow stream in the window had decreased to half its initial value at inlet to the window. By applying the momentum and continuity equations to this simple geometry the following implicit expression was derived:

$$f_p = 1 - \frac{1}{2} \exp(-a' f_p) \qquad (2.71)$$

where f_p is the penetration distance in the window as a fraction of the window height and the coefficient a' is a function of geometry and both crossflow and axial friction factors (assumed constant throughout).

Wills had no means of independently checking this model. Instead, he assessed the effect of the model, coupled with a method of accounting for baffle leakage in the window, on the total predicted baffle space pressure drop. The method proposed to account for both baffle leakage in the window and an assessment of the complete 'stream interaction' method are both discussed in the following section.

The results of three-dimensional flow modelling of shellside flow have permitted independent assessment of the crossflow penetration model. This is discussed in Chapter 8.

2.7.3 Baffle Leakage in the Window

Having shown that multi-stream baffle space methods underpredict the leakage flowrates in the window region (Section 2.6.2, Equations (2.55) to (2.58)), Wills illustrated the significance of this weakness by comparing the total baffle space pressure drop predictions of both Moore's and Grant and Murray's methods with the data of Macbeth (1973). Comparisons showed that for small baffle cuts, for which leakage in the window is small, both methods predicted the data to within ± 35%. For large baffle cuts, however, a considerable overprediction was observed, as much as 80% higher than the data. Wills concluded that since this effect was significant some means of accounting for it was necessary. Within the framework of baffle space methods, it is not possible to treat this leakage as a separate stream in a network, since total flow is necessarily assumed to exist at a node within the baffle space. Instead, Wills started from the continuity equations of the more fundamentally correct approach of Parker and Mok (1969) and defined an effective leakage area that, when used in a baffle space method, would give the same overall pressure drop as Parker and Mok's method. With reference to Figure 2.16, Parker and Mok define the following relationship for leakage in the window (ℓw):

$$\Delta p_{\ell w} = \frac{N_B}{2} n_{\ell w} \frac{\dot{M}_{\ell w}^2}{2 \rho A_{\ell w}^2} + \frac{N_B}{2} \Delta p_w \qquad (2.72)$$

and leakage in the overlap (ℓo):

$$\Delta p_{\ell o} = N_B n_{\ell o} \frac{\dot{M}_{\ell o}^2}{2 \rho A_{\ell o}^2} \qquad (2.73)$$

Wills assumed that leakage in the window suffers pressure loss in flowing through the baffle plate only. Then, Equation (2.72) reduces to

$$\Delta p_{\ell w} = \frac{N_B}{2} n_{\ell w} \frac{\dot{M}_{\ell w}^2}{2 \rho A_{\ell w}^2} \qquad (2.74)$$

Furthermore, since $n_{\ell w}$ and $n_{\ell o}$ are weak functions of Reynolds number, Wills assumed that

$$n_L = n_{\ell w} = n_{\ell o} \tag{2.75}$$

Thus from Equations (2.73) to (2.75) and assuming $\Delta p_{\ell w} = \Delta p_{\ell o}$, the following relationship was obtained:

$$\left(\frac{\dot{M}}{A}\right)_{\ell w}^2 = 2 \left(\frac{\dot{M}}{A}\right)_{\ell o}^2 \tag{2.76}$$

Wills defined the total pressure drop (over the complete length of the exchanger) in terms of an effective leakage area, A_e:

$$\Delta p_T = N_B \, n_L \, \frac{\dot{M}_L^2}{2 \rho A_e^2} \tag{2.77}$$

where

$$\dot{M}_L = \dot{M}_{\ell o} + 2 \dot{M}_{\ell w} \tag{2.78}$$

therefore

$$2 \left(\frac{\dot{M}_L}{A_e}\right)^2 = 2 \left(\frac{\dot{M}}{A}\right)_{\ell o}^2 = \left(\frac{\dot{M}}{A}\right)_{\ell w}^2 \tag{2.79}$$

Eliminating mass flow using the relationship given in Equation (2.78) gives the effective leakage area as

$$A_e = A_{\ell o} + A_{\ell w} \, 2^{3/2} \tag{2.80}$$

substantially larger than the true leakage area defined as

$$A_L = A_{\ell o} + A_{\ell w} \tag{2.81}$$

The qualitative result of using this effective leakage area would be to give a larger proportion of baffle leakage flow. As Wills pointed out, this method would not give the correct window flow fraction since the definition of Moore's network (or any other baffle space method) does not permit leakage to join the window flow. However,

since the bulk of the shellside pressure drop typically derives from crossflow and crossflow turning into the window, it was more important to obtain a good approximation to the crossflow rather than window flow fraction.

Wills did not assess the effective leakage area independently of the other models he proposed. Instead, he used the full Stream Interaction method to predict the data of Macbeth (1973). A comparison between predictions and measurement of total baffle space pressure drop showed no evidence of a systematic over-estimation of pressure drop for large baffle cuts with baffle leakage, as did both the Moore and Grant and Murray's method. All predictions fell within ± 30% of the experimental data, a significant improvement over the other methods reviewed.

2.8 General Summary

The large bulk of data relating to shellside flow and pressure drop might suggest that the field has been covered adequately and is well understood. The review of the literature, however, has shown this not to be the case. In particular, a theme evident throughout the whole review is the lack of information deriving from cylindrical baffled geometries. Moreover, a considerable amount of the limited data obtained from cylindrical geometries derives from small models with few tubes. There is clearly need for more data deriving from realistic geometries typical of commercial designs.

A further significant point raised by the review is that the majority of all shellside data were obtained by studying isolated flow phenomena in idealised models. Whilst this is undoubtedly a convenient and logical approach, considering the complexities of shellside flow, these data do not compare well with the limited data from cylindrical units. Clearly this is due to the lack of geometric similarity, but these differences have not been successfully quantified.

Ultimately, all investigations are aimed at producing more accurate and reliable shell-and-tube heat exchanger design methods. Whilst investigators such as Wills (1984) have contributed significantly to the improvement of design methods, it has become evident that until more information is obtained about the nature of shellside flow and pressure drop, further development of these methods will be hindered.

CHAPTER 3

AIMS OF THE CURRENT INVESTIGATION

3. AIMS OF THE CURRENT INVESTIGATION

The review of the literature highlighted a lack of understanding in certain aspects of shellside flow and pressure drop. In particular, because of the limited amount of data deriving from realistic shellside geometries, it remains to be shown whether empirical correlations, deriving from isolated flow phenomena, remain valid when applied to the design of commercial units.

In order to improve the current state of understanding and give plausible answers to, at least, some of the questions posed by the literature review, a number of objectives were laid down. These were as follows:

1) to obtain and analyse data on single-phase shellside flow for a number of realistic heat exchanger geometries;

2) to compare the results obtained with previous data deriving from both ideal and real exchanger geometries;

3) to assess, in the light of the newly acquired data, the components of flow stream models, in particular those in the HTFS design program TASC.

It was not an objective of this thesis to simply add to the data bank of overall baffle space pressure drop measurements; such data are restricted as to how much information they can supply. Rather, the aim is to gain a greater understanding of the nature of shellside flow through a more fundamental and comprehensive approach. The problem was attacked using three separate but complementary techniques: pressure drop measurements; flow visualisation and three-dimensional flow modelling.

To meet the requirements of the experimental programme, the Shellside Flow Visualisation Rig was designed and constructed at the Harwell Laboratories, under the auspices of HTFS. The rig was constructed from glass which afforded good visibility for flow visualisation photographic studies and its main flow areas were representative of industrial units. A further feature of the rig was the large number of pressure tappings available and the flexibility with which these could be positioned within the shellside flow.

Three-dimensional flow modelling was also used to complement the experimental programme. Modern vector computers coupled with powerful numerical techniques have enabled economic solutions to the flow equations, in three dimensions, to be obtained. One such code, known as FLOW3D, is currently under development at the Harwell Laboratory. These codes have mainly been used for modelling natural convection in simple geometries. In the present work this has been taken one stage further by modelling shellside flow, that is forced flow in complex geometries.

CHAPTER 4

EXPERIMENTAL APPARATUS

4. EXPERIMENTAL APPARATUS

4.1 Introduction

The Shellside Flow Visualisation Rig was designed and constructed to meet the demand from industry to gather more detailed information on the mechanisms of shellside flow and pressure drop.

The work presented in this thesis is the first part of a long-term research programme based at the Harwell Laboratories. As a result, the significance of some of the features of the rig are not immediately apparent. It is intended, eventually, to use the rig to measure local shellside velocities using Laser Doppler Anemometry (LDA). For this technique to be applied successfully, the model exchanger must allow access to laser light and, in addition, incorporate refractive index matching of the shellside fluid. To fulfil these requirements the rig was constructed from borosilicate glass and trichloroethylene would be used as the shellside fluid; at 34°C both have the same refractive index. Those materials in direct contact with the shellside fluid, used in construction of the rig, were dictated by the chemical nature of trichloroethylene (Sax, 1984), and were stainless steel, borosilicate glass and PTFE.

The good visibility afforded by the glass was exploited in a short programme of dye injection flow visualisation. The shellside fluid used was water and whilst refractive index matching could not be achieved, visibility was adequate enough to establish global flow patterns (Chapter 6).

4.2 General Layout

The shellside flow rig consisted of a glass shell-and-tube heat exchanger model, centrifugal pump, supply tank and glass piping system, three flowmeters, cooling coil and pressure measuring instrument tubes. The main features of the rig are shown schematically in Figure 4.1 and complemented by two photographs shown in Figures 4.2 and 4.3.

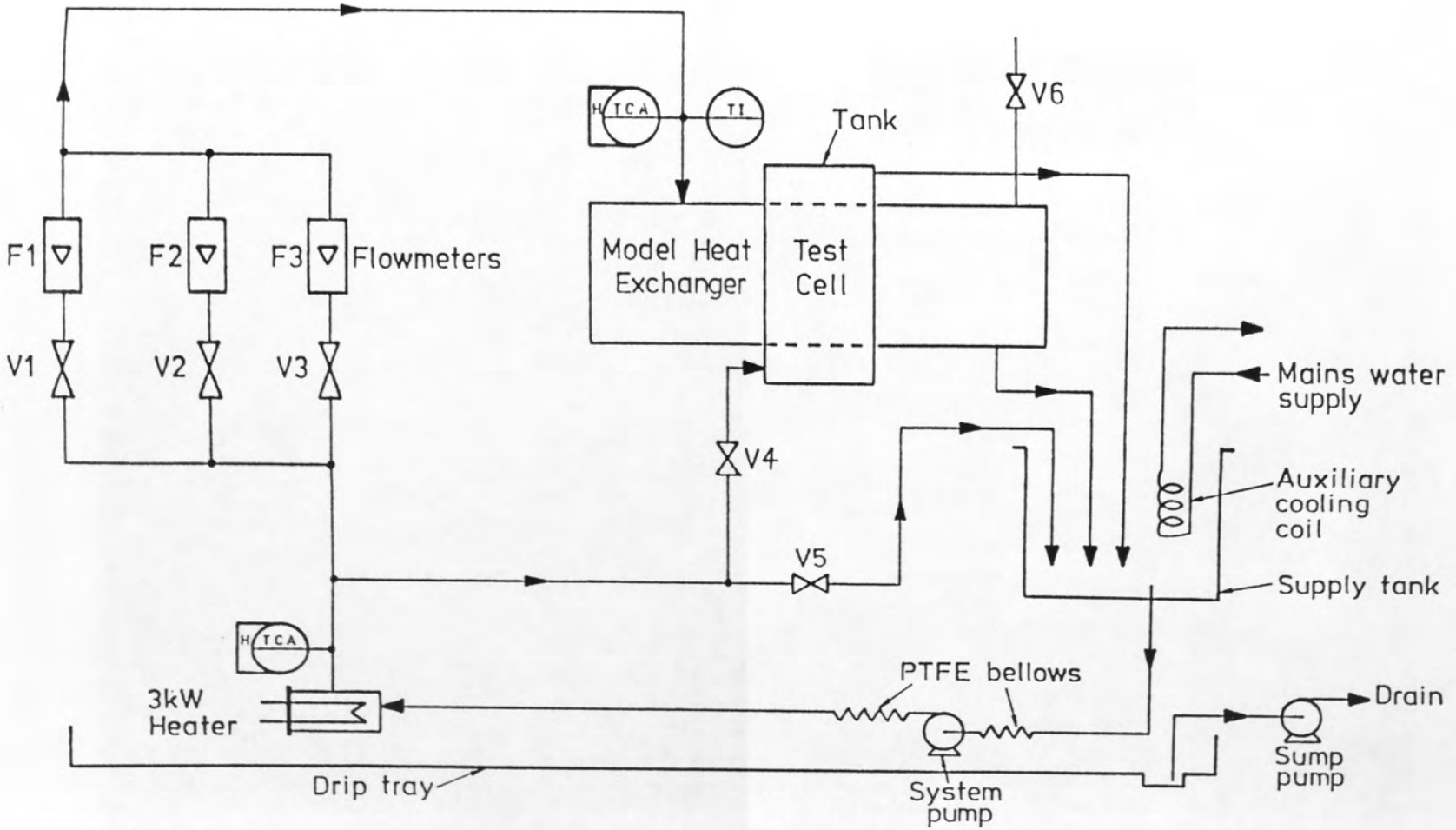

Figure 4.1: Schematic Showing General Layout of the Shellside Flow Rig.

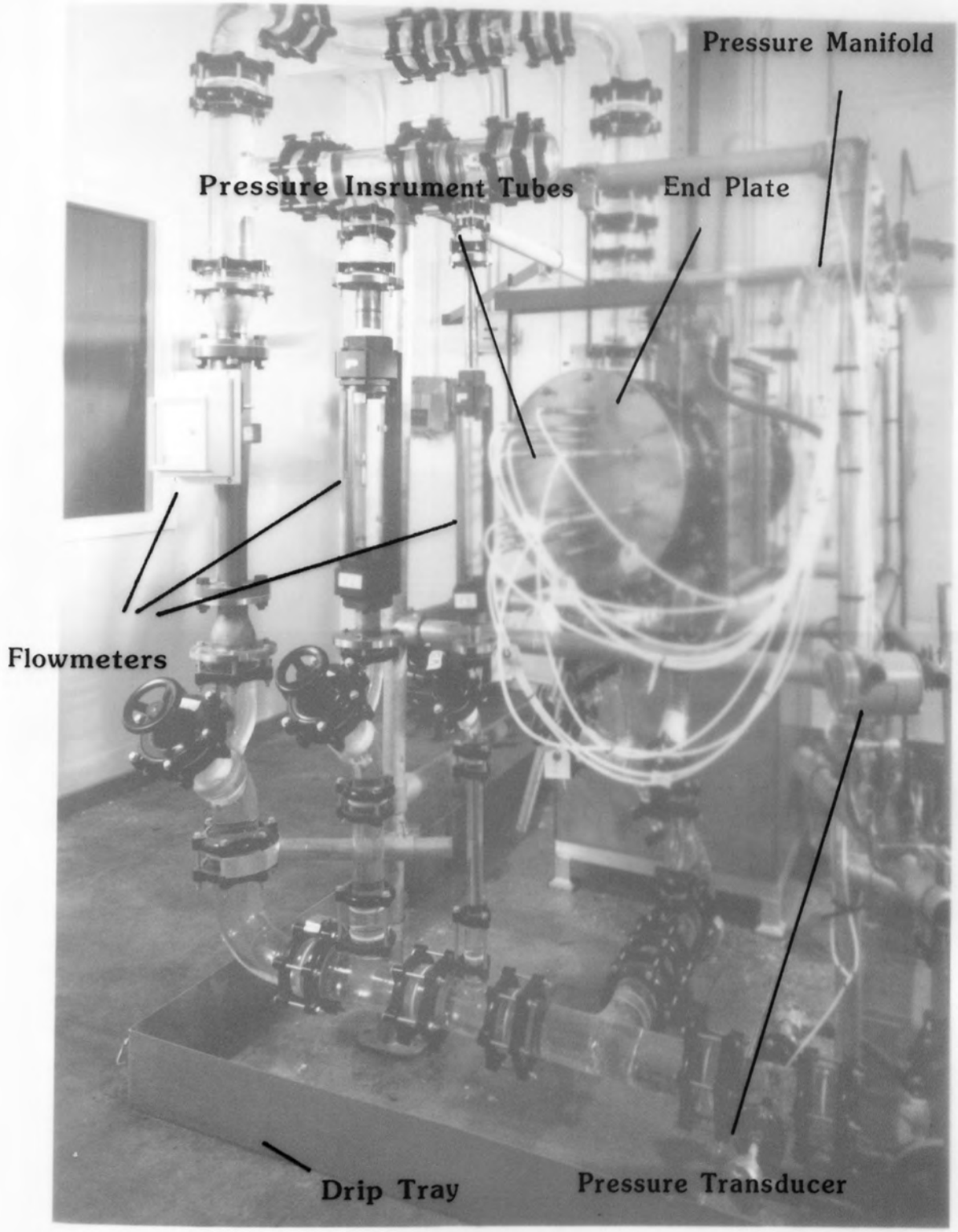

Figure 4.2 End View of Shellside Flow Rig

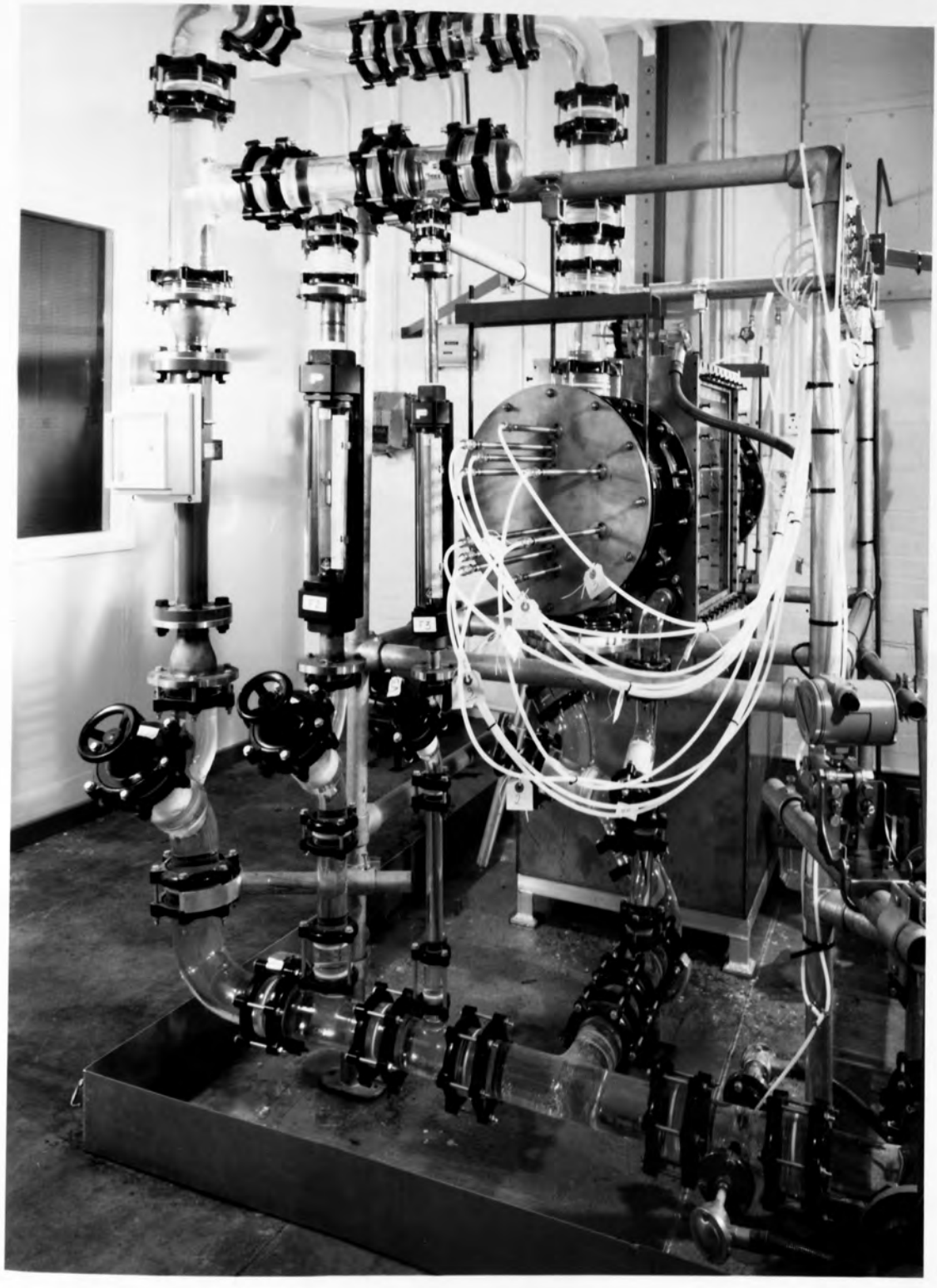

Figure 4.2 End View of Shellside Flow Rig

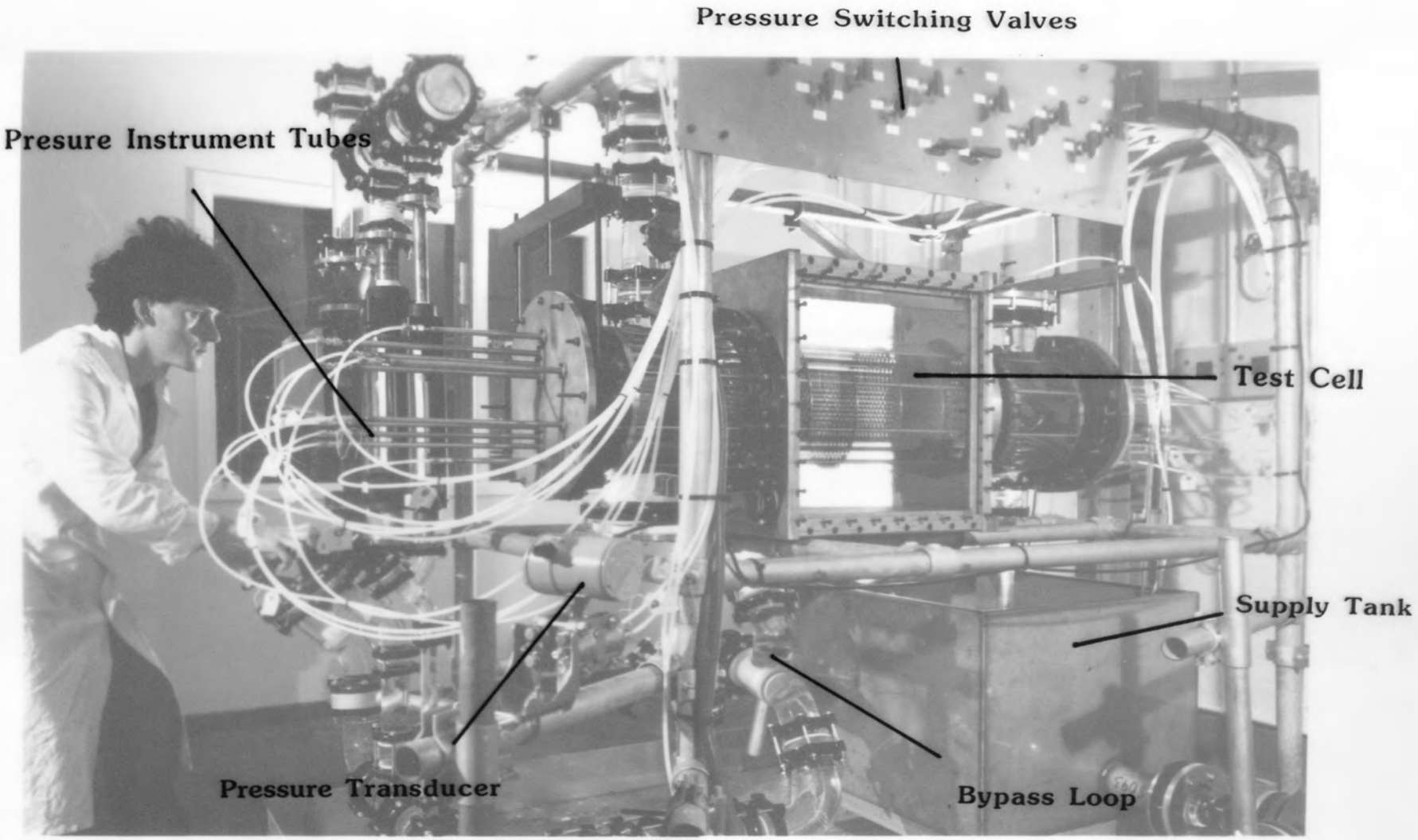

Figure 4.3 Side View of Shellside Flow Rig

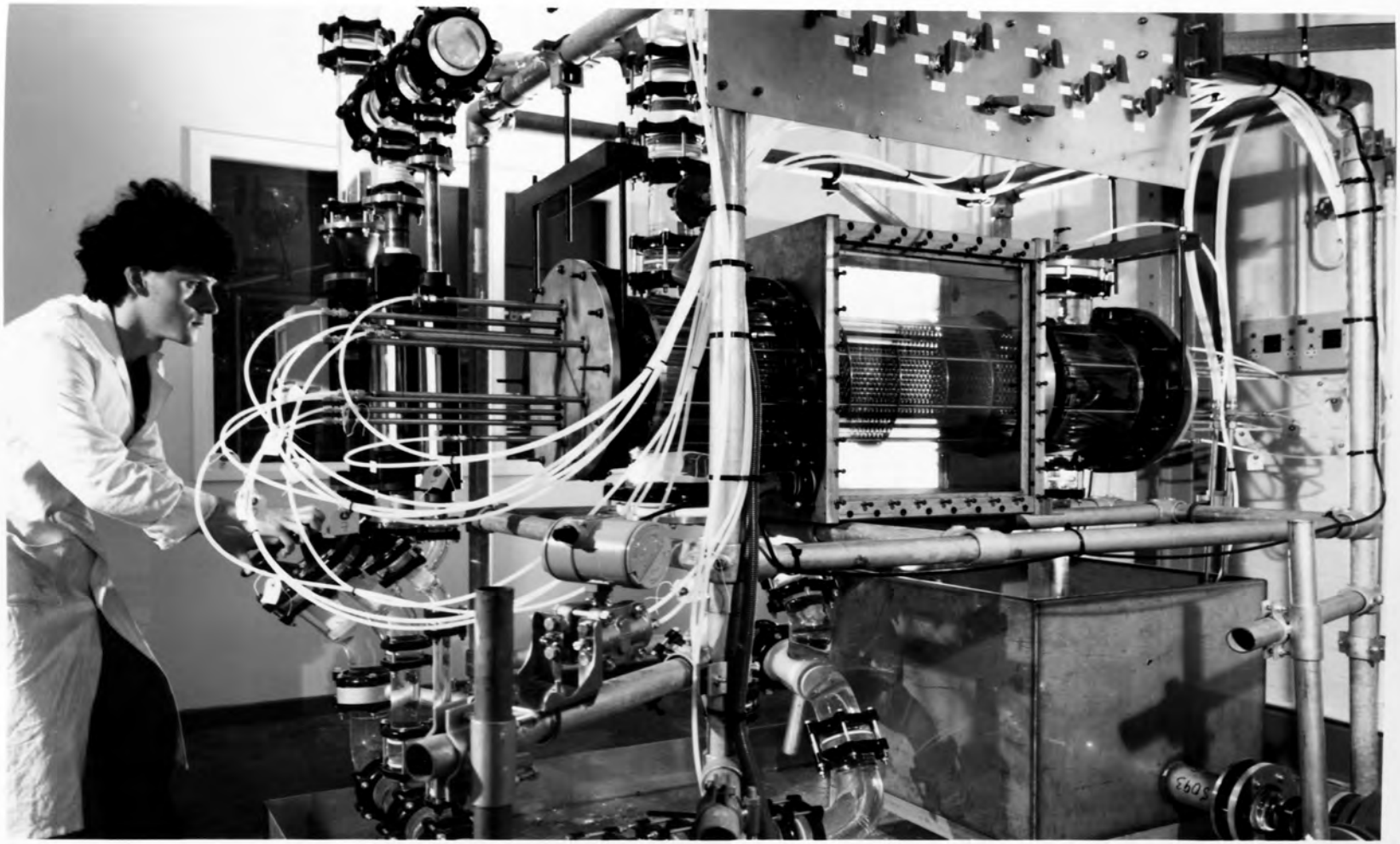

Figure 4.3 Side View of Shellside Flow Rig

The pump was fed from a floor level tank of 300 litres capacity. The fluid was pumped from the tank, through the flow metering system, into the shellside of the model heat exchanger and back into the supply tank. A proportion of the fluid was re-routed to the bypass circuit and the test cell tank, both streams feeding back to the supply tank. In this manner, the total flowrate remained approximately constant, such that the bypass value (V5) could be used for coarse adjustments to the shellside flow with finer control obtained from the flow metering system.

4.3 Model Exchanger

The model 'exchanger' consisted of a cylindrical shell, a 'tube' bundle framework, a number of glass rods and a test cell tank surround.

The shell was constructed from three Schott Duran borosilicate glass cylindrical sections, each of 300 mm internal diameter. The end cross-piece sections were 400 mm long and the central 'test section' was 500 mm long. The central section was held in place within the test cell surround, which was essentially a rectangular tank with borosilicate glass windows for observation purposes (see Figure 4.3).

The tube bundle framework is shown in Figure 4.4 and was constructed from the following:

1) A number (depending on the baffle spacing) of stainless steel single segmented baffles, each of 3 mm thickness with a 25% cut based on the shell inside diameter. Each had a diameter of 299.5 with 217 holes, 12.4 mm in diameter, on a rotated square layout and six holes, 9.7 mm in diameter for tie rods.

2) Eight stainless steel tie rods, each of 9.53 mm (3/8") diameter and 1206 mm in length. 10 mm of each end were threaded for bolting purposes. Two of the eight rods were 24 mm longer, at 1230 mm. These were used to align and locate the framework in relation to the shell and end plates.

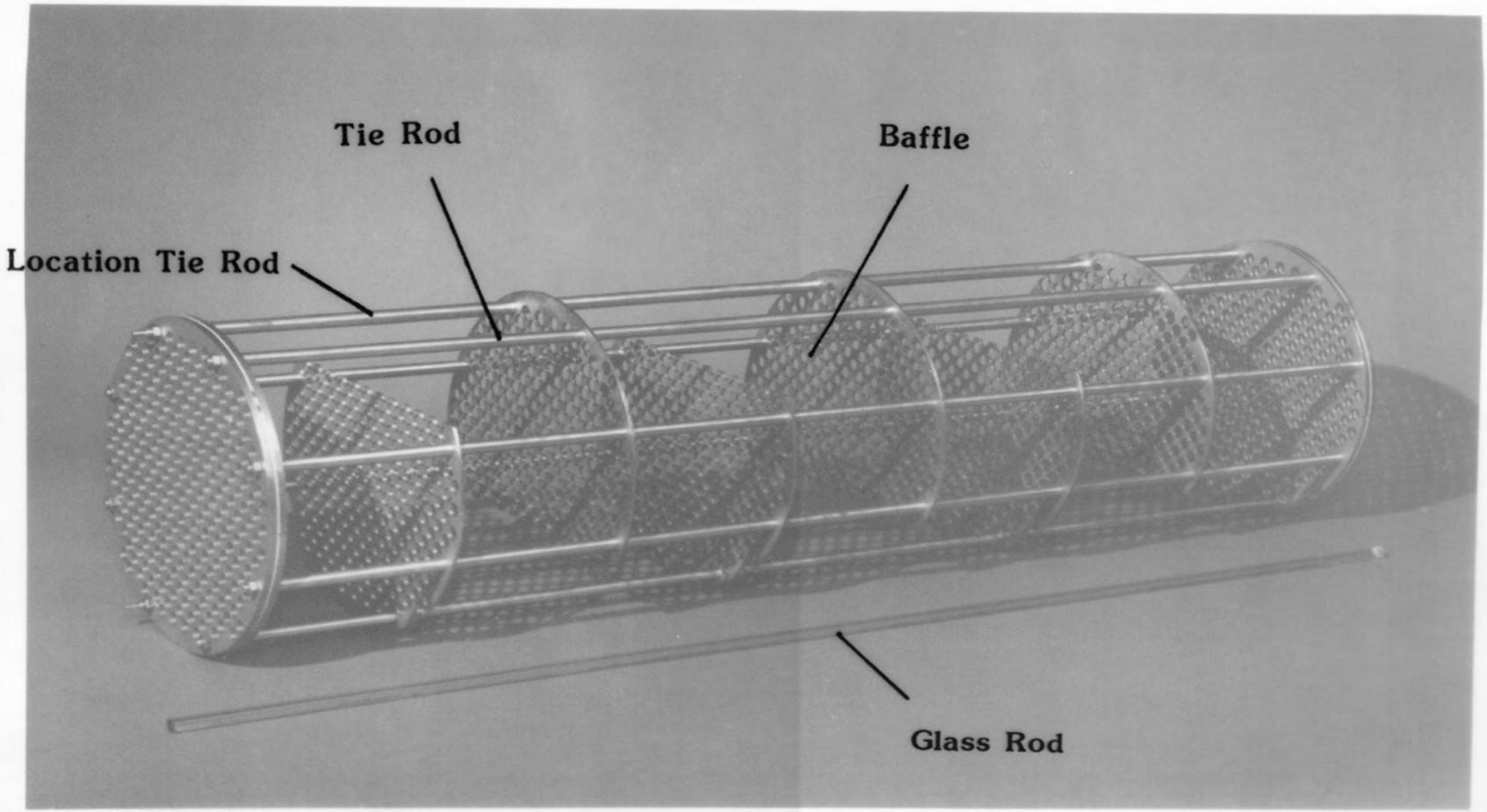

Figure 4.4 Rod Bundle Framework

Figure 4.4 Rod Bundle Framework

3) A number of stainless steel spacer tubes of variable length, each of 12 mm outside diameter and 1 mm wall thickness.

4) Four stainless steel tube sheets, 6.5 mm thick and 299.5 mm in diameter. Each had 278 drilled holes to accommodate tie rods and tube bundle. Both ends of the framework consisted of two tube sheets with a 1 mm thick PTFE gasket sandwiched in between. This was intended to afford a degree of sealing and hold the bundle firmly in position.

The tube bundle consisted of 260 Schott Duran borosilicate glass rods, each of 12 mm in diameter and 1206 mm in length and 10 pressure instrumented tubes of the same diameter. The shellside rig was operated under isothermal conditions so neither tubes nor tubeside headers were necessary (using rods instead of tubes reduces the number of interfaces that laser light would need to pass through in a future LDA study, minimising dispersion and preventing the need for a temperature controlled tubeside fluid).

A cross-section of the 'tube' bundle is shown in Figure 4.5a. One row of rods from the top and bottom of the bundle were removed to increase entrance and exit escape areas in accordance with the Tubular Exchangers Manufacturers Association (TEMA, 1978). The important dimensions of the rig are summarised in Table 4.1.

Three baffle spacing were studied and the baffled arrangements for each are shown in Figure 4.5b.

4.4 Assembly of Exchanger

The bundle framework (Figure 4.4) was assembled outside of the shell.

The tie rods were bolted at one end and fed through the tie rod holes drilled in the tube sheets. The first set of spacers were then fed onto the rods from the other end followed by the first baffle in the correct orientation. This process was continued until all the spacers and baffles were in place. The second pair of tube sheets were then positioned with the PTFE O-ring in place, aligned correctly with the tube sheets on the other end of the framework. The tie rods were then bolted firmly in place so that the framework became rigid. The

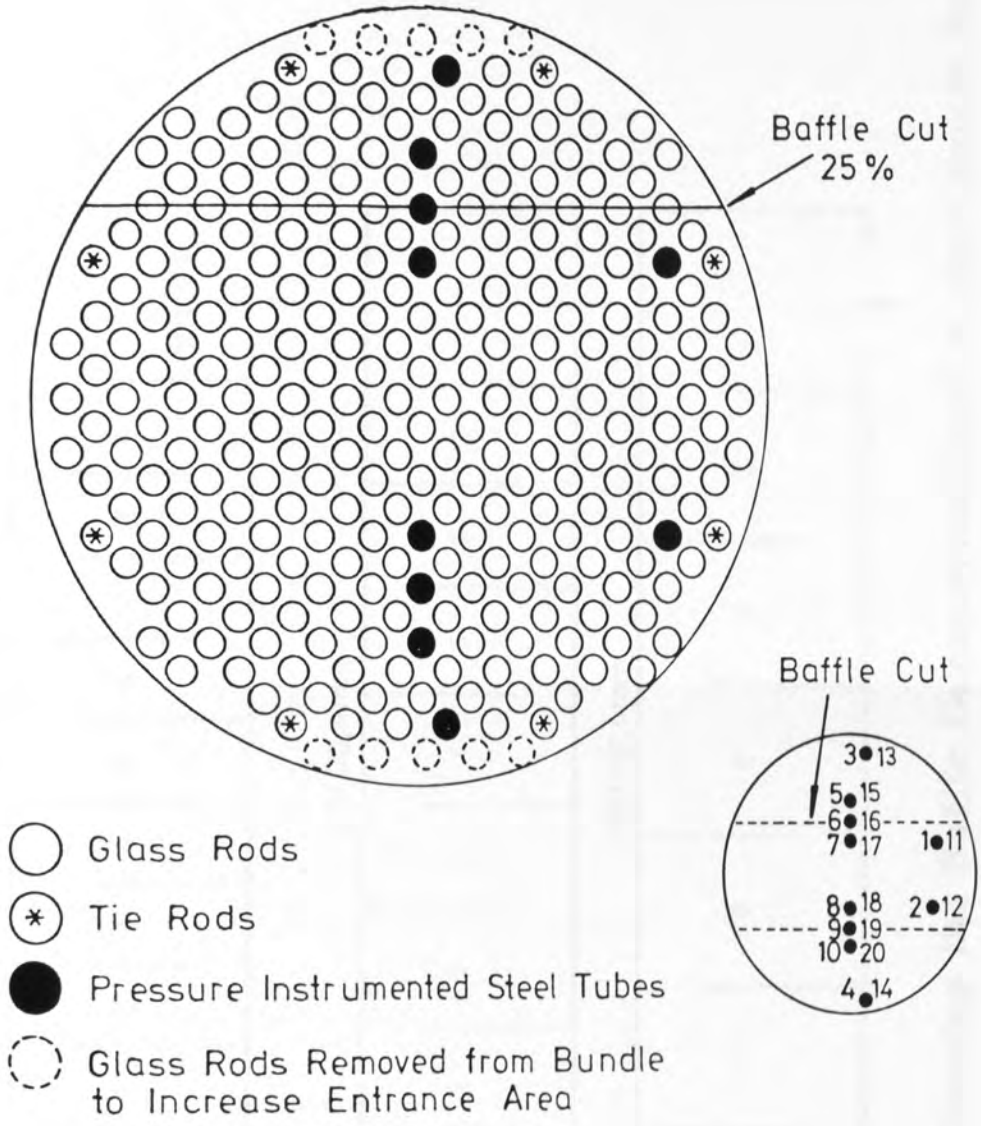

Figure 4.5a:Cross-Section of Rod Bundle Showing Locations of Pressure Instrumented Tubes.

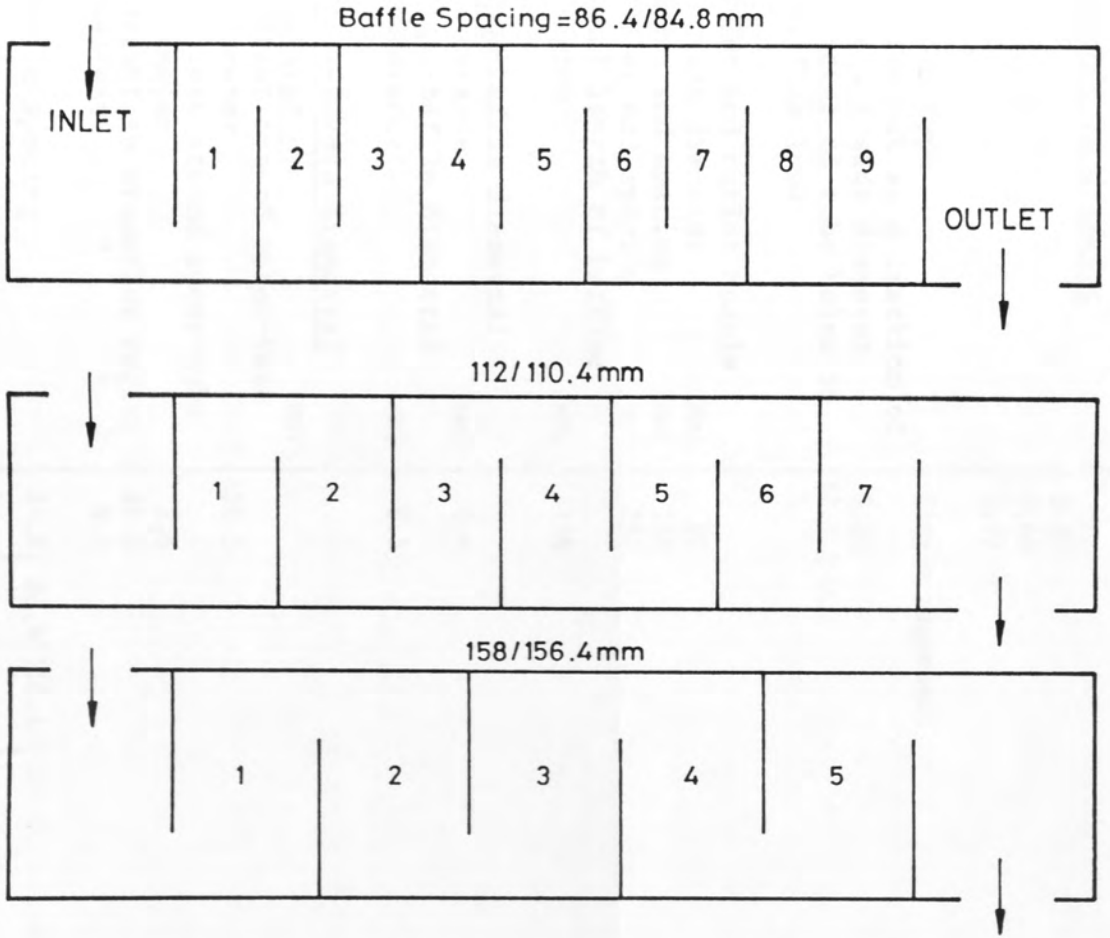

Figure 4.5b: Schematic Showing the Baffle Geometries Used in the Current Investigation.

Table 4.1: Main Dimensions of the Shellside Flow Rig Used in the Current Study

Item	Dimension/Description					
Inside diameter of shell (mm)	300 ± 0.1					
Diameter of glass rods (mm)	12 ± 0.4					
Length of glass rods (mm)	1206 ± 0.1					
Number of glass rods	270					
'Tube' layout	Rotated Square					
Pitch/tube diameter						
P_t/D_t	1.25					
P_x/D_t	0.88					
P_y/D_t	1.77					
Baffle type	Single segmental					
Baffle cut as a fraction of shell inside diameter	0.25					
Diameter of tube holes in baffles (mm)	12.4 ± 0.1					
Inlet and outlet nozzle inside diameter (mm)	80					
Inlet end spacing (mm)	150					
Outlet end spacing (mm)	250					
Total length of baffled region (mm)	1158					
Tube-baffle diametral clearance (mm)	0.4					
Shell-baffle diametral clearance (mm)	0.5					
Shell-bundle diametral clearance (mm)						
Largest around outer-tube diameter	29.1					
Smallest around outer-tube diameter	2.6					
Largest in crossflow region	25.6					
Smallest " "	9.0					
Baffle spacing	84.8	86.4	110.4	112.0	156.4	158.0
Number of baffles	10	10	8	8	6	6
Baffle thickness (mm)	4.59	3.00	4.59	3.00	4.59	3.00
Thickness of neoprene gaskets on baffles (mm)	1.59	-	1.59	-	1.59	-

baffled framework was then inserted into the shell, care being taken to ensure correct alignment of the baffles in relation to the shell.

When the bundle framework was in position within the shell, the glass rods were fed through the tube sheets and baffles. When the rod bundle was complete the stainless steel end plates, shown in Figure 4.6, were positioned with respect to the bundle by inserting the two location tie rods into the recesses on the end plates and bolted to the shell ends, sealed with PTFE O-rings. The pressure instrument tubes (see Section 4.7.2) were then pushed through the appropriate holes drilled in the end plates and sealed with PTFE O-rings.

4.5 Leakage Seals

Half of the experimental study was concerned with pressure measurements in the absence of baffle leakage flows. Both the tube-baffle and shell-baffle leakage areas were blocked by sticking thin (1/16") neoprene sheets to the baffles. Tube-baffle holes were punched such that a good seal was obtained when the glass rods were pushed through the baffle holes as shown in Figure 4.7a. The shell-baffle leakage area was sealed by leaving a skirt that overlapped the baffled edge as shown in Figure 4.7b.

A very good seal was seen to have been achieved using this method; air entrained during the start-up stage had to be vented from the top of each baffle compartment using the uppermost pressure instrument tube. For the cases in which baffle leakage flows were present, this never posed a problem since the air could leak freely down the length of the exchanger and be vented at the end using valve V6 (see Figure 4.1).

For each baffle spacing studied, new gaskets were manufactured to ensure a tight seal throughout the experimental programme.

4.6 Pump and Piping

The pipe system was constructed from 80 mm bore Schott Duran boro-silicate glass, connected by plastic flanges, sealed with PTFE O-rings.

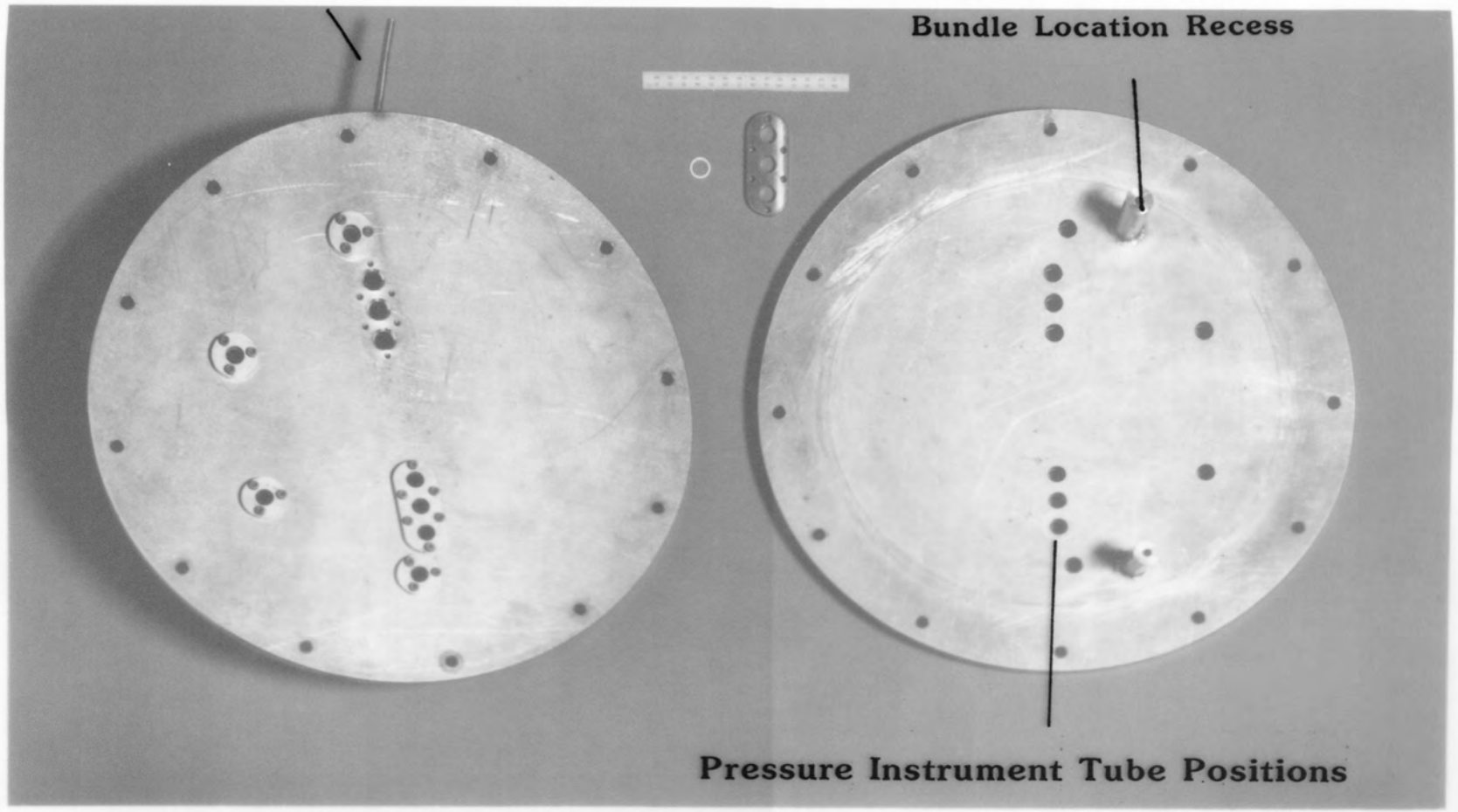

Figure 4.6 Shell End Plates Showing Rod
Bundle Location and Pressure Instrument Tube Positions

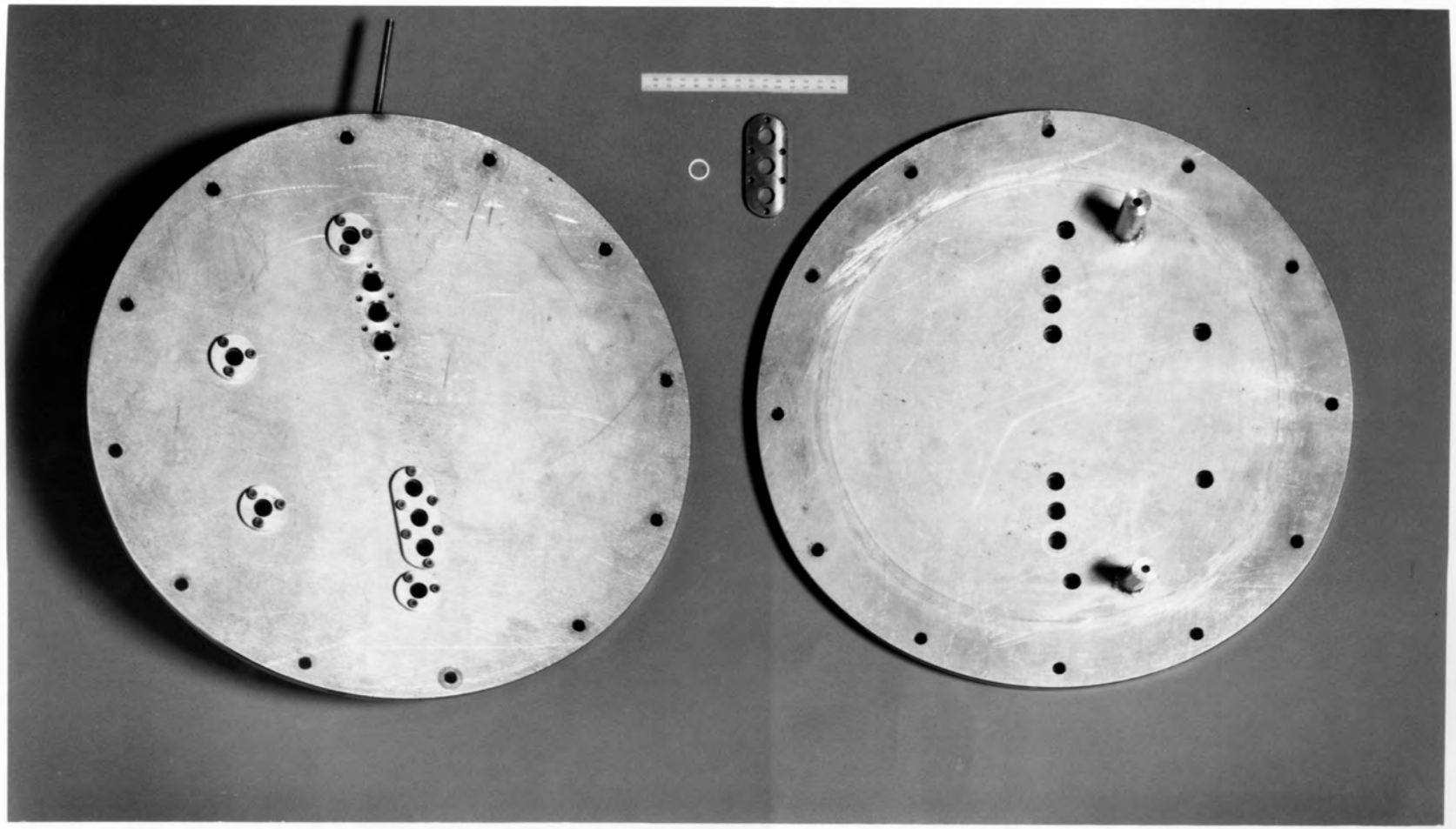

Figure 4.6 Shell End Plates Showing Rod Bundle Location and Pressure Instrument Tube Positions

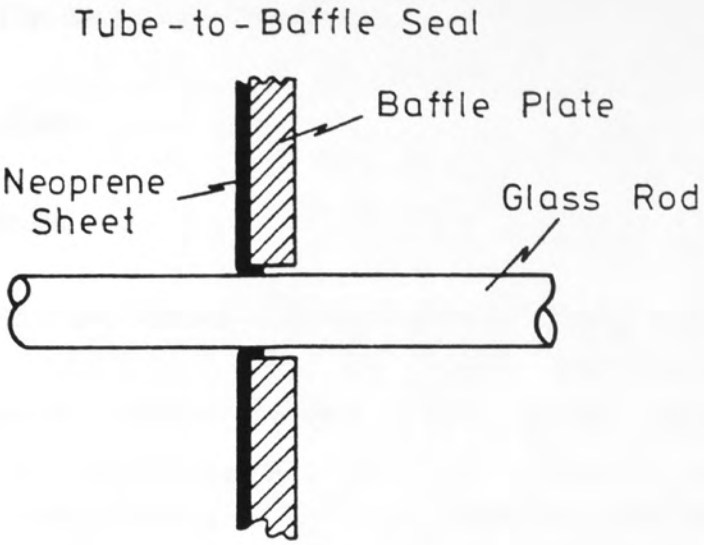

Figure 4.7 a: Tube–Baffle Leakage Seals.

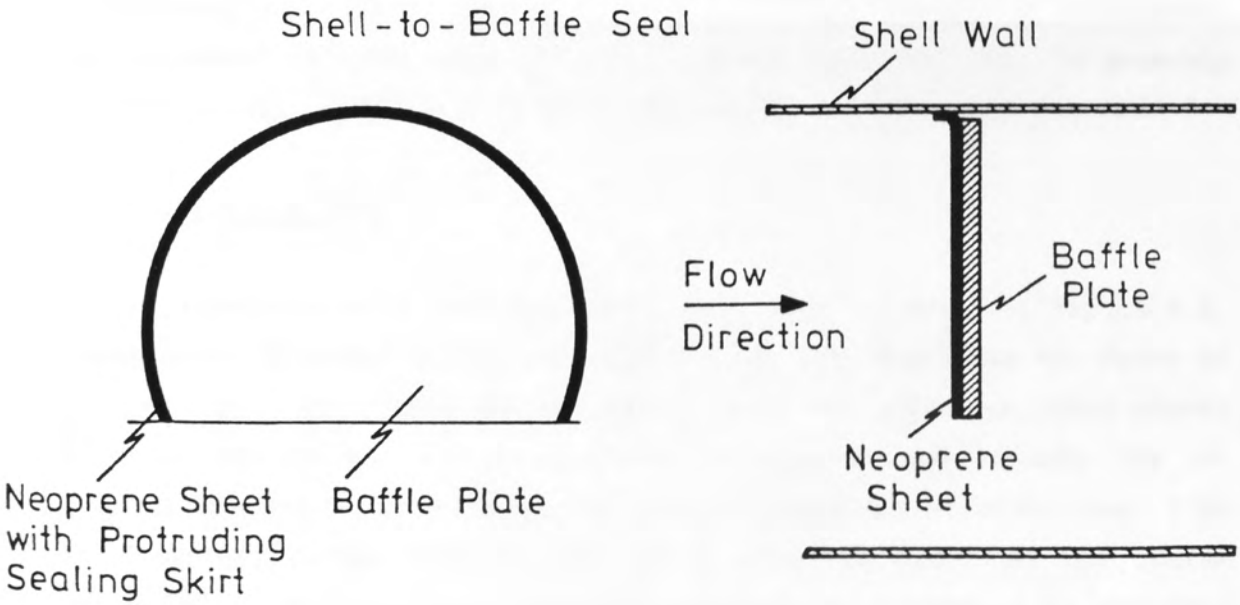

Figure 4.7 b: Shell–Baffle Leakage Seals.

The centrifugal pump used to circulate the working fluid could deliver to a maximum head of 17 m and had a maximum capacity of 32 m^3/hr. The pump was connected to the piping system via PTFE bellows to absorb potentially damaging vibrations.

4.7 Instrumentation

4.7.1 Flow Metering

The flow metering system consisted of two Fisher and Porter rotameters (series 056432843/4) and one Fisher and Porter "Armoured Thruflow' flowmeter (series 1045001). Each of the three flowmeters were calibrated by the manufacturers to cover a range of flows from 0 - 24 m^3/hr trichloroethylene at 34°C. Only the Armoured Thruflow meter was used in the current work since it covered adequately the Reynolds number range of interest. However, since this flowmeter was calibrated for trichloroethylene, Fisher and Porter supplied an appropriate conversion table, shown graphically in Figure 4.8. The calibration and conversion table were checked by collecting and weighing techniques. The agreement between indicated and measured flowrates was, in general, within ± 1.0%. Details of these measurements are given in Appendix D.

4.7.2 Pressure Drop

A schematic of a pressure instrument tube is shown in Figure 4.9. There were 10 tubes in all and these took the positions as shown in Figure 4.5a. Each tube was manufactured in two sections, then pinned together and welded. The pin served to support and isolate the two ends of the tubes. Two holes or pressure tappings were drilled, 1 mm in diameter, either side of the pin a distance equal to the baffle pitch being studied. All pressure tappings were cleaned by removing burrs and smoothing with fine emery paper.

These tubes protruded beyond each end of the shell, through O-ring seals in the end plates. This enabled the measurement points to be

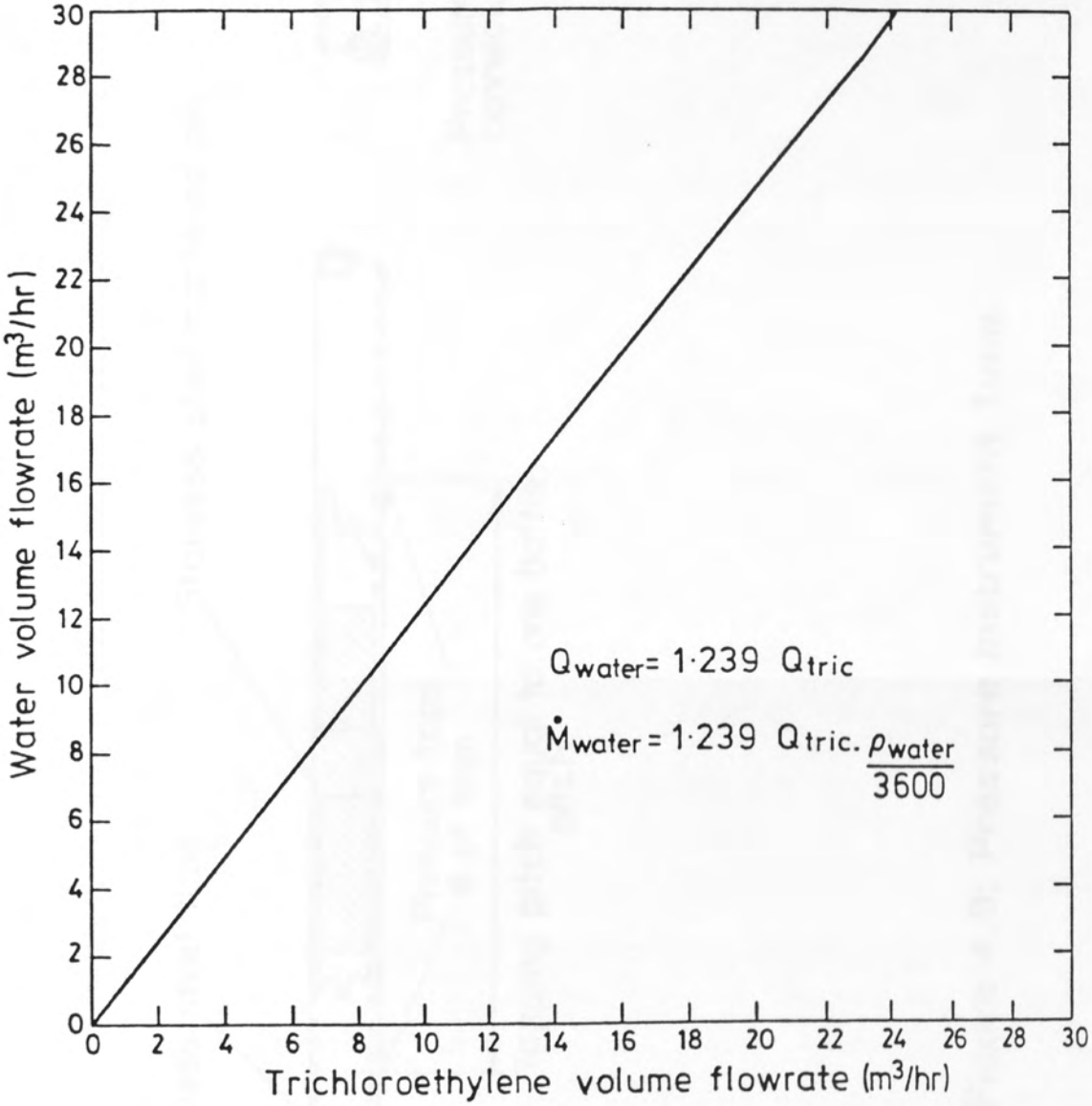

Figure 4.8: Chart for Converting Trichloroethylene to Water Volume Flowrate.

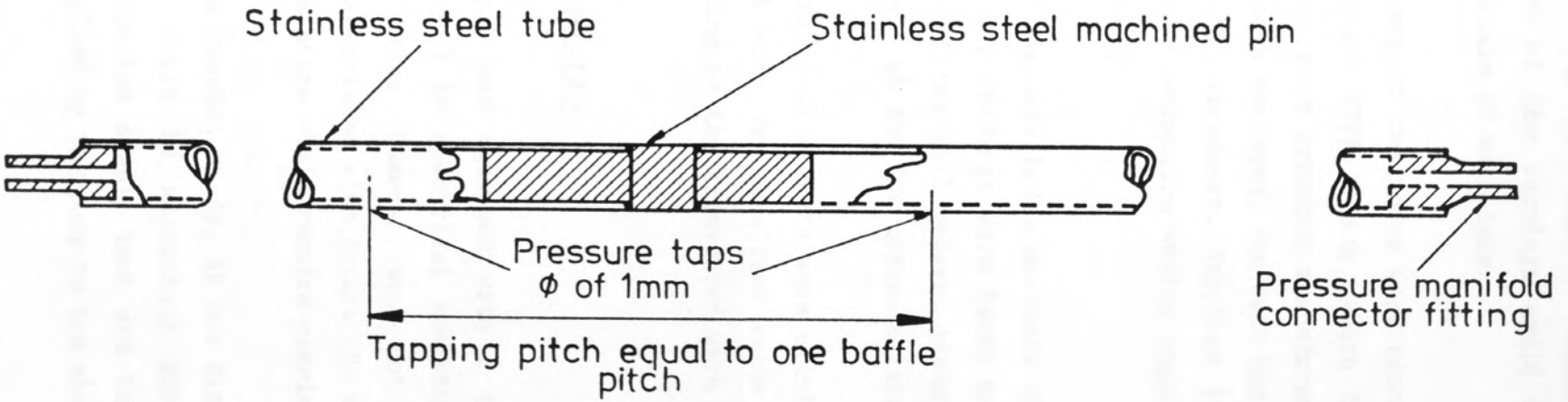

Figure 4.9: Pressure Instrument Tube.

traversed along the shell or rotated as required. The position and orientation of the tappings could be controlled accurately using a graduated scale on each tube.

All ends of the tubes were connected to ball valves via ¼" (outside diameter) PTFE tubing, which in turn were connected to a Kent Detapi electronic pressure transducer via a manifold arrangement. Two manifolds were employed, one each for the high and low pressure connections of the transducer. Tappings 1-10 (see Figure 4.5a) fed to the high pressure connection whilst tappings 11-20 fed to the low pressure connection.

The transducer had a accuracy of ± 0.2% of full scale deflection (66 mbar) and readings were taken manually from a digital meter. By adjustment of the ball valves, pressure differences could be measured between any high and low pressure tapping.

Gravitational effects were eliminated since all connecting tubing was filled with demineralised water and both high and low pressure lines feeding to the transducer were positioned on the same horizontal plane.

4.7.3 Temperature

The rig was equipped with a three-term temperature controller linked to a 3 kW electrical resistance heater via a thyristor unit. These facilities, however, were not used in the current study since they were associated with future LDA work in which refractive index and hence temperature would require precise control.

In the current study, it was discovered that constant temperature conditions could be maintained adequately using the cooling coil (situated in the supply tank and fed by mains water) to remove the energy supplied by the pump to the shellside fluid.

A platinum resistance thermometer, situated inside the glass pipe just upstream of the model heat exchanger, was used to indicate the shellside fluid temperature. The accuracy of these measurements was estimated to be ± 0.1°C.

CHAPTER 5

EXPERIMENTAL TECHNIQUES

5. EXPERIMENTAL TECHNIQUES

5.1 Introduction

Two complementary experimental techniques were used in the current study. These were dye injection flow visualisation and inter-baffle pressure measurements. Only a short programme of flow visualisation was carried out (Chapter 6), but the results aided the interpretation of pressure measurements and could be compared with the results from the three-dimensional flow modelling (Chapter 7). This chapter describes the techniques used to operate the rig and collect data. Both start-up and shut-down procedures are described in some detail since these are essential for safe operation of the glass rig.

5.2 Start-Up Procedure

The start-up procedure is described with reference to Figure 4.1.

With the rotameter valves (V1-V3) and the test tank supply valve (V4) isolated and both bypass value (V5) and exchanger vent valve (V6) fully open, the pump was activated such that all fluid flowed via the bypass loop (supply tank through V5 and back to supply tank). The rotameter valves (V1-V3) were then opened and the bypass valve (V5) throttled down to give a low flow into the model exchanger.

The exchanger could not be filled under these conditions since a throttling valve at the outlet was considered unwise due to the possibility of overpressurisation. Instead a vent pipe was fitted to the end plate, at the outlet end, and air was purged using a small vacuum pump via a non-return valve.

When the exchanger was full the two rotameter valves V2 and V3 were then isolated (only one flowmeter was used throughout the experimental programme, see Chapter 4) and finally by adjustment of flowmeter valve (V1) and bypass valve (V5) the desired flowrate was selected.

5.3 Pressure Drop

All differential pressure measurements were recorded with reference to one tapping which remained in the same position throughout the study of a particular baffle spacing. Measurements were taken with the tapping situated 135° to the main flow, in the minimum gap between tubes as shown in Figure 5.1. The code number of the reference tappings used and the baffle space in which these were employed are shown in Table 5.1. These tappings were located mid-way between consecutive baffles.

Table 5.1: Reference Tapping Code Number and Baffle Space Location

Baffle Spacing (mm)	Reference Tapping Code Number	Baffle Space Location
86.4/ 84.8	9	5
112/110.4	6	4
158/156.4	9	3

Prior to recording pressure differences all pressure sensing lines were filled with demineralised water and simultaneously purged of air, thus eliminating gravitational effects. The water was fed to the sensing lines via a small centrifugal pump. Purging was completed before start-up and subsequently repeated at regular intervals during a run. This was a precautionary measure to prevent small air bubbles, which were impossible to eliminate entirely, adhering to a pressure tapping orifice.

After purging, the zero setting on the pressure transducer was checked under static conditions. This was achieved by fully opening the bypass valve (V5) and isolating the flowmeter valve (V1). Static pressure readings were checked between a number of pressure tappings.

Three possible situations could arise from these checks:

1) All differential measurements were zero, in which case the experiment could continue.

2) Measurements were identical and non-zero. This signified that the pressure transducer required adjustment to zero.

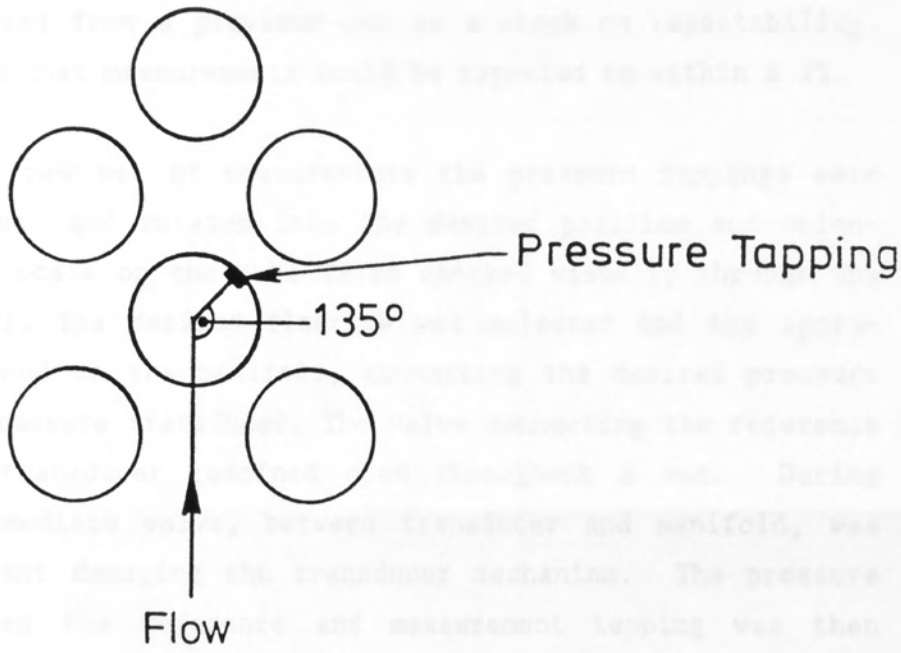

Figure 5.1: Orientation of the Pressure Tappings in Relation to the Main Flow Direction.

3) Measurements were non-zero but differed from tapping to tapping. This signified that some of the sensing lines were not completely purged of air plugs, in which case, the purging procedure was repeated under static conditions and pressure readings checked again and so on.

Once the pressure sensing lines were purged satisfactorily and the pressure transducer zero'd, measurements could commence. However, before recording a new set of data, a representative set of measurements were repeated from a previous run as a check on repeatability. It was discovered that measurements could be repeated to within ± 3%.

To record a new set of measurements the pressure tappings were firstly transversed and rotated into the desired position and orientation using the scale on the tube (also checked visually through the test cell window). The desired flowrate was selected and the appropriate valve opened on the manifold, connecting the desired pressure tapping to the pressure transducer. The valve connecting the reference tapping to the transducer remained open throughout a run. During purging an intermediate valve, between transducer and manifold, was isolated to prevent damaging the transducer mechanism. The pressure difference between the reference and measurement tapping was then recorded along with the fluid temperature and volume flowrate.

Data were obtained in two consecutive baffle spaces, for each of the geometries studied. These were spaces 5 and 6 for the small spacing, 4 and 5 for the medium spacing and 3 and 4 for the large spacing (see Figure 4.5b).

Pressure measurements were, in general, recorded at 45 different positions within a given baffle space. Of these, 35 were in the central vertical plane of the bundle (tappings 13-20) and 10 adjacent to the shell wall (tappings 11-12). These positions are characterised by the fractional distance at which the tappings were situated across the baffle spacing (B_f) and were B_f = 0.1, 0.3, 0.5, 0.7 and 0.9, as shown for the central vertical plane in Figure 5.2.

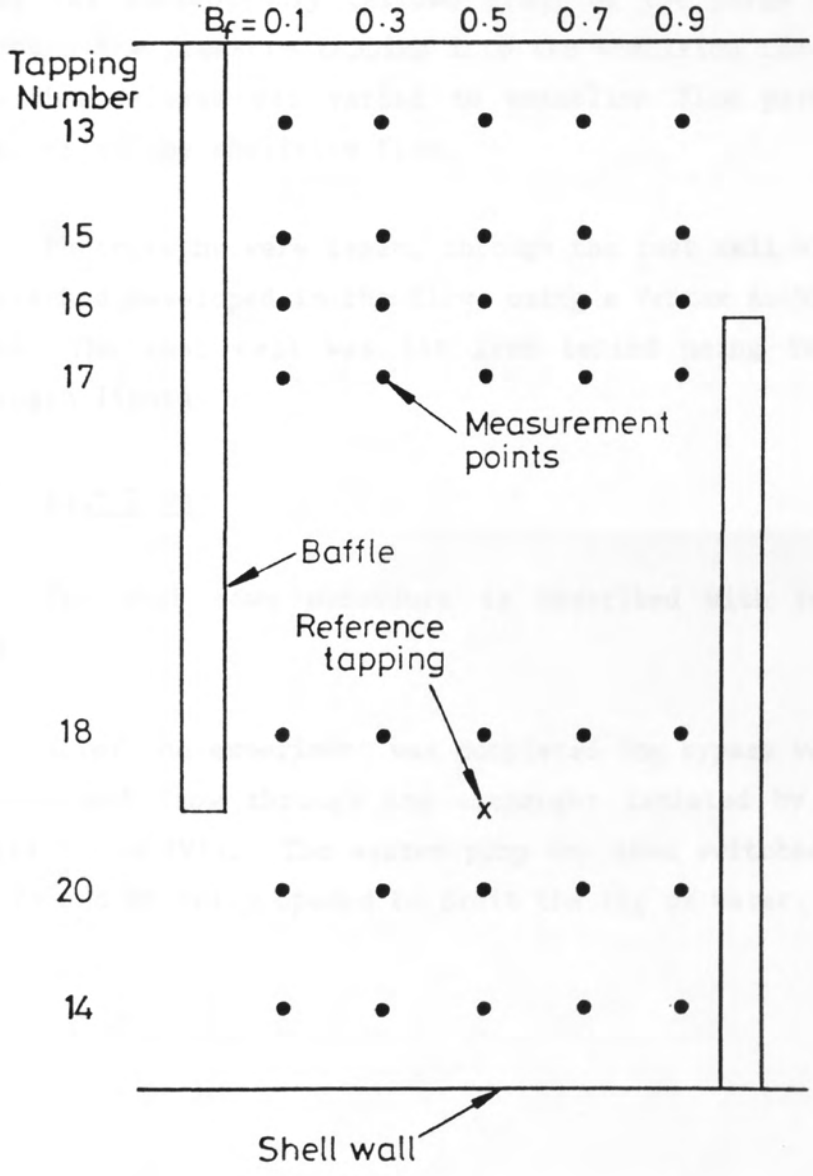

Figure 5.2: Pressure Measurement Positions in the Central Plane of the Bundle.

5.4 Flow Visualisation

The tubes used in the pressure study were also used for flow visualisation since they were a convenient vehicle for releasing dye into the shellside flow in an unobtrusive manner.

The dye (red food colouring) was injected into the pressure tubes through the PTFE connector tubing using a hypodermic syringe. The dye plug was subsequently carried along by the purge water and released through the pressure tapping into the shellside flow. The location of the dye release was varied to establish flow patterns in different regions of the shellside flow.

Photographs were taken, through the test cell window, once the dye trace had developed in the flow, using a Pentax Asahi SLR with a 135 mm lens. The test cell was lit from behind using two, 2 Kw tungsten/ halogen lights.

5.5 Shut-Down

The shut down procedure is described with reference to Figure 4.1.

After the experiment was completed the bypass valve (V5) was fully opened and flow through the exchanger isolated by closing the rotameter valve (V1). The system pump was then switched off and valves V1 to V4 and V6 fully opened to drain the rig of water.

CHAPTER 6

RESULTS I - FLOW VISUALISATION

6. RESULTS I - FLOW VISUALISATION

6.1 Introduction

Shellside flow patterns were visualised by releasing dye in various regions of the model heat exchanger. One baffle spacing was studied (112 mm with baffle leakage present) and results are presented for one mass flowrate only ($\dot{M}_T \approx 8.25$ kg/s); the basic flow features did not alter appreciably with Reynolds number which is in keeping with the findings of Guta and Katz (1957). Dye was released at three points across the baffle space from a number of tubes within the bundle. These positions are characterised by the fractional distance across the baffle space (B_f), measured from the upstream baffle face and were $B_f = 0.1$, 0.5 and 0.9.

6.2 Flow Patterns Near the Shell Vertical Centre-Line

Dye was released at both the inlet and outlet of the crossflow zone in baffle space 3, which was the first complete baffle compartment enclosed by the test cell glass tank. In this manner a picture of the flow in the whole compartment was constructed.

6.2.1 Dye released Near the Inlet to a Crossflow Region

Figures 6.1a, 6.1b and 6.1c show photographs of the resulting paths of dye, released at $B_f = 0.1$, 0.5 and 0.9 respectively, using tapping 19 (see Figure 4.5a for location of all dye release tube positions in relation to the tube bundle).

The dye released near the upstream baffle of the first compartment (Figure 6.1a) shows initially a degree of spreading in the vicinity of the release point. This is due to a small separated and recirculating region just downstream of the baffle tip (detected in the pressure drop study, Chapter 9) and subsequent entrainment of dye into this region. Thereafter the dye is carried along by the flow in the overlap (crossflow plus tube-baffle leakage) at an inclined angle to the tube bundle. The subsequent turning into and out of the window region appears as a smooth curved flow path and even towards the end of the second crossflow region the breadth of the dye trace remains relatively unchanged. This tends to suggest that the degree of mixing in the window region is relatively small.

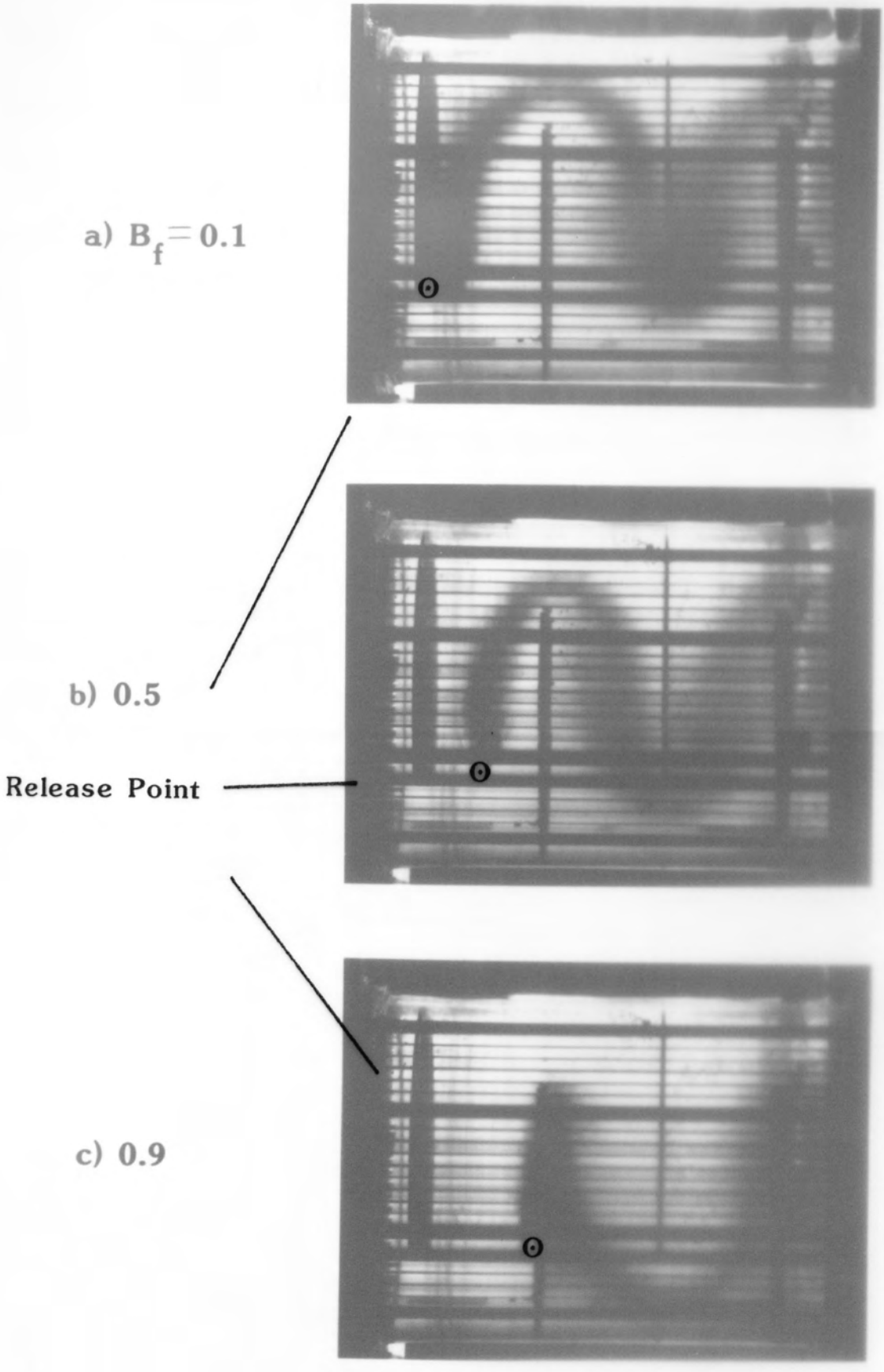

Figure 6.1a, b, c Flow Patterns Near the Shell Centre-Line. Dye Released at the Inlet to a Crossflow Region.

a) $B_f = 0.1$

b) 0.5

c) 0.9

Figure 6.1a, b, c Flow Patterns Near the Shell Centre-Line. Dye Released at the Inlet to a Crossflow Region.

Shellside heat transfer models rely on the assumption that the main flowstreams mix completely in the window. From this, correction factors to the overall mean temperature difference can be evaluated (for example, Whistler (1947) and Fisher and Parker (1969)). The strong mixing assumed does not appear to occur in the window. The only significant broadening of the dye trace stems from the subsequent separated region in the third baffle compartment

Figure 6.1b shows the resultant flow path of dye released from midway between baffles (B_f = 0.5). There is evidence of an axial velocity component close to the injection point, but this time the flow is well clear of the separated region and so the dye is not entrained back towards the upstream baffle face.

The asymmetry of flow around the baffle tip is evident, showing the presence of separation in the second compartment. The subsequent broadening of the trace in the crossflow region might also be due, in part, to the recirculating flows within the separated zone. Finally, none of the dye appears to leak through the baffle plates.

Figure 6.1c shows the resultant path of dye released near to the downstream baffle in the first compartment. All of the dye released at this point leaks through the tube-baffle clearances. The dye is initially swept along by the flow, without passing through the baffle. Thereafter, the dye leaks over most of the remaining baffle height. Towards the downstream baffle tip, however, very little or no leakage is observed, as exemplified by the absence of dye on the upstream side of the baffle. This is due to the low pressure driving force experienced across the baffle in this region. Therefore, the dye present on the downstream side, close to the tip, originates from upward entrainment into the separated region. This photograph clearly illustrates that tube-baffle leakage joins the crossflow after leaking through the baffle. In the heat transfer model used in TASC, it is assumed that leakage does not contribute towards heat transfer. However, since the leakage has been shown to follow the crossflow path after flowing through the baffle, these flows must contribute considerably more to heat transfer than assumed in the past. In fact, the HTFS program TASC

has had a history of underpredicting the crossflow heat transfer coefficient and this is possibly explicable in terms of the contribution due to baffle leakage. The final feature worthy of note is the leakage profile, which clearly demonstrates the variation of pressure driving force over the baffle height.

A key feature evident in all three figures is the inclination of flow in relation to the tube bundle. The dye traces exhibit a marked lack of crossflow normal to the tube bundle. Rather, the crossflow is always inclined towards the downstream baffle, this is more pronounced towards the crossflow outlet region. As a consequence, the fluid in crossflow turns through a considerable angle prior to entering the window region. This result is significant since Wills' (1984) window model, used in the current version of TASC, assumes that the window flow is subjected to two 90° bends in flowing from one crossflow region to the next. Clearly, this is an overestimation and, from the photographs, the angle through which the fluid turns in the window is approximately 100°, nearly half the value used in the current model. Moore's (1974) original model assumed that the main flow followed the chord joining the centre of gravity of successive window regions (see Figure 2.11). This method gives a total turning angle of 124° in the window (for the baffle spacing under consideration), closer to the value estimated from the dye traces than the current model used in TASC.

6.2.2 Dye Released Near the Outlet of a Crossflow Region

To build up a complete picture of the shellside flow near the shell centre-line, dye has also been introduced at three points across the baffle space near the outlet of a crossflow zone (using tapping 17). The photographs of the resultant dye traces are shown in Figure 6.2a, 6.2b and 6.2c.

Figure 6.2a shows the resultant path of dye released close to the upstream baffle (B_f = 0.1). Here the flow, although subject to longitudinal baffle leakage, remains in crossflow, inclined to the bundle, until the last two or three tube rows in the window. Only then does the

flow become free of the influence of the dominant crossflow stream. Thereafter, the fluid flows longitudinally through the window, turning into the next downstream crossflow region and simultaneously leaking through the baffle plate.

The flow path highlighted by the dye released midway between baffles (B_f = 0.5) is presented in Figure 6.2b. Comparison between this photograph and that shown in Figure 6.1a, show both to be following a similar flow path.

Figure 6.2c shows the flowpath of the the dye released close to the downstream baffle face (B_f = 0.9). The separated region, downstream of the baffle tip, is not shown clearly because of rapid entrainment of dye. The size of the region, however, was observed to be small.

If all of the flow patterns highlighted by the dye, close to the shell centre-line, are superimposed, a representation of the global flow distribution, as shown in Figure 6.3, can be obtained. Neglecting the small amount of overlap observed between dye traces released at various points, Figure 6.3 is almost identical to the two-dimensional representation of shellside flow presented by Tinker (1947) (see Figure 1.3). The solid lines should not be interpreted as rigid flow boundaries since they are meant simply as a guide to the main routes taken by different flowstreams.

6.3 Flow Patterns Adjacent to the Shell Wall

Dye was also released into the shellside flow at three positions across the baffle space (B_f = 0.1, 0.5 and 0.9, as before), adjacent to the shell wall using tappings 11 and 12 (located in Figure 4.5a). Since these tappings are situated two rows in from the bypass lane it was not possible to inject dye directly into this region. Two photographs, one taken immediately as the dye was released and the other taken between one and two seconds after, are shown for each dye release position. This approach was adopted to enable a clear description of the rather more complicated flow distribution discovered close to the shell wall.

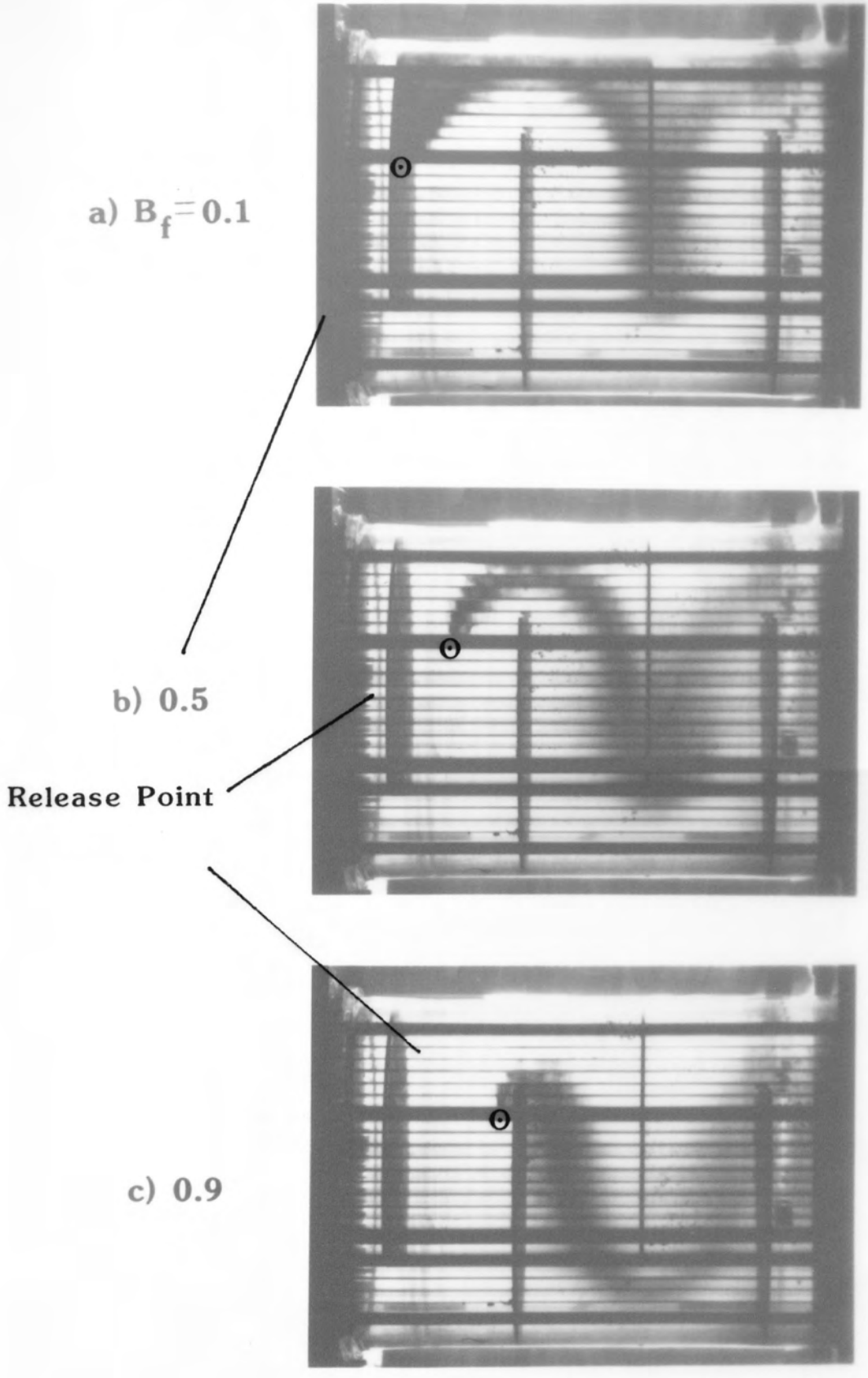

Figure 6.2a, b, c Flow Patterns Near the Shell Centre-Line. Dye Released at the Outlet of a Crossflow Region.

a) $B_f = 0.1$

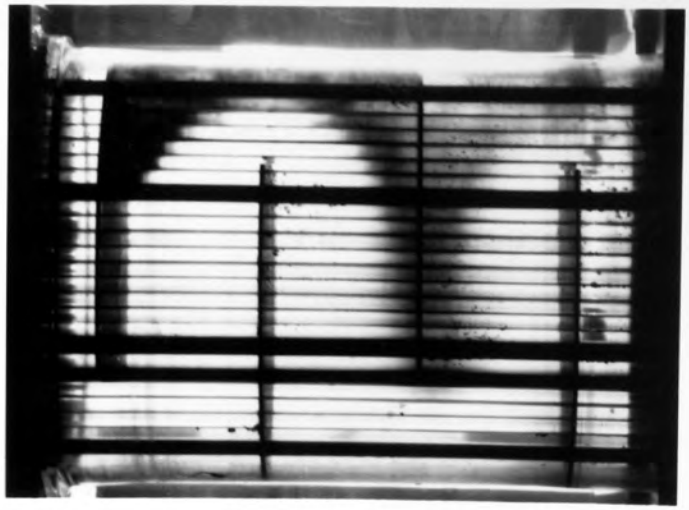

b) 0.5

c) 0.9

Figure 6.2a, b, c Flow Patterns Near the Shell Centre-Line. Dye Released at the Outlet of a Crossflow Region.

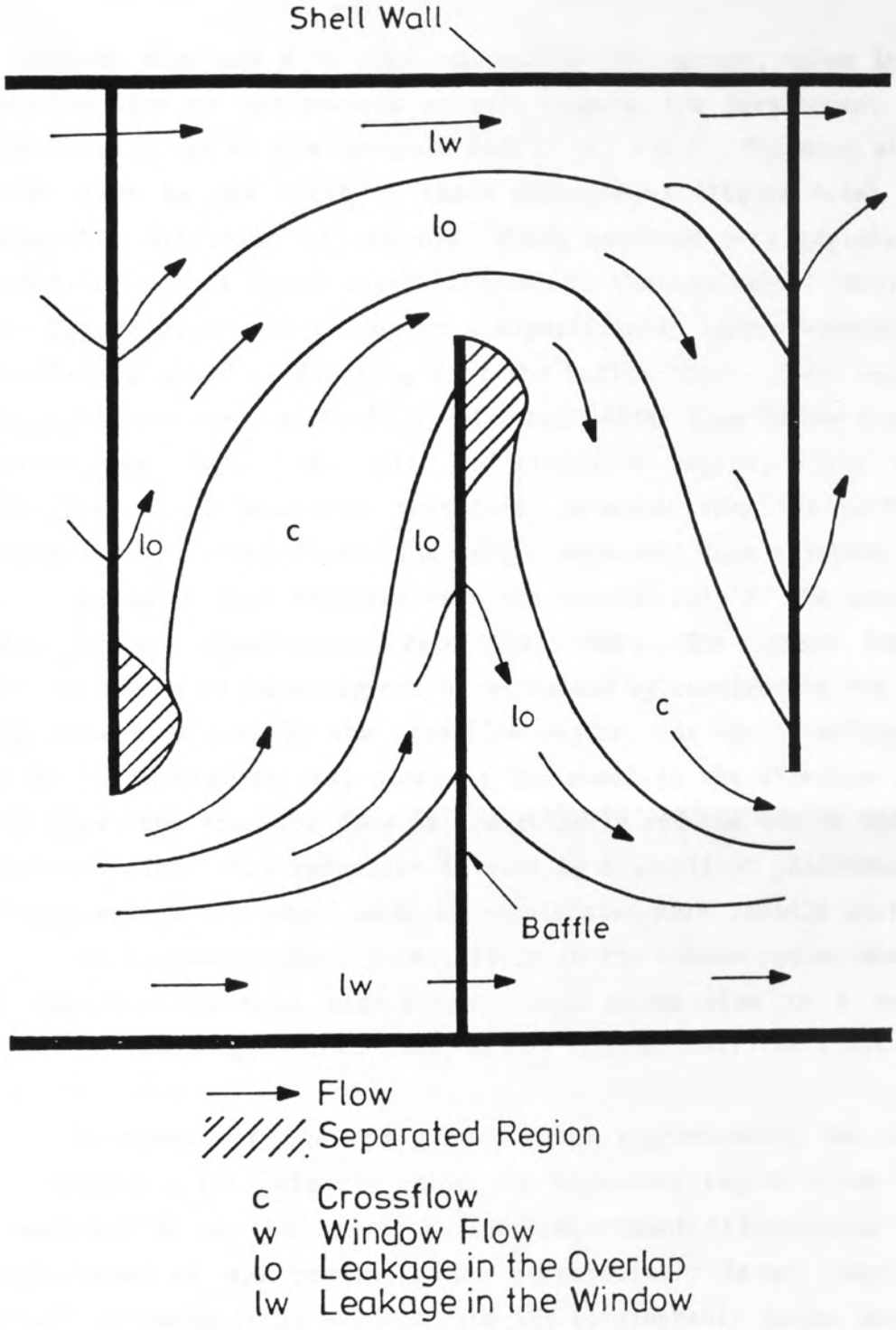

Figure 6.3: Observed Baffle Space Flow Distribution at the Central Vertical Plane of the Bundle.

6.3.1 Dye Released Near the Inlet to a Crossflow Region

Figures 6.4a and 6.4b show consecutive photograph, taken in close succession (one to two seconds apart), mapping the development of the dye released close to the upstream baffle (B_f = 0.1). The most striking feature shown by the first of these photographs (Figure 6.4a) is the considerable diffusion of the dye, which occurred very rapidly after introduction. This is in stark contrast to the equivalent centre-line trace (Figure 6.1a) and is due to a significantly larger separated and recirculating zone, originating from the baffle tips. These separated zones are caused by the inability of longitudinal flow in the window to negotiate the sharp turn into the crossflow region, close to the baffle. The fluid boundary, therefore, detaches from the baffle tip creating recirculating flows. The larger separated zone adjacent to the shell compared to that detected near the central axis of the exchanger, implies higher longitudinal velocities there. The reason for this radial variation in velocity can be explained by considering the nature of the free flow area in the crossflow region. As the crossflow flows from the horizontal central plane of the shell in the direction of the baffle tips, the area for flow is dramatically reduced due to the shell curvature. Since this reduction in area is a localised phenomenon, the flow adjacent to the shell wall is accelerated more rapidly there than near the shell centre-line, particularly in the window region where the area reduction is most significant. This gives rise to a velocity gradient in the longitudinal flow, with a maximum near the shell wall.

A photograph of the dye trace, taken approximately two seconds later (Figure 6.4b), clearly shows the separated region close to the upstream baffle in the second baffle compartment (illustrated by the reduced level of dye present). The comparatively large longitudinal component of velocity is evident from the considerably larger amount of baffle leakage than shown in the equivalent centre-line photograph (Figure 6.1a). The implications of this result are potentially significant. Firstly, the large separated zone would reduce the degree of crossflow bypassing*(in the sense of a flowstream model which assumes that bypass flows in parallel with the main crossflow and normal to the

---

* The separated region was seen to extend into the bypass lane.

a)

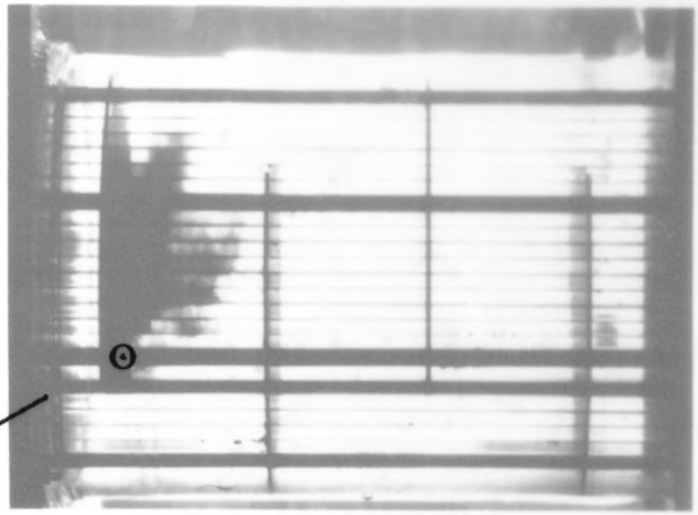

Release Point

b)

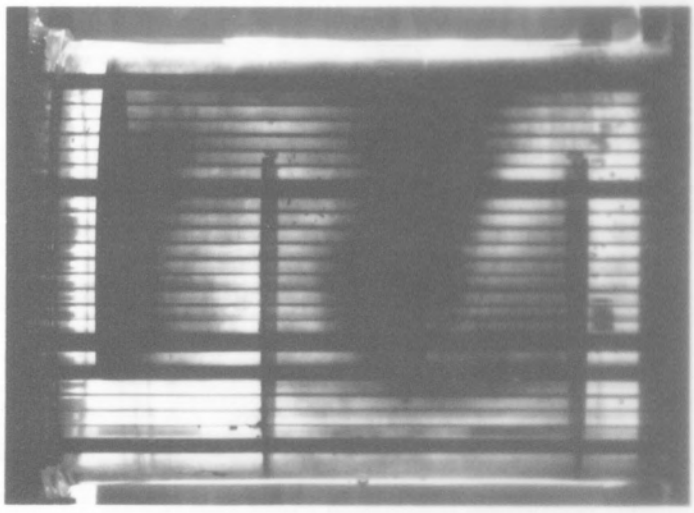

Figure 6.4a, b Flow Patterns Adjacent to the Shell Wall. Dye Released at the Inlet to a Crossflow Region, at $B_f = 0.1$.

a)

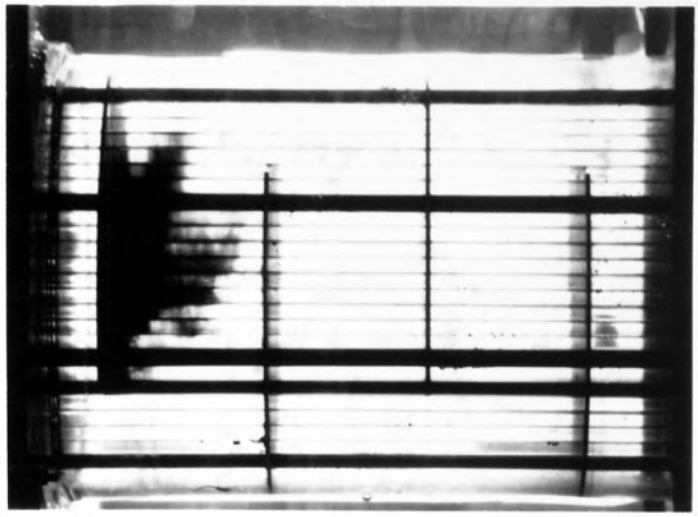

b)

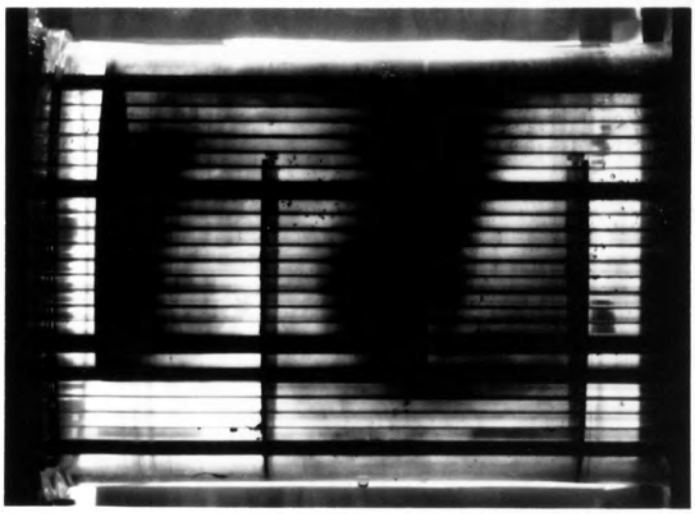

Figure 6.4a, b Flow Patterns Adjacent to the Shell Wall. Dye Released at the Inlet to a Crossflow Region, at $B_f = 0.1$.

tube bundle without leaking through a baffle) below what could be expected if the whole bypass lane was considered to be available for flow. Secondly, there may be implications for the design of sealing strips. These are placed axially, with a view to inhibiting circumferential flow adjacent to the shell wall. If there were, as is evident in Figure 6.4a, a substantial longitudinal component of flow, additional circumferential sealing strips would be called for.

Figures 6.5a and 6.5b show flow traces of the dye released mid-way between baffles (B_f = 0.5), one immediately after release, the other approximately two seconds later. In the first of the sequence of two photographs (Figure 6.5a), the dye is drawn back towards the upstream baffle face under the action of recirculating flows from within the separated zone. This region is shown to extend at least half way across the width of the baffle compartment.

The subsequent photograph (Figure 6.5b) shows the development of the dye downstream of the release point. The dye is shown to flow out from the rear of the separated region under the influence of baffle leakage.

Again, the comparatively strong component of longitudinal flow in the window is demonstrated. The region of low dye concentration, towards the downstream baffle face of the compartment in which dye was released, suggests that this region is occupied by crossflow. The equivalent region in the next, downstream, compartment illustrates the boundary of the separated region. Although not captured in this photograph, most of the dye leaked through the baffle. Contrast this with the equivalent centre-line photograph (Figure 6.1b) which showed little or no baffle leakage.

Attention is now focussed on the resultant traces of dye released close to the downstream baffle (B_f = 0.9), as shown in Figures 6.6a and 6.6b. The first photograph (Figure 6.6a) in the sequence of two, shows the development of the dye trace immediately after release. Here, as with the equivalent centre-line photograph (Figure 6.1c), the dye is

a)

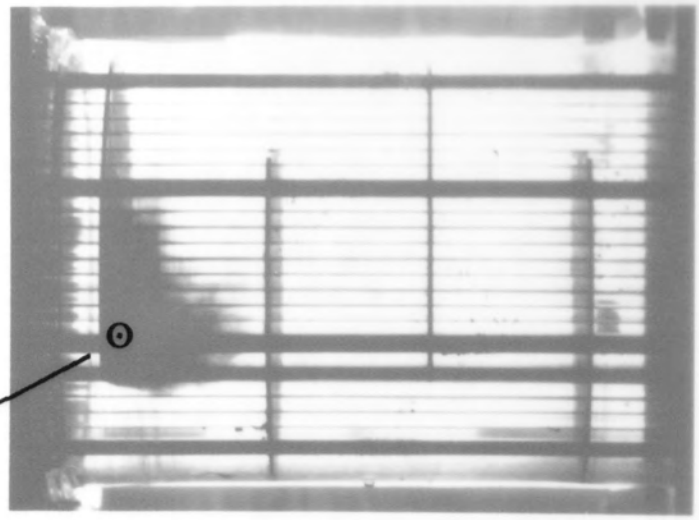

b)

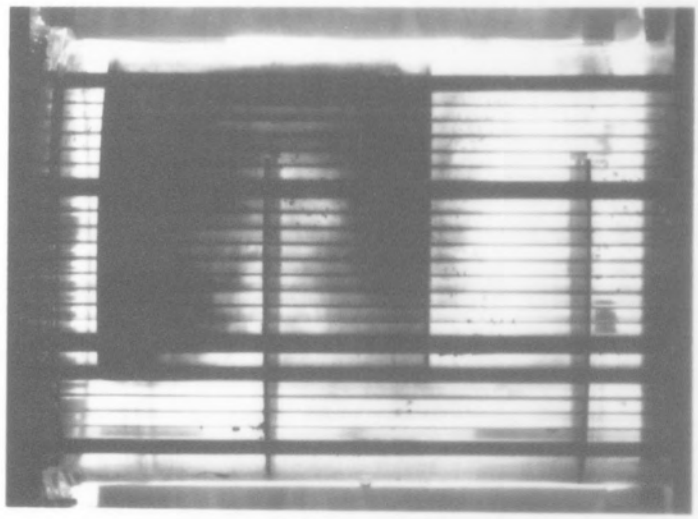

Figure 6.5a, b Flow Patterns Adjacent to the Shell Wall. Dye Released at the Inlet to a Crossflow Region, at $B_f = 0.5$.

a)

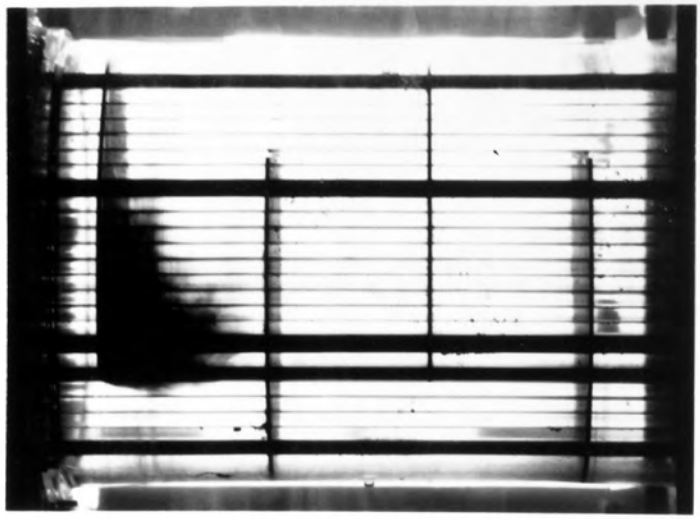

b)

Figure 6.5a, b Flow Patterns Adjacent to the Shell Wall. Dye Released at the Inlet to a Crossflow Region, at $B_f = 0.5$.

carried along by the crossflow and bypass flow, thereafter leaking over most of the remaining baffle height. Again, similarly to that at the centre line, little or no leakage is observed towards the baffle tip. However, the similarities cease there. Unlike the centre-line, the dye trace, in the compartment of release, broadens out towards the upstream baffle. This indicates that the crossflow, which is present close to the downstream baffle face, is no longer influenced by the reduced area for flow due to separation. The flow is clearly spreading out in an attempt to occupy the increased area available for flow. Another interesting feature is the jetting of flow over the baffle tip; the equivalent centre-line photograph (Figure 6.1c) gave no indications of flow into the window region and is explicable in terms of the localised reduction in flow area, causing the flow to accelerate. Furthermore, the curved trace of the dye, as fluid flows over the baffle tip, indicates the boundary of the separated region.

Finally, as in all the photographs of dye released adjacent to the shell wall, a substantial longitudinal component of flow (as compared to the centre-line) is observed; this is illustrated by the large proportion of the second baffle compartment occupied by dye which derives from leakage. This is also illustrated well by Figure 6.6b, which shows the development of the dye further downstream of the release point.

6.3.2 Dye Released Near the Outlet from a Crossflow Region

To give a complete picture of the flow distribution adjacent to the shell wall, dye was also released near the outlet of the crossflow zone of the first baffle compartment. Figures 6.7a, 6.7b and 6.7c show the resultant traces of dye released at three points across the baffle width, as before. The three figures will be discussed collectively since they exhibit similar flow features.

All three figures indicate the presence of a predominantly longitudinal flow in the window region. This is in contrast to the centre-line photographs (see Figures 6.2a, b and c) which showed features consistent with a strong component of crossflow. In particular, the separated region boundary is clearly shown in Figure 6.7c.

a)

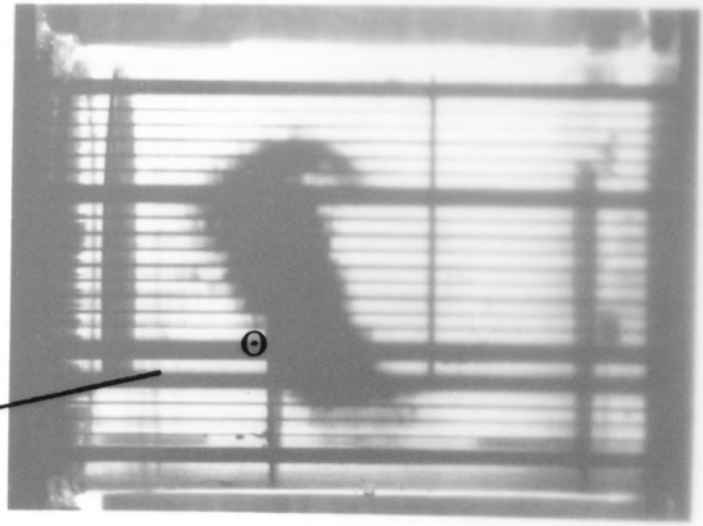

b)

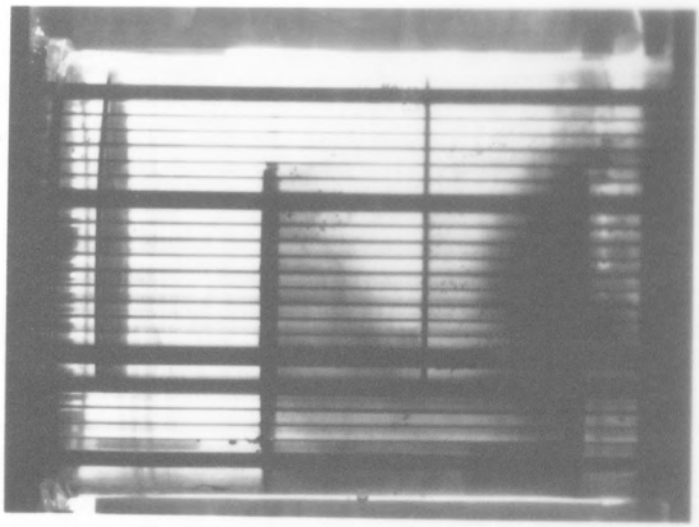

Figure 6.6a, b Flow Patterns Adjacent to the Shell Wall. Dye Released at the Inlet to a Crossflow Region, at $B_f = 0.9$.

a)

b)

Figure 6.6a, b Flow Patterns Adjacent to the Shell Wall. Dye Released at the Inlet to a Crossflow Region, at $B_f = 0.9$.

Finally, a representation of the flow distribution adjacent to the shell wall is presented in Figure 6.8. This figure may be compared directly with the equivalent centre-line distribution (Figure 6.3) and serves to exemplify the extreme radial flow variations that have been observed. It was difficult to interpret the flow distribution immediately behind the separated zone, however, it is likely that this region was occupied by flow deriving from baffle leakage.

6.4 Conclusions

Dye has been introduced into the shellside flow at points both across the width and breadth of a baffle compartment. Photographs of the subsequent dye traces have enabled a comprehensive picture of the shellside flow, for one baffle spacing, to be constructed. In particular, the flow distribution visualised near the shell centre-line and adjacent to the shell wall exhibit considerable differences: the flow near the shell centre-line was dominated by crossflow, whilst near the shell wall longitudinal flow controlled, particularly in the window region. Other features highlighted by the flow visualisation were separated regions (largest near the shell wall) and baffle leakage flows.

The flow patterns identified by the controlled release of dye have raised a number of interesting and potentially significant points:

1) The tube-baffle leakage in the baffle overlap region becomes part of the crossflow stream after leaking through the baffle and is not, therefore, simply a stream flowing longitudinally along the exchanger length (as assumed in flowstream models, see Section 2.6.2). This finding has implications on both heat transfer and pressure drop; flowstream models, such as TASC, use the crossflow flow fraction only to calculate the crossflow pressure drop and heat transfer coefficient. Clearly, from the flow visualisation results (see Figure 6.1), leakage in the overlap must contribute to both heat transfer and pressure drop. The design program TASC has been shown to consistently underpredict the crossflow heat transfer coefficient. This could be explained by the additional contribution of the leakage flows. A similar underprediction of pressure drop is also plausible.

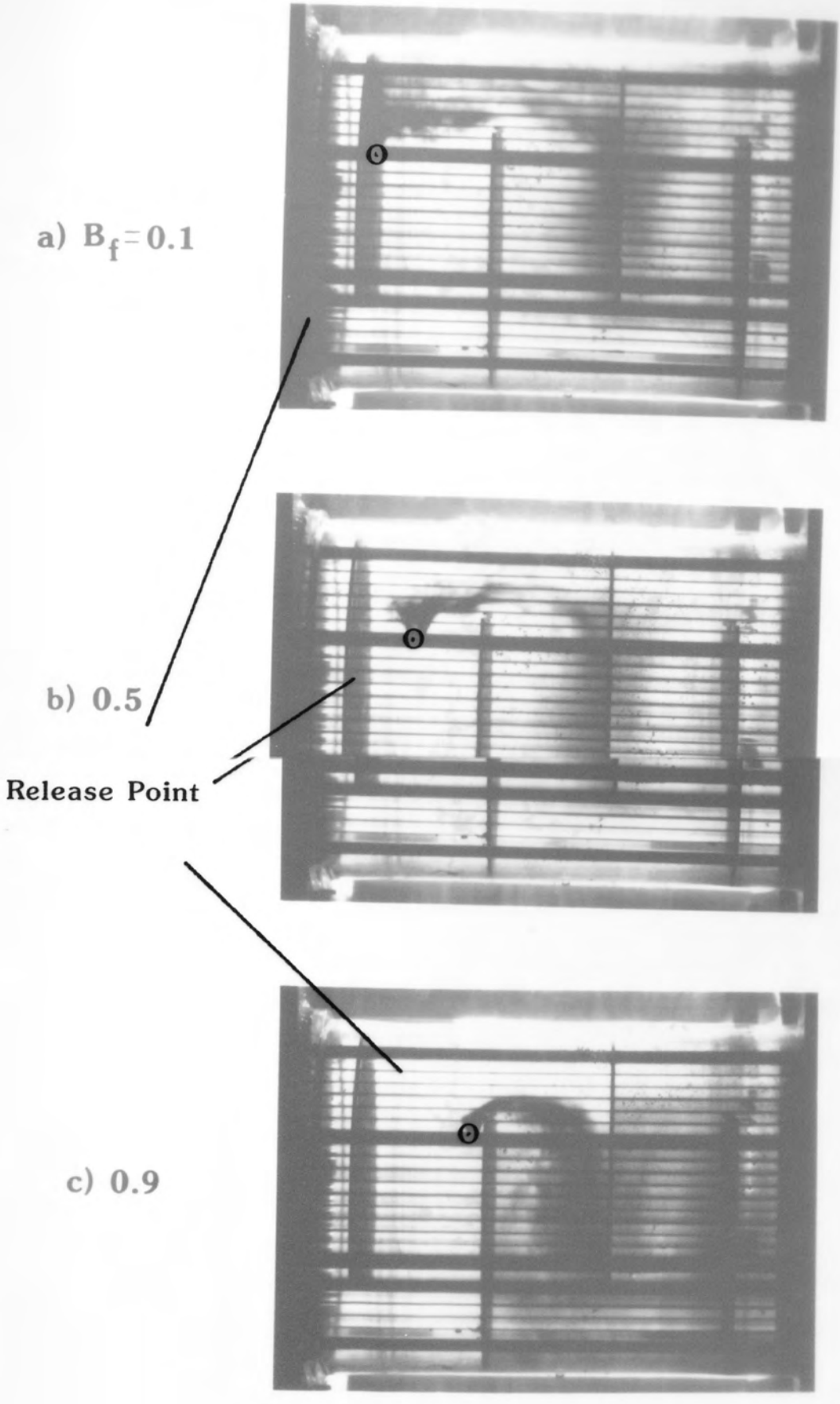

Figure 6.7a, b, c Flow Patterns Adjacent to the Shell Wall. Dye Released at the Outlet of a Crossflow Region.

a) $B_f = 0.1$

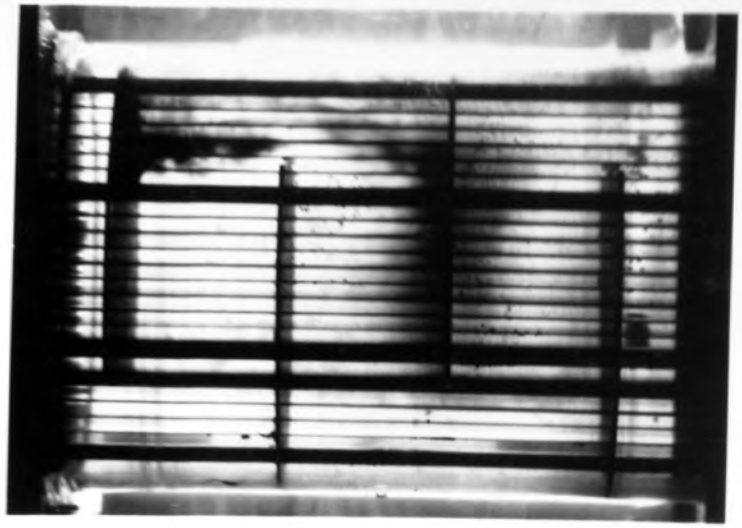

b) 0.5

c) 0.9

Figure 6.7a, b, c Flow Patterns Adjacent to the Shell Wall. Dye Released at the Outlet of a Crossflow Region.

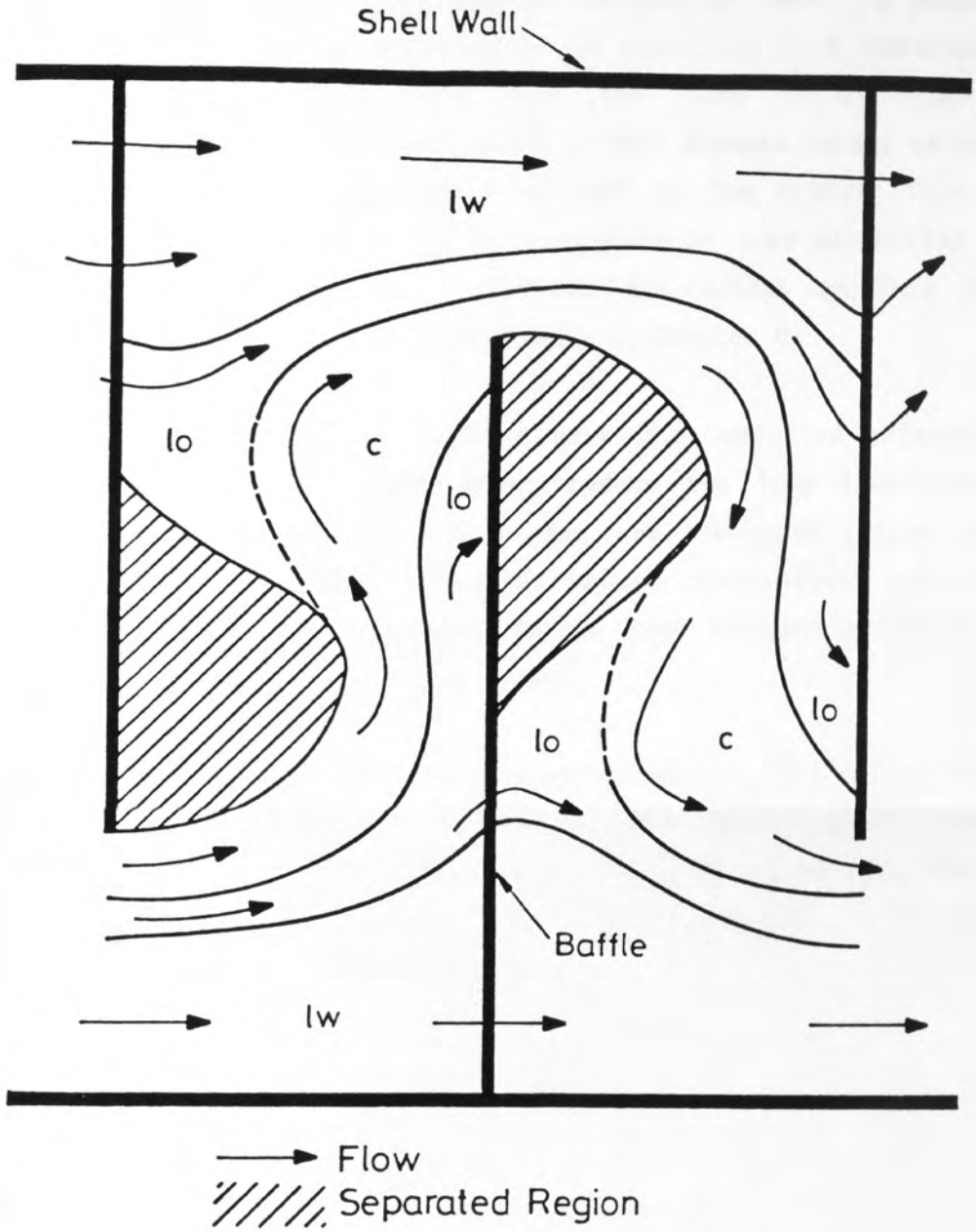

Figure 6.8: Observed Baffle Space Flow Distribution Adjacent to the Shell Wall.

2) The inclined angle of the crossflow, with respect to the tube bundle, has highlighted a potential weakness in the window model used in the current version of TASC. A direct consequence of the inclination of crossflow is a reduction in the angle through which the flow turns in a window region. Currently, the model used in TASC assumes normal crossflow and hence a turning angle of 180° in the window. This has been demonstrated to be a considerable over-estimation for the geometry studied. Further discussions on this aspect of shellside flow are presented in Chapter 9.

3) Large separated regions have been detected adjacent to the shell wall. These zones reduce the free flow area in the bypass lane and, therefore, are likely to reduce the bypass flow fraction. Clearly, bypass correlations used in modern design methods, which derive from rectangular bundles, could not account for this effect.

Many of the flow features identified from this study are used to aid the interpretation of pressure drop measurements presented in Chapter 9. In addition these flow visualisation results are compared with the data calculated from three-dimensional flow modelling, presented in the following chapter.

CHAPTER 7

RESULTS II - THREE-DIMENSIONAL FLOW MODELLING

7 RESULTS II - THREE-DIMENSIONAL FLOW MODELLING

7.1 Introduction

Until recently, state of the art methods of modelling shellside flow involved 'flow stream models'. These represented the flow by a number of one-dimensional flowstreams in a series/parallel network. One example of a 'flow stream' method is the HTFS program TASC (see Section 2.6). Such models, however, are of little use for increasing understanding of shellside flow since they depend on the definition of the flow network which in turn relies on a number of assumptions and simplifications about the flow distribution.

Whilst photographic flow visualisation studies (such as those presented in Chapter 6) are useful in describing the global flow patterns, they are of limited use when more detail flow information is required. Recent advances in vector computers and numerical methods, however, have made it possible to solve the flow equations in three-dimensions for complex geometries. Development of three dimensional modelling codes are of particular interest since they are comparatively inexpensive to use, very versatile and can yield specific information that could not realistically be obtained through experiment.

The purpose of this chapter is threefold:

1) to describe how tube bundles, baffles plates and leakage streams can be modelled using the three-dimensional flow code FLOW3D (Jones, Kightley, Thompson and Wilkes (1985)), which is currently under development at Harwell;

2) to verify the various modelling techniques by comparing the results from FLOW3D with experimental measurements from the shellside flow rig;

3) to discuss some of the detailed flow features produced from the flow modelling.

7.2 FLOW3D Problem Specification

FLOW3D is a finite difference code for solving the flow equations, in three dimensions, for simple and complex geometries. The problem specification is the three-dimensional isothermal, steady-state flow of water on the shellside of a practical shell-and-tube heat exchanger. The main features of the geometry were chosen to be essentially the same as the shellside flow rig used in the experimental work (see Table 4.1).

7.2.1 Geometry

To simplify the problem somewhat, only four baffle spaces within a cylindrical shell were modelled. The window regions into baffle space one and out of baffle space four were defined as the inlet and outlet respectively, as shown in Figure 7.1a and b.

The finite difference grid was defined in cylindrical polar co-ordinates, which consisted of 10 grid spacings along the radius (r), 18 around the circumference (θ, only half the shell needed to be modelled because of symmetry) and various number of grid spacings along the length (z) of the four baffle spaces, depending on the baffle space being modelled (158 mm, 112 mm or 86.4 mm).

Because of the difficulty in defining straight line boundaries with cylindrical polar coordinates, the baffle edge, for the 25% baffle cut, follows the jagged boundary defined by the intersections of the radial and circumferential grid lines, as shown in Figure 7.1a. The finer the grid definition then the closer this boundary would approximate to a horizontal line, but considerably more computational time would be required to reach a solution. However, since this 'jaggedness' is on a scale comparable with the physical reality of tubes in the experimental rig, the simple grid was thought to be adequate.

7.2.2 Modelling of the Tube Bundle

It is impractical to model the local flow in the gaps between tubes for an entire exchanger because of the large number of surface boundaries that exist; this would require the use of a grid size

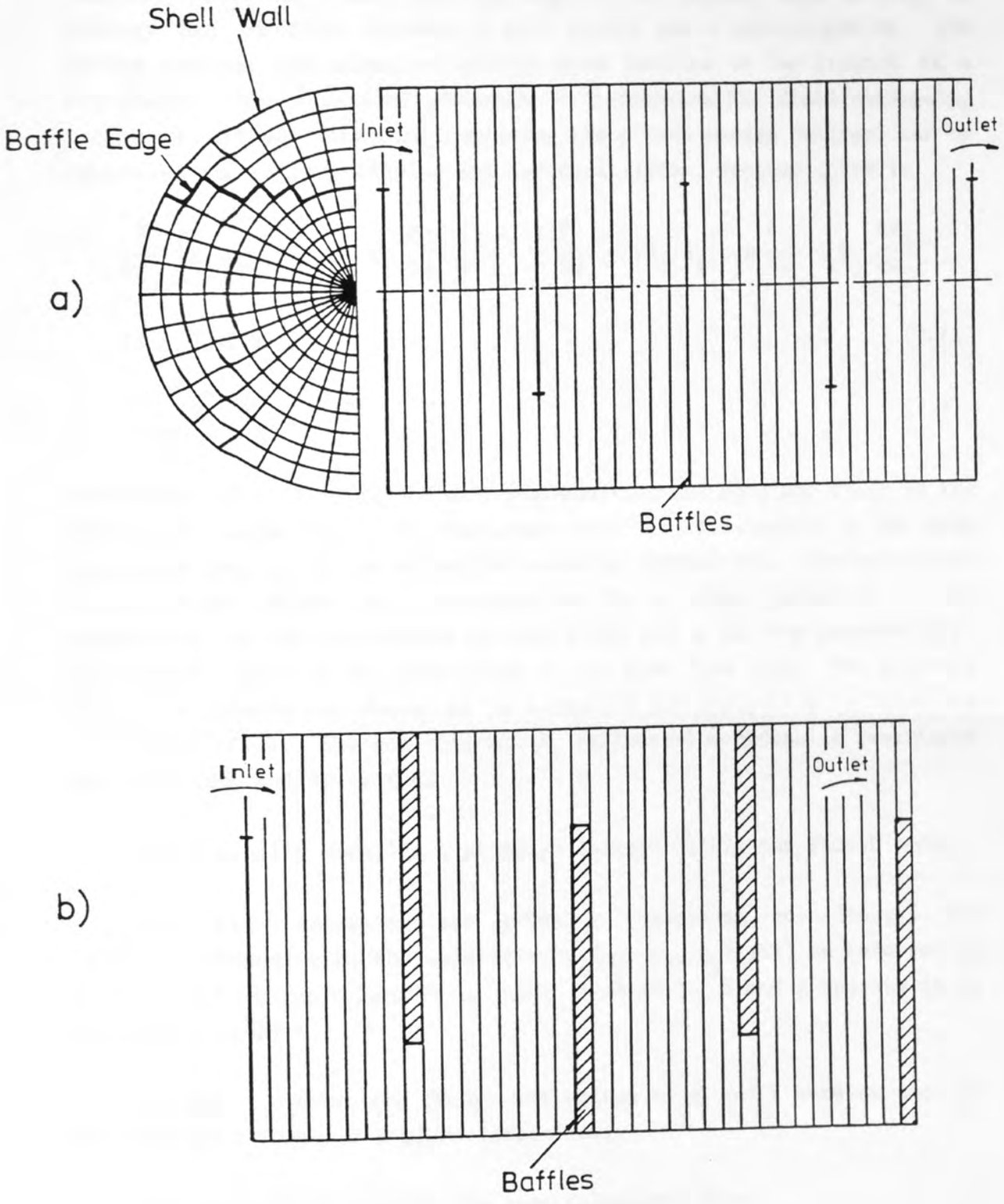

Figure 7.1 a,b: Grid Geometry Used in the Modelling of Shellside Flow Using FLOW3D; a) Non—Leakage, b) Leakage.

smaller than the inter-tube spacing. To circumvent this problem an analogy can be drawn between a tube bundle and a porous medium. The porous medium approximation allows tube bundles to be treated as a continuum. The equations governing an incompressible fluid undergoing isothermal steady flow, incorporating the porous medium analogy, can be expressed as follows (Rhodes and Carlucci (1983), Webster (1984)):

$$\frac{\partial}{\partial x_j}\left[K_j u_k u_i - \nu_e K_j \frac{\partial u_i}{\partial x_j}\right] = -\frac{\gamma}{\rho}\frac{\partial p}{\partial x_i} - \gamma R_i |u_i| u_j + \frac{\partial}{\partial x_j} \nu_e K_j \frac{\partial u_j}{\partial x_j}$$

$$(i = 1,2,3) \qquad (7.1)$$

$$\frac{\partial}{\partial x_j}(K_j u_j) = 0 \qquad (7.2)$$

where Equation (7.1) is the momentum equation and Equation (7.2) is the continuity equation, u is the mean local fluid velocity, p the mean pressure and ν_e is the effective momentum diffusivity. The properties of a porous medium are characterised by a volume porosity, γ, the proportion of space occupied by the fluid and a surface permeability, K_j, which reflects the proportion of the free flow area. The geometry of a tube bundle can therefore be accounted for implicitly in Equations (7.1) and (7.2). The coefficients R_i reflects the hydraulic resistance due to tubes and/or baffles.

The porosity model is a standard feature within the FLOW3D code.

The flow equations are given in Cartesian co-ordinates for brevity. Henceforth, the velocities $u_i(u_r, u_\theta, u_z)$ will be referred to in cylindrical co-ordinates (r,θ,z), in which K, R and γ operate in an identical fashion.

In this preliminary study, the values of K and R were assumed to be isotropic in the r-θ plane (crossflow).

The surface permeabilities were calculated from:

$$K_r = K_\theta = \frac{W}{P_y} = 0.3 \qquad (7.3)$$

for the two crossflow components, where W is the minimum gap per transverse pitch (P_y), as shown in Figure 2.2, and

$$K_z = \frac{P_t^2 - (\pi/4\ D_t^2)}{P_t^2} = 0.5 \qquad (7.4)$$

for the longitudinal component.

The volume porosity was calculated from

$$\gamma = \frac{P_t^3 - (\pi/4\ D_t^2\ P_t)}{P_t^3} = 0.5 \qquad (7.5)$$

where P_t is the diagonal pitch for a rotated square layout (15 mm for the experimental rig) and D_t is the tube outer diameter (12 mm).

For crossflow, the resistance term was defined as

$$R_i|u_i|u_i = \frac{2\ f_i\ u_i^2}{P_x} \qquad (i = r,\theta) \qquad (7.6)$$

where f_i is the crossflow friction factor for turbulent flow (Moore (1974)) and P_x is the longitudinal tube pitch. The same velocity appears on both sides of Equation (7.6) since the surface permeabilities were based on the minimum flow area between tubes, as used in the friction factor definition.

For longitudinal flow, parallel to tubes, the corresponding equations are:

$$R_z|u_z|u_z = \frac{2\ f_z\ u_z^2}{D_z} \qquad (7.7)$$

$$D_z = D_o\ [4/\pi\ (P_t/D_o)^2 - 1] \qquad (7.8)$$

where D_z is the hydraulic diameter and f_z the longitudinal friction factor and was defined using the pipe flow relationship of Wilson et al. (1922). As for the crossflow case, the same velocity appears on both sides of Equation (7.7) since the longitudinal surface permeability (K_z) was based on the hydraulic diameter used in the friction factor definition.

A further simplification was made regarding the tube bundle: it was assumed that the bundle extended to the shell wall and hence occupied the whole volume of the shell. The effect of this is complete elimination of the crossflow bypass lane. This is a reasonable first approximation for modelling the HTFS shellside flow rig since the minimum gap between the shell and the outermost tube is only 0.25 tube diameters.

The TASC design program predicts crossflow bypass fractions of 0.08 and 0.11 for leakage and non-leakage respectively, which are small but significant proportions of the total flow. However, the flow visualisation results (Chapter 6) indicated that a large separated region occupied a significant proportion of the bypass lane. It is plausible that this would result in lower bypass fractions than predicted by TASC. The effect of neglecting the bypass lane may be qualified by comparing experimental results with those from FLOW3D.

7.2.3 Baffles

The experimental work covered both leakage and non-leakage conditions. Both situations have been modelled using FLOW3D.

Non-leakage baffles were defined as infinitely thin, impermeable, boundaries between grid planes, as shown in Figure 7.1a. The definition of solid boundaries is a standard feature within the code.

For the leakage case, baffles were defined as one axial grid spacing thick, as shown in Figure 7.1b. These baffle regions were assumed to have the same porosity as the bundle, but were allocated a different flow resistance. The transverse resistances were set infinitely large, whilst the longitudinal resistance was set to:

$$R_z |u_z| u_z = \frac{1}{2} n_\ell u_z^2 \phi^2 / t_b \qquad (7.9)$$

where t_b is the baffle thickness equal to the axial grid spacing and $\phi (= 14.6)$ is the ratio of the axial flow area in the bundle to the leakage area through the tube-baffle leakage paths. The number of

velocity heads lost (n_ℓ) was defined using the empirical relationship of Haseler and Murray (1985).

The area scaling factor, ϕ, is required since the baffle leakage correlation of Haseler and Murray gives the number of velocity heads lost based on leakage velocities. The pressure loss through the baffle depends on Z, the ratio of radial clearance (c/2) to baffle thickness (t_b) and to a lesser extent on the Reynolds number in the baffle. The Reynolds number dependence was ignored (Re was set to 10000), however, the dependence on Z was retained since the true baffle thickness (3 mm) was used in the Z factor giving a constant value of n_ℓ (= 1.6).

The thickness of the baffles used in the experimental work (3 mm) is considerably less than the axial grid spacing used (16, 14 or 9 mm, for a baffle spacing of 158 mm, 112 mm and 86.4 mm respectively). However, since the experimental baffle thickness was used to describe the pressure loss across the modelled baffle, the use of thicker baffles in the code should not affect the leakage flows. To check this hypothesis, calculations were performed for the tightest baffle spacing for which baffle leakage would be most significant. The baffle thickness was set to one half the basic axial grid spacing (4.5 mm). This was achieved using a non-uniform axial grid. FLOW3D can accommodate varying grid spacings, as long as the variation is gradual. Whilst convergence of the calculations was much slower (three times the basic case), the final results were unchanged. A uniform fine grid could have been used but the convergence time would have increased further still.

An alternative method of modelling the baffle regions could have been to ascribe an appropriate porosity to them, rather than assuming the bundle porosity. However, this was not done for two reasons:

1) the resistance correlations used already contain allowances for momentum losses associated with flow entering and leaving the leakage areas;

2) if an accurate representation of the large velocity gradient which occurs in the vicinity of baffles is to be achieved a tight mesh should be used in these locations.

7.2.4 Boundary Conditions

For the non-leakage cases, a uniform velocity profile was specified for longitudinal flow (z-direction) at the window region of the first baffle space, in the plane of the first baffle. Velocities in the transverse plane were set to zero.

In the leakage cases, the inlet velocity needed to be specified over the complete inlet face of the model (both the first baffle and the window region in the plane of the baffle). To ensure steady-state conditions over the four baffle spaces, FLOW3D was started with a uniform velocity profile over the inlet plane and subsequently replaced by the resultant profile in the plane of the third baffle. This served as a closer approximation to the leakage inlet profile.

All solid boundaries were treated as non-slip walls with a prescribed zero pressure drop normal to these boundaries.

7.2.5 Turbulence Model

The turbulence model incorporated in FLOW3D is based on that presented by Lonsdale (1984) and is specifically for use in porous media/tube bundle analogies.

7.3 Results from FLOW3D

The flow field data produced by FLOW3D can be shown by plotting isobars and velocity vectors for various grid planes over all four baffle spaces. The results from FLOW3D relate to a water mass flowrate of 8.25 kg/s at each of the three baffle spacings studied in the present experimental work.

7.3.1 Non-leakage: Velocity Vectors on the Central Vertical Plane

Velocity vector plots for non-leakage are shown in Figure 7.2, one for each baffle spacing studied experimentally. The length of the arrows are proportional to the local velocity.

Each plot exhibits similar flow features, many of which were observed in the flow visualisation study (Chapter 6), but the details vary significantly with baffle spacing:

1) Low velocity regions occur in the corners between baffles and the shell, as might be expected. These regions were indicated by the experimental studies (Chapter 6).

2) Low velocity regions also occur just downstream of the baffle tips. This is clearly shown in the plot for the largest baffle spacing and involves separation and recirculating flows. The flow field data from FLOW3D also indicated some recirculation for the two smaller spacings but in such a small region close to the baffle that it does not appear on the graphic output. Observations (Chapter 6) and local pressure measurements (Chapter 9) in the HTFS shellside flow rig have also indicated these separated, recirculating flow regions.

3) Highest velocities occur near the baffle tips and in the crossflow inlet region.

4) Higher velocities occur in the vicinity of the downstream than upstream baffle face in the crossflow region. The fluid emerging from the window region cannot turn abruptly into the crossflow zone because of the high axial momentum and the relatively low resistance to flow in this direction; the baffle plate poses the only significant opposition to the window flow.

5) As the fluid flows further into the crossflow region the initially high axial momentum and the effect of the separated

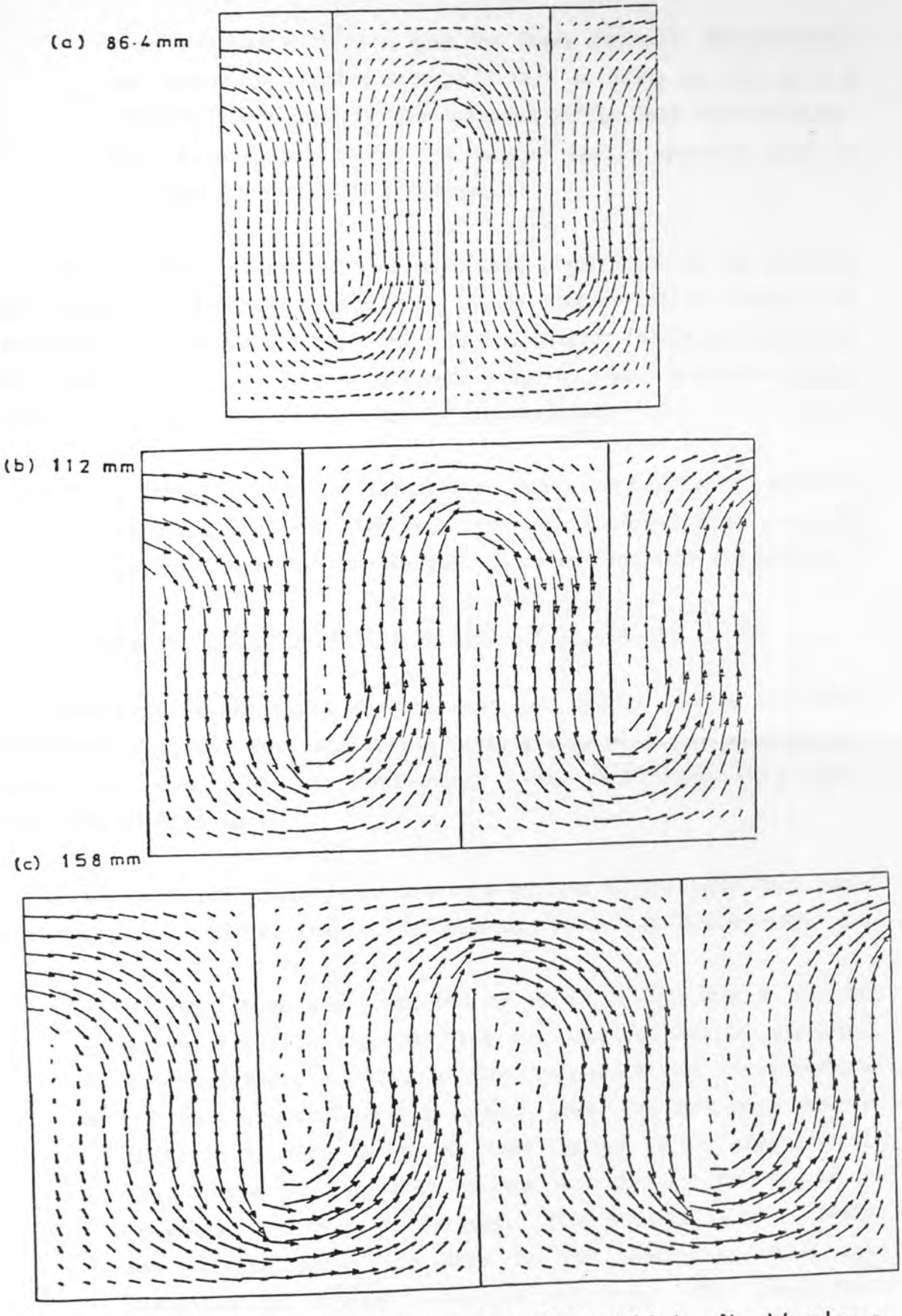

Figure 7.2: Non–Leakage: Predicted Velocity Vectors on the Central Vertical Plane.

zone (reduced effective area for flow) diminish. Consequently, the crossflow becomes more uniform. In doing so, the vectors indicate flow towards the upstream baffle face (z-direction). This is most marked for the largest baffle space in which an 'S' type crossflow is observed.

In all cases these features are least significant in the smallest baffle spacing and most significant in the largest baffle spacing. The relatively low crossflow resistance of the largest baffle spacing means that non-uniformities across the baffle space, which arise because of momentum effects, can be more easily accommodated.

These results clearly illustrate corrosion/fouling prone areas (low velocity regions) and high velocity vibration prone area (near the baffle tips, particularly the unsupported tubes just into the window).

7.3.2 Leakage: Velocity Vectors on the Central Vertical Plane

Velocity vector plots for the case with baffle leakage are shown in Figure 7.3, one for each baffle spacing studied in the experimental programme. As with the non-leakage case, each refer to a water flowrate of 8.25 kg/s.

Superficially these plots are very similar to the equivalent non-leakage plots. Closer inspection, however, shows some differences:

1) No separation was predicted by FLOW3D in the region of the upstream baffle tips for the two smallest baffle spacings. However, there is clearly flow separation and recirculation for the largest baffle spacing. Local pressure measurements (Chapter 9) also indicated these regions in the experimental rig. However, separated regions were present for all three spacings, not just the largest. This anomaly is most likely due to the grid size used in the modelling, which was plausibly too coarse to resolve relatively small local flow phenomena.

2) The flow in the overlap region, for each baffle spacing is more inclined to the normal than the equivalent cases in which baffle leakage was absent.

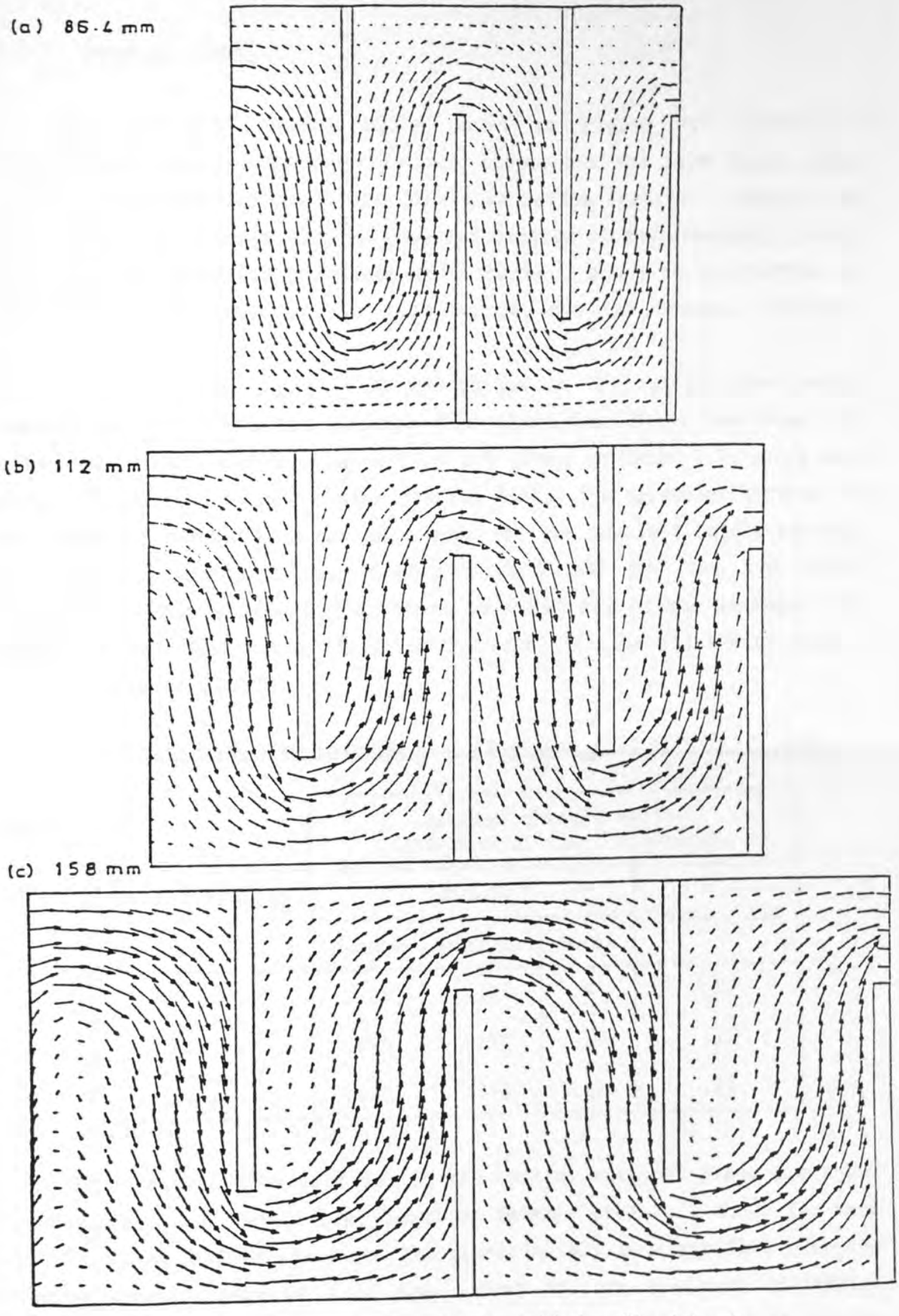

Figure 7.3: Leakage: Predicted Velocity Vectors on the Central Vertical Plane.

7.3.3 Leakage Flows

The velocity vector plots shown in Figure 7.3 indicate a significant axial velocity component throughout the flow field, which is characteristic of shellside flow with baffle leakage. However, the detail of the leakage flow is obscured because of the averaging process used in the graphics procedure and, further, since in the baffle the velocities are based on the tube bundle, not the leakage, porosity.

The values of axial flow velocities in the baffle plane can be summed to calculate the leakage flow fractions. These fractions, for both the window and overlap region are given in Table 7.1, along with those calculated by the design program TASC. The agreement between the two sets of predictions is quite good for the smallest baffle spacing, but TASC predicts rather higher than FLOW3D for the two larger spacings. The window region which provides 25% of the leakage area, accounts for nearly one third of the total leakage flows according to the results of FLOW3D.

Table 7.1: Predicted Leakage Flow Fractions from FLOW3D and TASC

	Leakage through baffle (fraction of total flowrate)			
Baffle spacing (mm)	FLOW3D			Total, TASC
	Window	Overlap	Total	
86.4	.123	.287	.41	.43
112	.090	.210	.30	.37
158	.075	.175	.25	.32

The leakage flow profiles in the central vertical plane are shown in Figure 7.4. Velocities, based on leakage area, are shown for each of the three baffle spacings. The approximately constant flow over the window region results from the almost uniform pressure difference driving the flow, as observed in the isobar plots (Figure 7.7). In the overlap region the flow falls off towards the baffle tip but does not tend to zero. This result might be due to the coarse grid used.

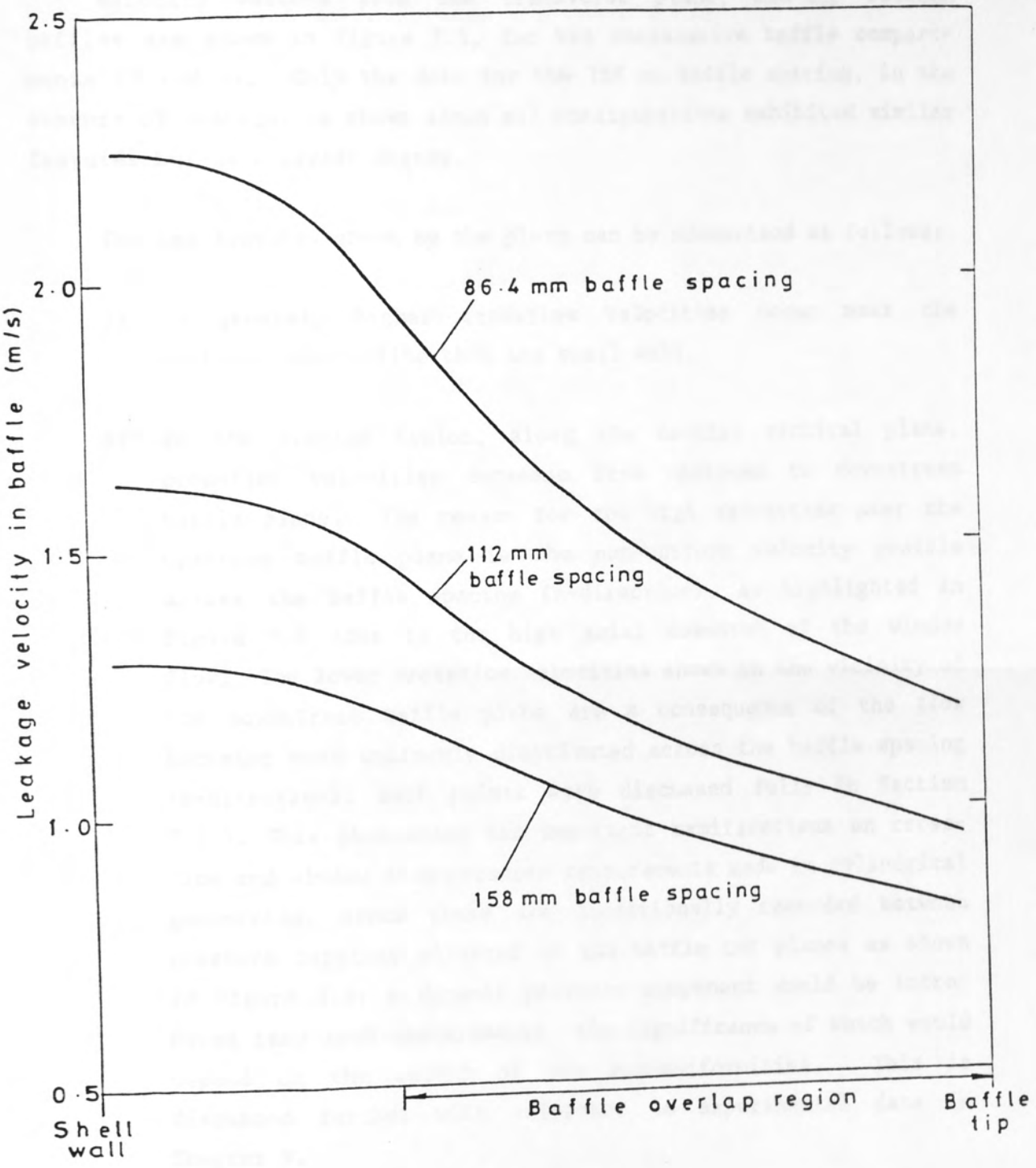

Figure 7.4: Predicted Leakage Velocity Profiles in the Central Vertical Plane.

7.3.4 Velocity Vectors on Various Transverse Planes (r-θ)

Velocity vectors from the transverse plane, mid-way between baffles are shown in Figure 7.5, for two consecutive baffle compartments (2 and 3). Only the data for the 158 mm baffle spacing, in the absence of leakage, is shown since all configurations exhibited similar features but to a lesser degree.

The key features shown by the plots can be summarised as follows:

1) In general, higher crossflow velocities occur near the vertical centre-line than the shell wall.

2) In the overlap region, along the central vertical plane, crossflow velocities decrease from upstream to downstream baffle plane. The reason for the high velocities near the upstream baffle plane is the non-uniform velocity profile across the baffle spacing (z-direction), as highlighted in Figure 7.2 (due to the high axial momentum of the window flow). The lower crossflow velocities shown in the vicinity of the downstream baffle plane are a consequence of the flow becoming more uniformly distributed across the baffle spacing (z-direction). Both points were discussed fully in Section 7.3.1. This phenomenon has important ramifications on crossflow and window flow pressure measurements made in cylindrical geometries, since these are traditionally recorded between pressure tappings situated on the baffle cut planes as shown in Figure 2.8; a dynamic pressure component would be introduced into such measurements, the significance of which would depend on the extent of the non-uniformities. This is discussed further with reference to experimental data in Chapter 9.

3) There is a degree of asymmetry between the vector plots in consecutive baffle spaces; space 2 exhibits a more uniform velocity distribution than space 3. It would appear that after the relatively uniform crossflow in space 2, the flow

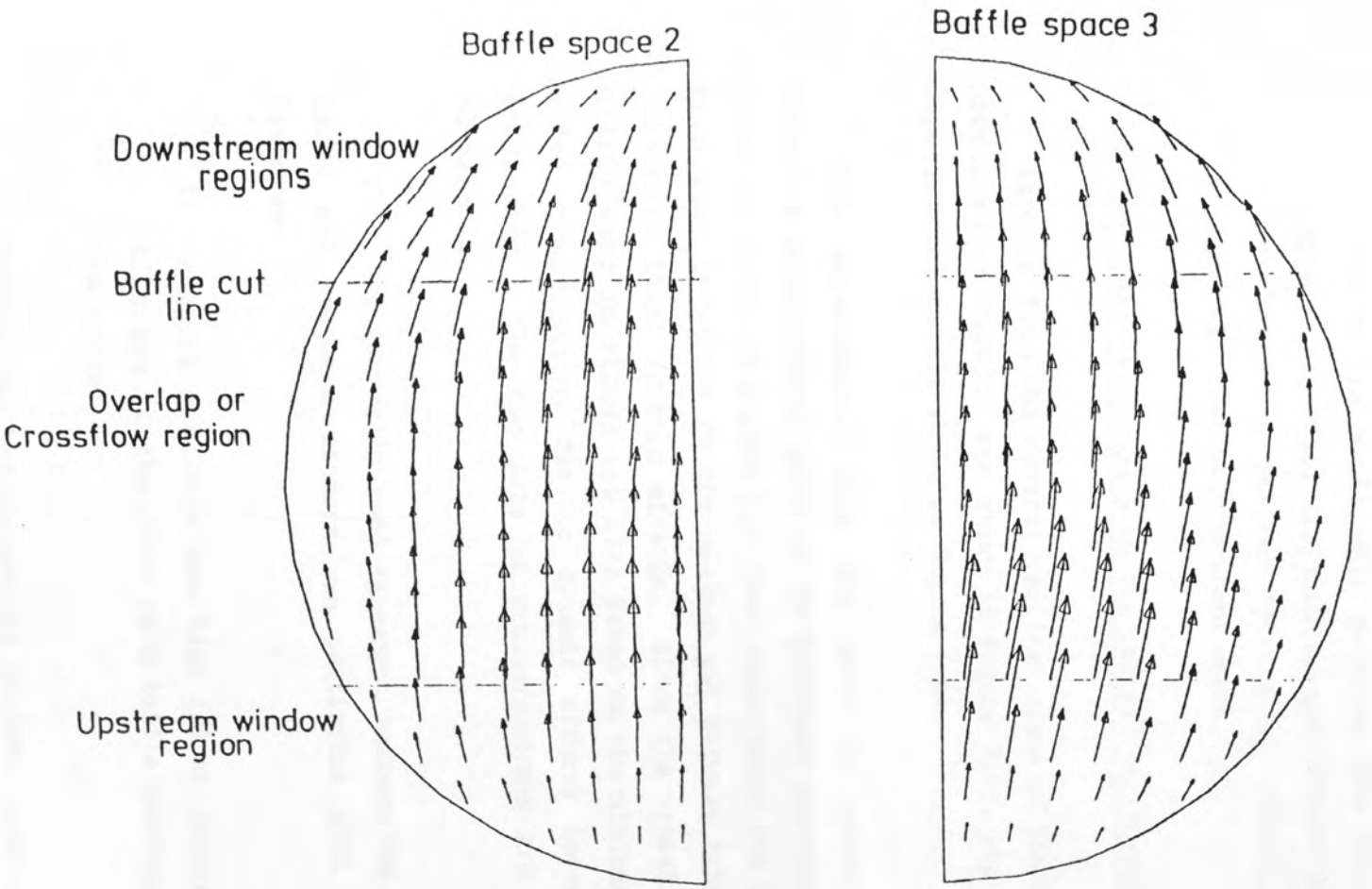

Figure 7.5: Predicted Velocity Vectors on Various Transverse Planes.

near the shell wall, while turning in the window region to the next baffle space, is constrained by the shape of the shell and moves towards the vertical centre plane. The flow thus 'piles up' giving a relatively non-uniform flow in baffle space 3. This is illustrated by the direction of the vectors which imply a higher degree of flow towards the shell wall than in space 2. This relatively strong component of flow towards the shell wall persists into the window region and appears to delay the constraining effect of the shell. This results in a smaller 'piling up' effect, so the crossflow becomes relatively uniform again.

7.3.5 Non-leakage: Isobars on the Central Vertical Plane

Isobars from the central vertical plane of the exchanger model, as predicted by FLOW3D, are shown in Figure 7.6a, with the corresponding experimental result shown in Figure 7.6b.

The experimental data are based on linear interpolation of pressure measurements made at 35 different positions within a baffle space as shown in Figure 5.2. Each measurement was made at 135° to the main flow direction in the minimum gap between tubes in an attempt to eliminate local dynamic effects. Since the crossflow surface permeability used in FLOW3D was also based on the minimum gap, there are no added complications due to dynamic effects between experiment and prediction. The two sets of pressure drops are therefore directly comparable.

There is generally good agreement between the form of the calculated and measured isobars, in particular both show the following features:

1) Pressure gradients are high (close isobars) near the baffle tips and at the inlet to a baffle overlap region, but low at the outlet.

2) Within the baffle overlap regions, gradients are higher near the downstream, than upstream, baffle. This is most marked at the largest baffle spacing.

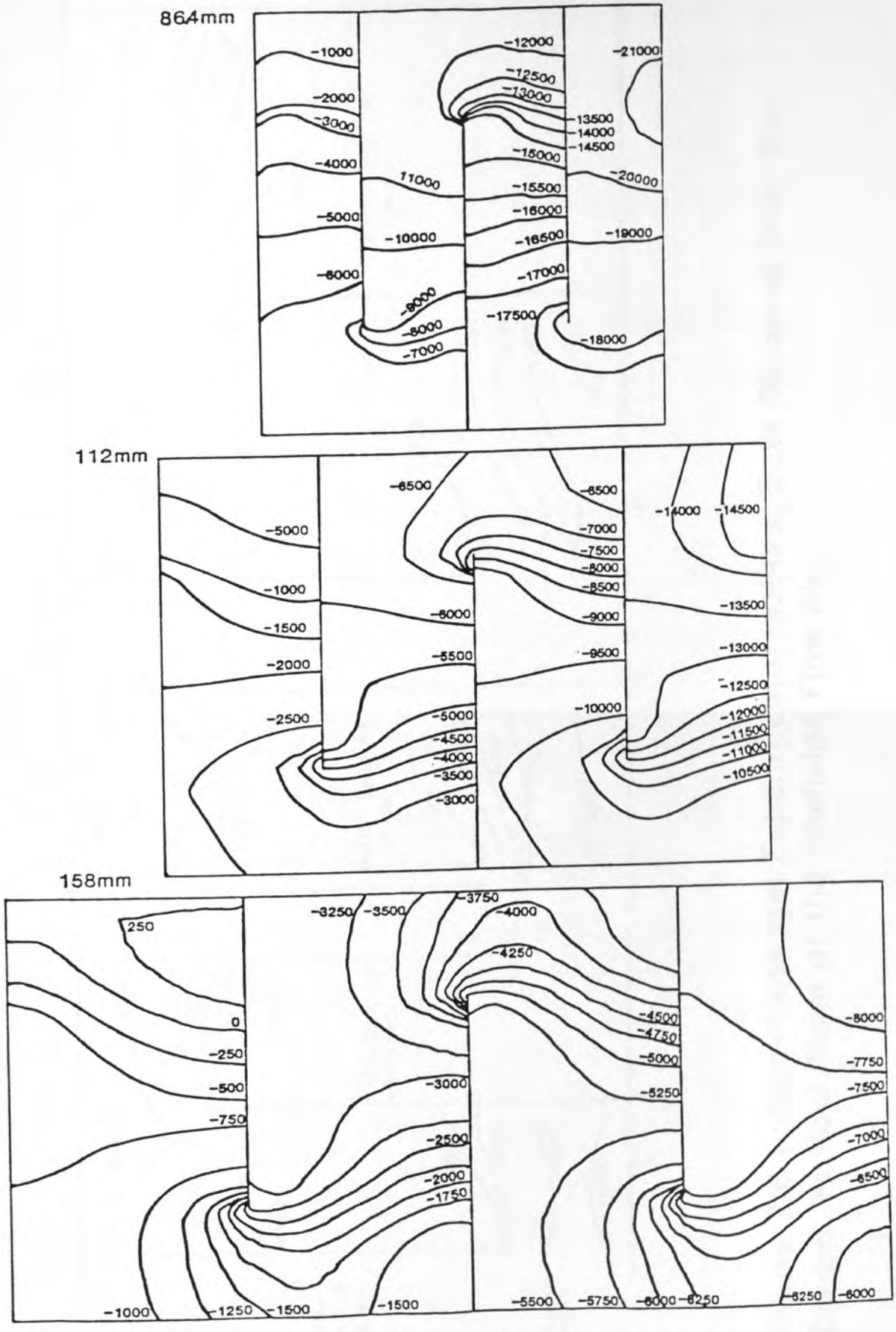

Figure 7.6 a: Non–Leakage: Predicted Isobars on the Central Vertical Plane.

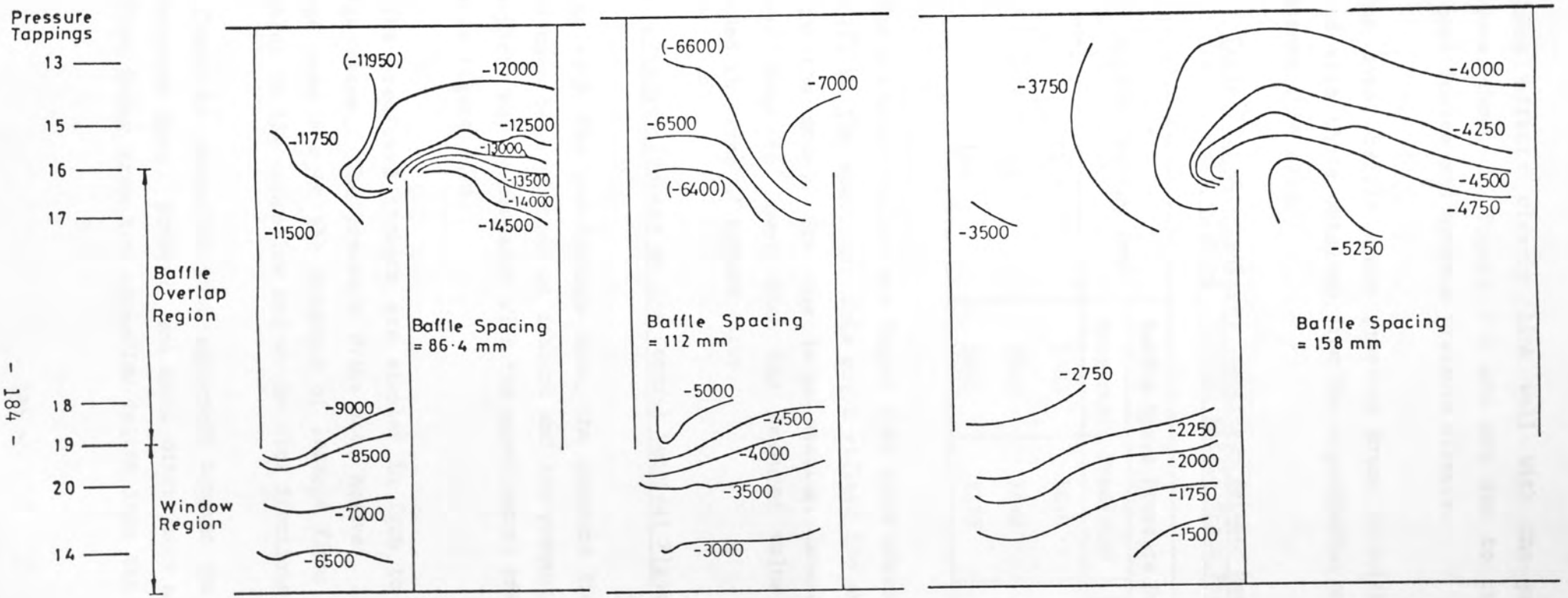

Figure 7.6 b: Non—Leakage: Experimental Isobars; Data Obtained from the Central Vertical Plane of the Shellside Flow Rig.

These effects clearly link well with the predicted velocity variations shown in Figure 7.2 and are due to the combination of frictional losses and dynamic pressure effects.

The total baffle space pressure drops calculated by FLOW3D are compared with those obtained from the experimental work in Table 7.2. The agreement is good.

Table 7.2: Non-Leakage: Comparison Between Measured and Predicted (FLOW3D) Baffle Space Pressure Drops

Baffle Spacing (mm)	Baffle Space Pressure Drop (N/m^2)		
	Measured	Predicted	Measured / Predicted
86.4	5480	5910	0.93
112	3520	3840	0.92
158	2465	2330	1.06

The predicted values are higher than those measured for the medium and small baffle spacings; this might reflect the absence of a bypass lane in the model. For the large spacing, however, the predicted pressure drop is lower than the measured value which cannot be explained in terms of bypass flows.

7.3.6 Leakage: Isobars on the Central Vertical Plane

As with the non-leakage case, the pressure fields calculated by FLOW3D have been plotted as isobars and are presented in Figure 7.7a. These plots may be compared with the experimental pressure measurements shown in Figure 7.7b.

The predicted isobars are similar in form to those in the non-leakage cases. The pressure drops are, however, lower than the non-leakage case due to the presence of leakage flows and the subsequent reduction in the crossflow and window flow fractions.

There is generally good agreement between the form of predicted and measured data. However, one small discrepancy may be noted. Where the flow turns from the crossflow region into the window region, the

measured isobars show a curvature not present in the predicted results. Close to the upstream baffle, measured pressure drops are higher than those predicted by FLOW3D. A possible reason for this is the presence of high local axial velocities, close to the tube surface, due to jetting of the leakage flows entering the bundle. Such high velocities would reduce the static pressures measured in the vicinity of the upstream baffle thereby increasing the measured pressure drops, but could not be predicted using the constant porosity model incorporated in FLOW3D.

The total baffle space pressure drops calculated by FLOW3D are compared with those obtained from the experimental work in Table 7.3.

Table 7.3: Leakage: Comparison Between Measured and Predicted (FLOW3D) Baffle Space Pressure Drops

Baffle Spacing (mm)	Baffle Space Pressure Drop (N/m^2)		
	Measured	Predicted	$\frac{\text{Measured}}{\text{Predicted}}$
86.4	2025	2030	1.00
112	1625	1760	0.92
158	1315	1250	1.05

The total baffle space pressure drops predicted by FLOW3D are in good agreement with those measured, as were the non-leakage values (Table 7.2).

7.3.7 Isobars Plots on Various Transverse Planes (r-θ)

The current experimental pressure measurements in these planes were not comprehensive enough to produce isobars to compare with the results from FLOW3D. For completeness, however, isobar plots for the largest baffle spacing in the absence of baffle leakage are presented in Figure 7.8. These refer to the central transverse planes, midway between baffles, for two consecutive baffle spaces (2 and 3).

Highest pressure gradients occur in the upstream window region.

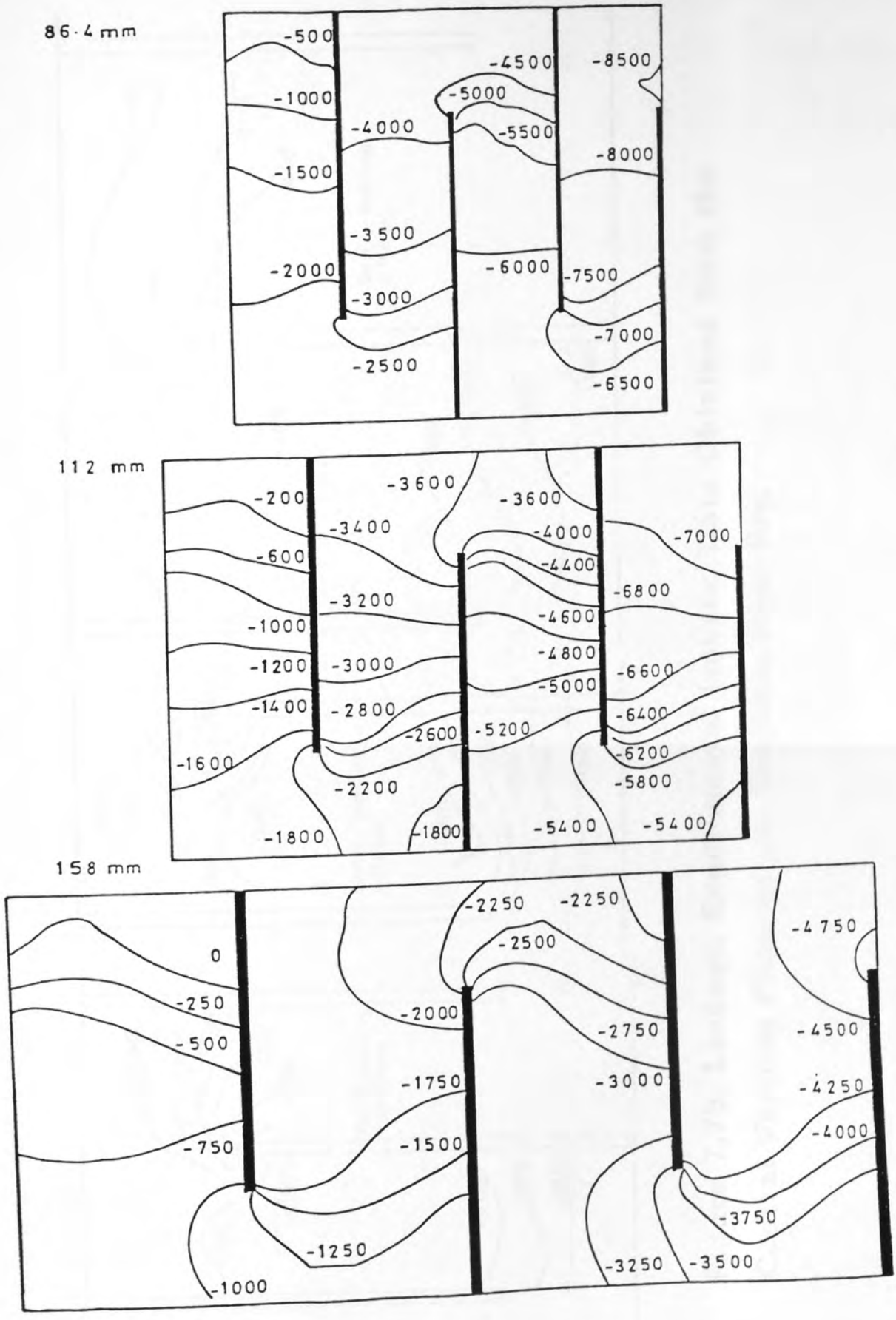

Figure 7.7 a: Leakage: Predicted Isobars on the Central Vertical Plane at Three Baffle Spacings.

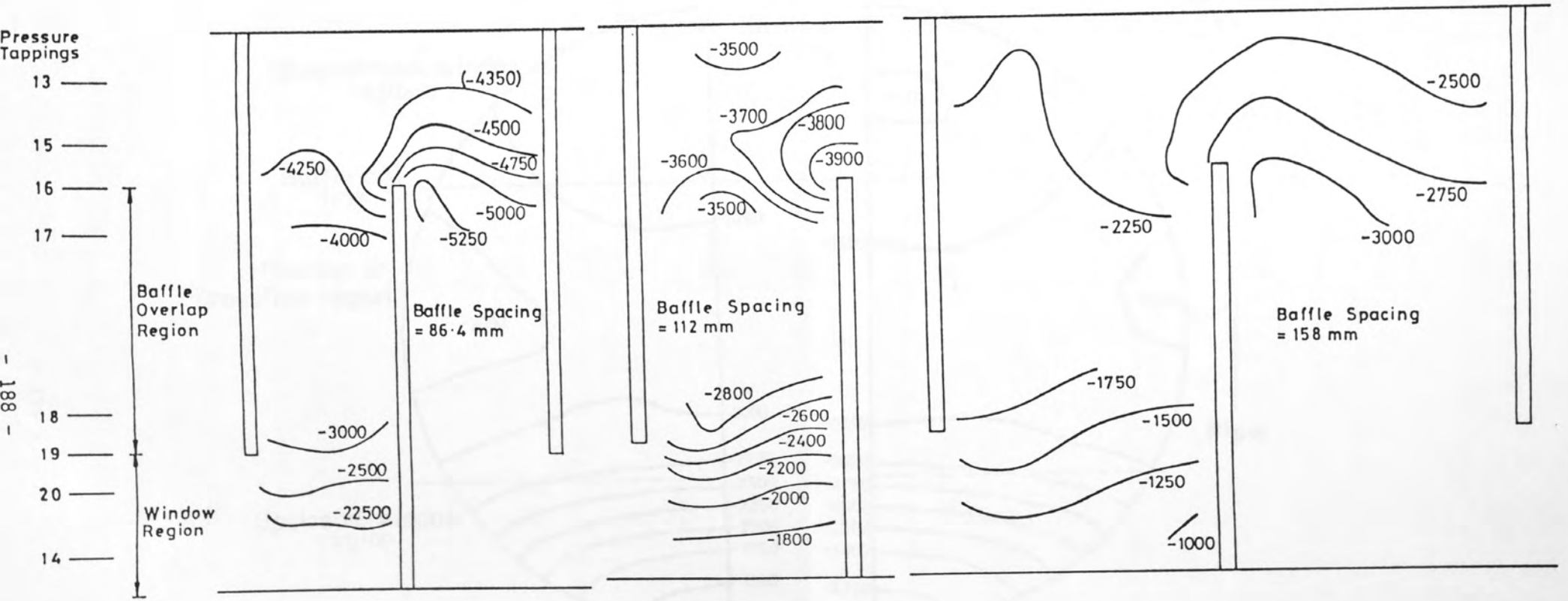

Figure 7.7b: Leakage: Experimental Isobars; Data Obtained from the Central Vertical Plane of the Shellside Flow Rig.

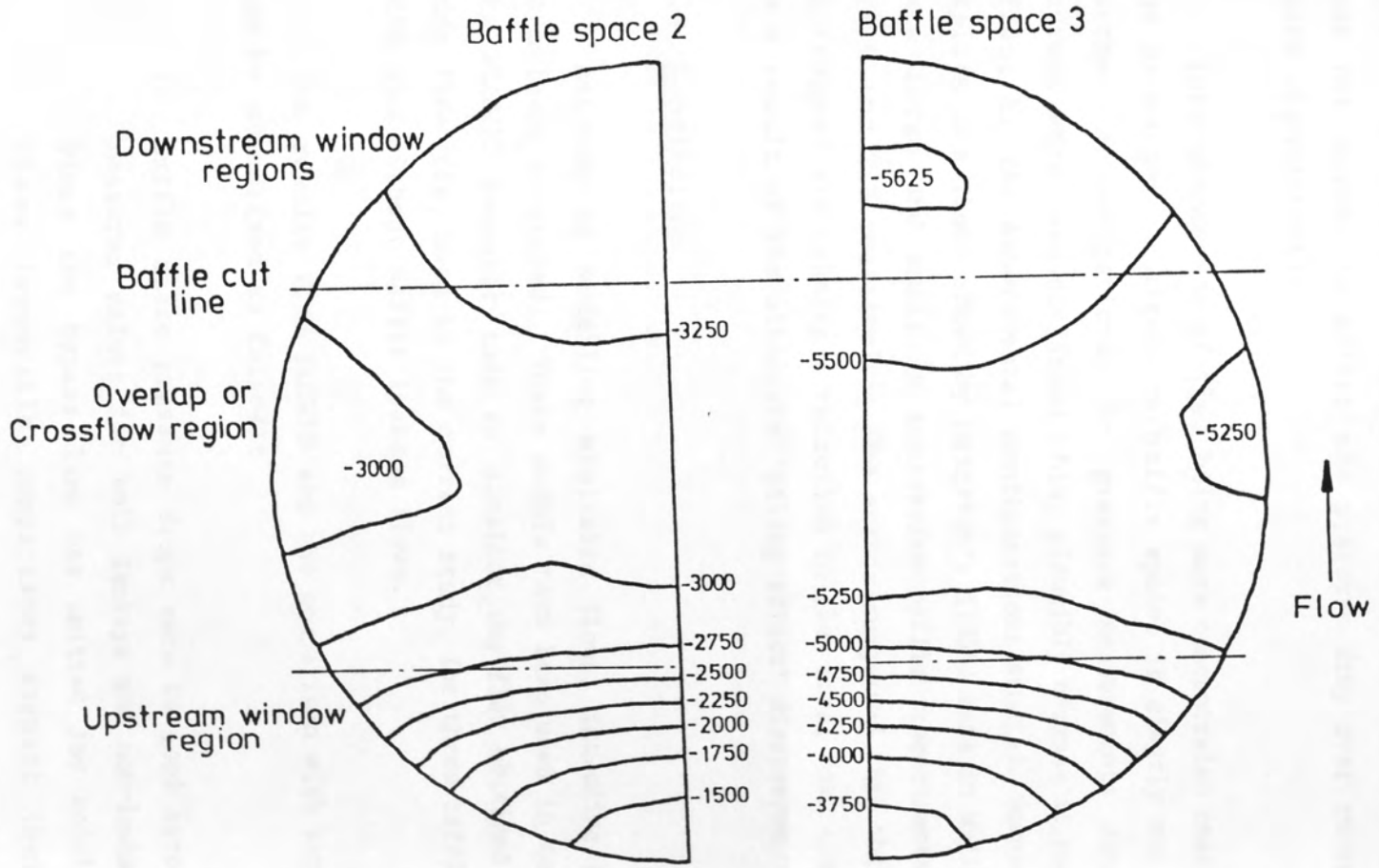

Figure 7.8: Predicted Isobars on Various Transverse Planes.

Low pressure gradients occur over the rest of the baffle space, with some pressure recovery in the vicinity of shell wall in the cross-flow region.

The pressure drop for the relatively non-uniform flow baffle space (3) is only marginally larger than for the more uniform flow in space (2). The effect of the periodic nature of the flow (Section 7.3.4) does not appear to affect the pressure drop over consecutive baffle space significantly.

This phenomenon of flow being more concentrated near the centre of the exchanger in alternate baffle spaces is clearly one that warrants further investigations. No pressure measurements obtained in the current work have confirmed this, plausibly because it has only a small effect in the experimental configurations studied. However, this could explain the trend shown by Leighton's (1955) data in which measurements were large and small in successive baffle compartments (see Section 2.1.4 and 2.3 relatively). The author suggested that this might be due to trapped air causing a reduction in flow area, but, clearly, it could be a result of the alternate 'piling effect' discovered.

7.4 Conclusions

Methods of modelling shellside flows, including baffle leakage have been described. These models have been used in conjunction with the FLOW3D computer code to simulate the flow obtained in the shell-side flow rig, used in the current study, for three baffle spacing each with and without baffle leakage flows.

The results from FLOW3D and the comparison with experimental data may be summarised as follows:

1) Baffle space pressure drops were in good agreement with the measured values for both leakage and non-leakage geometries. Since the bypass lane was omitted for modelling purposes, these favourable comparisons suggest that bypass flow fractions were small in the current experimental rig. This concurs with the conclusion drawn from direct observation of the shellside flow (Chapter 6).

2) Detailed velocity measurements are not available for comparison with the results of FLOW3D, but the broad features of the predicted flows agree with experimental observations (Chapter 6). Small separated zones detected in the shellside flow rig just downstream of the baffle tips were predicted for all geometries apart from the two smaller baffle spacings in the leakage case. In addition, the regions of low and high velocity predicted by FLOW3D illustrate areas that could be prone to fouling and tube vibration.

3) A non-uniform crossflow was predicted, with higher flows near the centre line of the exchanger than the shell wall. The non-uniformity appeared to be relatively large and relatively small in successive baffle space. However, this had only a marginal effect on the pressure drop in successive baffle spaces.

4) The values of axial flow velocities were summed to calculate leakage flow fractions. Corresponding flow fractions obtained using the simpler flow network model used in TASC were broadly in agreement. However, it should be stressed that the TASC network does not permit a realistic treatment of leakage flows (see Section 2.6.2) and as such these discrepancies are likely to be more significant than might appear from Table 7.1.

Although a simplified resistance model was used for both bundle and baffles, the favourable comparison between measurement and predictions suggest that the FLOW3D code and the models used were given the correct interpretation.

The potential of three-dimensional computer modelling, combined with detailed experimental data, have thus been demonstrated to assist in providing a clearer understanding of shellside flow.

Throughout the remainder of this thesis the results from FLOW3D, along with those obtained from flow visualisation, will be drawn upon to clarify various aspects of shellside flow.

In the following Chapter the 'Crossflow Penetration' model (see Section 2.7.2) presented by Wills (1984) is assessed, along with an improved model, using the velocity field data predicted by FLOW3D.

CHAPTER 8

PENETRATION OF THE CROSSFLOW IN THE WINDOW REGION

8. PENETRATION OF THE CROSSFLOW IN THE WINDOW REGION

8.1 Introduction

To allow a more physical approach to modelling individual flows, design methods such as TASC separate the crossflow pressure drop from the window pressure drop. A problem encountered with this approach is that there is no distinct boundary between crossflow and flow turning around in the window region. Clearly, crossflow does not suddenly desist at the plane described by the baffle tips, but continues, gradually diminishing in the window to zero at the shell wall. The difficulty arises in deciding how far, on average, crossflow persists into the window region. This is important since it defines the total number of tube rows crossed in crossflow so that design correlations can be applied to establish the crossflow pressure loss.

In an earlier version of TASC, crossflow in the window was assumed to extend from the baffle tip to the centre of gravity of the window region (Moore, 1974). This distance was assumed to be the same for any baffle configuration. More recently Wills (1984) derived a simple one-dimensional model that predicts the extent of crossflow in the window, taking account of the shellside geometry. This is known as the crossflow penetration model and is currently used in TASC. However, he did not find an exact mathematical solution to the problem posed. Instead he resorted to an ad hoc method to satisfy boundary conditions. The lack of relevant flow information available to Wills meant that he was unable to assess the model and the limitations imposed by the ad hoc solution.

The purpose of this chapter is threefold:

1) to present Wills' model and discuss its limitations;

2) to present the exact mathematical solution to the crossflow penetration problem posed by Wills;

3) to use the flow field results calculated by FLOW3D (Chapter 7) to independently evaluate the crossflow penetration distance, for the shellside configurations used in the current experimental work, and compare these values with those given by the two models.

8.2 Theory

Wills (1984) derived his one-dimensional model by considering a simple two-dimensional representation of the window region. Within this region the single one-dimensional crossflow stream progressively decreased due to increases in the axial flows along the window, which subsequently recombined into a single crossflow stream in the next baffle space. He defined the crossflow penetration distance as the point at which the crossflow stream, in the window, had decreased to half its value at inlet to the window region. The model was thus equivalent to two manifolds (the crossflow streams) connected by multiple small pipes (axial flow in the window region) as shown in Figure 8.1. The flowrate $\dot{M}_y$ along the manifolds decreases from inlet. Both $\dot{M}_y$ and $\dot{M}_z$ are functions of y but not z.

Wills' analysis resulted in the following equation:

$$\dot{M}_y^2 + Y^3 \frac{d\dot{M}_y}{dy} \cdot \frac{d^2\dot{M}_y}{dy^2} = 0 \qquad (8.1)$$

and

$$Y^3 = \frac{f_z P_y}{D_h f_y} B_s^3 \qquad (8.2)$$

where f_y and f_z are crossflow and longitudinal flow friction factors, and D_h is the hydraulic diameter of the window region.

Defining

$$x = y/Y \ , \quad m = \dot{M}_y / \dot{M}_c \qquad (8.3)$$

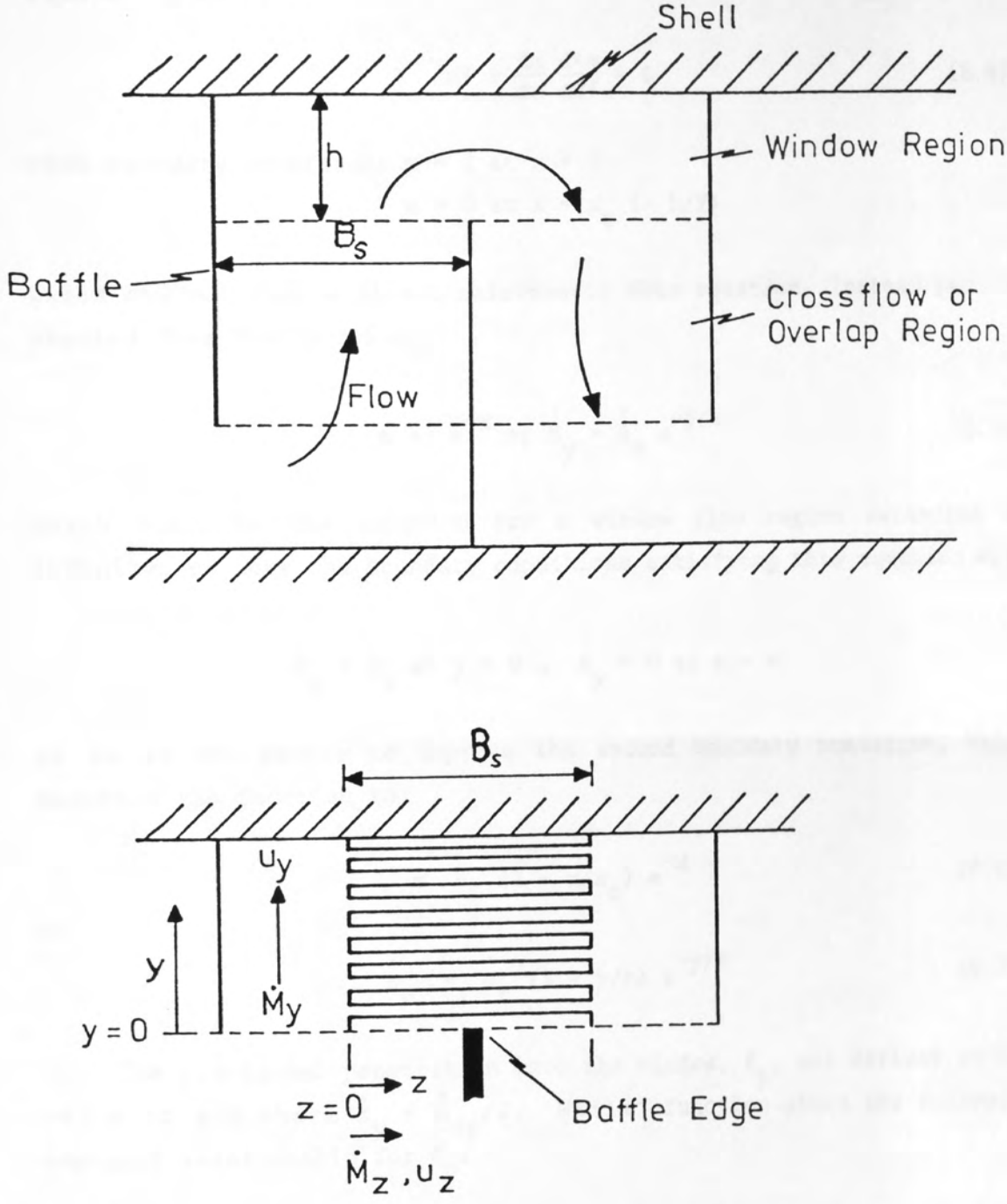

Figure 8.1: Geometry Used for the Derivation of the Crossflow Penetration Model (Wills,1984), Equation (8.4).

where $\dot{M}_c$ is the flowrate at x = 0, that is the baffle edge, the equation reduces to

$$m^2 + \frac{dm}{dx}\frac{d^2m}{dx^2} = 0 \qquad (8.4)$$

with boundary conditions m = 1 at x = 0

m = 0 at x = x_o (= h/Y)

Wills did not find a direct solution to this equation. Instead he started from the function

$$m = e^{-x} \text{ or } \dot{M}_y = \dot{M}_c\, e^{-y/Y} \qquad (8.5)$$

which would be the solution for a window flow region extending to infinity, so that the boundary conditions satisfying this equation are

$$\dot{M}_y = \dot{M}_c \text{ at } y = 0\,, \quad \dot{M}_y = 0 \text{ at } y = \infty$$

As an ad hoc device to improve the second boundary condition, Wills modified the function to

$$m = (1 - x/x_o)\, e^{-x} \qquad (8.6)$$

or

$$\dot{M}_y = \dot{M}_c\, (1 - y/h)\, e^{-y/Y} \qquad (8.7)$$

The fractional penetration into the window, f_p, was defined as the value of y/h where $\dot{M}_y = \dot{M}_{cr}/2$. Wills' function gives the following implicit relationship for f_p:

$$f_p = 1 - \tfrac{1}{2} \exp\,(f_p h/Y) = 1 - \tfrac{1}{2} \exp\,(f_p x_o) \qquad (8.8)$$

which must be evaluated numerically.

The correct solution to Equation (8.4) is actually (Birchenough, 1985)

$$x + I_2 = \frac{1}{3}\left[\frac{1}{2}\ln\frac{(e-a)^3}{e^3-a^3} + \sqrt{3}\tan^{-1}\left(\frac{2e+a}{a\sqrt{3}}\right)\right]_{e_1}^{e_2} \qquad (8.9)$$

where

$$e = (m^{-3} + a^3)^{1/3} \qquad a^3 = (3I_1)^{-1} \qquad (8.10)$$

and I_1 and I_2 are constants of integration.

This function requires numerical evaluation to calculate relative flow m as a function of scaled distance x (see Appendix E). This was done, and the corresponding fractional penetration f_p, evaluated. It was found that the values of f_p obtained could be fitted very accurately by the following explicit relations, giving f_p as a function of dimensionless window height x_o (= h/Y):

$$f_p = \tfrac{1}{2} \qquad (x_o <= 1.25) \qquad (8.11a)$$

$$f_p = 0.1133 + \frac{0.45}{x_o} \qquad (1.25 < x_o < 2.25) \qquad (8.11b)$$

$$f_p = \frac{\ln(2)}{x_o} \qquad (x_o => 2.25) \qquad (8.11c)$$

A plot of these are presented in Figure 8.2 and compared with Wills' predictions (Equation (8.8)).

It can be seen that there are significant differences between the two curves.

It must be pointed out, however, that the basic model proposed by Wills has two very fundamental limitations. Firstly, it does not allow for the reduction in available crossflow area, due to the curvature of the shell, as the flow penetrates into the window region. This would lead to a considerably more complicated equation than Equation (8.4). Secondly, it was derived for a non-leakage situation; industrial units always have a degree of leakage and the presence of these flow could have a significant effect on the penetration distance.

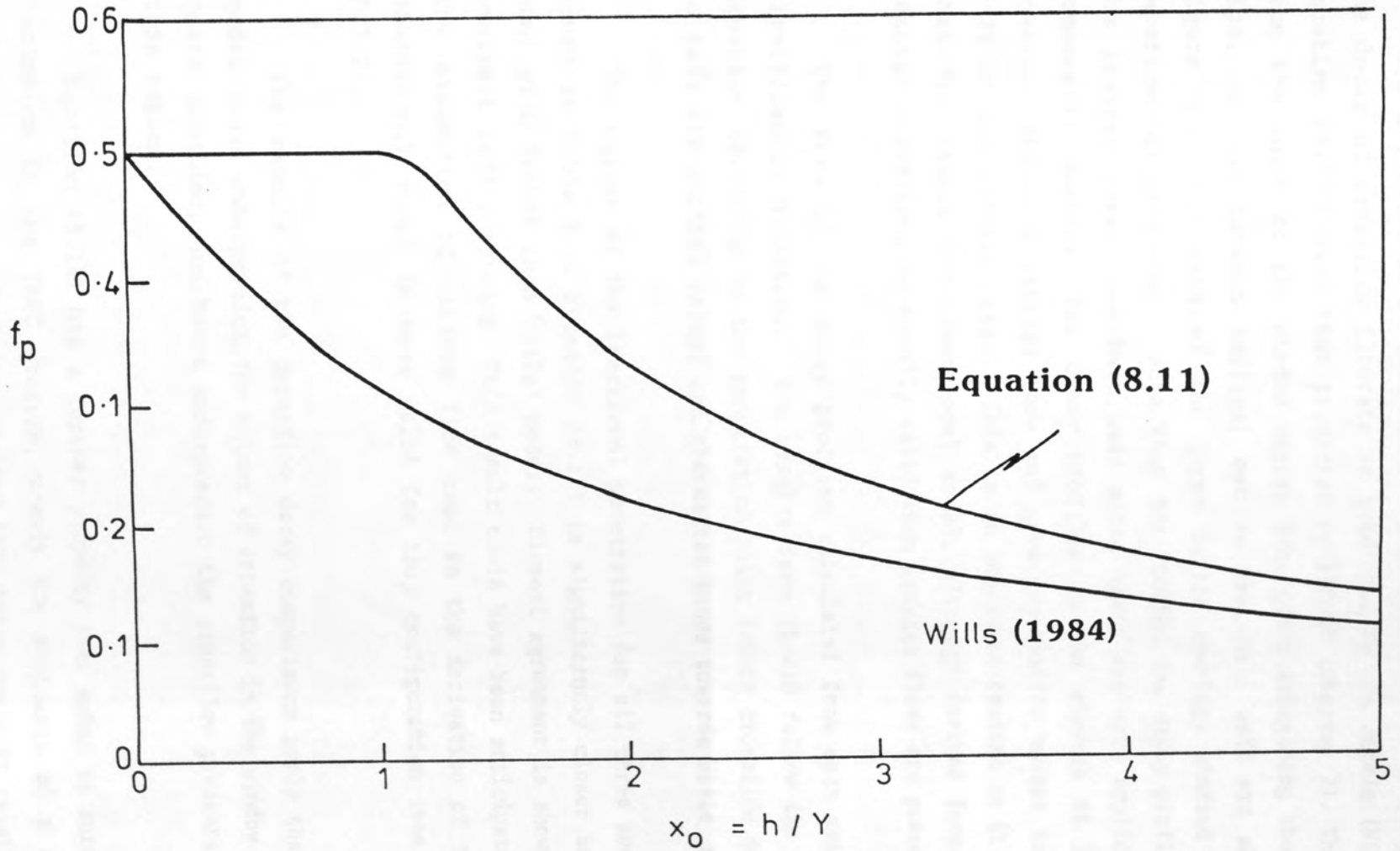

Figure 8.2: Fractional Crossflow Penetration Distance into the Window(f_p) as a Function of Dimensionless Window Height(x_o).

8.3 Assessment of the Penetration Model

The significance of these limitations can be assessed by comparing the decay of crossflow flowrate as predicted by the models (Wills and Equation (8.11)) with that predicted by FLOW3D (Chapter 7). The decay from the inlet to the window region (the plane containing the baffle tips, mid-way between baffles) out to the shell wall are shown in Figure 8.3, for each of the three baffle spacings studied in the experimental programme. Note that for FLOW3D, the decay profiles for the leakage cases have been used since these are more applicable to commercial designs. The decay profiles in the absence of leakage, however, showed a similar form and gave penetration values to within ± 2% of the leakage cases. This is an important feature as it implies that the simple one-dimensional model, although derived from a non-leakage situation, is equally valid when leakage flows are present.

The form of the decay profiles calculated from each method are significantly different. The results from FLOW3D follow the form of Equation (8.11) up to the penetration point (where crossflow decreases to half its initial value) and thereafter tends towards Wills' model.

The values of the fractional penetration for all three models are given in Table 8.1. Equation (8.11) is significantly closer in agreement with FLOW3D than Wills' model. Closest agreement is shown at the smallest baffle spacing. This result could have been anticipated since the assumption of uniform flow used in the derivation of the one-dimensional model is most valid for this configuration (see Section 7.3.2).

The results of the crossflow decay comparisons imply that Wills' model would underpredict the extent of crossflow in the window, for the cases examined, and hence underpredict the crossflow pressure loss in this region.

Equation (8.11) has a further property that makes it suitable for inclusion in the TASC program, namely the avoidance of a numerical solution since it has been resolved into three explicit relationships. Therefore, less computer time is required to evaluate the penetration distance than the existing method.

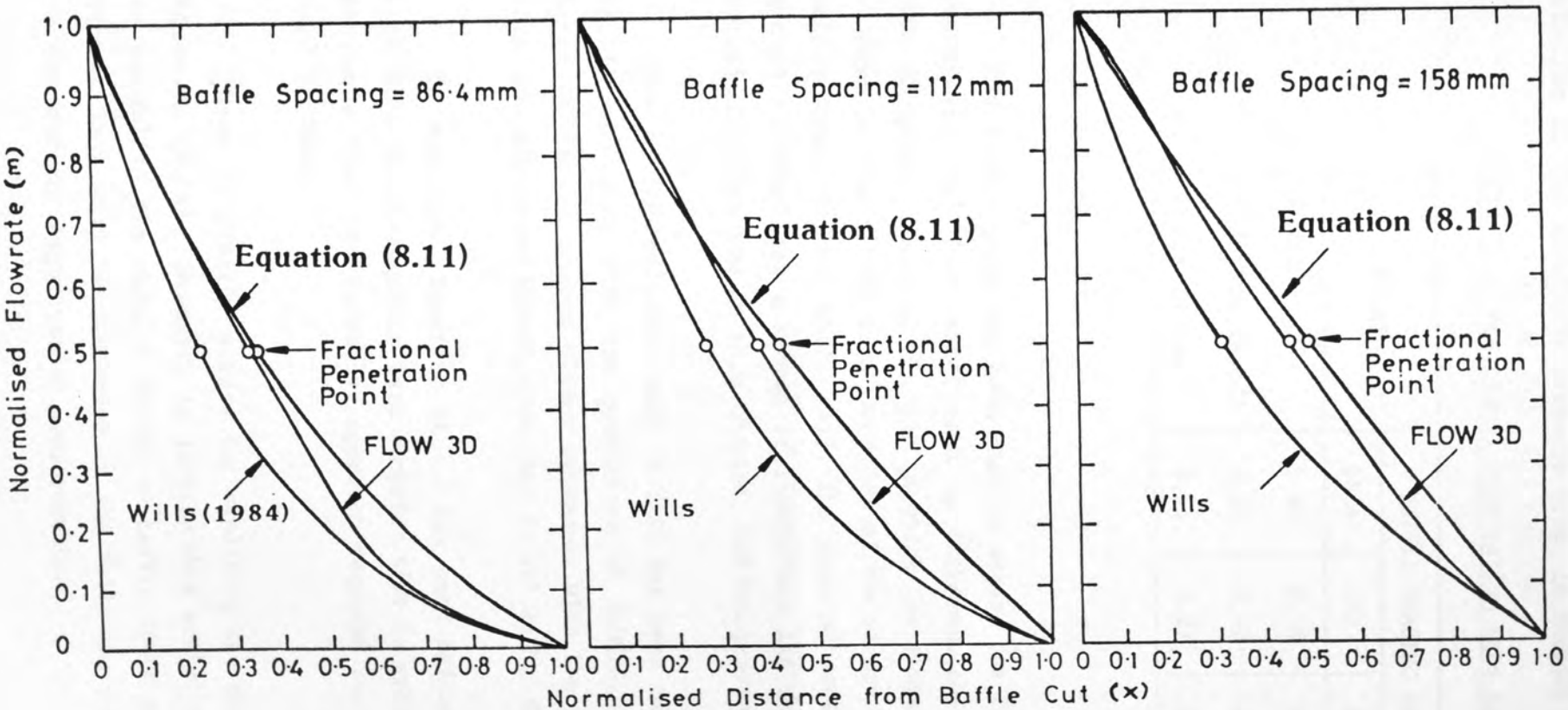

Figure 8.3: Decay of Crossflow in the Window Region as Predicted by Wills(1984), FLOW3D and Equation (8.11).

The effects of the penetration model will be discussed further, in relation to the shellside pressure drop, in Chapter 9.

Table 8.1: Fractional Penetration into the Window

MODEL	BAFFLE SPACING (mm)		
	86.4	112	158
FLOW3D	0.33	0.38	0.46
Equation (8.11)	0.36	0.42	0.50
Wills (1984)	0.23	0.27	0.32

8.4 Conclusions

The FLOW3D code has been used to assess one feature of the simple one-dimensional flow model used to represent shellside flows in the TASC program. This is the way in which the crossflow flowrate decays to zero in travelling from the inlet of the window region (plane of the baffle tips) to the shell wall. The physical model on which the TASC method is based has a number of limitations and the exact mathematical solution, presented in this chapter, had not previously been obtained.

The ad hoc solution used in TASC has been compared with Equation (8.11) and also with the prediction of FLOW3D. It was found that Equation (8.11) showed closer agreement with the predictions from the more soundly based FLOW3D code than Wills' ad hoc model.

In addition, Equation (8.11) has been reduced to three explicit equations which requires less computer time to evaluate the penetration distance than the iterative approach required for the model currently used in TASC.

There is clearly a case for replacing the method used in TASC by Equation (8.11). However, to justify this action it is first necessary to establish the model's effect on baffle space pressure drop predictions. This will be discussed in the following chapter with reference to the current experimental measurements.

Finally, the potential of three-dimensional modelling has been demonstrated to assist in assessing the simple flow models which are likely to continue to be used for design purposes for some time. This is clearly an area where there is ample scope for future advances.

CHAPTER 9

PRESSURE DROPS - RESULTS III

9. PRESSURE DROPS - RESULTS III

9.1 Introduction

The purpose of this chapter is firstly, to present and discuss pressure measurements obtained in the current work and, secondly, to compare these results with previously obtained data and commonly used design methods.

Four categories of pressure measurement were obtained in the current work: total baffle space pressure drops, which were subdivided into crossflow and window pressure drops, and circumferential variations of pressure around individual tubes within the bundle. For each category the variation of pressure drop with Reynolds number, leakage and non-leakage, baffle spacing, measurement position across the length and width of the baffle compartment are discussed.

In the foregoing chapters, shellside flow has been demonstrated to be a very complicated three-dimensional process. The large variations of velocity within a baffle compartment and inclination of flow to the tube bundle complicates the interpretation of pressure drop measurements considerably. This is compounded further by the presence of baffle leakage and bundle bypass flow.

It is apparent, therefore, that discussions of pressure drops (crossflow and window) obtained in cylindrical baffled units must be accompanied by considerations of flow non-uniformities and possible dynamic pressure effects. This has been attempted with the aid of the flow modelling and flow visualisation results.

Estimates of the maximum possible errors in the experimental measurements are discussed in Appendix F.

9.2 Crossflow Pressure Drops

Crossflow pressure drops are presented, in non-dimensional form, as the number of velocity heads lost ($\bar{n}_{ct}$) against Reynolds number ($\overline{Re}^{m}_{ct}$):

$$\bar{n}_{ct} = \frac{2\,\Delta P_c\,\rho}{N_c\,(\dot{M}_{ct}/\bar{A}^{m}_{ct})^2} \qquad (9.1)$$

$$\overline{Re}^{m}_{ct} = \frac{\dot{M}_{ct}\,(P_t - D_o)}{\eta\,\bar{A}^{m}_{ct}} \qquad (9.2)$$

where $\dot{M}_{ct}$ is the crossflow mass flowrate based on the total shellside flow and $\bar{A}^{m}_{ct}$ is the average minimum crossflow area including the bypass lane. Moore's (1974) definition of flow area has been used since it accounts for the variation of area due to the shell curvature (see Section 2.1.4).

Normalised pressure drops obtained over three regions in the overlap are reported. These relate to measurements between tappings 16-19, 17-18 and 11-12. For the purpose of this discussion these regions are referred to as A, B and B' respectively, as shown in Figure 9.1. The number of major restrictions to crossflow, N_c, and the average minimum crossflow areas (including the bypass lane), for each region, are shown in Table 9.1.

Table 9.1: Total Crossflow Areas and the Number of Major Restrictions to Flow

Baffle Spacing (mm)	Region	Crossflow Area $\bar{A}^{m}_{ct}$ x 10^3 (m^2)	Number of Restrictions N_c
86.4 (Leakage)	A	7.379	14
	B,B'	7.544	10
84.8 (Non-Leakage)	A	7.240	14
	B,B'	7.405	10
112.0 (Leakage)	A	9.562	14
	B,B'	9.780	10
110.4 (Non-Leakage)	A	9.428	14
	B,B'	9.640	10
158.0 (Leakage)	A	13.498	14
	B,B'	13.798	10
156.4 (Non-Leakage)	A	13.358	14
	B,B	13.658	10

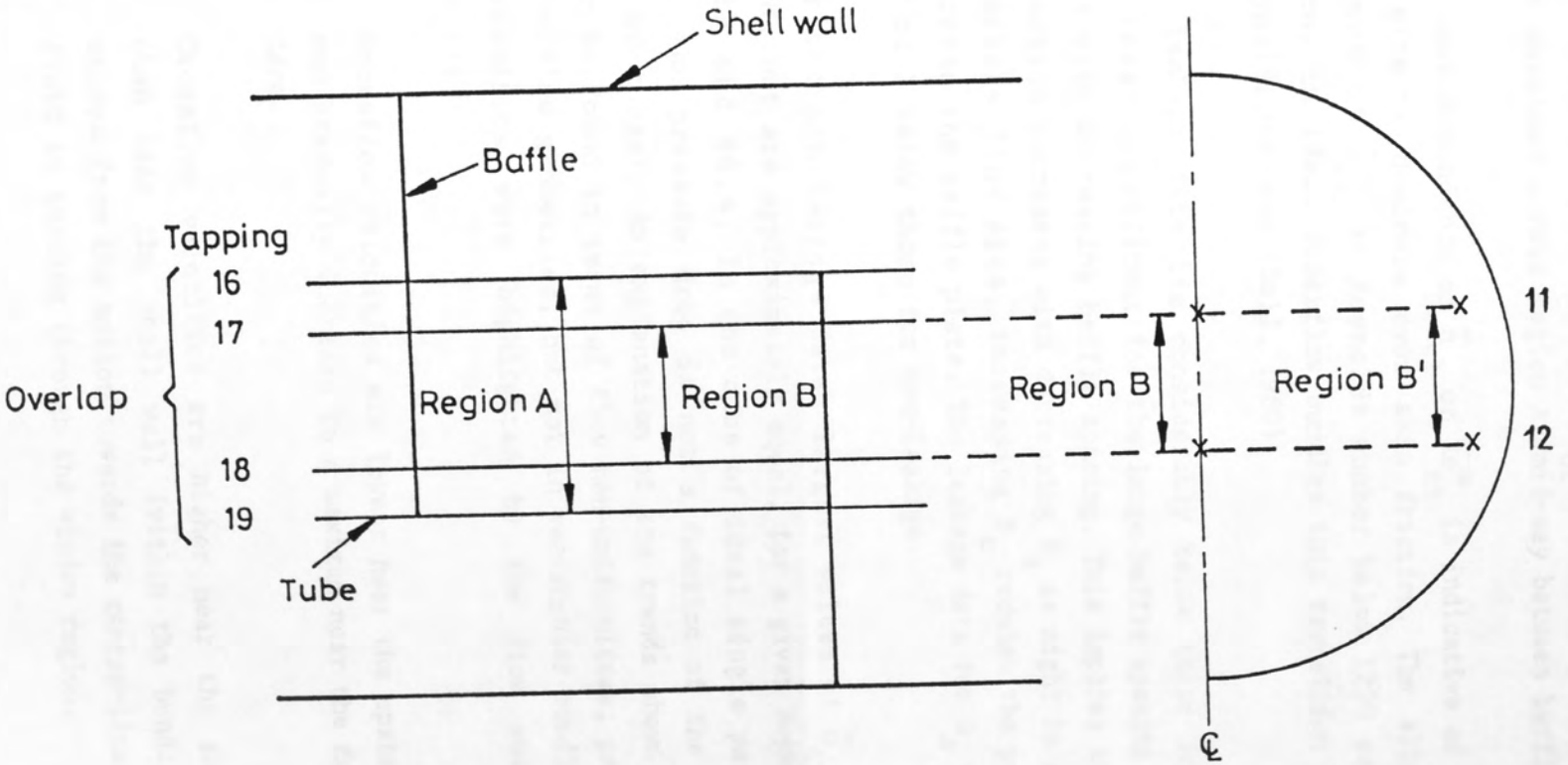

Figure 9.1: Regions over which Crossflow Pressure Measurements were Obtained.

9.2.1 Pressure Drop Variations with Reynolds Number and Baffle Spacing

The dependence, of $\bar{n}_{ct}$ with $\overline{Re}^{m}_{ct}$ are shown in Figures 9.2. These data were obtained across region A, mid-way between baffles (B_f =0.5).

The weak dependence of $\bar{n}_{ct}$ on $\overline{Re}^{m}_{ct}$ is indicative of flows in which inertia effects dominate over skin friction. The slightly stronger dependence of $\bar{n}_{ct}$ at Reynolds number below 1200 suggests a flow transition; in ideal crossflow bundles this transition occurs at much lower Reynolds numbers (Bell, 1960).

The leakage data lie considerably below those for non-leakage; this is least significant for the large baffle spacing (B_s = 158) and increases with decreasing baffle spacing. This implies that the leakage flow fraction increases with decreasing B_s as might be expected; for a given leakage flow area, increasing B_s reduces the pressure driving force across the baffle plate. The leakage data for B_s = 86.4 are over a factor of 3 below those for non-leakage.

For the non-leakage data, largest values of $\bar{n}_{ct}$ are shown at B_s = 158, but are approximately equal, for a given Reynolds number, at B_s = 112 and 86.4. In the case of ideal single pass rectangular bundles, the pressure drop is not a function of the baffle spacing (length of tubes). An explanation of the trends shown by the current data can be found in terms of flow non-uniformities, present in cylindrical baffled geometries, but not in rectangular bundles. Three basic non-uniformities were highlighted by the flow modelling results (Chapter 7):

1) Crossflow velocities are lowest near the upstream baffle face and gradually increase to a maximum near the downstream baffle face.

2) Crossflow velocities are higher near the shell centre-line than near the shell wall (within the bundle). This effect arises from the motion towards the centre-line imparted to the fluid in turning through the window region.

3) Crossflow velocities are generally higher in the inlet to an overlap region (away from the separated zone) than at outlet from it.

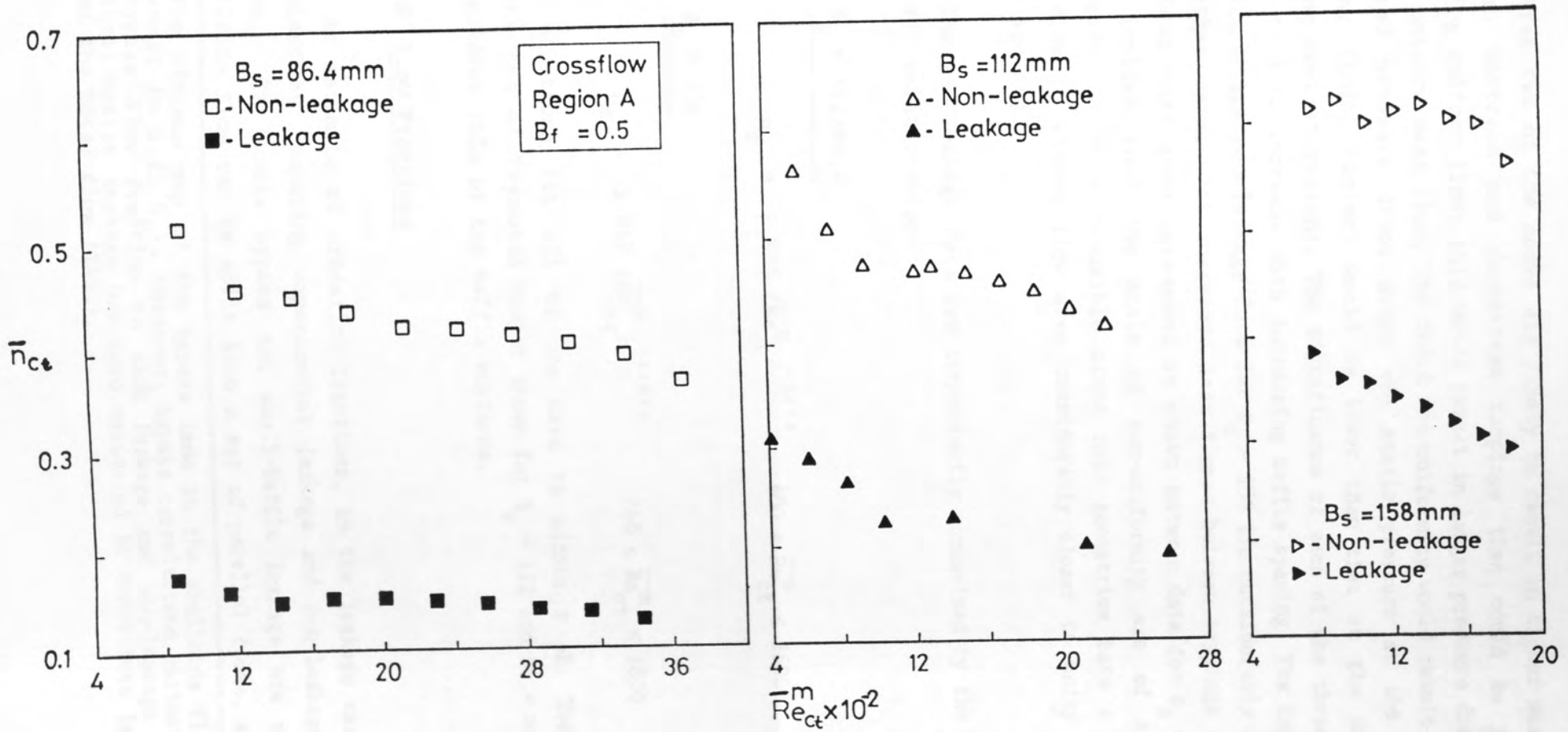

Figure 9.2: Comparisons of Leakage and Non– Leakage Pressure Drops. Data Obtained Over Region A at B_f=0.5.

The first two of the above are likely to result in higher mass fluxes between upstream and downstream tappings than could be predicted assuming uniform flow; this would result in larger pressure drops for a given uniform mass flux. The third non-uniformity would result in lower measured pressure drops since the static pressure at the upstream tapping (inlet region) would be lower than that at the downstream tapping (outlet region). The significance of each of the three effects would tend to increase with increasing baffle spacing. The implication is, since the non-leakage data for B_s = 158 lie considerably above the two other sets, that increased mass fluxes between tappings controls. The fact that good agreement is shown between data for B_s = 112 and 86.4 implies that the scale of non-uniformity are of a similar magnitude. This is plausible since both geometries have a ratio of crossflow to window flow area considerably closer to unity than the large spacing.

The non-leakage data are conveniently summarised by the following best fit relationships:

$B_s = 112/86.4$

$$n_c = 1.835\ (\overline{Re}^m_{ct})^{-0.19} \qquad 400 \leq \overline{Re}^m_{ct} \leq 3600 \qquad (9.3)$$

$B_s = 158$

$$n_c = 1.017\ (\overline{Re}^m_{ct})^{-0.074} \qquad 760 \leq \overline{Re}^m_{ct} \leq 1800 \qquad (9.4)$$

Both equations fit all of the data to within ± 4%. The stronger dependence of Reynolds number shown for B_s = 112 and 86.4 may reflect the greater role of the baffle surfaces.

9.2.2 Flow Fractions

An estimate of crossflow fractions, in the leakage case, can be obtained by comparing experimental leakage and non-leakage pressure drops. If bundle bypass and shell-baffle leakage are neglected*, shellside flow can be split into a set of parallel flows, as shown in

* The minimum gap of the bypass lane in the shellside flow rig was small (= 0.25 D_o). Moreover, bypass correlations estimate the same bypass flow fraction in each leakage and non-leakage situation. Shell-baffle leakage has been estimated to constitute less than 2% of the total flow (TASC).

Figure 9.3. Within this representation the leakage flow in the crossflow and window region (ℓo and ℓw) each occur twice within a baffle space. Using $x_{\ell o}$, $x_{\ell w}$ and x_c to represent the flow fractions, the following relationship is obtained:

$$2\,(x_{\ell o} + x_{\ell w}) + x_c = 1 \qquad (9.5)$$

Assuming further that the overlap region leakage falls off uniformly towards the baffle tip, the total crossflow fraction within the overlap remains uniform at $(x_{\ell o}+x_c)$. Therefore, the difference in crossflow fraction between leakage and non-leakage arrangements is $(x_{\ell o}+2x_{\ell w})$, which is reflected by the difference in Reynolds numbers at a given pressure drop. The method used to estimate crossflow fractions from the experimental measurements is given, along with a sample calculation, in Appendix I. The resulting crossflow fractions are shown in Table 9.2 and compared with those derived from the results of FLOW3D (for the highest Reynolds number in each case, using Table 7.1).

Table 9.2: Derived Crossflow Fractions Compared with those Predicted by FLOW3D

Baffle Spacing (mm)	Reynolds No. $\overline{Re}^m_{ct}$	Crossflow Fraction, x_c	
		Derived	Predicted
86.4	3427	0.53	0.47
	3142	0.54	
	2856	0.55	
	2571	0.56	
	2285	0.55	
	1999	0.55	
	1714	0.54	
	1428	0.52	
	1143	0.53	
112	2582	0.67	0.61
	2129	0.64	
	1398	0.66	
	1024	0.64	
	819	0.69	
158	1829	0.69	0.68
	1677	0.70	
	1524	0.71	
	1372	0.72	
	1219	0.73	
	1067	0.74	
	914	0.74	
	762	0.76	

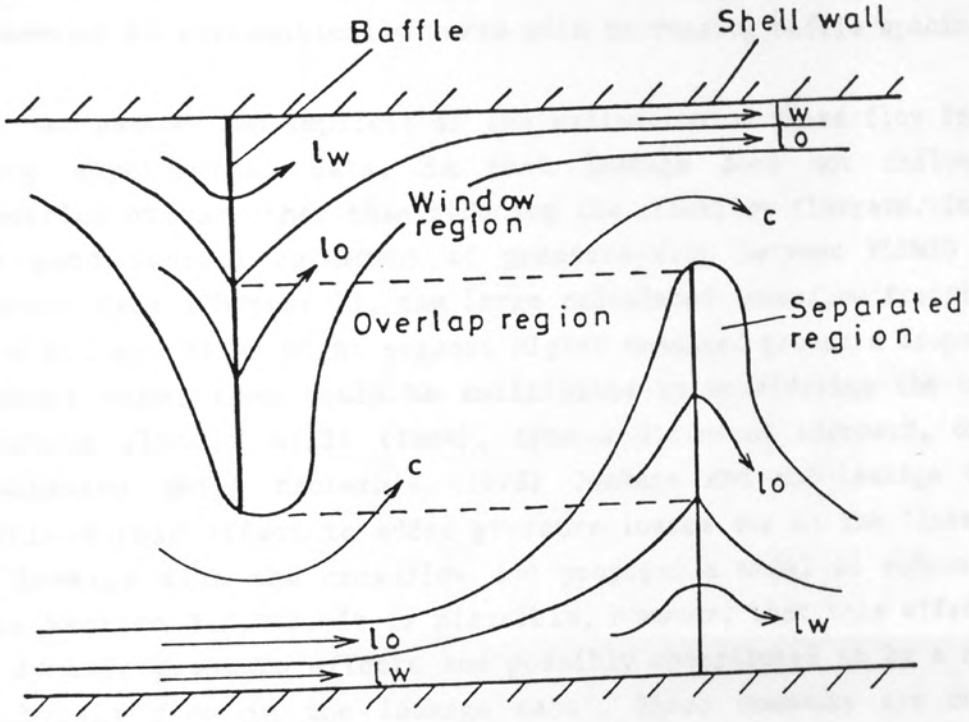

x_{lw} - Leakage in the window

x_{lo} - Leakage in the overlap

$x_{lo} + x_c$ - Crossflow

$x_{lw} + x_{lo} + x_c$ - Window flow

Figure 9.3: Two Dimensional Representation of Single-Phase Shellside Flow.

The crossflow flow fractions calculation for B_s = 158 increases with decreasing Reynolds number which suggests a gradual decrease of leakage. The flow fractions for B_s = 112 and 86.4 show no systematic tendency to increase or decrease with Reynolds number.

Closest agreement between calculated (current data) and predicted (FLOW3D) flow fractions occur at the largest baffle spacing. The agreement is systematically worse with decreasing baffle spacing.

An assumption implicit in the estimation of these flow fractions, using experimental data, is that leakage does not influence the crossflow stream other than reducing the crossflow flowrate. In view of the good overall agreement of pressure drop between FLOW3D and the current data (Chapter 7), the large calculated crossflow fractions (for B_s = 112 and 86.4) might suggest higher measured pressure drops, in the leakage case, than could be anticipated by considering the crossflow flowrate alone. Wills (1984), from a different approach, drew this conclusion using Macbeth's (1973) leakage and non-leakage data. He ascribed this effect to added pressure losses due to the 'interaction' of leakage with the crossflow and proposed a model to account for it (see Section 2.7.1). It is plausible, however, that this effect is due to dynamic pressure effects and possibly contributed to by a reduction of bypass flow in the leakage case*. These comments are considered further in Section 9.5.3, in which Wills' analysis is applied to the current data.

Clearly, some oversimplification in the assumptions leading to the two-dimensional representation of shellside flow cannot be discounted, although the flow visualisation results appears to support its general form.

9.2.3 Periodicity of the Flow

So far, crossflow pressure drop data have been presented for one compartment only (Figure 9.2). These refer to space 3, 4 and 5 for the large, medium and small baffle spacings respectively (see Figure 4.5b) However, measurements were also obtained in the next downstream compartment for each baffle spacing studied (4, 5 and 6 respectively).

* The evidence suggests that bypass flow fractions are small and it is, therefore, unlikely that this could be the primary cause of the effect shown.

For the medium and small spacings, measurements (leakage and non-leakage) in consecutive compartments were generally within 3% of each other, suggesting fully developed periodic flow. However, crossflow data for the large spacings differed considerably between consecutive compartments.

Leakage and non-leakage data, for B_s = 158, obtained across region B are compared in Figure 9.4 for both upflow and downflow (space 3 and 4).

Both leakage and non-leakage data in the downflow compartment are significantly lower than in the upflow. This discrepancy is most apparent for the leakage case; these downflow data lie between 40% (high $\overline{Re}^m_{ct}$) and 55% (low $\overline{Re}^m_{ct}$) below the upflow data.

Crossflow fractions have been derived for the downflow data using the method described in Appendix I and are shown in Table 9.3. These values are considerably lower than calculated for upflow (Table 9.2).

Table 9.3: Derived Crossflow Fraction for Downflow Compartment in the Large Baffle Spacing

Reynolds number $\overline{Re}^m_{ct}$	Derived crossflow fraction x_c
1789	0.59
1640	0.60
1491	0.60
1342	0.60
1193	0.60
1043	0.60
895	0.59
745	0.57

Moreover, they are lower than those derived for the medium baffle spacing, suggesting larger leakage flow fractions which is contrary to expectations. This anomaly is thought to be due to outlet end-space effects which can be illustrated by plotting crossflow pressure drop measurements for each compartment over the length of the 'exchanger'. Measurements of this type were only obtained for the medium baffle spacing, with baffle leakage present, but are adequate to illustrate the end-space effect. Crossflow pressure measurements, from each baffle compartment, are shown in Figure 9.5 and relate to region B, mid-way between baffles.

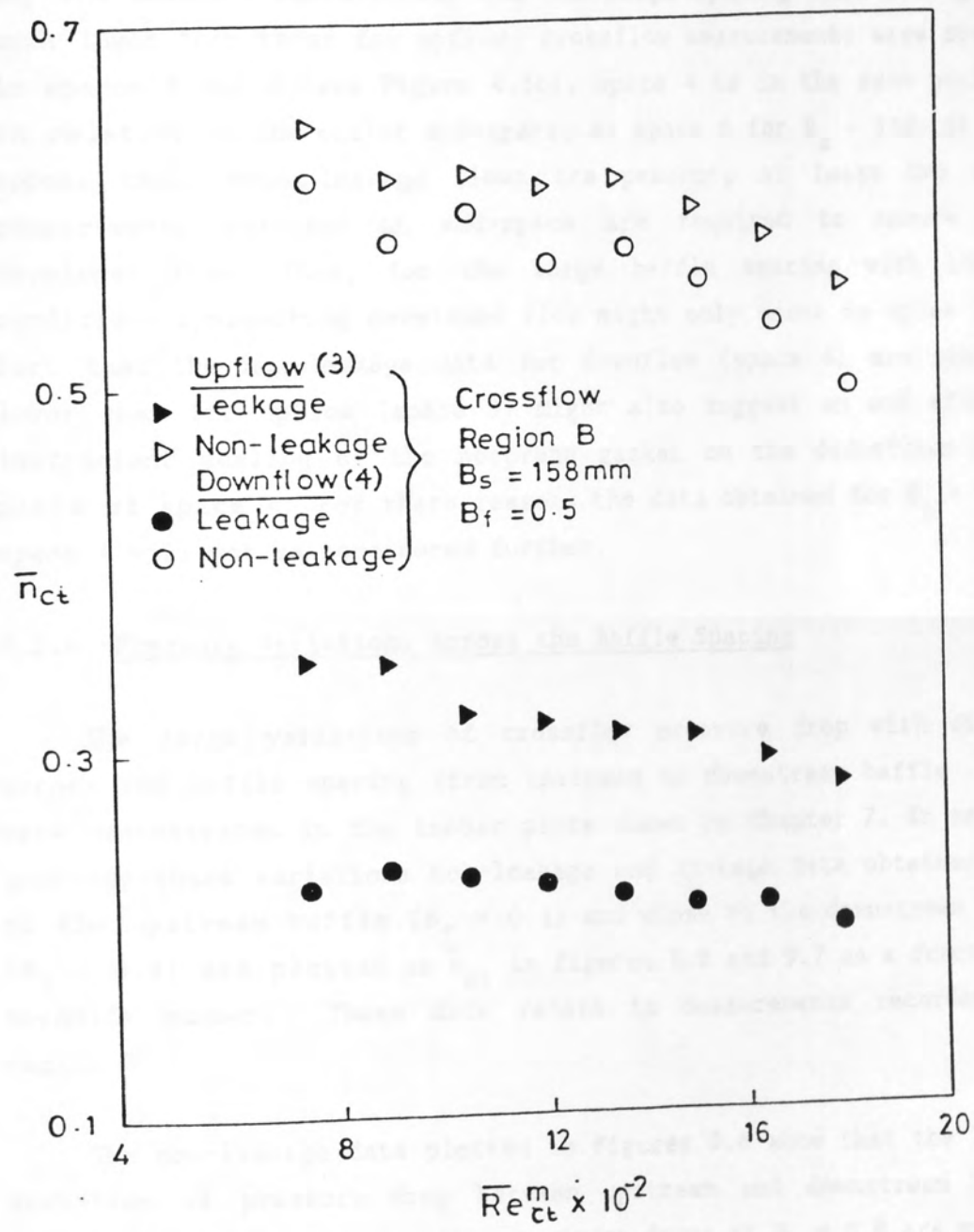

Figure 9.4: Comparison Between Crossflow Pressure Drops Obtained in Consecutive Compartments(3 and 4). Data Obtained Over Region B at B_f=0.5.

Largest pressure drops occur in the central compartments 3, 4 and 5, lowest pressure drops occur in compartments 2 and 6 with intermediate values shown in 1 and 7. The physical reasoning behind such effects are not fully understood but are thought to be a consequence of the comparatively large end-space. However, these features clearly show why the downflow measurements for the large spacing with leakage were much lower than those for upflow: crossflow measurements were obtained in spaces 3 and 4 (see Figure 4.5b), space 4 is in the same position, in relation to the outlet end-space, as space 6 for B_s = 112. It would appear that, when leakage flows are present, at least two baffle compartments and and an end-space are required to ensure fully developed flow. Thus, for the large baffle spacing with leakage, conditions approaching developed flow might only occur in space 3. The fact that the non-leakage data for downflow (space 4) are similarly lower than for upflow (space 3) might also suggest an end effect or inefficient sealing of the neoprene gasket on the downstream baffle plate of space 4. For these reasons the data obtained for B_s = 158 in space 4 will not be considered further.

9.2.4 Pressure Variations Across the Baffle Spacing

The large variations of crossflow pressure drop with distance across the baffle spacing (from upstream to downstream baffle faces) were demonstrated in the isobar plots shown in Chapter 7. In order to quantify these variations non-leakage and leakage data obtained close to the upstream baffle (B_f = 0.1) and close to the downstream baffle (B_f = 0.9) are plotted as $\overline{n}_{ct}$ in Figures 9.6 and 9.7 as a function of Reynolds number. These data relate to measurements recorded over region B.

The non-leakage data plotted in Figures 9.6 show that the largest variation of pressure drop between upstream and downstream baffles occurs at the largest spacing; pressure drops at B_f = 0.9 are approximately 160% higher than at B_f = 0.1, clearly demonstrating the extreme crossflow velocity variations. The equivalent values for B_s = 112 and 86.4 are 57% and 43% respectively, suggesting a considerably more uniform flow distribution.

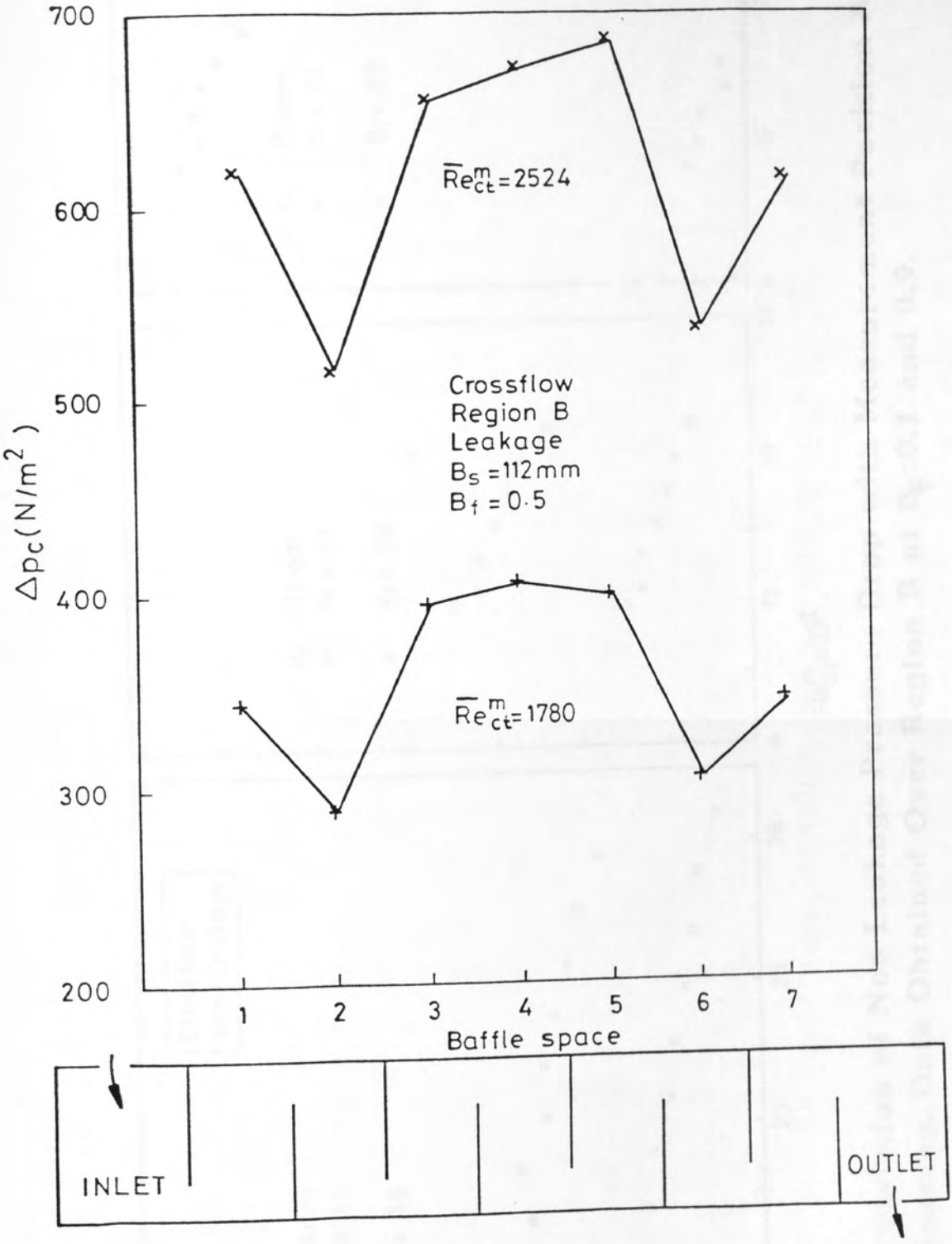

Figure 9.5: Variation of Crossflow Pressure Drops with Baffle Compartment. Data Obtained with Leakage Over Region B at B_f=0.5.

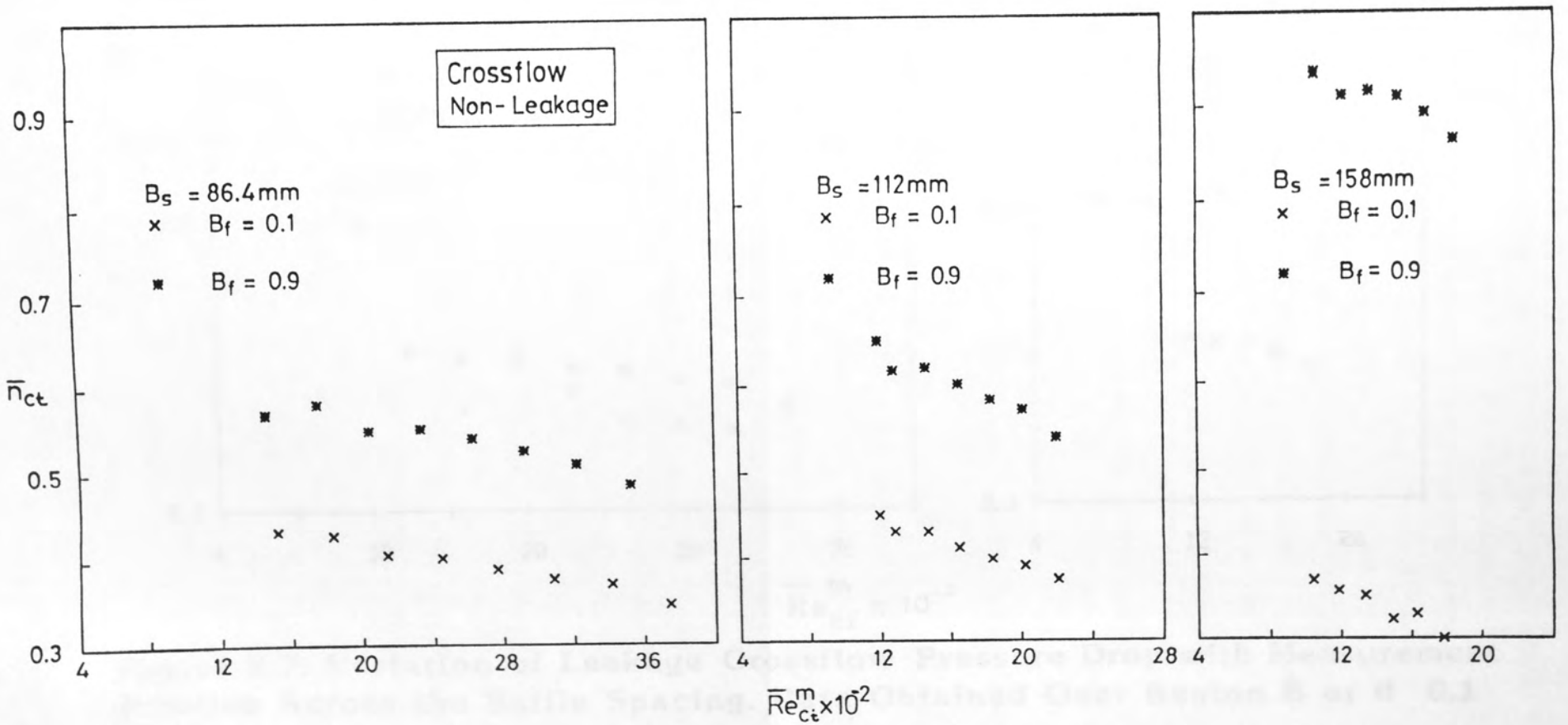

Figure 9.6: Variation of Non-Leakage Pressure Drop with Measurement Position Across the Baffle Spacing. Data Obtained Over Region B at B_f=0.1 and 0.9.

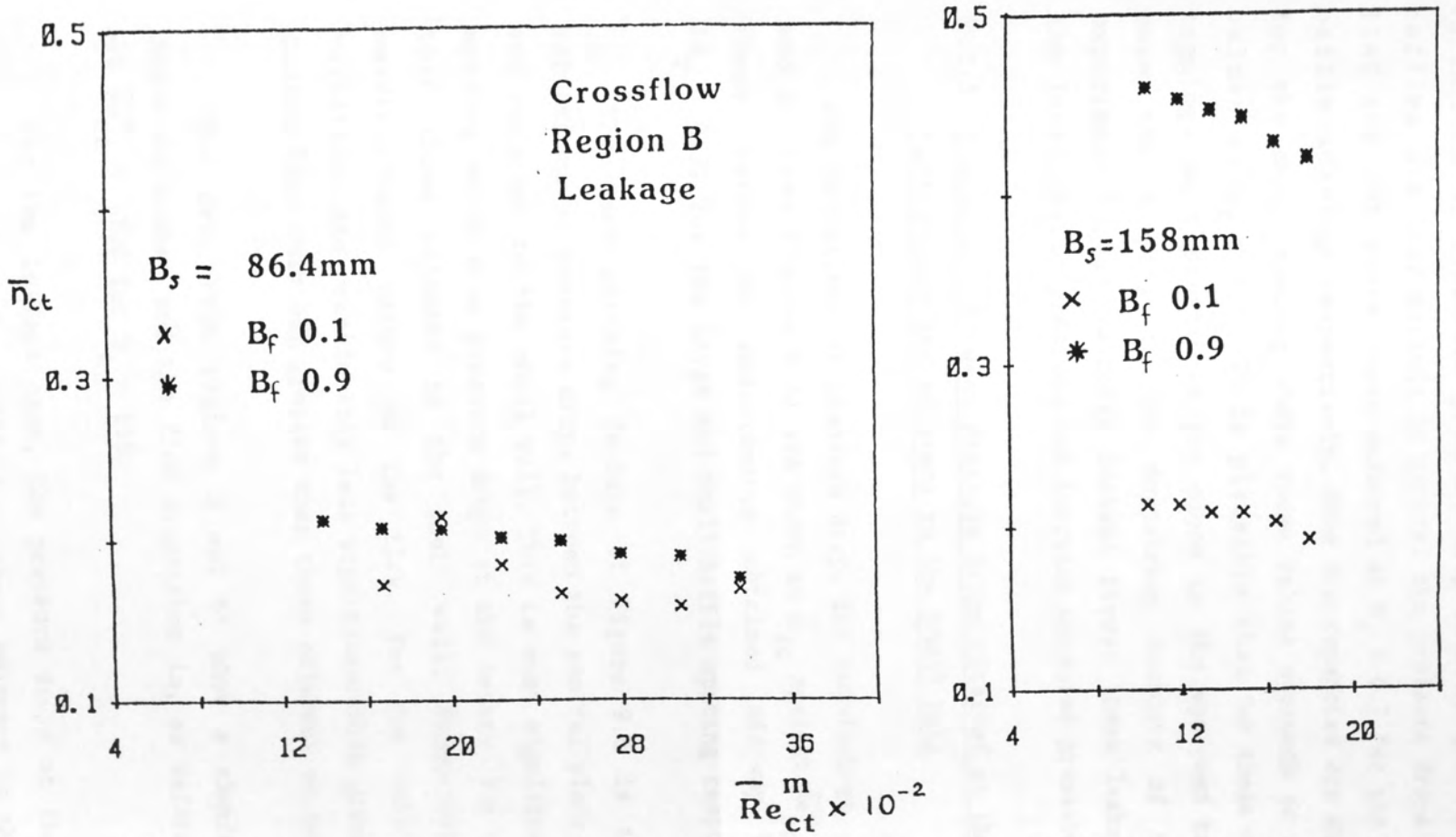

Figure 9.7: Variation of Leakage Crossflow Pressure Drop with Measurement Position Across the Baffle Spacing. Data Obtained Over Region B at B 0.1 and 0.9.

The leakage data presented in Figures 9.7 (insufficient data for B_s = 112) show similar features to the non-leakage case. However, the variations of crossflow pressure drop between upstream and downstream baffles are less marked; in general the pressure drops at B_f = 0.9 are 114% and 20% above those measured at B_f = 0.1 for the large and small baffle spacings respectively. Some discrepancies are shown at B_f = 0.1 for the small spacing where these values approach or even exceed the values at B_f = 0.9. It is plausible that for these measurements the tappings were positioned too close to the upstream baffle, in which case the tapping at the downstream boundary of region B would experience higher velocity leakage flows; these leakage flows reduce the local static pressure and increase measured pressure drops.

9.2.5 Comparison Between Pressure Drops Obtained at the Shell Centre-Line and Adjacent to the Shell Wall

The variations of pressure drop, for non-leakage, across regions B and B' (see Figure 9.1) are shown as $\bar{n}_{ct}$ against $\overline{Re}^m_{ct}$ in Figures 9.8. These relate to measurements obtained mid-way between baffles (B_f = 0.5) for the large and small baffle spacing respectively.

The most striking feature of Figure 9.8 is the large radial variations of pressure drop, between the central plane of the exchanger and adjacent to the shell wall. This is most significant for the large spacing which show pressure drops at the centre-line to be 200% higher than those adjacent to the shell wall, demonstrating further the maldistributed nature of the flow. For the small spacing, these variations are considerably less significant with pressure drops at the centre-line only 86% greater than those adjacent to the shell wall.

The data from regions B and B' show a similar dependence on Reynolds number and the flow transition is, as before, shown to occur at $\overline{Re}^m_{ct} \simeq 1200$ for B_s = 158.

For the leakage case, the pressure drops at the centre-line are approximately 138% and 65% above those adjacent to the shell wall, for large and small spacings respectively. Again, signifying a moderately more uniform crossflow.

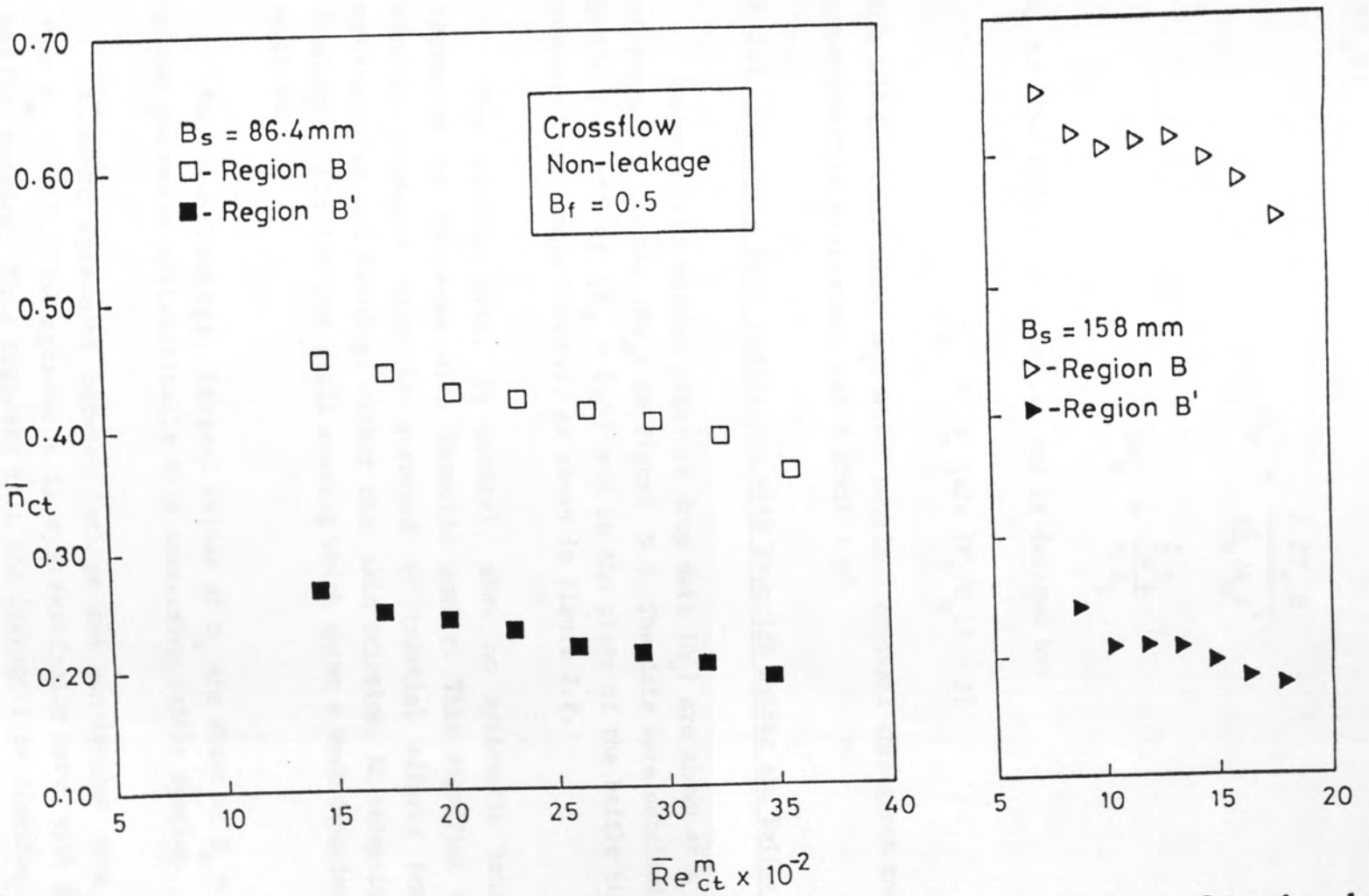

Figure9.8: Comparison of Non-Leakage Crossflow Pressure Drops Obtained in the Bundle Central Plane and Adjacent to the Shell Wall.

9.3 Window Pressure Drop

Window pressure drops are presented, in non-dimensionalised form, as the total number of velocity heads lost (n_w) against Reynolds number (Re_w):

$$n_w = \frac{2\,\Delta P_w\,\rho}{(\dot{M}_w/A_w)^2} \tag{9.6}$$

$$Re_w = \frac{\dot{M}_w D_h}{\eta\, A_w} \tag{9.7}$$

D_h is the hydraulic diameter and is defined by:

$$D_h = D_o\,[4/\pi\,(P_t/D_o)^2 - 1] \tag{9.8}$$

The window flow area, A_w, which remained constant throughout the experimental programme, was 8.22×10^{-3} m^2.

9.3.1 Pressure Drop Variations with Reynolds Number and Baffle Spacing

Normalised window pressure drop data (n_w) are shown as a function of Reynolds number (Re_w) in Figure 9.9. The data were obtained mid-way between baffles (B_f = 0.5) and in the plane of the baffle tips (over consecutive compartments), as shown in Figure 2.8.

The window data, in general, show no systematic tendency to increase or decrease with Reynolds number. This signifies that the window pressure drop is governed by inertial effects (expansion, contraction and turning) rather than skin friction. An exception is the leakage data for the small spacing which shows a weak dependence of n_w with Re_w.

For non-leakage, largest values of n_w are shown at B_s = 86.4 and these decrease systematically with increasing baffle spacing.

Closest agreement between leakage and non-leakage data is shown for B_s = 158. The agreement is systematically worse with decreasing baffle spacing. This suggests that the leakage flow fraction increases with decreasing baffle spacing, as was shown to be the case for crossflow (Section 9.2.1). The leakage data for B_s = 86.4 are up to a factor of 2.5 below those for non-leakage.

The window pressure drop is thought to be governed by a number of interrelated factors such as the velocity in the crossflow and window regions (Bell (1960)), the number of tube rows crossed in the window (Bell (1960) and Moore (1974)) and expansion and contractions in flowing from crossflow through the window region (Wills (1984)) as well as flow non-uniformities and dynamic pressure effects. A simple empirical fit of the data could not hope to account for all the variables in a realistic manner and has, therefore, been ruled out. However, a revised window model is presented in Section 9.5.2, along with a semi-empirical fit to the current window data.

Pressure drop variations across the width and breadth of a baffle space are not presented here since the window data show opposite but complimentary trends to the crossflow data; pressure drops are highest when measured near the upstream baffle space and lowest when measured near the downstream baffle face and so on. This is to be expected since the total baffle space pressure drop is the same from whichever position it is measured over. The current total pressure drops, measured from all possible tappping positions, were, in general, within ±3% of the mean values.

9.3.2 Flow Fractions

An estimate of the window flow fractions, in the leakage cases, can be obtained by comparing leakage and non-leakage data, as discussed in relation to the crossflow measurements. From the two-dimensional representation of shellside flow shown in Figure 9.3, the window flow fraction (x_w) is

$$x_w = x_{\ell w} + x_{\ell o} + x_c \qquad (9.9)$$

where subscripts ℓw, ℓo and c refers to leakage in the window, leakage in the overlap and the crossflow fraction that emerges from the window, respectively.

The values of x_w are reflected by the difference in Reynolds number, between leakage and non-leakage data, at a given pressure drop. The method used to estimate flow fractions is presented in Appendix I.

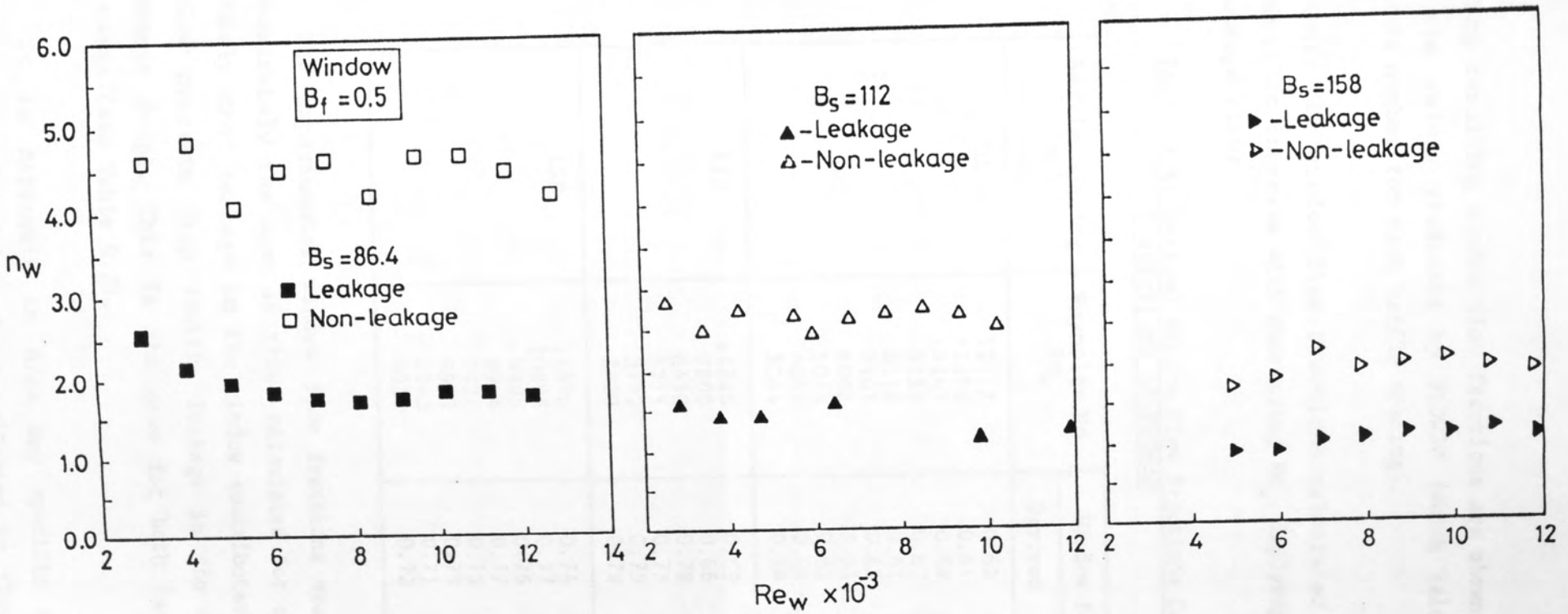

Figure 9.9: Comparison of Leakage and Non-Leakage Window Pressure Drops.

The resulting window flow fractions are shown in Table 9.4 along with the values predicted by FLOW3D (which relate to the largest Reynolds number for each baffle spacing).

Only the window flow fractions calculated for B_s = 112 show a tendency to increase with decreasing Re_w, implying a gradual decrease in leakage flows.

Table 9.4: Derived Window Flow Fractions Compared with Predictions of FLOW3D

Baffle Spacing (mm)	Reynolds No. Re_w	Window Fraction, x_w	
		Derived	Predicted
86.4	12117	0.62	0.59
	11162	0.64	
	10147	0.64	
	9133	0.62	
	8118	0.61	
	7103	0.62	
	6088	0.63	
	5074	0.65	
	4059	0.68	
	3044	0.74	
112	11886	0.69	0.70
	9800	0.66	
	6438	0.78	
	4715	0.75	
	3772	0.75	
	2829	0.79	
158	11886	0.74	0.75
	10895	0.77	
	9905	0.76	
	8914	0.77	
	7924	0.75	
	6933	0.75	
	5942	0.71	
	4952	0.72	

The experimental window flow fractions would be expected to be approximately the same as those calculated for crossflow, since it is unlikely that leakage in the window contributes significantly to the window pressure drop (unlike leakage in the overlap and crossflow pressure drop). This is the case for both large and medium baffle spacings (see Table 9.2).

It is difficult to draw any specific conclusion, since the situation is likely to be complicated by flow non-uniformities and dynamic pressure effects.

9.4 Circumferential Pressure Variations

A limited, but nevertheless informative, set of local static pressure measurements, around the circumference of tubes in the cross-flow region, have been obtained. Pressure measurements were made at 20° intervals (by rotating the instrumented tubes) at three positions across the baffle spacing (B_f = 0.1, 0.5 and 0.9).

The data were normalised using the following relationship (Achenbach (1969)):

$$n_\theta = 1 - \frac{\Delta p_\theta}{\frac{1}{2} \rho \left(\dot{M}_{ct}/A^m_{ct}\right)} \qquad (9.10)$$

where n_θ is the number of velocity heads lost between the forward stagnation point (fsp) and the angle θ around the circumference, Δp_θ is the pressure drop between the fsp and θ. The flow area, A^m_{ct}, is the minimum total crossflow area at the row in which measurements were obtained and $\dot{M}_{ct}$ is the total shellside mass flowrate.

The data reported were obtained from tappings 17, 18, 11 and 12, situated in the fourth baffle compartment (downflow, see Figure 4.5b), using the medium baffle spacing with leakage flows present. Tappings 17 and 11 were situated just within the inlet of a crossflow region, tappings 18 and 12 were situated just within the outlet of a crossflow region (see Figure 4.5a). The measurement were obtained using at total shellside flowrate of 8.25 kg/s and the flow area was $9.438 \times 10^{-3} m^2$ throughout.

These results can be related to the flow patterns presented in Chapter 6.

To aid in the discussion of results the variation of a normalised gap between tubes, y^* $\left(= \frac{y_\theta}{y_{\theta=0}}\right)$, as a function θ is given in Figure 9.10

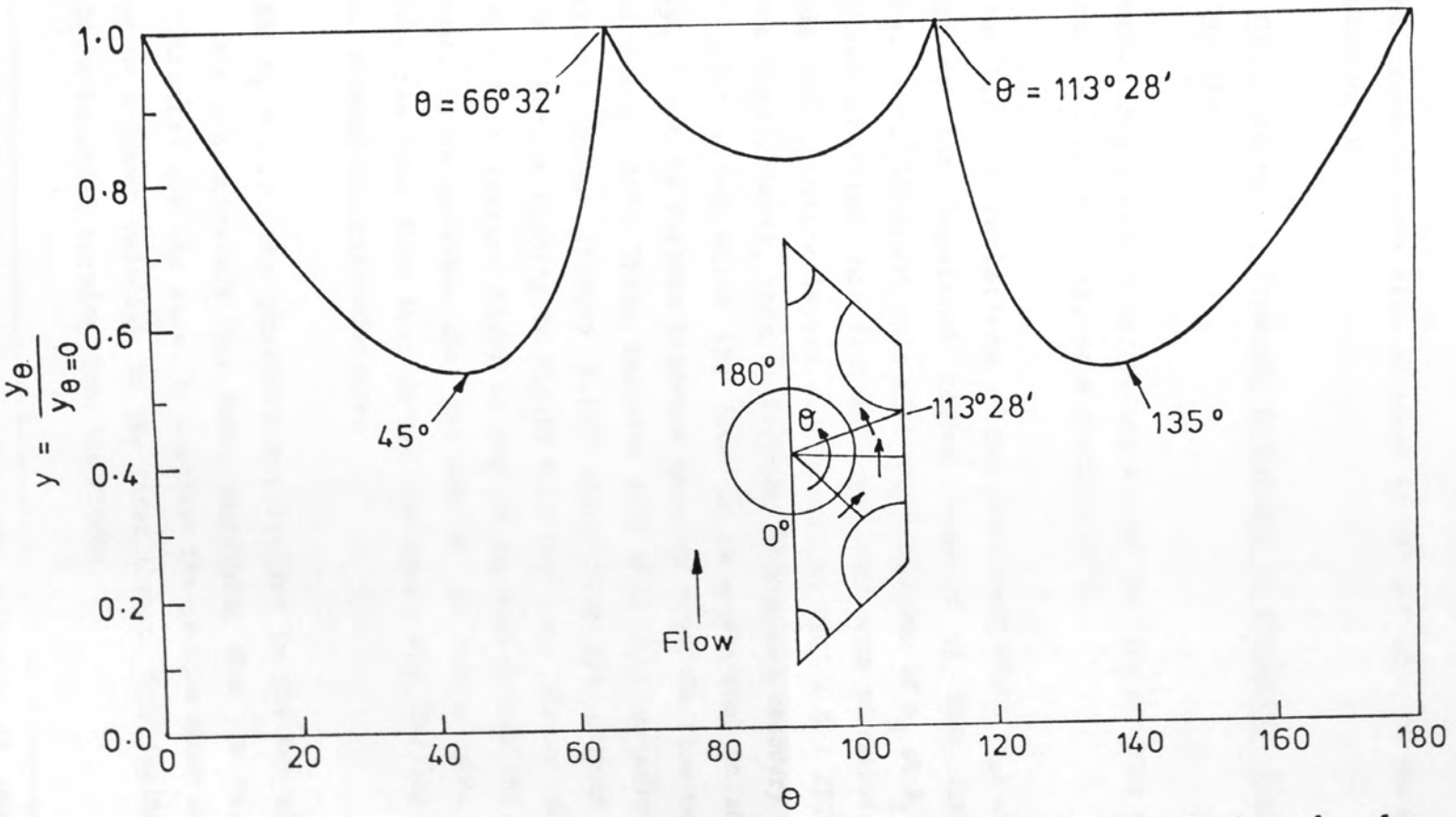

Figure 9.10: Variation of Flow Gap Between Adjacent Tubes in the Bundle as a Function of θ.

A minimum gap, or 'throat', occurs at 45° and 135° and maxima at 0°, 66°32' and 113°28'. These values were obtained assuming that the flow around tubes is always normal to the radii, drawn from the centre of tubes to a given angle.

Measurements were also obtained at 45° and 135°, in the minimum gaps between tubes.

9.4.1 Circumferential Pressure Variations in the Central Plane of the Bundle

Normalised pressure variations around the tube carrying tapping 17 are shown in Figure 9.11a, as a function of θ.

The lack of variations of pressure coefficient (n_θ) at $B_f = 0.1$ illustrates the separated region detected by flow visualisation (Chapter 6)*. Contrast this with the variations of n_θ at $B_f = 0.5$ and 0.9. These profiles show features consistent with crossflow. The flow (outside the boundary layer) accelerates to $160° < \theta < 180°$ (minimum pressure coefficient), this is followed by pressure recovery up to $100° < \theta < 120°$ after which the flow is re-accelerated to about 135°. Finally, there is further pressure recovery until the flow separates at approximately 160°. These features link well with variations of flow gap around tubes (Figure 9.10) apart from the minimum shown at $60° < \theta < 80°$. According to Figure 9.10 the first 'throat' should occur at 45°. This feature might be due to separation from the preceeding tube row. It is possible that the wake at the rear of tubes in one row modifies the free flow area in the subsequent row, forcing the throat further around the circumference.

At $B_f = 0.5$, the pressure coefficient in the two minimum flow areas are approximately the same, signifying that the velocities in both 'throats' are the same. In contrast the profile shown at $B_f = 0.9$ indicates a lower velocity in the first throat. This implies that the main flow is still turning from the window.

---

* Circumferential variations showed the existence of separation for all baffle spacings with both leakage and non-leakage configurations.

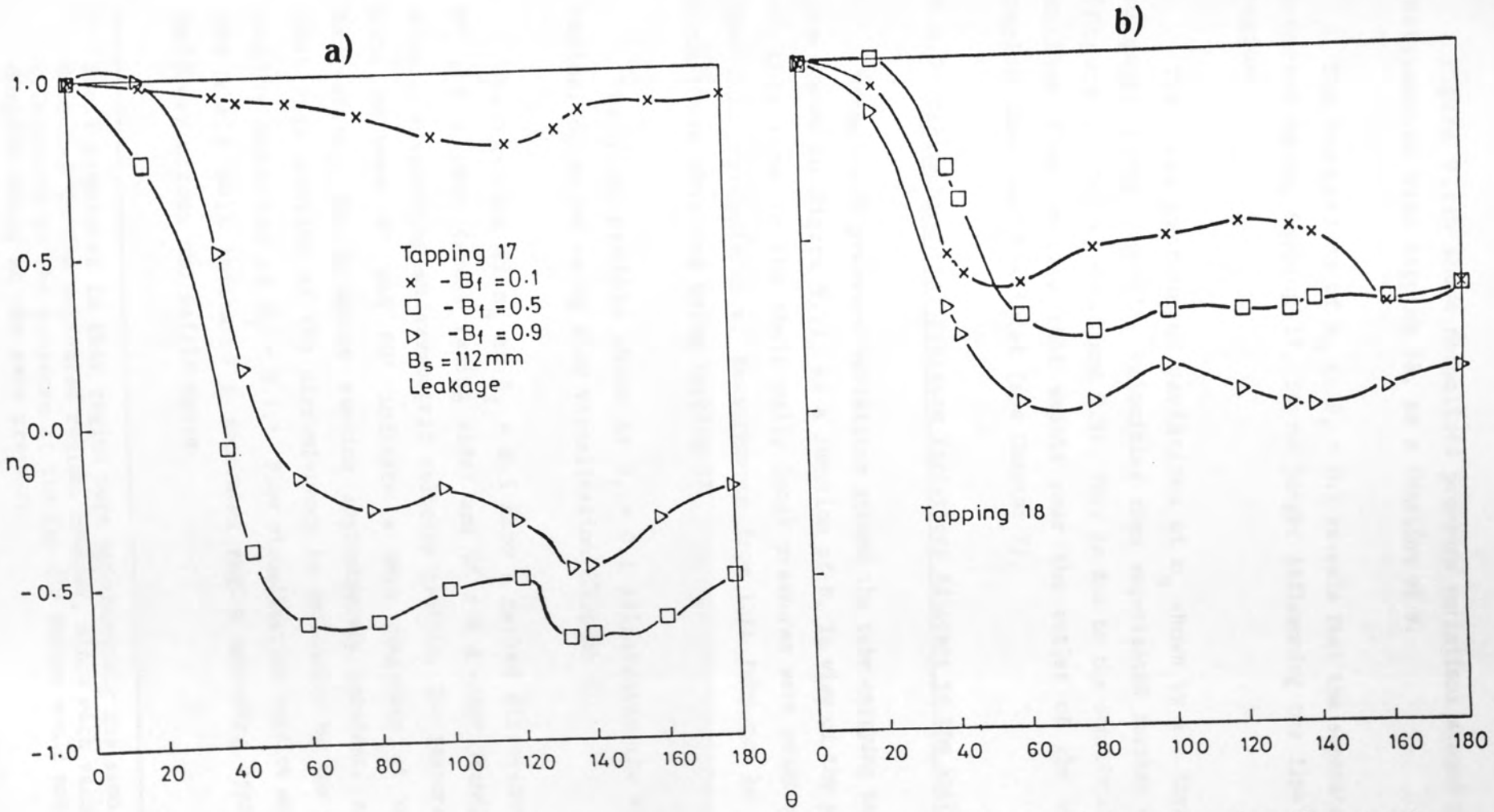

Figure 9.11: Circumferential Pressure Variations About Tubes in the Central Plane of the Bundle, a) Tapping 17, b) Tapping 18.

Figure 9.11b shows normalised pressure variations around the tube instrumented with tapping 18, as a function of θ.

The variations of n_θ at $B_f = 0.1$ reveals that the separated zone, detected using tapping 17, is no longer influencing the flow in this region.

The less pronounced variations of n_θ shown by all three plots suggests lower crossflow velocities than experienced further upstream (Figure 9.11a, $B_f = 0.5$ and 0.9). This is due to the considerably more uniform flow profile that exists near the outlet of the crossflow region than near the inlet (see Chapter 7).

9.4.2 Circumferential Pressure Variations Adjacent to the Shell Wall

Normalised pressure variations around the tube carrying tapping 11 are shown in Figure 9.12, as a function of θ. In view of the proximity of this tube to the shell wall, local pressures were measured around the full circumference. Measurements from this tube can be compared with those obtained using tapping 17.

The flat profile shown at $B_f = 0.1$ illustrates the separated region, detected using flow visualisation (Chapter 6).

Variations of n_θ at $B_f = 0.5$ show a marked difference between $0° \leq \theta \leq 180°$ (shell facing side) and $0° \leq \theta \leq -180°$ (bundle facing side), suggesting an asymmetric velocity profile. The features of the plot between 0° and 60° indicate a weak component of crossflow. Thereafter, the pressure remains approximately constant, suggesting that this section of the circumference is influenced by the separated region detected of $B_f = 0.1$.* Flow visualisation results adjacent to the shell wall indicated a separated region extending approximately half way across the baffle space.

---

* Local pressures in this region were approximately the same as those detected in the separated region. However, since each value of n_θ is referenced to the pressure at the fsp the curves would not coincide despite being at the same pressure.

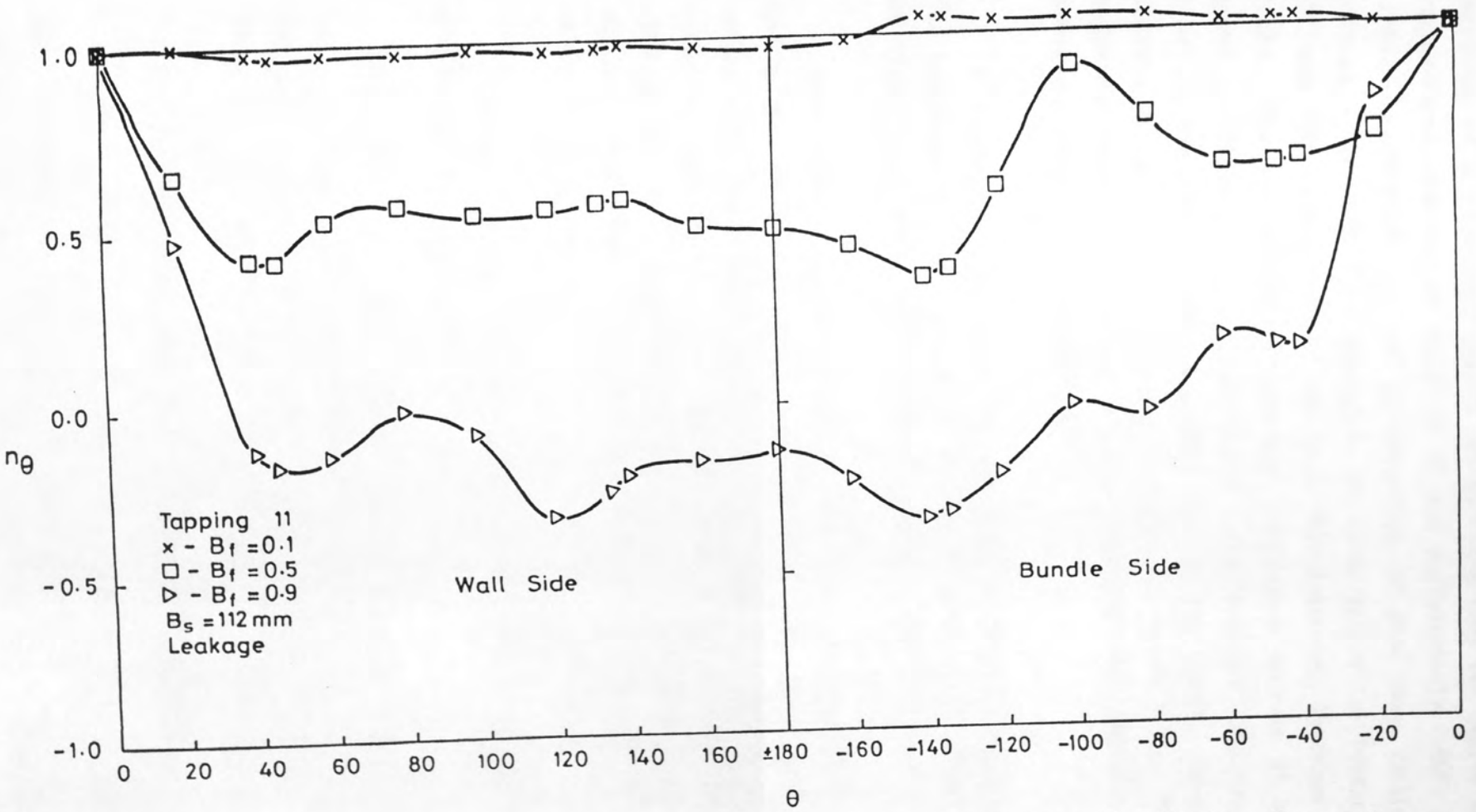

Figure 9.12: Circumferential Pressure Variations About the Tube Carrying Tapping 11, Adjacent to the Shell Wall (Within the Bundle).

The profile between 0° and -180° (bundle facing side) show no features of a separated region (originating from the baffle tip). Flow impingement appears to occur at 0° and approximately -100°. Zukauskus (1981) discovered, in an investigation of flow over in-line square bundles, that the flow impinged, on tubes within the bundle, between 50° and 75° either side of the main flow direction, as shown in Figure 9.13a. The variations of pressure coefficient between 0° and -100°, shown in Figure 9.12, reflect these characteristics, implying that the flow is inclined at approximately 45° to the normal, flowing in the direction of the bypass lane, as shown in Figure 9.13b. The minimum pressure coefficient shown at approximately -50° reflects the wake pressure from the proceeding row.

A comparison between the pressure profiles obtained at $B_f = 0.5$ for tappings 11 and 17 (central plane) illustrates the radial variation of flow, also shown by flow visualisation (Chapter 6).

The variations of pressure coefficient obtained at $B_f = 0.9$ does not show the marked asymmetry observed at $B_f = 0.5$. There are no indications of the separated region (see Chapter 6) nor of flow inclined towards the bypass lane. The features shown by this plot are very similar to those obtained using tapping 17 (Figure 9.11a) and likewise suggest that the flow from the window is still turning into the crossflow region.

Normalised pressure variations around the tube carrying tapping 12 are shown in Figure 9.14.

Each of the three profiles exhibit similar features. The absence of pronounced maxima and minima suggests that the flow in this region is predominantly longitudinal. This concurs with the conclusions drawn from the flow visualisation results presented in Chapter 6.

9.5 Comparisons Between Data and Design Correlations

The purpose of this section is to compare the current experimental measurements with previously obtained data, commonly used design correlations and predictions from modern design methods. Three sets of

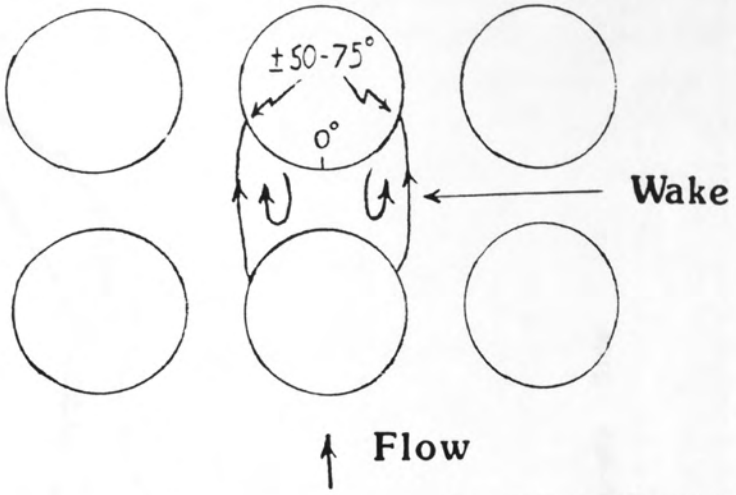

Figure 9.13a: Flow Across In-Line Square Bundles Showing Flow Impingement and Wake at the Rear of Tubes. [after Zukauskus, 1981].

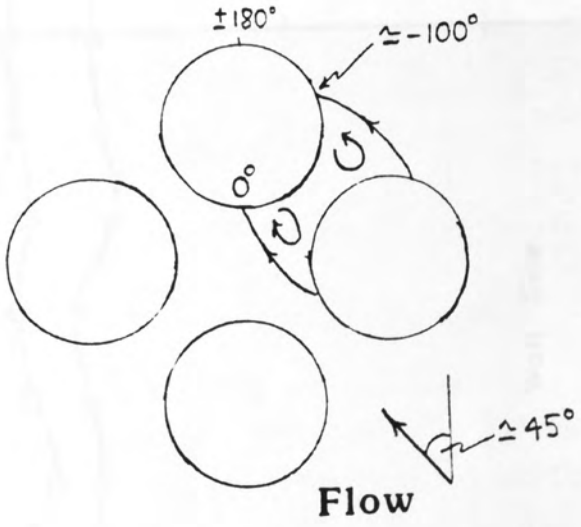

Figure 9.13b: Apparent Flow Direction and Flow Impingement Shown by Circumferential Pressure Variations Using Tapping 11 (Figure 9.12).

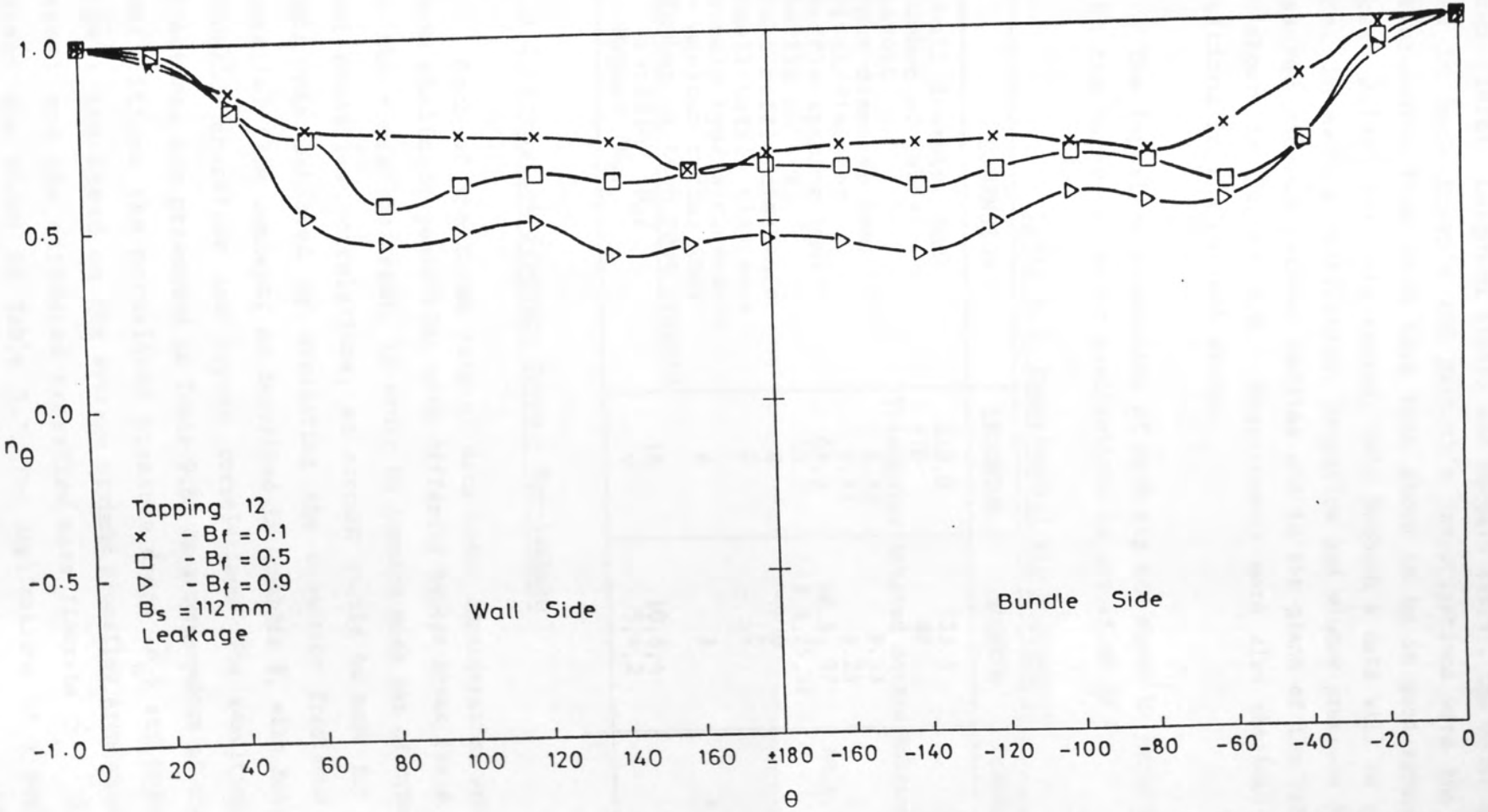

Figure 9.14: Circumferential Pressure Variations About the Tube Carrying Tapping 12 , Adjacent to the Shell Wall (Within the Bundle).

pressure drop data were discovered in the literature which relate to crossflow and window measurements in cylindrical baffled geometries: Brown (1956), Leighton (1955) and Macbeth (1973). The model exchangers used in both Brown's and Macbeth's investigations were the same and measurements from each have been shown to be in good agreement (see Figure 2.19). For this reason, only Macbeth's data will be considered here. In each investigation, crossflow and window pressure drops were measured mid-way between baffles and in the plane of the baffle tips, as shown in Figure 2.8. Measurements were also obtained at these positions in the current study.

The important dimensions of each rig are shown in Table 9.5, along with the number of major restrictions to crossflow (N_c).

Table 9.5: Experimental Rig Dimensions

DIMENSION	LEIGHTON	MACBETH	CURRENT WORK
Shell diameter (mm)	212.8	133.5	300
Number of tubes	470	80	270
Layout	Triangular	Rotated square	Rotated square
Tube diameter (mm)	6.35	9.53	12
Pitch/diameter	1.33	1.25	1.25
Baffle spacing (mm)	65.5	48.5, 97	86.4,112,158
Baffle cut (%)	18.7	18.4,25,37.5	25
Tube-baffle clearance	0	0	0
Shell-baffle clearance	0	0	0
Bundle bypass clearance - minimum radial (mm)	6	3	4.5
Number of tube rows crossed			
Crossflow (N_c)	18	10,8,4	14
Bypass (N_b)	9	5,4,2	7

9.5.1 Crossflow Pressure Drops - Non-leakage

Each of the three sets of data under consideration were obtained from shellside geometries with differing bypass areas (as a proportion of the crossflow area). In order to compare each set of crossflow data and crossflow correlations, an account should be made for bypassing. This was achieved by evaluating the crossflow fractions using the parallel flow concept, as described in Appendix F, with Moore's (1974) 'ideal' crossflow and bypass correlations. The resulting crossflow fractions are presented in Table 9.6. As a consequence of these revised definitions the normalised pressure drops ($\bar{n}_c$) and Reynolds number ($\overline{Re}_c^m$) are based on the average minimum crossflow area only (no bypass area) and the estimated crossflow mass flowrate ($\dot{M}_c$). The crossflow areas are shown in Table 9.7. The implications of a possible over-prediction of bypass flow fractions using ideal relationships is discussed.

Table 9.6: Crossflow Fraction Estimated Using the Parallel Flow Concept and the Correlations of Moore (1974)

Baffle Cut (-)	Baffle Spacing (mm)	Crossflow Fraction of the Total Flowrate
Leighton (1955)		
0.187	65.5	0.67
Macbeth (1973)		
0.184	48.5	0.85
0.184	97.0	0.84
0.250	48.5	"
0.250	97.0	"
0.375	48.5	"
0.375	97.0	"
Current Work		
0.25	86.4	0.89
"	84.8	"
"	112.0	"
"	110.4	"
"	158.0	"
"	156.4	"

Table 9.7: Crossflow and Bypass Flow Areas

Geometry		Flow Areas	
Baffle Cut (-)	Baffle Spacing (mm)	Crossflow ($m^2 x 10^3$)	Bypass ($m^2 x 10^3$)
Leighton (1955)			
0.187	65.5	2.767	0.275
Macbeth (1973)			
0.184	48.5	1.589	0.231
"	97.0	3.141	0.462
0.250	48.5	1.647	0.231
"	97.0	3.251	0.462
0.375	48.5	1.729	0.231
"	97.0	3.415	0.462
Current Work			
0.25	86.4	6.861	0.518
"	84.8	6.731	0.509
"	112.0	8.890	0.672
"	110.4	8.766	0.662
"	158.0	12.550	0.948
"	156.4	12.420	0.938

Normalised crossflow pressure drop data are compared with Moore's crossflow correlation* in Figures 9.15a and b, for rotated square layouts (Macbeth and the current work) and triangular layouts (Leighton), respectively.

Both Leighton's and the current data lie significantly above the ideal correlation. Leighton's measurements lie, on average, 28% above the ideal correlations. For the current data, these values are 46% for the large spacing and approximately 13% for the medium and small spacings. It is possible that these features are due to the radial non-uniformity in crossflow velocities discovered in the flow modelling work. This resulted in a higher mass flowrate near the central plane of the bundle (where measurements were obtained) than could be expected assuming uniform flow (see Section 9.2.1).

Macbeth's data, in general, lie significantly below the correlation and these discrepancies are worse for large spacings coupled with small baffle cuts.

Both Leighton's and the current data have a similar Reynolds number dependence to Moore's correlations. In contrast, Macbeth's data exhibit a much stronger Reynolds number dependence and, again, the greatest discrepancy occurs at large baffle spacings.

The low values of Macbeth's data are believed to be due to the presence of a large separated region downstream of the leading baffle tip, in the central plane of the bundle. In such circumstances the area for flow at the crossflow inlet region is reduced considerably below that at the outlet region, as shown in Figure 9.16a. The result is that higher velocities exist in the vicinity of the upstream (inlet) than downstream (outlet) measurement tappings. This asymmetry in the velocity imparts a dynamic component of pressure onto the irrecoverable pressure loss, giving pressure differences less than the true loss. Large separated zones are to be expected when crossflow resistances are relatively small, as was the case in Macbeth's work (Macbeth's rig had many fewer, larger tubes than either Leighton's or the current rig). Moreover, the reduced pressure drop effect would be most pronounced

* Moore's correlation was shown to be at least as good as all others reviewed in Chapter 2. In addition, Moore's correlation accounts for the variation of crossflow area.

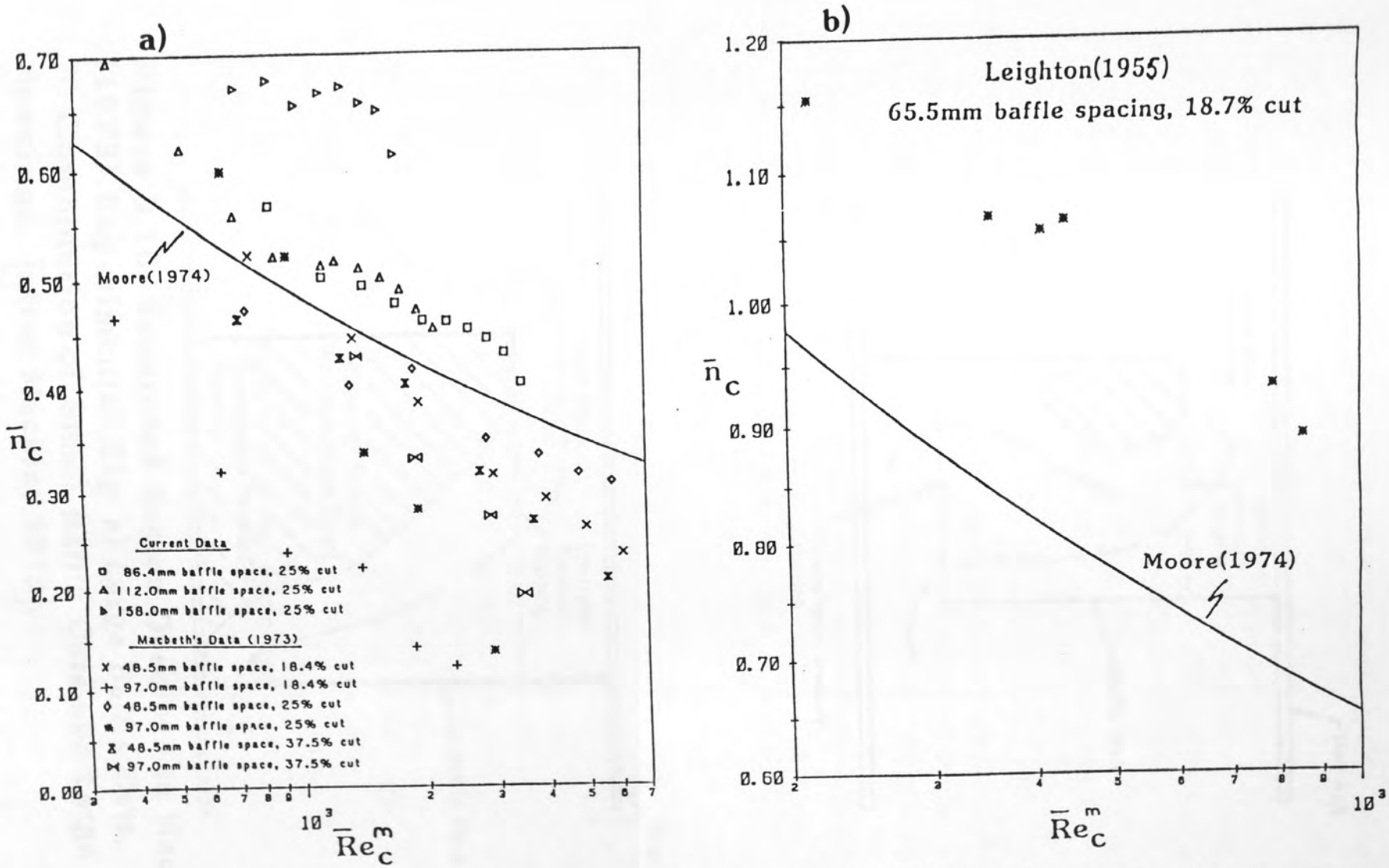

Figure 9.15: Comparison Between Moore's(1974) Crossflow Correlation and Experimental Measurements: a) Macbeth's(1973) and the Current Data, b) Leighton's(1955) Data.

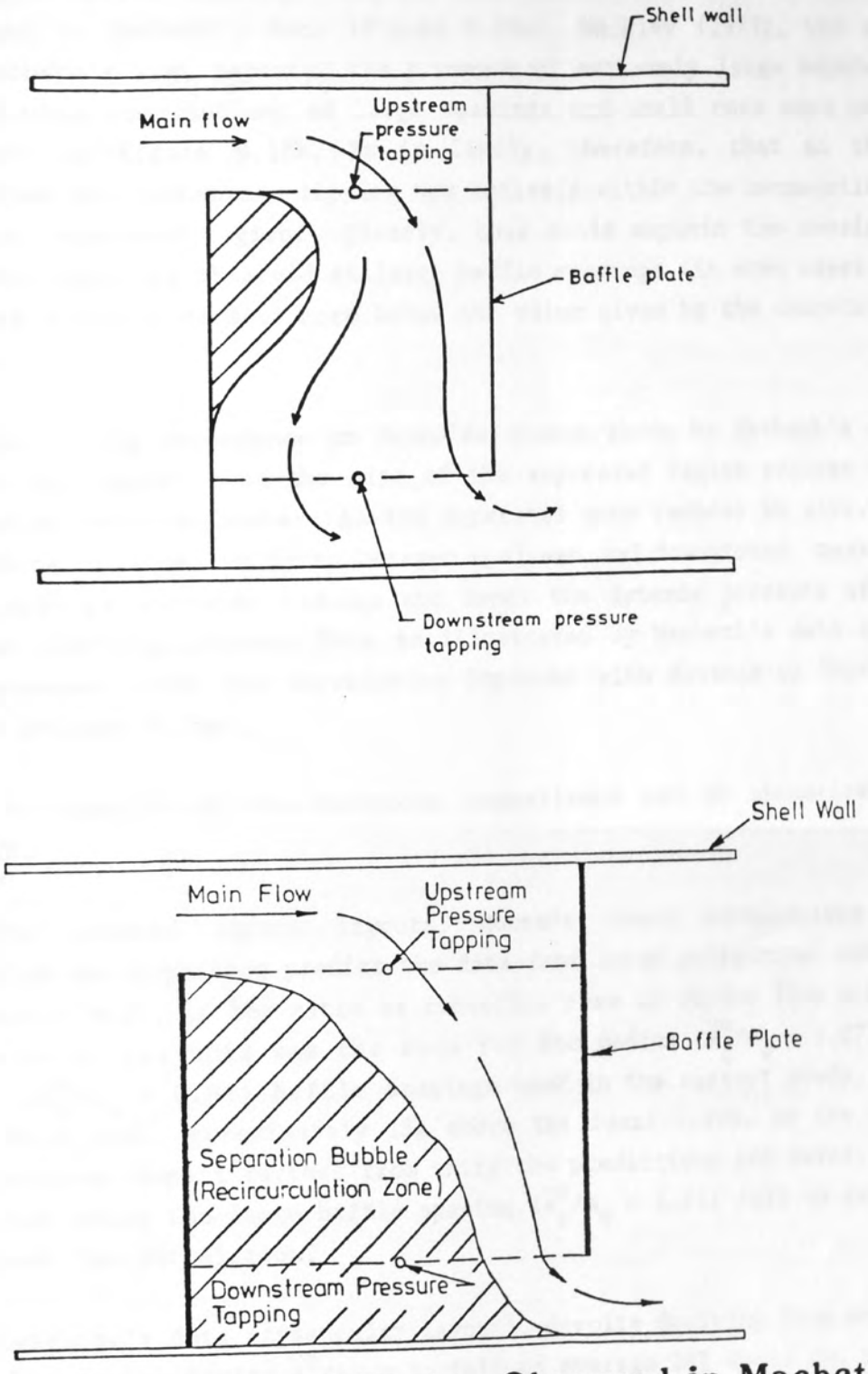

Figure 9.16: Separated Region Observed in Macbeth's (1973) Experimental Rig: a) Large Baffle Cuts, b) Combination of Small Baffle Cuts and Large Baffle Spacings. [after Mackley,1973].

for large baffle spacings coupled with small baffle cuts. This is supported by Macbeth's data (Figure 9.15a). Mackley (1973), who also used Macbeth's rig, reported the presence of extremely large separated regions when combinations of large spacings and small cuts were used, as shown in Figure 9.16b. It is likely, therefore, that in these geometries the downstream tapping was entirely within the comparatively stagnant separated region. Clearly, this could explain the considerable discrepancies observed at large baffle spacings (in some cases the data are a factor of 3 or more below the value given by the correlation).

The strong dependence on Reynolds number shown by Macbeth's data appears to suggest that the size of the separated region reduces with decreasing Reynolds number. As the separated zone reduces in size, the difference in local velocity between upstream and downstream measurement tappings likewise reduces and hence the dynamic pressure effect becomes less significant. This is illustrated by Macbeth's data since the agreement with the correlation improves with decreasing Reynolds number (Figure 9.15a).

The results of the foregoing comparisons can be summarised as follows.

For rotated square layouts, Moore's ideal correlations for crossflow and bypassing predict the data from large cylindrical bundles reasonably well, if the ratio of crossflow area to window flow area is close to unity; this was the case for the medium ($\overline{A}_c^m/A_w = 1.07$) and small ($\overline{A}_c^m/A_w = 0.81$) baffle spacings used in the current study, data from which fell approximately 13% above the ideal curve. As the ratio of flow areas depart further from unity the predictions are worse; data obtained using the large baffle spacing ($\overline{A}_c^m/A_w = 1.51$) fell an average 46% above the correlation.

Leighton's data (triangular layout), despite deriving from experimental geometry having $\overline{A}_c^m/A_w = 1$, fell on average 28% above the correlation.

The results from the small-scale rig of Macbeth, and Brown before him, illustrate large-scale flow non-uniformities not discovered in larger more typical units. These data are, therefore, likely to be misleading. This brings into question the use of small-scale models with comparatively few tubes, which is rather disturbing since most of the cylindrical baffled data derives from such units. This also has

ramifications on heat transfer data, the large bulk of which also derive from small-scale models.

Reducing the degree of bypassing, assuming that the crossflow fractions given in Table 9.6 are underestimated, would not alter significantly the above discussion. For example, if it is assumed that the true bypass flow fraction is half that predicted by Moore's relationship, the following results would be obtained. Macbeth's data would show worse agreement with the correlation. Leighton's data would lie below the correlation but the agreement would be marginally better. For the current measurements, the small and medium baffle spacing data would agree within a few percent of the correlation, but the large spacing data would still lie considerably above (= 28%).

Russell and Wills' (1984) correlation, which is based on Lee's (1981) measurements of bypass flow (see Section 2.1.3), calculates larger bypass fractions than Moore's relationship. These are, for the current geometries, 0.18, 0.21 and 0.25 for the large, medium and small baffle spacings respectively.

9.5.2 Window Pressure Drop - Non-Leakage

The window pressure drop data were normalised using Equations (9.6) and (9.7). The window areas for each of the three experimental rigs (Leighton, Macbeth and the current model) are given in Table 9.8.

Table 9.8: Window Flow Areas

	Baffle Cut (-)	Window Flow Area ($m^2 x 10^3$)
Current Work	0.25	8.220
Leighton (1955)	0.187	2.959
Macbeth (1973)	0.184 0.25 0.375	1.133 1.697 2.882

Normalised window pressure drop data are compared with the correlations of Grant and Murray (1974) and semi-empirical models of Bell (1960) and Wills (1984)* in Figure 9.17 (current data), 9.18 (Leighton's data) and 9.19 (Macbeth's data).

* Wills' model incorporates crossflow frictional losses which are a function of the crossflow distance into the window and the change in crossflow area due to shell curvature. The method used to obtain this component of the window pressure drop is shown in Appendix I.

The overall picture from Figure 9.17, 9.18 and 9.19 is somewhat complicated but some general themes can be discerned.

Bell's semi-empirical model (Equation (2.33)), which is based on Brown's (1956) data, shows the worst agreement with the data. However, very good agreement is shown for two sets of Macbeth's data (Figure 9.19): 48.5 mm baffle spacing, 18% baffle cut and 97 mm baffle spacing, 25% cut. The first of these two geometries was also studied by Brown and so the favourable comparisons could have been anticipated. The second geometry was not studied by Brown and so the agreement appears to be fortuitous.

Grant and Murray's correlation (Equation (2.35)), based on a simple empirical fit to the data of Macbeth and Brown (1956), consistently overpredicts these data, by as much as 60% in some cases (Figure 9.19).

Wills' semi-empirical model shows, in general, good agreement with Macbeth's data. This is to be expected since, although the model is partly theoretical, the detailed choice of terms considered were based on an attempt to fit Macbeth's data. This is demonstrated by the poor agreement with the current measurements, for the medium and small baffle spacings, and Leighton's data.

The current data (Figure 9.17) fall systematically below the design methods. However, the agreement improves with decreasing baffle spacing. Since both Grant and Murray's correlation and Wills' model are based on Macbeth's data, it is likely that this feature is due to the separated zone discussed in relation to Macbeth's crossflow data. The large separated zone observed in his model exchanger (Mackley (1973)) apparently caused measured crossflow pressure drops to be rather lower than the irrecoverable pressure loss. An exactly compensating effect must be present in Macbeth's window measurements, whereby these data exceed the irrecoverable pressure loss (dynamic effects cancel over a complete baffle compartment). Both Grant and Murray's correlation and Wills' model would, therefore, be expected to overpredict the other data. This is seen, in general, to be the case (see Figures 9.17 and 9.18). For the current data the overpredictions range from 0% to 25%,

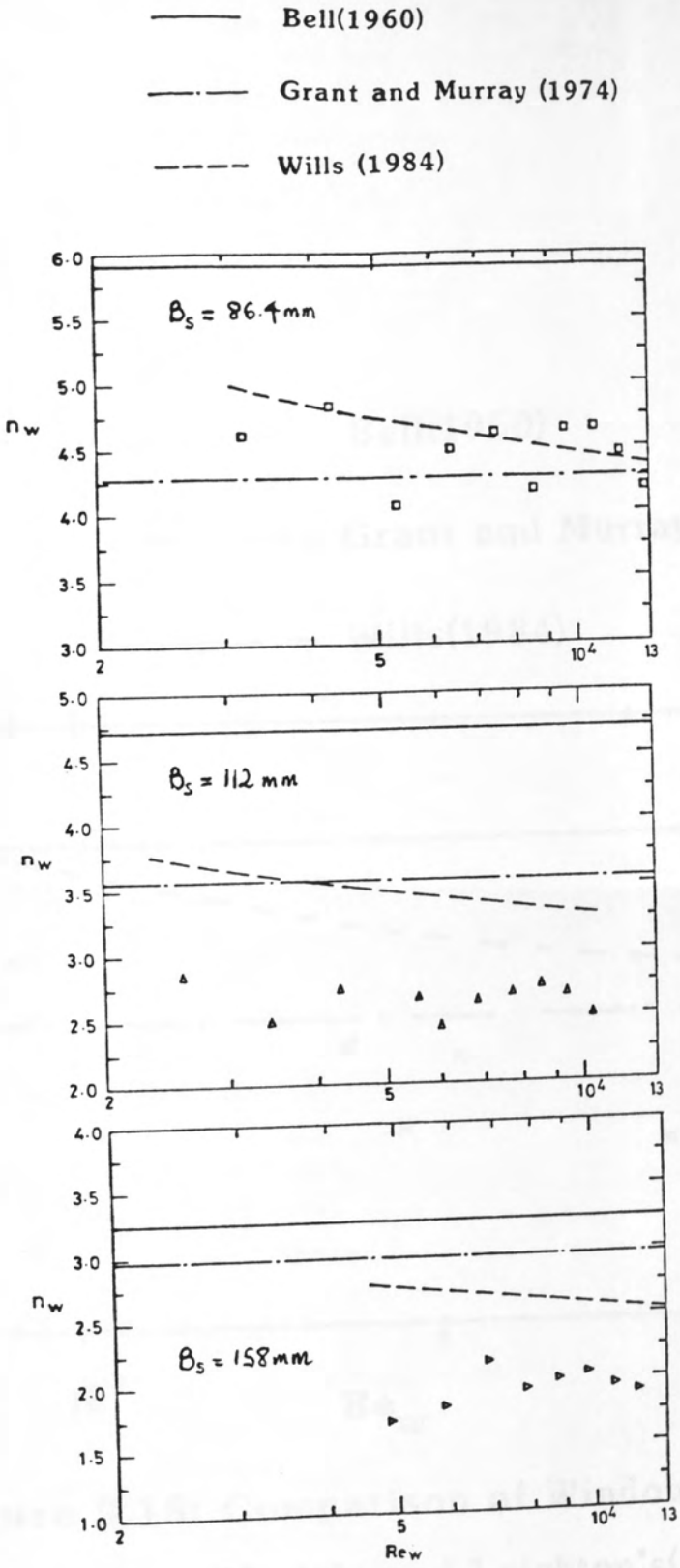

Figure 9.17: Comparison of Window Pressure Drop Correlations/Models and the Current Data.

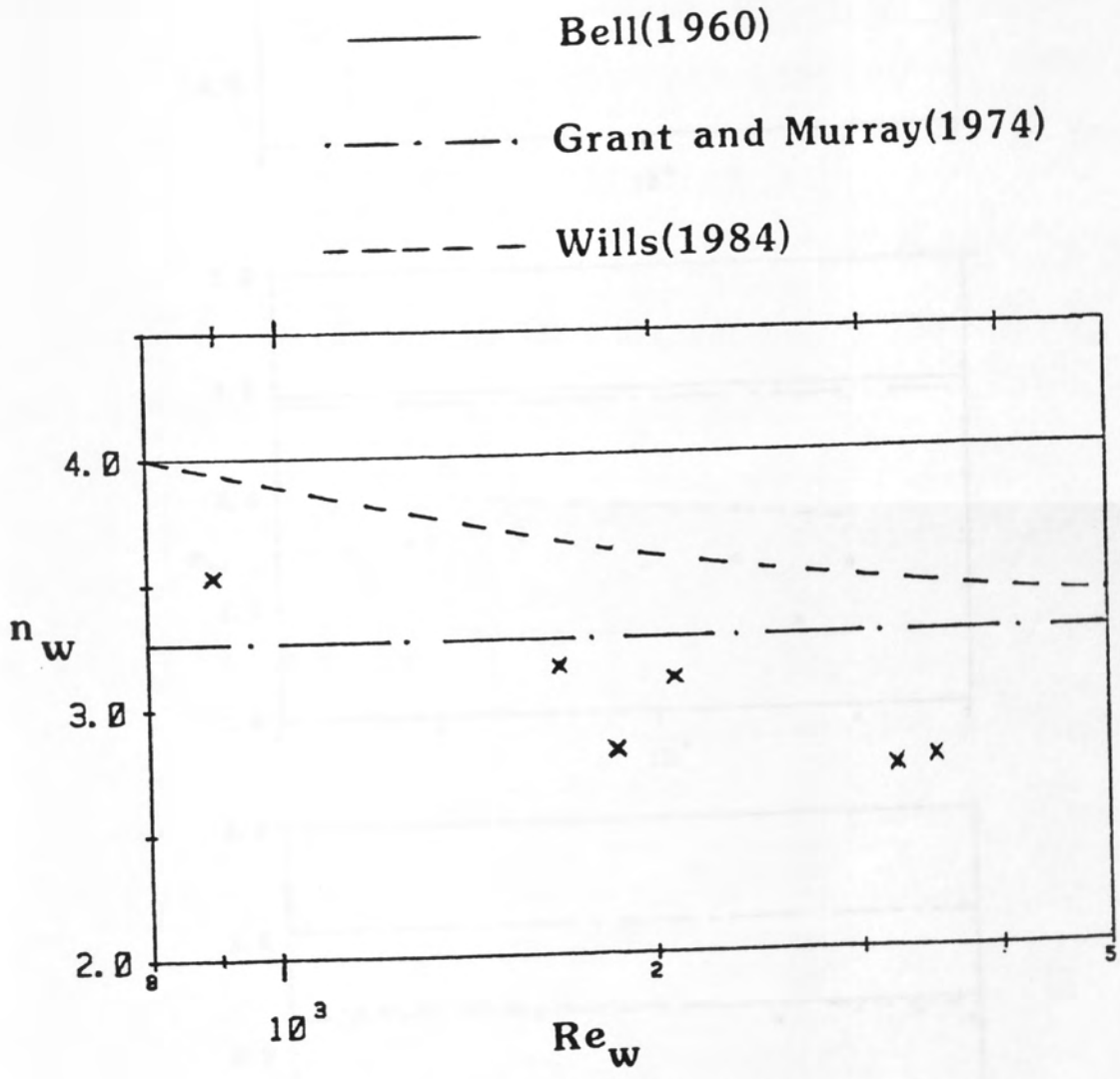

Figure 9.18: Comparison of Window Pressure Drop Correlations/Models and Leighton's(1955) Data.

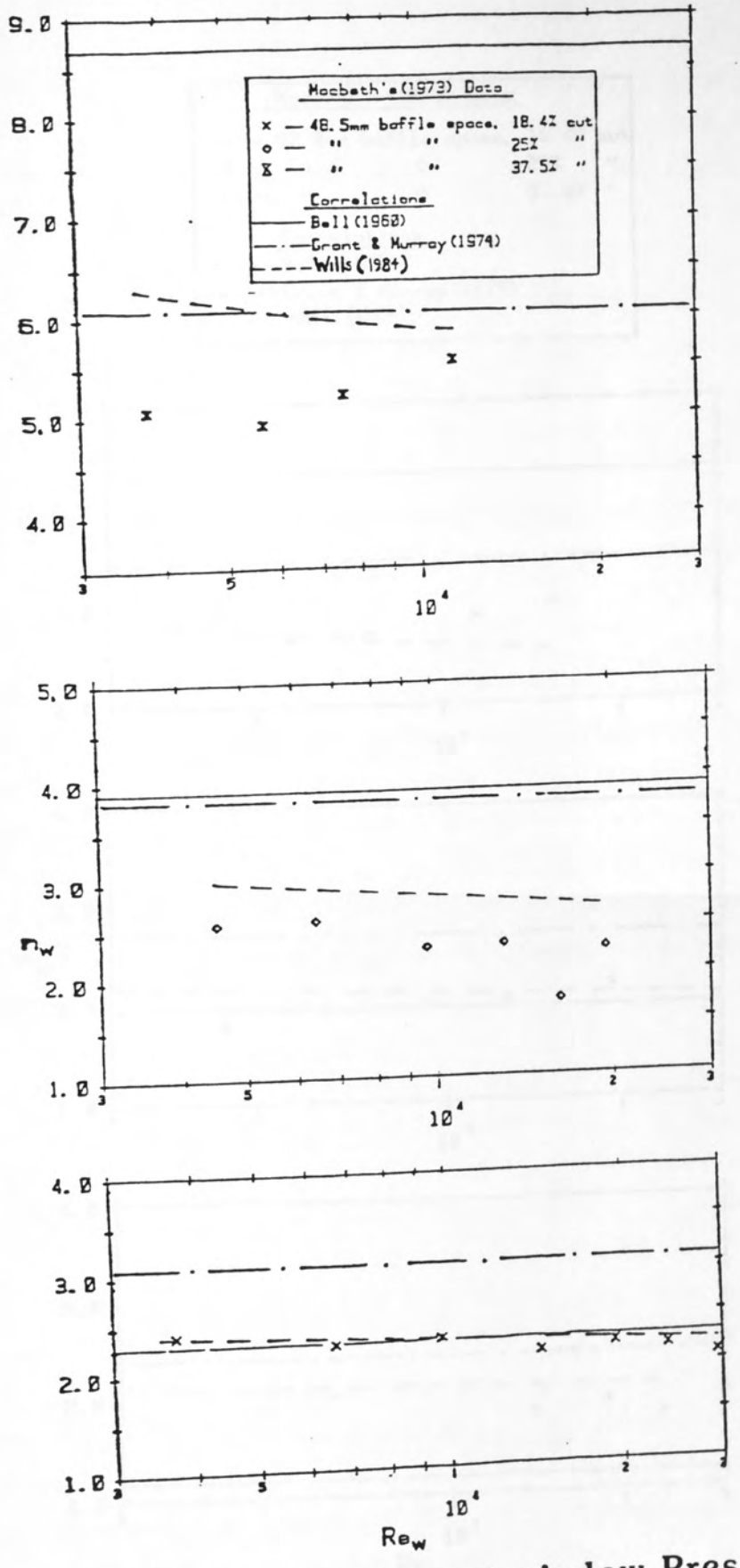

Figure 9.19: Comparison of window Pressure Drop Correlations/Models and Macbeth's(1973) Data.

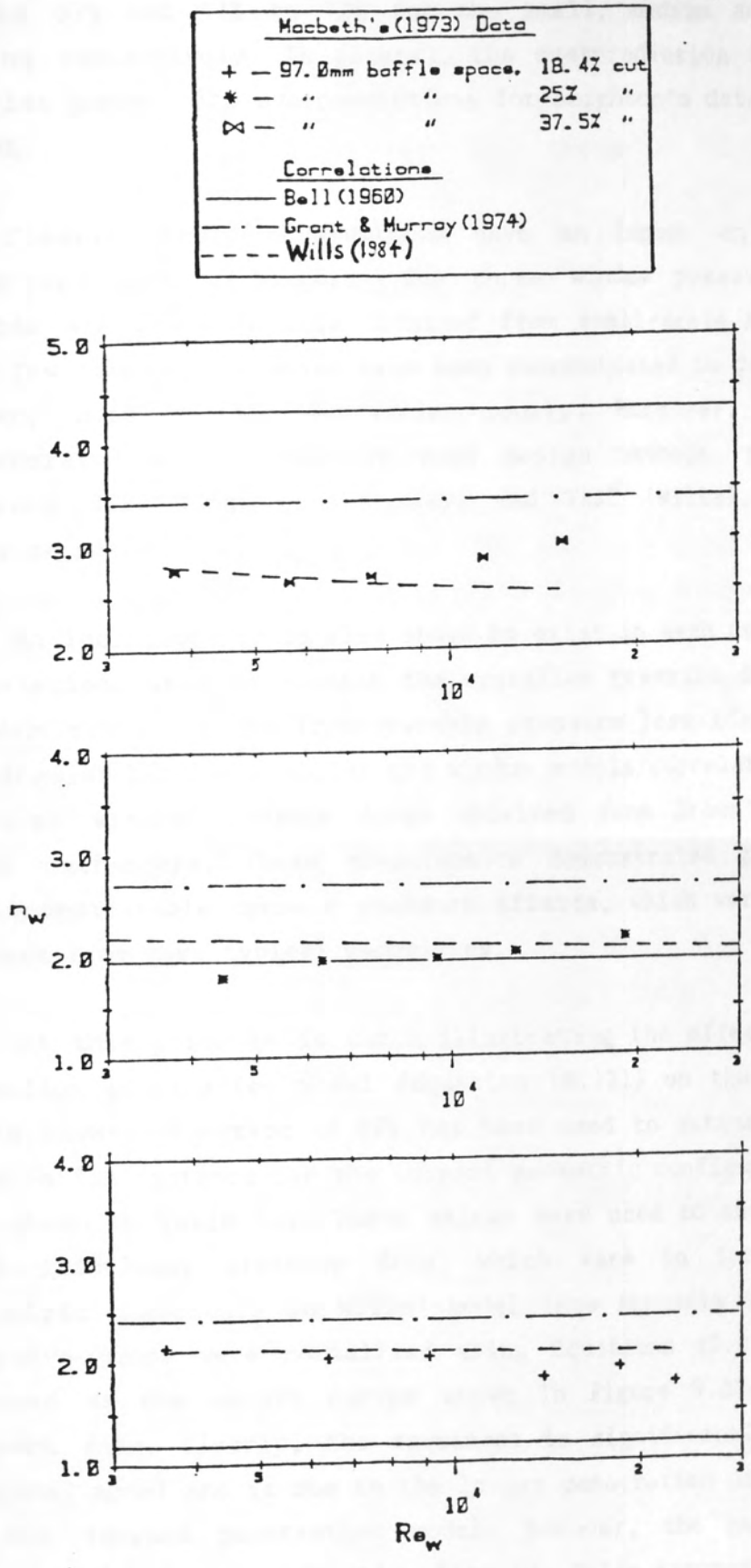

Figure 9.19: Continued

30% to 57% and 41% to 72% for the small, medium and large baffle spacing respectively. In general, the overprediction is worse at low Reynolds number. The overpredictions for Leighton's data range from 14% to 30%.

Clearly, these observations have an impact on the design of commercial heat exchangers. The three window pressure drop design methods are based on data obtained from small-scale model exchangers with few tubes (80), which have been demonstrated to predict data from larger, more typical geometries poorly. Moreover, all three are incorporated within commonly used design methods, namely the HTFS programs STEP (Grant and Murray) and TASC (Wills), and the Bell-Delaware method (Bell).

An inconsistency is also shown to exist in each design method: the correlations used to predict the crossflow pressure drop within these methods represent the irrecoverable pressure loss (derived from ideal rectangular bundles), whilst the window models/correlations reflect the measured window pressure drops obtained from Brown's and Macbeth's model exchangers. These measurements demonstrated trends consistent with considerable dynamic pressure effects, which were not discovered in data from more typical geometries.

At this point it is worth illustrating the effect of the revised crossflow penetration model (Equation (8.12)) on the window model of Wills (1984). Equation (8.12) has been used to estimate the crossflow penetration distance for the current geometric configurations and these are shown in Table I.1. These values were used to estimate the cross-flow frictional pressure drop, which were in turn added to the geometric components in Wills' model (see Appendix H). The resulting pressure drops were normalised using Equations (9.6) and (9.7), and plotted as the smooth curves shown in Figure 9.20a along with the current data. Clearly, the agreement is significantly worse than the original model and is due to the larger penetration distances predicted by the revised penetration model. However, the geometric terms in Wills' model are questionable. Firstly, Wills assumes that the flow in the window turns through 180°, which is believed to be a considerable overestimation. Secondly, Wills assumes that the individual components

of the geometric losses may be treated independently. This is not strictly true since the interaction between bends, expansions and contractions would, for most circumstances, result in lower pressure losses than the sum of the individual components (Miller (1978)). For example, Miller states that two 90° pipe bends, connected together, can yield a combined pressure loss of as little as 54% of the sum of the two considered independently.

If it is assumed that the main flow follows the chord joining the centroids of consecutive window regions (Moore (1974)), as shown in Figure 2.11, the angle through which the fluid must turn through the window may be estimated. These values are shown in Table 9.9 for the current geometry and are considerably less than 180°. Also included in Table 9.9 are the number of velocity heads lost, estimated from Miller, for the bend angles calculated. Again, these are considerably lower than assumed by Wills. These revised loss coefficients were incorporated into the window model giving the following expression:

$$n_w = N_w n_f \left(\frac{A_{cb}^m}{A_w}\right) + n_{tn} + n_e + n_{cn} \qquad (9.11a)$$

where N_w is the number of major restrictions to crossflow in the window, the values of which are given in Table 9.9. The subscripts w, f, tn, e and cn denote window, frictional, turning, expansion and contraction respectively.

Table 9.9: Window Turning Loss Coefficients (n_{tn}) and the Number of Restrictions to Crossflow in the Window for the Current Geometry

Baffle Spacing (mm)	Turning angle in the window (deg)	Number of velocity heads lost δ(-)	Number of major restrictions to crossflow in the window N_w(-)
86.4	136	0.40	5
112.0	124	0.33	6
158.0	106	0.26	7

The number of velocity heads lost due to friction is calculated from the crossflow correlation of Moore (1974) and the other terms are:

$$n_{tn} = \delta \left(1 + (A_w/A^m_{cb})^2\right) \tag{9.11b}$$

$$n_e = (1 - A_w/A^m_{cb})^2 \tag{9.11c}$$

$$n_{cn} = a_w \left(b_w - (A_w/A^m_{cb})\right) \qquad (A_w < A^m_{cb}) \tag{9.11d}$$

$$n_{cn} = a_w' \left(b_w' (A_w/A^m_{cb})^2 - (A_w/A^m_{cb})\right) \qquad (A_w > A^m_{cb}) \tag{9.11e}$$

where $a_w = 0.4$, $b_w = 0.715$ if $\dfrac{A_w}{A^m_{cb}} < 0.715$

or $a_w = 0.5$, $b_w = 1.0$ if $1 > \dfrac{A_w}{A^m_{cb}} > 0.715$

and $a_w' = 0.4$, $b_w' = 1.25$ if $\dfrac{A^m_{cb}}{A_w} < 0.715$

or $a_w' = 0.4$, $b_w' = 1.0$ if $1 > \dfrac{A^m_{cb}}{A_w} > 0.715$

The crossflow area, A^m_{cb}, is the flow area at the baffle tip plane and δ is the estimated number of velocity heads lost in turning through the window region (Table 9.9).

The total number of velocity heads lost calculated from Equation (9.11) are shown in Figure 9.20b. The revised turning loss improves significantly the agreement with the current data, however, this model is only marginally better than the original proposed by Wills. Furthermore, both these models have a significant Reynolds number dependence which is not generally shown by the data.

The current data have also been fitted semi-empirically by maintaining the revised geometric losses and backing out the number of

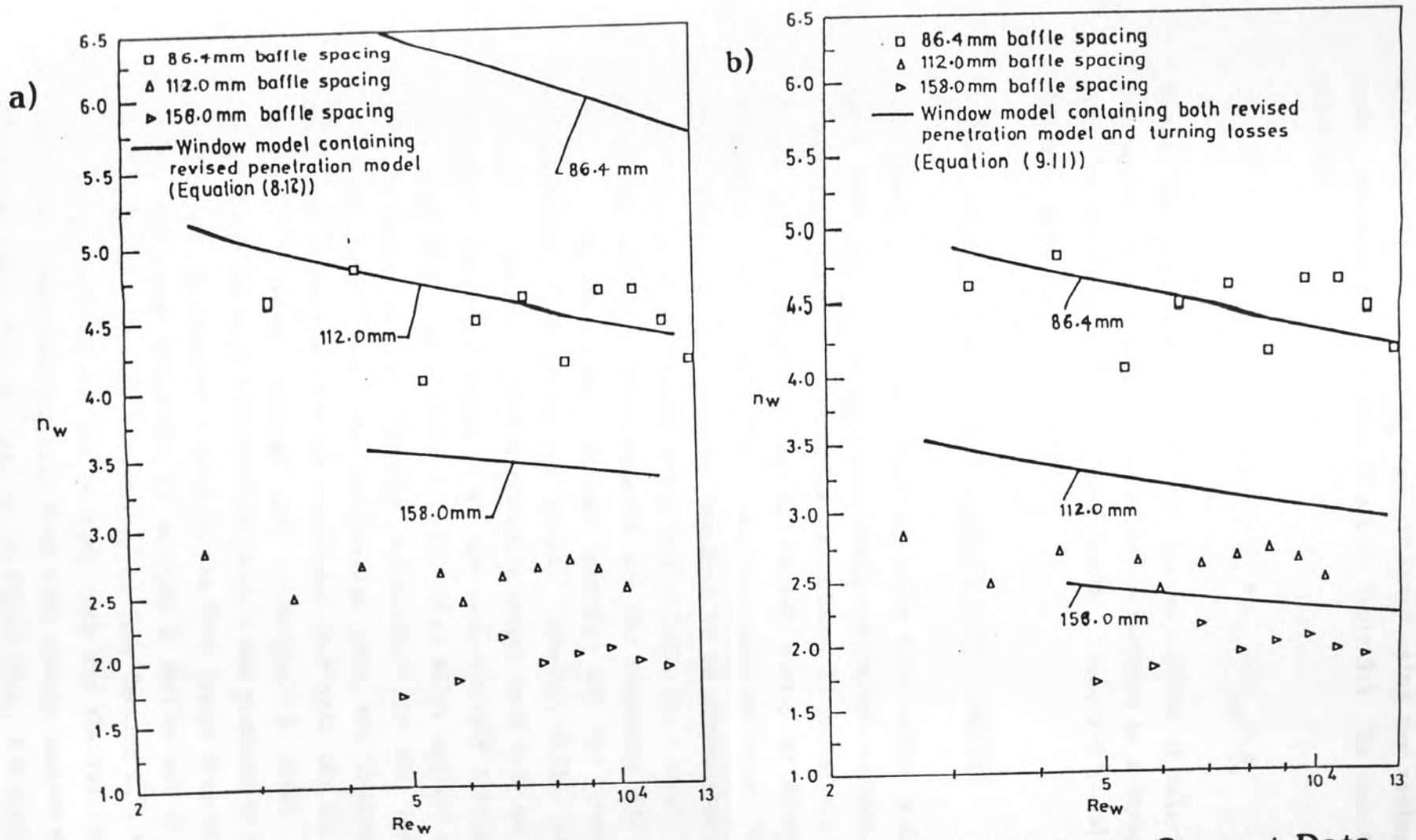

Figure 9.20: Comparison of the Revised Window Model and the Current Data, a) Effect of the Revised Penetration Model (Equation(8.12)), b) Combined effect of Revised Penetration Model and Turning Loss Coefficients.

velocity heads lost per major restriction (N_w) to crossflow in the window. The value of N_w was obtained using the revised penetration model (Chapter 8) and are shown in Table 9.9. The resulting relationship is

$$n_w = 0.517\ N_w + n_{tn} + n_{cn} + n_e \qquad (9.12)$$

where the coefficient 0.517 is the mean number of velocity heads lost per major restriction. This value corresponds to a Reynolds number of 1000 in Moore's crossflow correlation. Equation (9.12) fits all the current data to within ± 16%.

9.5.3 Crossflow and Window Pressure Drops - Leakage

Pressure drops obtained in tests with baffle leakage are rather more difficult to compare with design correlations; when baffle leakage flows are present, crossflow and window flowrates are less than the total and neither can be determined easily by direct measurement. Crossflow and window flow fractions were estimated from the current data, however, the results appeared to be complicated by a number of other effects (Sections 9.2.2 and 9.3.2). In a sense, therefore, the main use of these measurements are for comparing with predictions of modern 'multi-stream' design methods and the results of three-dimensional flow modelling codes. However, Wills (1984) proposed a method in which crossflow pressure drops, made with and without baffle leakage, could be compared at the same absolute flowrate. This method was discussed in Section 2.7.1. When Wills applied it to Macbeth's (1973) data a considerable enhancement in the leakage crossflow pressure drop, over the non-leakage case, was observed for the same absolute flowrate. Wills concluded that this was due to the 'interaction' between leakage and crossflow. A model, known as the 'crossflow-leakage interaction' model, was proposed to account for this effect and is currently used in the HTFS design program TASC. However, using the same procedure to analyse a further set of Macbeth's data, contradictory trends were observed (see Section 2.7.1) This analysis has been applied to the current data and the results are plotted as measured crossflow pressure drop with leakage against derived crossflow pressure drop with no leakage in Figure 9.21. A detailed description of

how the derived crossflow pressure drop is arrived at and a sample calculation are given in Appendix J.

The current data lie, in general, below the line describing equal pressure drops for both leakage and non-leakage conditions, at the same absolute flowrate. This is in stark contrast to Macbeth's data (also included in Figure 9.21) which show considerably larger pressure drops in the leakage case.

An assumption implicit in Wills' analysis, which appears to have been overlooked, is that the pressure drop in the window has the same functional relationship with flowrate in both leakage and non-leakage configurations*. This could only be true if the maldistributions discovered in Macbeth's non-leakage geometry (large separated regions) were also present in his leakage geometry. Mackley (1973), however, who also used Macbeth's experimental rig, observed that the large separated zone detected in the non-leakage geometries, was absent in the leakage geometries. It can be concluded, therefore, that the apparent 'crossflow-leakage interaction' effect, discovered by Wills, is not due to added pressure losses, but the dynamic pressure effects that have been shown to exist in Macbeth's non-leakage pressure drop measurements.

The model Wills put forward was based on two-dimensional flow in a porous medium, following Butterworth (1977). From this he deduced that the crossflow pressure drop should be multiplied by a scaling factor dependent on the tube-baffle leakage flowrate (Equation (2.68)). He also proposed that the bypass pressure drop (in parallel with the crossflow, but between the bundle and shell) should similarly have a scaling factor based on the shell-baffle leakage. This was, however, not based on experimental data but on an analogy to the crossflow case.

Wills' (1984) model has been applied to Macbeth's (1973) and the current leakage geometries, to establish the magnitudes of the two leakage interaction factors. Surprisingly the crossflow-leakage inter-

* This is because Wills' analysis uses the measured leakage window pressure drop in a correlation of the non-leakage window pressure drop to estimate the crossflow fraction in the leakage case (see Appendix J)

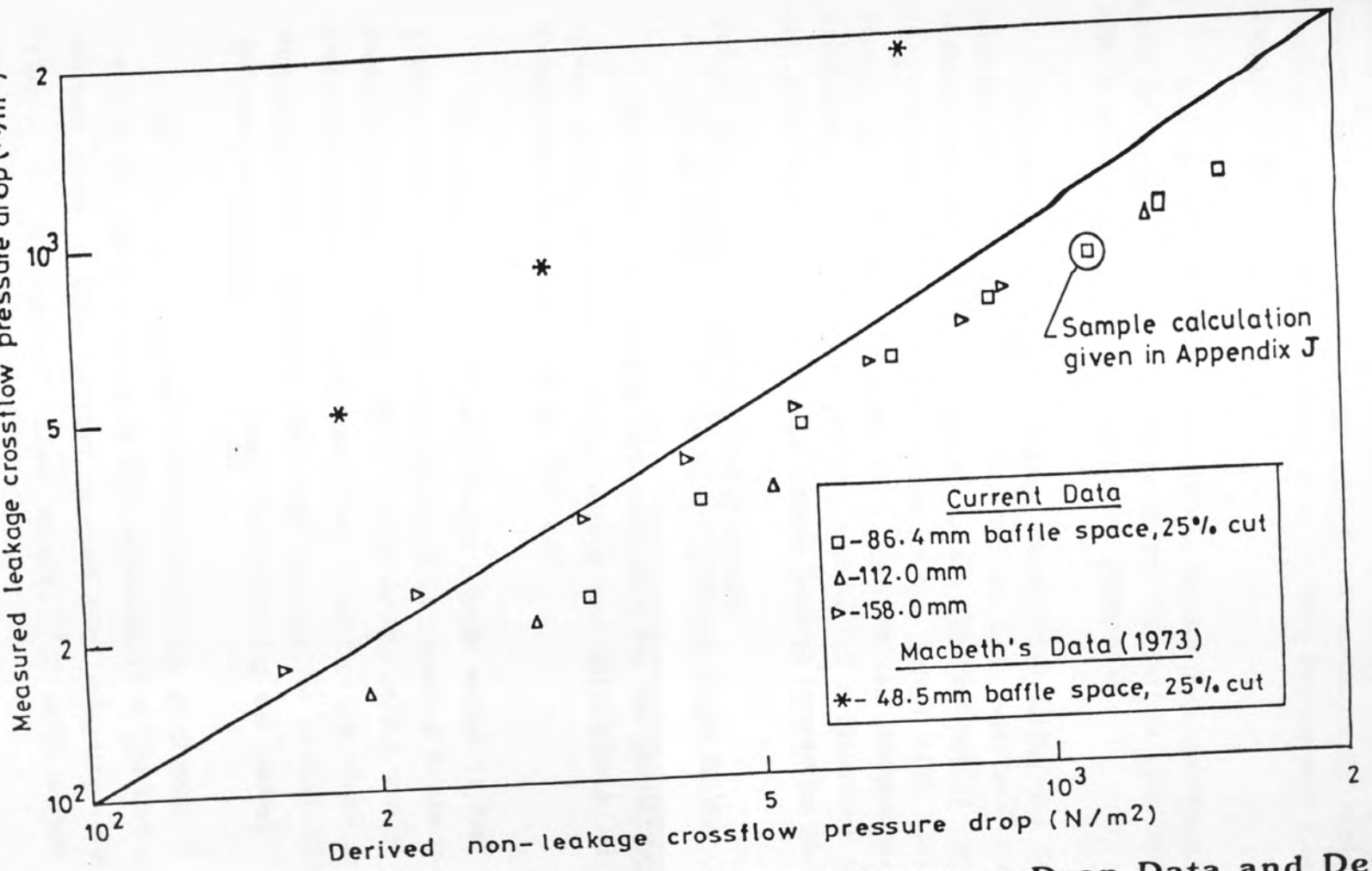

Figure 9.21: Comparison of the Current Leakage Pressure Drop Data and Derived Non-Leakage Crossflow Pressure Drops (Using Wills'(1984)Method). One Set of Macbeths Data also Included.

action factor represents an increase in pressure drop of a few percent only for all cases tested. The bypass-leakage interaction, however, was found to be large, increasing the bypass pressure drop by up to a factor of 8. This has the effect of dramatically increasing the resistance of the bypass lane thus in turn forcing more flow into the crossflow stream.

The increased resistance in the bypass lane constituted a reduction in bypass flows from 11% to 8% for the current geometries and from 15% to as little as 3% for Macbeth's geometries.

Although the bypass-leakage interaction factor was based on an analogy to the crossflow case, and as such must be questioned, its effect appears to conform with direct observations of the flow. The large separated region observed in the bypass lane (Chapter 6) is likely to reduce the bypass flow fraction and increase the crossflow fraction. Fortuitously, in the context of a flowstream model, this could be reflected as a large bypass-leakage interaction factor.

9.5.4 Total Baffle Space Pressure Drops - Comparison with the Predictions of Design Method

Two distinct methods are available for the predictions of baffle space pressure drops: single-stream and multi-stream (also known as flowstream) methods (see Section 2.6).

The only commonly used single stream method is that due to Bell (1960), the current version of which is presented in the Heat Exchanger Design Handbook (HEDH, 1983). This method relies solely on empirical relationships and is non-iterative. Crossflow and window pressure drops are calculated assuming that total flow exists in each, then correction factors are applied to account for bypassing and leakage.

Of the multi-stream methods reviewed in Chapter 2, the current version of the HTFS program TASC appeared to be the most reliable. This method uses a flow network coupled with empirical relationships and simple one-dimensional flow models. All multi-stream methods are necessarily iterative.

Both methods have been used to predict the total baffle space pressure drops measured by Leighton (1955), Macbeth (1973) and those obtained in the current investigation.

9.5.4.1 Non-Leakage

Comparisons between the current, Macbeth's and Leighton's data with the design methods predictions are shown in Tables 9.10, 9.11 and 9.12 respectively.

The TASC program predicts the current data remarkably well considering the poor predictions of the crossflow and window pressure drops (Figures 9.15 and 9.17). The largest deviation observed for all three baffle spacings is 9%. The Bell method shows reasonable agreement with current data, but consistently underpredicts. Since the window pressure drop model (Bell (1960)) consistently overpredicts these data (see Figure 9.17) and the crossflow correlation shows good agreement with Moore's (used in TASC), this suggests that the bypass correction factor is rather low; this can be interpreted as an overestimation of bypass flows.

The predictions of TASC shows only reasonable agreement with Macbeth's data, despite the fact that the window model incorporated in TASC (Wills (1984)) was based on these data. In general, TASC overpredicts the pressure drop and this is due to a considerable overestimation of the crossflow component of pressure drop, particularly at high Reynolds numbers (see Figure 9.15). The Bell method shows considerably poorer agreement. The measured values are underpredicted for baffle cuts of 25% or less, with deviations from the data as large as 55%, but are overpredicted at large baffle cuts. This trend is due to the combination of a poor, rather eratic, window model (see Figure 9.19) and, in effect, an overestimation of bypass flow fractions.

Leighton's data are consistently underpredicted by both methods and again Bell's fairs least well.

The three sets of results are plotted as error ratio of predicted to measured total baffle space pressure drops as a function of mass flowrate in Figure 9.22a, for TASC and Figure 9.22b, for Bell. For TASC, all of the data, bar two points, fall within an error band of ±20%. The root mean square errors (rms) are 5%, 13% and 15% for the current, Macbeth's and Leighton's data respectively.

Table 9.10: Comparison of the Current Non-Leakage Data with the Predictions of TASC and the Bell Method (HEDH (1983))

	Total Baffle Space Pressure Drops Predicted/Measured	
Flowrate (kg/s)	TASC	BELL
Baffle Spacing = 86.4 mm		
8.23	0.97	0.87
7.54	0.92	0.82
6.87	0.91	0.80
6.18	0.91	0.79
5.49	0.95	0.82
4.80	0.93	0.81
4.12	0.95	0.80
3.43	0.99	0.82
2.74	0.95	0.78
2.05	0.93	0.75
Baffle Spacing = 112 mm		
8.25	1.03	0.96
7.56	1.00	0.93
6.88	0.99	0.91
6.19	0.99	0.91
5.50	1.00	0.91
4.81	1.03	0.93
4.47	1.05	0.91
3.44	1.07	0.91
2.75	1.00	0.91
Baffle Spacing = 158 mm		
8.25	0.99	0.90
7.56	0.96	0.80
6.87	0.95	0.80
6.18	0.95	0.80
5.50	0.98	0.90
4.81	1.02	0.90
4.12	1.03	0.90
3.44	1.09	0.90

Table 9.11: Comparison of Macbeth's (1973) Non-Leakage Data Data and the Predictions of TASC and the Bell Method (HEDH (1983))

	Total Baffle Space Pressure Drops Predicted/Measured	
Flowrate (kg/s)	TASC	BELL
Baffle Spacing = 48.5 mm, Baffle Cut = 18.4%		
4.75	1.12	0.77
3.96	1.08	0.75
3.17	1.05	0.72
2.37	1.06	0.72
1.58	0.98	0.66
1.11	0.97	0.62
Baffle Spacing = 97.0 mm, Baffle Cut = 18.4%		
3.96	1.26	0.54
3.17	1.17	0.50
2.38	1.20	0.51
1.58	1.10	0.46
1.11	1.08	0.45
Baffle Spacing = 48.5 mm, Baffle Cut = 25%		
4.75	1.12	0.99
3.96	1.29	1.14
3.16	1.11	0.97
2.37	1.13	0.97
1.58	1.03	0.85
1.11	1.10	0.89
Baffle Spacing 97.0 mm, Baffle Cut = 25%		
4.75	1.11	0.76
3.16	1.11	0.62
2.37	1.11	0.74
1.58	1.04	0.68
1.11	1.08	0.70
Baffle Spacing = 48.5 mm, Baffle Cut = 37.5%		
4.75	1.18	1.15
3.17	1.20	1.14
2.37	1.23	1.14
1.58	1.16	1.04
1.11	1.20	1.04
Baffle Spacing = 97.0 mm, Baffle Cut = 37.5%		
6.33	0.96	1.12
4.75	0.98	1.12
3.17	1.00	1.14
2.37	1.02	1.10
1.58	0.95	1.00
1.11	0.97	0.98

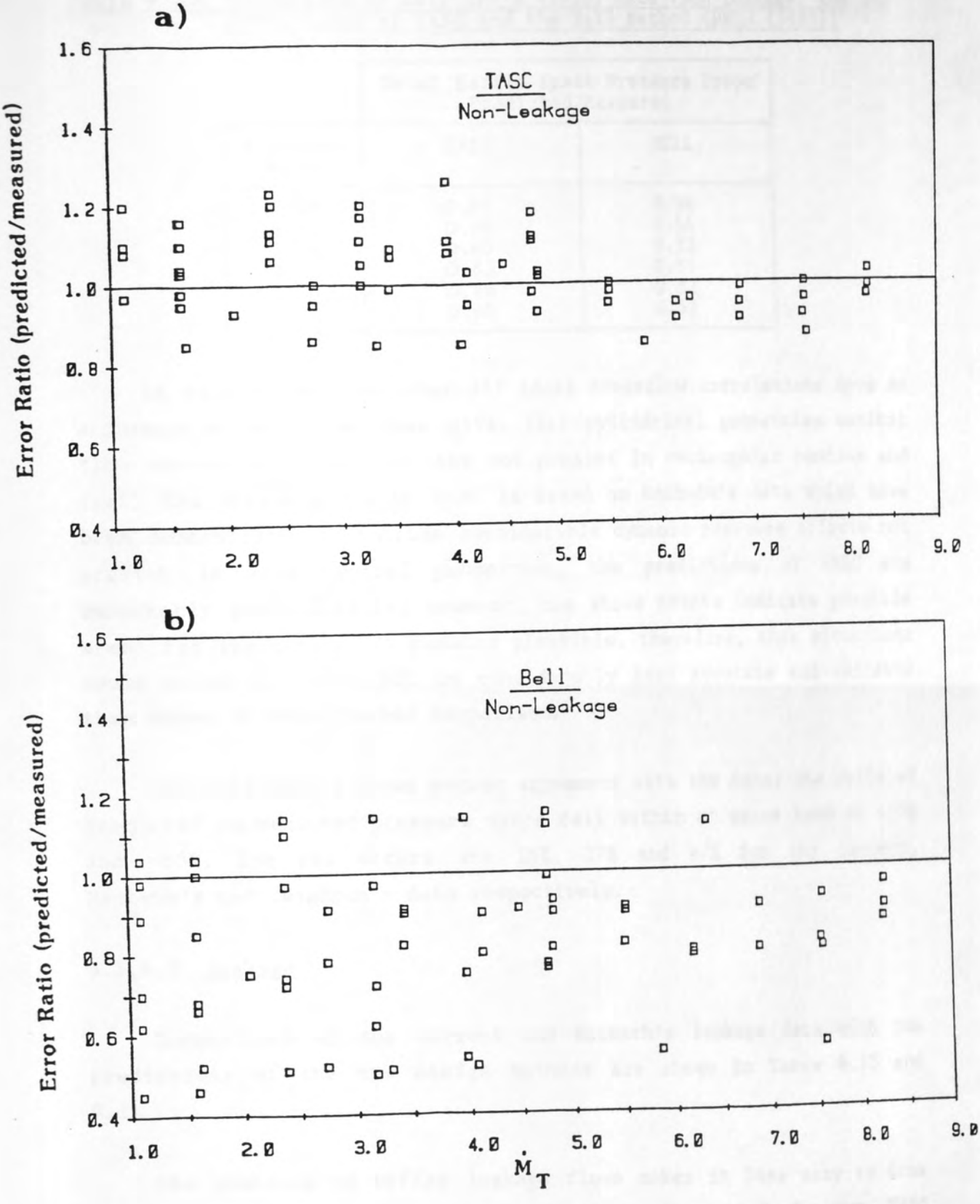

Figure 9.22: Error Ratio of Predicted to Measured Total Non-Leakage Baffle Space Pressure Drops, a) TASC, b) Bell (HEDH (1983)).

Table 9.12: Comparison of Leighton's (1955) data (Non-Leakage) and the Predictions of TASC and the Bell Method (HEDH (1983))

	Total Baffle Space Pressure Drops Predicted/Measured	
Flowrate (kg/s)	TASC	BELL
7.58	0.87	0.56
5.85	0.85	0.55
4.06	0.85	0.52
3.31	0.85	0.51
2.73	0.86	0.52
1.62	0.85	0.52

In view of the fact that (i) ideal crossflow correlations have an accuracy of no better than ±15%, (ii) cylindrical geometries exhibit flow non-uniformities that are not present in rectangular bundles and (iii) the window model in TASC is based on Macbeth's data which have been demonstrated to include considerable dynamic pressure effects not present in more typical geometries, the predictions of TASC are remarkably good. Clearly, however, the above points indicate possible areas for inaccuracy. It remains plausible, therefore, that situations could arise in which TASC is considerably less accurate and reliable than shown in this limited comparison.

The Bell method shows poorer agreement with the data; the ratio of predicted to measured pressure drops fall within an error band of +15% and -55%. The rms errors are 15%, 27% and 47% for the current, Macbeth's and Leighton's data respectively.

9.5.4.2 Leakage

Comparisons of the current and Macbeth's leakage data with the predictions of the two design methods are shown in Table 9.13 and 9.14.

The presence of baffle leakage flows makes it less easy to draw specific conclusions about the trends shown. In general, however, TASC predicts the data considerably better than the Bell method which, in general, overpredicts the data. This clearly demonstrates the advantages of a flow network model over the single-stream method coupled with simple empirical correction factors.

Table 9.13 : Comparison of the Current Leakage Data with the Predictions of TASC and the Bell Method (HEDH (1983))

	Total Baffle Space Pressure Drops Predicted/Measured	
Flowrate (kg/s)	TASC	BELL
Baffle Spacing = 86.4 mm		
8.23	0.89	1.30
7.54	0.88	1.25
6.87	0.92	1.24
6.18	0.96	1.24
5.49	0.94	1.25
4.80	0.96	1.23
4.12	1.00	1.24
3.43	1.06	1.23
2.74	1.06	1.15
2.05	1.05	1.03
Baffle Spacing = 112 mm		
8.25	0.93	1.25
6.88	0.95	1.24
6.19	1.01	1.27
4.47	0.91	1.06
3.44	0.98	1.13
2.75	0.98	1.03
2.06	0.94	0.96
Baffle Spacing = 158 mm		
8.25	0.90	1.09
7.56	0.87	1.04
6.87	0.90	1.04
6.18	0.89	1.02
5.50	0.92	1.02
4.81	0.94	1.01
4.12	1.03	1.06
3.44	1.04	1.02

Table 9.14: Comparison of Macbeth's (1973) Leakage Data and the Predictions of TASC and the Bell Method (HEDH (1983))

Flowrate (kg/s)	Total Baffle Space Pressure Drops Predicted/Measured	
	TASC	BELL
Baffle Spacing = 48.5 mm, Baffle Cut = 18.4% Tube-Baffle Clearance = 0.66 mm, Shell-Baffle Clearance = 2.668 mm		
7.91	0.92	1.25
4.74	0.94	1.28
3.16	0.90	1.34
2.37	0.85	1.31
1.58	0.76	1.14
1.11	0.84	0.98
Baffle Spacing = 48.5 mm, Baffle Cut = 18.4% Tube-Baffle Clearance = 0.33 mm, Shell-Baffle Clearance = 1.334 mm		
4.74	0.72	0.72
3.16	0.76	0.72
2.37	0.82	0.77
1.58	0.78	0.68
1.11	0.70	0.68
Baffle Spacing = 48.5 mm, Baffle Cut = 25% Tube-Baffle Clearance = 0.66 mm, Shell-Baffle Clearance = 2.668 mm		
7.91	1.14	1.63
4.74	1.15	1.63
3.16	1.16	1.62
2.37	1.14	1.57
1.58	1.16	1.54
1.11	1.05	1.36
Baffle Spacing = 48.5 mm, Baffle Cut = 37.5 % Tube-Baffle Clearance = 0.66 mm, Shell-Baffle Clearance = 2.668 mm		
7.91	1.01	1.54
4.75	1.07	1.58
3.16	1.14	1.67
2.37	1.07	1.50
1.58	1.01	1.39
1.11	1.03	1.34

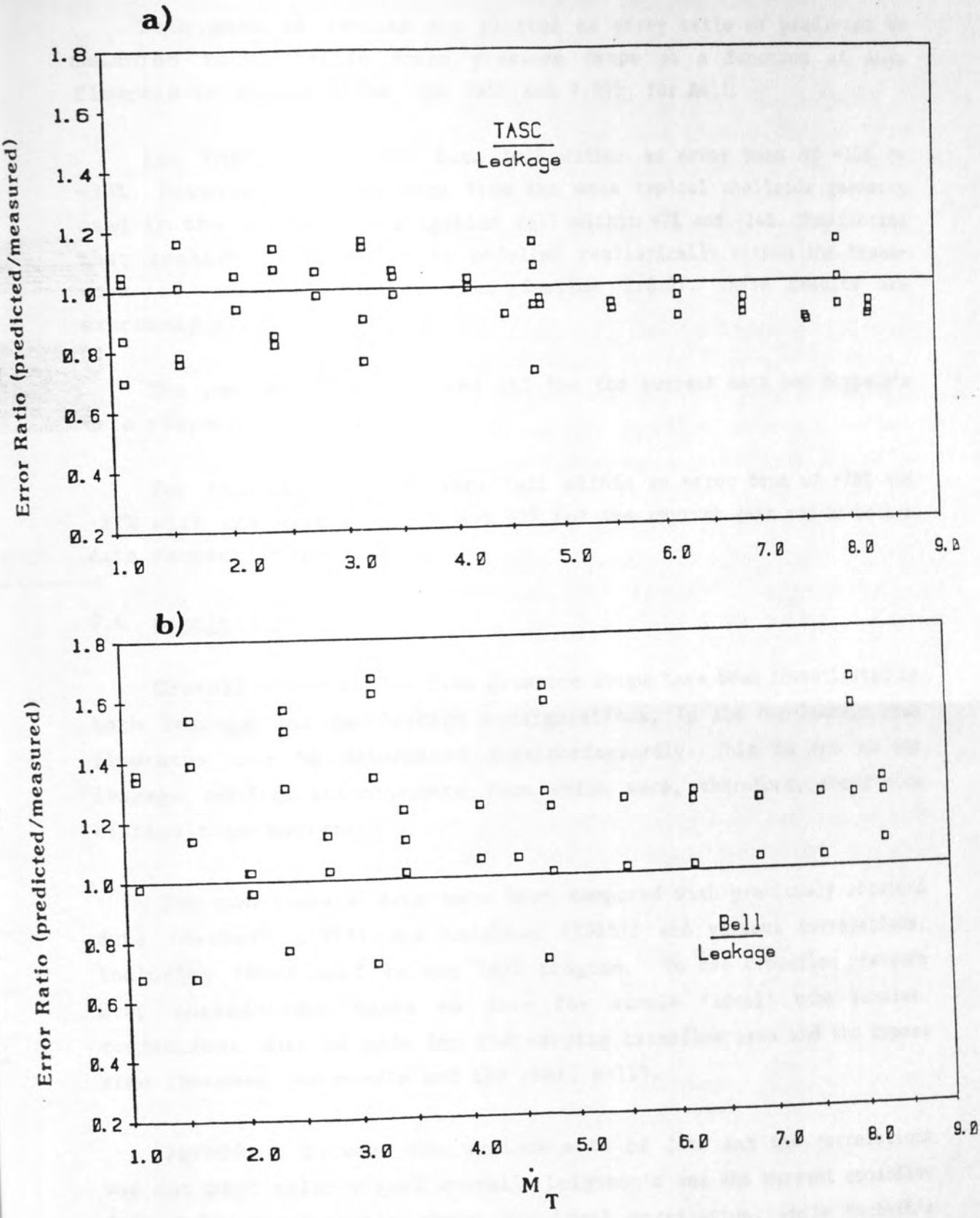

Figure 9.23: Error Ratio of Predicted to Measured Total Leakage Baffle Space Pressure Drops, a) TASC, b) Bell (HEDH (1983)).

Both sets of results are plotted as error ratio of predicted to measured total baffle space pressure drops as a function of mass flowrate in Figure 9.23a, for TASC and 9.23b, for Bell.

For TASC, all of the data fell within an error band of +15% to -30%. However, data deriving from the more typical shellside geometry used in the current investigation fall within +7% and -14%. Considering that leakage flows cannot be modelled realistically within the framework of the TASC method (see Section 2.6.2), these results are extremely good.

The rms errors are 7% and 16% for the current data and Macbeth's data respectively.

For the Bell method, data fell within an error band of +78% and -33% with rms errors of 17% and 43% for the current data and Macbeth's data respectively.

9.6 Conclusions

Crossflow and window flow pressure drops have been investigated in both leakage and non-leakage configurations. In the non-leakage case flowrates can be determined straightforwardly. This is not so for leakage configurations, data from which were, therefore, found more difficult to analyse.

The non-leakage data have been compared with previously obtained data (Macbeth (1973) and Leighton (1955)) and various correlations, including those used in the TASC program. To use crossflow pressure drop correlations based on data for simple 'ideal' tube bundles, corrections must be made for the varying crossflow area and the bypass area (between the bundle and the shell wall).

Agreement between the various sets of data and the correlations was not particularly good overall. Leighton's and the current crossflow data fell consistently above the ideal correlation, while Macbeth's data fell significantly below, particularly at high Reynolds numbers. For the window, Leighton's and the current data fell consistently below the correlations, while Macbeth's data showed reasonably good agreement. This was expected since these correlations were based either on

Macbeth's or Brown's (1956) data, both of which derive from identical small-scale experimental rigs.

It has been possible to account for most of these discrepancies in terms of the improved understanding of shellside flow, derived from the flow visualisation and three-dimensional modelling of shellside flows.

There is a low velocity separated and recirculating zone just downstream of each baffle tip. In exchangers with a relatively low crossflow resistance, the low velocity region can occupy a substantial proportion of the crossflow zone. Macbeth's experimental rig appears to have exhibited this feature to an exceptionally large extent. The end result, because of dynamic pressure effects, was that his measured window pressure drops were higher and his crossflow pressure drops were lower than the irrecoverable pressure losses. This served to explain why Macbeth's data fell considerably below the crossflow correlation. The large-scale flow non-uniformities observed in Macbeth's rig were not apparent in either the current or Leighton's rig, both of which used larger more typical geometries. This brings into question the use of small-scale models with relatively few tubes in the bundle.

In addition, crossflow velocities in the baffle overlap region are not uniform across the baffle space. The window geometry causes velocities to be higher near the downstream baffle and higher near the shell central plane than near the shell wall. Both effects cause the crossflow pressure drop to exceed that calculated assuming uniform flow. This served to explain why Leighton's and the current crossflow data fell significantly above the ideal correlation.

The TASC program and the Bell method have been used to predict the overall baffle space pressure losses for the three rigs under consideration.

TASC predicted the current data extremely well: the maximum deviations observed were 9% and 13% with corresponding root mean square errors of 5% and 7% for non-leakage and leakage respectively. Leighton's and Macbeth's data generally showed poorer agreement, although all of the data considered fell within an error band of ±30%.

The Bell method showed the poorest agreement with all the data sets considered. In general, the non-leakage data were underpredicted whilst the leakage data were overpredicted. All of the data considered fell within an error band of +78% and -55%.

Results from the current data may be summarised as follows:

1) The non-leakage crossflow data exhibited a baffle spacing dependency, an effect not shown in single pass rectangular bundles. This was explained in terms of flow non-uniformities present in cylindrical geometries, but not in rectangular bundles.

2) Leakage flows were shown to be most significant in the smallest baffle spacing, for which the leakage pressure drops were reduced by up to a factor of 3, below the non-leakage, for crossflow and 2.5 for window flow.

3) Crossflow and window flow fractions were estimated from the experimental data. Only the window flow fractions showed general agreement with those predicted by three-dimensional flow modelling. The poorer agreement between crossflow fractions were thought to be due to flow non-uniformities.

4) Large variations of crossflow pressure drop were illustrated by the data, both across the length and width of the baffle compartment. These variations were most significant in the largest baffle spacing.

5) A revised window model was presented which is thought to contain more realistic terms than the original proposed by Wills (1984). However, the revised model agreed only marginally better with the current data than the original. A semi-empirical model was presented which fitted the current window data to within ±16%.

6) Measurements have also been reported of the circumferential variations of local pressure around tubes located at various positions within the overlap region. The basic features of these were explicable in terms of local axial and crossflow velocities over the tubes. In particular separated regions, originating from the baffle tips, were identified. This region appeared to be larger near the shell wall than the shell central plane.

CHAPTER 10

GENERAL SUMMARY OF CONCLUSIONS

10. GENERAL SUMMARY OF CONLUSIONS

This chapter brings the main conclusions drawn from Chapters 6, 7, 8 and 9 together, in an edited form.

10.1 Flow Visualisation

1) Separated regions were detected, originating from the baffle tips. These were observed to be small near the central plane but large adjacent to the shell wall. As a consequence bypass flows are likely to be reduced.

2) Tube-baffle leakage in the overlap region was demonstrated to be a modified form of crossflow. As such, baffle leakage would be expected to contribute towards both heat transfer and pressure drop. This is not accounted for in multi-stream design methods.

3) Crossflow was shown to be inclined at a considerable angle to the bundle and not normal to it as is generally assumed.

10.2 Three-Dimensional Flow Modelling

1) Calculated baffle space pressure drops were in good agreement with the measured values. This suggests that bypass flow fractions were small in the experimental rig, since the bypass lane was omitted for modelling purposes.

2) Separated regions, detected by flow visualisation and local pressure measurements, were predicted for all geometries apart from the medium and small baffle spacing in the leakage case. This was thought to be a consequence of the coarse grid used.

3) Regions of high and low velocity predicted by FLOW3D illustrate areas that could be prone to fouling and tube vibration.

4) A non-uniform crossflow was predicted, with, in general, higher flows near the centre line of the bundle than near the shell wall.

5) Crossflow fractions calculated from FLOW3D were broadly in agreement with those obtained using the simpler flow network model used in TASC.

10.3 Penetration of Crossflow in the Window

1) The model used in TASC was compared with a revised model and the results from FLOW3D. It was found that the revised model showed closest agreement with FLOW3D. In addition, the revised model was reduced to an explicit form, thus requiring less computer time than the iterative approach required with the model currently in TASC.

10.4 Pressure Drops

1) The crossflow pressure drops showed a baffle space dependence, not shown in single pass rectangular tube bundles.

2) Crossflow and window flow fractions, for the leakage data, were estimated from the leakage and non-leakage pressure drops. Only the window flow fractions showed reasonable agreement with those calculated from FLOW3D.

3) Large variations of crossflow pressure drop were illustrated by the data, both across the length and breadth of a baffle compartment. These variations were most significant for the large baffle spacing.

4) Crossflow and window pressure measurements were compared with previously obtained data and commonly used design correlations. Overall, the agreement was not very good.

It has been possible to account for most of the observations, listed above, in terms of the improved understanding of shellside flow, derived from flow visualisation and three-dimensional modelling of shellside flows.

5) Leakage flows were shown to be most significant in the smallest baffle spacing, for which the leakage pressure drops were reduced by up to a factor of 3 for both crossflow and window flow.

6) A revised window pressure drop model was proposed which is thought to contain more realistic terms than the original proposed by Wills (1984). However, this model agreed only marginally better with the current data than the original. A semi-empirical model was also presented which fitted the current window data to within ±16%.

7) The single-stream design method of Bell (HEDH, 1983) and the multi-stream design program TASC were used to predict overall baffle space pressure drops. TASC predicted all of the data considered (Leighton's (1955), Macbeth's (1973) and the current data) to within ±30%. The Bell method, however, was considerably less reliable, with maximum deviations from the data of +78% and -55%.

8) Data deriving from small-scale rigs with few tubes have been shown to be unrepresentative of typical commercial units.

CHAPTER 11

RECOMMENDATIONS FOR FUTURE WORK

11. RECOMMENDATIONS FOR FUTURE WORK

The following investigations are recommended for future work:

1) Shellside flow visualisation in other goemetries, both with and without baffle leakage. The dye release technique proved very useful in obtaining qualitative flow distribution information. This technique could be extended to measure average velocities over various flow paths using high speed ciné.

2) Extension of three-dimensional flow modelling to include a bypass lane. This would enable the significance of bypass flows to be quantified and allow the simple 'ideal' correlations to be checked.

3) Extension of the inter-baffle pressure drop measurements to include all baffle compartments and end-spaces. This would enable an investigation into the end-space effect discovered in the current leakage test. Flow visualisation could also play a useful role.

4) In the current investigation only baffle spacing was varied. Clearly, there is a wide scope for future experimental work. This could include variation of baffle cut, leakage and bypass areas. In particular, this would allow a thorough analysis of the effect of leakage and bypassing on pressure drop and flow distribution. Sealing strips could also be investigated. Furthermore, the large bank of data obtained from such an investigation would be invaluable for checking modern shellside design methods. This could also assist in the development of such methods.

Some of the above recommendations are already under way at the Harwell Laboratory.

REFERENCES

ACHENBACH, E. (1969). "Investigations of the flow through a staggered tube bundle at Reynolds numbers up to Re - 10^7". Wärmer-und Stoffübertragung, Vol.2, pp.47-52.

BELL, K.J. and BERGELIN, O.P. (1957). "Flow through annular orifices". ASME Trans., Vol.79, pp.593-601.

BELL, K.J. (1960). "Exchanger design based on the Delaware Research Programme". Petro. Chem. Engng., Vol.32, pp.C26-C40.

BELL, K.J. (1963). "Final report of the cooperative research program on shell and tube heat exchangers". University of Delaware, Engineering Experimental Station, Bulletin No.5.

BELL, K.J. (1980). "Delaware method for shellside design. Heat exchangers: thermal-hydraulic fundamentals and design". Nato Adv. Study Institute, Istanbul, Turkey. Hemisphere Pub. Corp., ISBN -07-033284, pp.581-618.

BERGELIN, O.P., BROWN, G.A. and DOBERSTEIN, S.C. (1952). "Heat trasnfer and fluid friction during flow across banks of tubes - IV: A study of the transition zone between viscous and turbulent flow". Trans. ASME, Vol.74, pp.953-960.

BERGELIN, O.P., BROWN, G.A. and COLBURN, A.P. (1954). "Heat transfer and fluid friction during flow across banks of tubes - V: A study of a cylindrical baffled exchanger without internal leakage". Trans. ASME, Vol.74, pp.841-850.

BERGELIN, O.P., LEIGHTON, M.D., LAFFERTY, W.L. and PIGFORD, R.L. (1958). "Heat transfer and pressure drop during viscous and turbulent flow across baffled and unbaffled tube banks". Bulletin No.4, Engng. Exptle. St., University of Delaware, USA.

BERGELIN, O.P., BELL, K.J. and LEIGHTON, M.D. (1959). "Heat transfer and fluid friction during flow across banks of tubes: VII. Bypassing between tube bundle and shell". Chem. Engng. Symp. Series, Vol.55, No.29, pp.45-58.

BERNER, C., DURST, F. and McELIGOT, D.M. (1984). "Flow around baffles". J. Heat Transfer, Vol.106, pp.743-749.

BIRCHENOUGH, P. (1985). Private communication.

BOUCHER, D.F. and LAPPLE, C.E. (1948). "Pressure drop across tube banks: A critical comparison of available data and the proposed method of correlation". Chem. Eng. Prog., Vol.44, pp.117-134.

BRISKIN, J. (1951). "Leakage through tube hole clearances in tubular heat exchangers". MChE Thesis, University of Delaware, USA.

BROWN, G.A. (1956). "Heat transfer and fluid friction during turbulent flow through baffled shell-and-tube heat exchanger". PhD Thesis, University of Delaware, USA.

BRYCE, C.A. (1957). "The effect of tube bundle bypassing on pressure drop and heat transfer in laminar and turbulent regions". MChE Thesis, University of Delaware, USA.

BUTTERWORTH, D. (1977). "The development of a model for three-dimensional flow in tube bundles". Int. J. Heat and Mass Transfer, Vol.21, pp.253-256.

BUTTERWORTH, D. (1979). "The correlation of crossflow pressure drop by means of the permeability concept". UKAEA Harwell Report, AERE-R9435.

CERNIK, R.J. (1955). "Velocity distribution across banks of tubes". MChE Thesis, University of Delaware, USA.

CHILTON, T.H. and GENEREAUX, R.P. (1933). "Pressure drop across tube banks". Trans. AIChE, Vol.29, pp.161-173.

CHISHOLM, D. (1980). "Developments in heat exchanger technology - 1". Development Series, Applied Science Publishers, London.

CURRIE, I.G. (1983). "Flow measurements around heat exchanger tubes and sealing strips". Laser-Doppler Anemometry Laboratory, Dept. of Mech. Engng., University of Toronto.

DESTREMPS, E.A. (1956). "The effect of tube bundle bypassing on pressure drop and heat transfer in the laminar region". MChE Thesis, University of Delaware, USA.

DONOHUE, D.A. (1949). "Heat transfer and pressure drop in heat exchangers". Ind. Engng and Chem., Vol.41, No.11, pp.2499-2511.

EMERSON, W.H. (1963). "Shellside pressure drop and heat transfer with turbulent flow in segmentally baffled shell-and-tube heat exchangers". Int. J. Heat Mass Transfer, Vol.6, pp.649-668.

ENGINEERING SCIENCES DATA UNIT (ESDU, 1974). "Pressure loss during crossflow of fluid with heat transfer over plain tube banks without baffles". Item No. 74040, 251-9 Regent Street, London.

ENGINEERING SCIENCES DATA UNIT (ESDU, 1979). "Crossflow pressure loss over banks of plain tubes in square and triangular arrays including the effects of flow directions". Item No.79034, 251-9 Regent Street, London.

FISHER, J. and PARKER, R.O. (1969). "New ideas on heat exchanger design". Hydrocarbon Processing, Vol.48, No.7, pp.147-154.

GRANT, I.D.R. and MURRAY, I. (1972). "Shellside performance of segmentally baffled shell-and-tube heat exchangers by Divided Flow method. Part 1 (Revised): Derivation of the method". HTFS Design Report 24, AERE-R7781.

GRANT, I.D.R. and MURRAY, I. (1974). "Shellside performance of segmentally baffled shell-and-tube heat exchangers by Divided Flow method. Part 3: Development of the method and extension to double-segmental baffles". HTFS Design Report 24, AERE-R7781.

GRIMISON, E.D. (1937). "Correlation of new data on flow resistances and heat transfer for crossflow of gases over tube banks". Trans. ASME, Vol.59, pp.583-594.

GUNTER, A.Y. and SHAW, W.A. (1945). "A general correlation of friction factors for various types of surfaces in crossflow". Trans. ASME, Vol. 65, pp.643-660.

GUPTA, R.K. and KATZ, D.L. (1957). "Flow patterns for predicting shellside heat transfer coefficients for baffled shell-and-tube heat exchangers". Indust. Engng. Chem., Vol.49, No.6, pp.998-999.

HASELER, L.E. AND MURRAY, P.W. (1985). "Baffle leakage in shell-and-tube heat exchangers". UKAEA Harwell Report, AERE-R9435.

HEAT EXCHANGER DESIGN HANDBOOK (HEDH, 1983). Part 3: "Thermal and hydraulic design of heat exchangers". Hemisphere Publishing Corporation.

HOLLAND, F.A. (1973). "Fluid flow for Chemical Engineers". Edward Arnold, 1st Edition.

HUGE, E.C. (1937). "Experimental investigation of the effects of equipment size on convection of gases over tube banks". Trans. ASME, Vol.59, pp.573-581.

JAKOB, M. (1938). "Discussion of Pierson, Huge and Grimison Papers". Trans. ASME, Vol.60, pp.384-386.

JONES, I.P., KIGHTLEY, J.R., THOMPSON, C.P. and WILKES, N.S. (1985). "FLOW3D, release 1: User manual". UKAEA Report AERE-R11893.

KERN, D.Q. (1950). "Process heat transfer". McGraw-Hill, New York.

KOPP, S., SENNSTROM, H.R. and GUNTER, A.Y. (1947). "A study of flow patterns in baffled heat exchangers". ASME paper 47.103.

LEE, N.K. (1981). "Simulation of condenser pressure losses by porous tubes with suction". PhD Thesis, University of Bristol.

LEE, N.K., MAYHEW, Y.R. and HOLLINGSWORTH, M.A. (1983). "Effect of pitch-diameter ratio and bypass lanes on pressure loss in condenser tube banks". University of Bristol.

LEIGHTON, M.D. (1955). "Pressure drop in a baffled tubular exchanger without internal leakage". MChE Thesis, University of Delaware, USA.

LONSDALE (1984). "A simple turbulence model for flow in anisotropic porous media". Dounreay, ND-M-2947.

MACBETH, R.V. (1973). "Shell-and-tube heat exchanger data produced by the diffusion controlled mass transfer modelling technique". UKAEA Report AEEW-R 898, HTFS RS78.

MACBETH, R.V. (1974). "Further shell-and-tube heat exchange data produced by the diffusion controlled electrochemical mass transfer modelling technique". UKAEA Report AEEW-R983, HTFS RS126.

MACBETH, R.V. (1975). "Further shell-and-tube heat exchanger data produced by the electrochemical modelling technique using a large model heat exchanger". UKAEA Report AEEW-R1026, HTFS RS145.

MACBETH, R.V. (1979). "Obtaining uniform crossflow distribution in shell and tube heat exchangers". UKAEA Report AEEW-R1247, HTFS RS303.

MACBETH, R.V. and NEILSON, A.J. (1977). "Heat transfer and pressure drop in a shell-and-tube heat exchanger using orifice baffles". UKAEA Report AEEW-R1048, HTFS RS169.

MACBETH, R.V. and ANDERSON, A.R. (1983). "Pressure loss characteristics of heat exchanger tube/baffle and shell/baffle clearances". UKAEA Report AEEW-R1644, HTFS RS472.

MACBETH, R.V. (1984). "Pressure drop calculations in baffled shell-and-tube heat exchangers". UKAEA Report AEEW-R1783, HTFS RS527.

MARTIN, D.J., HASELER, L.E., HOLLINGSWORTH, M.A. and MAYHEW, Y.R. (1987). "The effect of bypass lanes and sealing strips in shell-and-tube heat exchangers". UKAEA Harwell Report, AERE-R12710.

MILLER, D.S. (1979). "Internal flow systems". BHRA Fluid Engineering, ISBN 0 099083 78 7.

MOORE, M.J.C. (1974). "Pressure drop and heat transfer calculations on the shellside of shell-and-tube heat exchangers". UKAEA Harwell Report, HTFS RS110.

MOORE, M.J.C. (1979). "HTFS-Dr11 Shell-and-tube condenser design and performance calculations, Part 4: Shellside heat transfer and pressure drop calculation methods". UKAEA Harwell Report AERE-R7546.

PALEN, J.W. and TABOREK, J. (1969). "Solution of shellside flow pressure drop and heat transfer by stream analysis method". 10th Nat. Heat Transfer Conf., AIChE-ASME, Philadelphia, pp.53-65.

PARKER, R.O. AND MOK, Y.I. (1968). "Shellside pressure loss in baffled heat exchangers". Brit. Chem. Engng., Vol.13, No.3, pp.366-368.

PEARCE, H.R. (1973). "Noise and vibration in heat exchangers". Ph.D. Thesis, University of Oxford.

PEREZ, J.A. (1984). "Internal heat transfer and pressure drop measurements in a variously baffled shell-and-tube heat exchanger". PhD Thesis, University of Minnesota.

PIERSON, O.L. (1937). "Experimental investigation of the influence of tube arrangement on convection heat transfer and flow resistance in crossflow of gases over tube banks". Trans. ASME, Vol.59, pp.563-572.

RHODES, D.B. and CARLUCCI, L.N. (1983). "Predicted and measured velocity distributions in a model heat exchanger". Int. Conf. on Numer. Methods in Nucl. Eng., Montreal, Canada, Vol.2, pp.935-948.

ROGERS, G.F.C. and MAYHEW, Y.R. (1980). "Thermodynamic and transport properties of fluids". Third Ed. Basil Blackwell, Oxford.

RUSSELL, M.A. and WILLS, M.J.N. (1983). Private communication.

SAX, N.I. (1984). "Dangerous properties of industrial materials". Van Nostrand Reinhold Col, 6th Edition.

SULLIVAN, F.W. and BERGELIN, O.P. (1956). "Heat transfer and fluid friction in a shell-and-tube exchanger with a single baffle". Engng. Prog. Symp. Series, No.18, Vol.52, pp.85-94.

TABOREK, J. (1979). "Evolution of heat exchanger design techniques". Heat Transfer Engineering, Vol.1, No.1, pp.15-29.

TEMA (1978). Standard of Tubular Exchanger Manufacturers Association, 5th Edition, New York, Tubular Exchanger Manufacturers Association Inc.

TINKER, T. (1947). "Shellside heat transfer characteristics of segmentally baffled shell and tube heat exchangers". ASME, Annual Meeting, pp.293-343.

TINKER, T. (1948). "Shellside characterisics of shell-and-tube heat exchangers". Trans. ASME, pp.89-116.

TINKER, T. (1958). "Shellside characteristics of shell-and-tube heat exchangers". Inst. Mech. Engng., Proceedings of general discussion on heat transfer, pp.36-49.

TOPPING, J. (1962). "Errors of observation and their treatment". Chapman and Hall Ltd., London, Reinhold Pub. Corp., New York.

WHISTLER, A.M. (1947). "Effect of leakage and cross-baffle in a heat exchanger". Petroleum Refiner, Vol.26, pp.114-118.

WHITLEY, D.L. (1961). "Calculating heat exchanger shellside pressure drop". Chem. Engng. Progress, Vol.57, No.9.

WILLIAMS, R.B. and KATZ, D.L. (1952) "Performance of finned tubes in shell-and-tube heat exchangers". Trans. ASME, No.74, pp.1307-1320.

WILLS, M.J.N. (1984). "Studies of the shell-side performance of a shell-and-tube heat exchanger". PhD Thesis, University of Aston in Birmingham, Birmingham.

WILSON, R.E., McADAMS, W.H. and SELTZER, M. (1922). Ind. Engng. Chem., Vol.14, pp.105-119.

WEBSTER, R. (1984). "A calculation method for three-dimensional, transient, thermal hydraulic analysis of complex plant components: The INCA code". ND-M-2509(D).

ZUKAUSKAS, A. (1972). "Heat transfer of banks of tubes in crossflow at high Reynolds numbers". International Centre for Heat and Mass Transfer. International Seminar, Trojir, Yugoslavia, Aug. 30 - Sept.6, Session C.

ZUKAUSKAS, A. and ULINSKAS, R. (1983). "Banks of plain and finned tubes". Heat Exchanger Design Handbook (HEDH), Sec. 2.2.4, Hemisphere Pub. Corp.

APPENDICES

APPENDIX A

STANDARDISATION OF CROSSFLOW CORRELATIONS FOR ROTATED SQUARE LAYOUTS

A.1 Introduction

To enable a simple unambiguous comparison between various crossflow correlations, each must be reduced to a standard form so that they may be plotted on a common basis. The standard definitions chosen for friction factor and Reynolds number are:

$$f_c^m = \frac{2 \rho \Delta p_c}{4 N_c \dot{m}_m^2} \qquad (A.1)$$

and

$$Re_c^{mt} = \frac{\dot{m}_m D_t}{\eta} \qquad (A.2)$$

where $\dot{m}_m$ is the mass flux based on the minimum crossflow area.

On this basis the correlations of Grimison (1937), Grant and Murray (1972), ESDU (1974) and Zukauskas (HEDH, 1983) need no adjustment since each used the standard definition.

A.2 Relationship of the Moore Correlation to the Standard Form

Moore (1974) defined the friction factor in the standard form (Equation (A.1)). However, the Reynolds number was defined using the minimum clearance between tubes as the characteristic length:

$$Re_c^m = \frac{\dot{m}_m (P_t - D_t)}{\eta} \qquad (A.3)$$

Since the minimum clearance between tubes changes from the gap between the diagonal pitch (P_t) to the gap between the transverse pitch (P_y) at a $P_t/D_t > 1.71$, two expressions are required to relate Re_c^m to Re_c^{mt}:

For $P_t/D_t \leq 1.71$

$$\frac{Re_c^{mt}}{Re_c^{m}} = \frac{D_t}{(P_t - D_t)}$$

normalising using the expressions given in Figure 2.2 gives

$$Re_c^{mt} = \frac{Re_c^{m}}{(t-1)} \qquad (A.4)$$

For $P_t/D_t > 1.71$

$$\frac{Re_c^{mt}}{Re_c^{m}} = \frac{D_t}{(P_y - D_t)}$$

therefore

$$Re_c^{mt} = \frac{Re_c^{m}}{(r-1)} \qquad (A.5)$$

where t and r are the diagonal and transverse pitch-diameter ratios respectively. It is a simple matter to calculate the friction factor based on Re_c^m and convert the Reynolds number to the standard form for plotting.

A.3 Relationship of the Butterworth Correlation to the Standard Form

Butterworth defined the friction factor using the superficial area and the crossflow length divided by the tube diameter (L_c/D_t) rather than N_c:

$$f_c^{s} = \frac{2 \rho \Delta p_c}{4 \left(\frac{L_c}{D_t}\right) \dot{m}_s^2} \qquad (A.6)$$

Relating f_c^s to f_c^m gives

$$\frac{f_c^{m}}{f_c^{s}} = \left(\frac{L_c}{D_t}\right) \left(\frac{1}{N_c}\right) \left(\frac{A_c}{A_s}\right)^2 \qquad (A.7)$$

Two expressions are necessary to relate the friction factors.

For $P_t/D_t \leq 1.71$

$$\frac{f_c^m}{f_c^s} = \left(\frac{L_c}{D_t}\right)\left(\frac{1}{N_c}\right)\left[\frac{2\,(P_t-D_t)}{P_y}\right]^2 \qquad (A.8)$$

The crossflow length (L_c) can be related to the number of tube rows crossed and the longitudinal pitch:

$$L_c = N_c P_x$$

therefore

$$\frac{L_c}{D_t} = N_c s \qquad (A.9)$$

where s is the longitudinal pitch-diameter ratio.

Substituting Equations (A.9) into (A.8) and normalising gives, noting that s = r/2 for rotated square,

$$f_c^m = 2 f_c^B \frac{(t-1)^2}{r} \qquad (P_t/D_t \leq 1.71) \qquad (A.10)$$

For $P_t/D_t > 1.71$

$$\frac{f_c^m}{f_c^s} = s\,\frac{(P_y-D_t)^2}{P_y^2}$$

$$f_c^m = f_c^B \frac{(r-1)^2}{2r} \qquad (P_t/D_t > 1.71) \qquad (A.11)$$

Likewise, two expressions relate the standard to Butterworth's Reynolds number, which is based on the superficial area and tube diameter,

$$Re_c^{mt} = Re_c^{st} \frac{r}{2(t-1)} \qquad (P_y/D_t \leq 1.71) \qquad (A.12)$$

and

$$Re_c^{mt} = Re_c^{st} \frac{r}{(r-1)} \qquad (P_y/D_t > 1.71) \qquad (A.13)$$

In this case Butterworth's friction factors are found using Re_c^{st}, then both the friction factor and Reynolds number must be converted to the standard before comparisons can be made.

A comparison between a number of ideal crossflow correlations is shown in Figure 2.3.

APPENDIX B

CORRECTION TO IDEAL BUNDLE FRICTION FACTORS FOR USE IN CYLINDRICAL BUNDLES

B.1 Introduction

Ideal tube bundle correlations only strictly apply to rectangular geometries for which the cross-sectional area for flow remains constant. In cylindrical geometries the crossflow is subjected to changes in velocity due to variations in the area for flow. Moore (1974) integrated the standard crossflow pressure drop equation over the crossflow length, assuming a constant friction factor and obtained the following relationship:

$$\bar{n}_c = 2 f_c \left(\frac{D_{ot}}{P_x}\right) \left(\frac{C_w}{D_{ot}}\right)^2 \ln \left[\frac{\frac{D_{ot}}{2} + \frac{L_c}{2}}{\frac{D_{ot}}{2} - \frac{L_c}{2}}\right] \qquad (B.1)$$

The pressure drop was given as

$$\Delta p_c = n_c \frac{1}{2\rho} \left(\frac{M_c}{\bar{A}_c^m}\right)^2 \qquad (B.2)$$

where $\bar{A}_c^m$ is the average minimum crossflow area and $\bar{n}_c$ the total number of velocity heads lost. Equation (B.1) implicitly accounts for the number of tube rows crossed. This relationship is different from that given in the main text (Equation (2.29)), but Equation (B.1) can be readily converted into a friction factor form. The total number of velocity heads lost can be related to the friction factor by

$$n_c = 4 N_c \bar{f}_c^m \qquad (B.3)$$

where $\bar{f}_c^m$ is the friction factor corrected to a circular geometry.

Furthermore, the longitudinal pitch (P_x) can be related to the total crossflow length (L_c) and the number of tube rows crossed (N_c) by

$$N_c = \frac{L_c}{P_x} \tag{B.4}$$

Substituting Equations (B.3) and (B.4) into (B.1) gives

$$\overline{f}_c^m = \frac{f_c^m}{2} \left(\frac{D_{ot}}{L_c}\right) \left(\frac{C_w}{D_{ot}}\right)^2 \ln \left[\frac{\frac{D_{ot}}{2} + \frac{L_c}{2}}{\frac{D_{ot}}{2} - \frac{L_c}{2}}\right] \tag{B.5}$$

which is the same as Equation (2.29) from the main text.

B.2 Assessment of Moore's Correction

In order to assess the significance of Moore's correction, in a generalised manner, Equation (B.5) can be reduced to a function of friction factor and B_c (the baffle cut expressed as a fraction of the shell diameter) only.

The average superficial crossflow width, C_w, can be expressed as

$$C_w = \frac{D_{ot}^2}{2L_c} \left[\frac{1}{2} \sin 2\left(\sin^{-1}\frac{L_c}{D_{ot}}\right) + \sin^{-1}\left(\frac{L_c}{D_{ot}}\right)\right] \tag{B.6}$$

Using Moore's assumption that the crossflow extends from the crossflow, or baffle overlap region to the centroid of the window region, the crossflow path can be expressed as

$$L_c = D_{ot} (1-1.2B_c) \tag{B.7}$$

this relates to the case of no shell to bundle bypass lanes: the shell inside diameter (D_s) equals the outer tube limit diameter (D_{ot}).

On substituting equations (B.6) and (B.7) into (B.5), the following relationship is obtained:

$$\frac{\bar{f}_c^{\,m}}{f_c^{\,m}} = \frac{1}{8}\,\xi^{-3}\,\phi^2\,\ln\left[\frac{\xi-1}{1-\xi}\right] \qquad \text{(B.8)}$$

where $\xi = (1-1.2B_c)$

and

$$\phi = \frac{1}{2}\sin 2(\mathrm{Sin}^{-1}\xi) + \sin^{-1}\xi$$

A plot of Equation (B.8) is given in Figure 2.7 as $\bar{f}_c^{\,m}/f_c^{\,m}$ against ξ. It shows that for typical design practice ($0.58 \leq 1-1.2B_c \leq 0.76$), the correction to the ideal friction factor is less than 5%.

APPENDIX C

ITERATIVE SOLUTION TO BAFFLE SPACE MULTI-STREAM METHODS

C.1 Flowstreams, Continuity and Pressure Drop Equations

The flowstreams defined by the network under consideration (see Figure 1.4) are as follows:

1) Crossflow ($\dot{M}_c$)
2) Bypass ($\dot{M}_b$)
3) Window flow ($\dot{M}_w$)
4) Shell-baffle leakage ($\dot{M}_s$)
5) Tube-baffle leakage ($\dot{M}_t$)

These flowstreams are related through the following continuity equations:

$$\dot{M}_T = \dot{M}_c + \dot{M}_b + \dot{M}_s + \dot{M}_t \tag{C.1}$$

$$\dot{M}_w = \dot{M}_c + \dot{M}_b \tag{C.2}$$

where $\dot{M}_T$ is the total baffle space mass flowrate.

The pressure drops can be related, assuming that parallel flowstreams suffer the same pressure drop, by

$$\Delta p_c = \Delta p_b \tag{C.3}$$

$$\Delta p_T = \Delta p_s = \Delta p_t \tag{C.4}$$

$$\Delta p_T = \Delta p_c + \Delta p_w \tag{C.5}$$

The pressure drop in each stream can be written as the number of velocity heads lost, n_i, (derived from experimental data where $n_i = 4f_i$):

$$\Delta p_i = n_i \frac{1}{2\rho} \left(\frac{\dot{M}_i}{A_i}\right)^2 \qquad (C.6)$$

where

$$n_i = fn\ (Re_i) \qquad (C.7)$$

Equation (C.7) can be simplified to

$$\Delta p_i = s_i \dot{M}_i^2 \qquad (C.8)$$

where

$$s_i = \frac{n_i}{2\rho} (A_i)^{-2} \qquad (C.9)$$

Substituting Equations (C.9) into (C.1) to (C.6) gives the following relationships:

$$\Delta p_w = s_w \dot{M}_w^2 \qquad (C.10)$$

$$M_w = \frac{\dot{M}_T}{1 + (s_s^{-\frac{1}{2}} + s_t^{-\frac{1}{2}})[(s_c^{-\frac{1}{2}} + s_b^{-\frac{1}{2}})^{-2} + s_w]^{\frac{1}{2}}} \qquad (C.11)$$

$$\Delta p_c = (s_c^{-\frac{1}{2}} + s_b^{-\frac{1}{2}})^{-2} \dot{M}_w^2 \qquad (C.12)$$

$$\dot{M}_c = \left(\frac{\Delta p_c}{s_c}\right)^{\frac{1}{2}} \qquad (C.13)$$

$$\dot{M}_b = \left(\frac{\Delta p_c}{s_b}\right)^{\frac{1}{2}} \qquad (C.14)$$

$$\dot{M}_s = \left(\frac{\Delta p_T}{s_s}\right)^{\frac{1}{2}} \qquad (C.15)$$

$$\dot{M}_t = \left(\frac{\Delta p_T}{s_t}\right)^{\frac{1}{2}} \qquad (C.16)$$

C.2 Iterative Solution

The following iterative scheme may be used to solve the pressure drop and flow distribution:

1) Estimate s_c, s_b, s_s and s_t.

2 Calculate $\dot{M}_w$ from Equation (C.11). If $\dot{M}_w$ is equal to that calculated from the previous loop, within reasonable accuracy, then stop the iterative procedure, otherwise continue.

3) Calculate s_w from Equations (C.7) and (C.9).

4) Calculate streams pressure drops Δp_c and Δp_w from Equations (C.12) and (C.11) respectively. Calculate Δp_T from Equations (C.5).

5) Calculate new flowsplits using Equations (C.13) to (C.16) and new values of s_i from Equation (C.9). Continue from step 2.

This process continues until convergence of $\dot{M}_w$ is achieved.

Wills (1984) suggests a means of simplifying multi-stream iterative techniques for use in simple hand calculation design methods. He noted that since the number of velocity heads lost were, to a good approximation, independent of Reynolds number for all flowstreams except crossflow, only n_c (or s_c in the above scheme) needs to be re-evaluated. If this approximation is imposed on the method described above, only Equations (C.5) and (C.9) to (C.13) are required to reach a solution.

APPENDIX D
CHECK ON FLOWMETER CALIBRATION

D.1 Introduction

Only one of the three available flowmeters was used in the current study, that being the Fisher and Porter 'Armoured Thruflow' meter. This meter was originally calibrated for trichloroethylene at 34°C (ρ =1440, η = 0.53 Ns/m²). The manufacturers supplied a conversion chart for use with demineralised water (Figure 4.8). This opened up two possible areas for inaccuracy: the original calibration and the supplied conversion chart. Clearly, a check on the calibration using demineralised water was necessary. This was facilitated by collecting and weighing the water that was discharged through the meter at various flow settings. High flowrates (> 3.5 kg/s), however, could not be assessed using this technique since the large volumes of water involved were impractical to collect and transport for weighing.

D.2 Results

The results of the flowmeter calibration check are shown in Table D.1. Over the flow range studied the agreement between indicated and measured flowrate was within ± 2%. Although the higher flowrates could not be checked it was felt safe to extrapolate this accuracy over the full range covered by the flowmeter.

Table D.1: Comparison Between Measured and Metered Flowrates

Temperature = 15°c		Volume flowrate (m³/hr)			
Mass of water collected (kg)	Time of collection (s)	Flowmeter reading Q_{tric}	Meter reading converted to water (Fig.4.8) Q_{water}	From collecting and weighing Q_{water}	Percentage difference
58.4	42.8	4	4.96	4.92	- 0.8
67.1	38.6	5	6.20	6.26	+ 1.0
54.4	26.3	6	7.43	7.45	+ 0.3
55.6	22.9	7	8.67	8.75	+ 0.9
54.9	20.3	8	9.91	9.74	- 1.7
61.6	19.8	9	11.15	11.21	+ 0.5
61.1	18.1	10	12.40	12.16	- 1.9
Temperature = 25°C					
60.2	43.6	4	4.96	4.99	+ 0.6
57.8	28.5	6	7.43	7.32	- 1.5
61.3	22.0	8	9.91	10.05	+ 1.4

APPENDIX E

SOLUTION TO THE CROSSFLOW PENETRATION EQUATION

E.1 Introduction

Flowstream models, such as TASC, separate the crossflow pressure drop from the window pressure drop. This procedure allows a more physical approach to modelling individual flowstream. A problem encountered, however, is in deciding the extent of crossflow into the window region. Wills (1984) derived a simple one-dimensional model of the extent of 'crossflow-in-the-window' by considering a simple two-dimensional representation of the window region (see Figure 8.1). Wills was unable to find a direct solution to the resulting equation. Instead an ad hoc solution was introduced that satisfied the boundary conditions. The purpose of this appendix is, firstly, to show how the correct solution to the problem posed is arrived at and, secondly, to present the numerical integration techniques used to evaluate the crossflow penetration distance into the window region.

E.2 Reduction of Penetration Equation to a Standard Form

Starting from the normalised non-linear second order penetration equation:

$$m^2 + \frac{dm}{dx} \cdot \frac{d^2m}{dx^2} = 0 \qquad \text{(E.1)}$$

where $x = y/Y$, $m = \dot{M}_y/\dot{M}_c$

with boundary conditions

$m = 1$ at $x = 0$

$m = 0$ at $x = h/Y \; (= x_o)$

Let

$$E = \frac{dm}{dx} \qquad \text{(E.2)}$$

therefore

$$\frac{d^2m}{dx^2} = \frac{dE}{dx} = \frac{dE}{dm} \cdot \frac{dm}{dx} \qquad (E.3)$$

Substitute Equations (E.2) and (E.3) into (E.1)

$$m^2 + E^2 \frac{dE}{dm} = 0 \qquad (E.4)$$

Rearrange, separate the variables and integrate:

$$\int E^2 \, dE = - \int m^2 \, dm \qquad (E.5)$$

giving

$$E = [-m^3 + 3I_1]^{1/3} = \frac{dm}{dx} \qquad (E.6)$$

where I_1 is a constant of integration.

Separating the variables and integrating again gives

$$x + I_2 = \int_m^1 \frac{dm}{[-m^3 + 3I_1]^{1/3}} \qquad (E.7)$$

Let

$$a^3 = 1/3I_1 \qquad (E.8)$$

and

$$m = (e^3-a^3)^{-1/3} \qquad (E.9)$$

Differentiate (E.9) with respect to e:

$$\frac{dm}{de} = -\frac{1}{3}(e^3-a^3)^{-4/3} \cdot 3e^2 \qquad \text{(E.10)}$$

Substitute Equation (E.10) into (E.7) which gives, on rearrangement and changing limits of integration,

$$x + I_2 = \int_{e_1}^{e_2} \frac{e^2(e^3-a^3)^{-1}\,de}{[1 + 3I_1(e^3-a^3)]^{1/3}} \qquad \text{(E.11)}$$

Substitute Equation (E.8) into (E.12) and rearrange gives

$$x + I_2 = a\int_{e_1}^{e_2} \frac{e\,de}{(e^3-a^3)} \qquad \text{(E.12)}$$

The integral has thus been reduced to a standard form which on integration gives

$$x + I_2 = \frac{1}{3}\left[\frac{1}{2}\ln\frac{(e-a)^3}{e^3-a^3} + \sqrt{3}\tan^{-1}\left(\frac{2e+a}{a\sqrt{3}}\right)\right]_{e_1}^{e_2} \qquad \text{(E.13)}$$

where a and e are defined by Equations (E.8) and (E.9) respectively.

Equation (E.13) requires a numerical solution which is discussed in the next section.

E.3 Numerical Solution of Equation (E.13)

Step 1: Calculation of I_2

I_2 may be calculated from the lower boundary conditions: x=0, m=1.

Equation (E.9), when rearranged and boundary conditions imposed, becomes

$$e_1 = (1 + a^3)^{1/3} \qquad \text{(E.14)}$$

Substituting Equation (E.14) into (E.13) gives

$$I_2 = \frac{1}{3}\left[\frac{1}{2}\ln\frac{((1+a)^{1/3}-a)^3}{(1+a^3)-a^3} + \sqrt{3}\tan^{-1}\left(\frac{2(1+a^3)^{1/3}+a}{a\sqrt{3}}\right)\right] \qquad \text{(E.15)}$$

and hence the value of I_2.

Step 2: Evaluation of x_0 (= h/Y)

At x_0, m = 0 and therefore Equation (E.9) reduces to

$$e_2 = \infty \tag{E.16}$$

Substituting Equation (E.16) into Equation (E.13) gives the following relationship

$$x_0 + I_2 = \frac{1}{3}[\frac{1}{2}\ln(\frac{\infty}{\infty}) + \sqrt{3}\tan^{-1}(\infty)] \tag{E.17}$$

The logarithmic term in Equation (E.17) is indeterminant, so L'Hopital's rule may be applied to determine the value of the quotient:

$\frac{(e-a)^3}{e^3-a^3}$ is in the form $\frac{e^3}{e^3} \rightarrow 1$

Therefore,

$$\ln(\frac{\infty}{\infty}) = 0$$

The tangent term in Equation (E.17) is equal to $\pi/2$ and therefore reduces to

$$x_0 + I_2 = \frac{\sqrt{3}}{3} \cdot \frac{\pi}{2}$$

where I_2 is calculated from Equation (E.15).

Step 3: Evaluation of $\bar{x}$

At $\bar{x}$, m = 0.5 and therefore Equation (E.9) reduces to

$$e_2 = ((\frac{1}{2})^{-3} + a^3)^{1/3} \tag{E.16}$$

By substituting Equation (E.16) into (E.13) $\bar{x}$ may be found, which is the non-dimensional penetration distance and is related to x_0

(the non-dimensional window height) through the fractional penetration:

$$f_p = \bar{x}/x_0 \qquad \text{(E.17)}$$

The computer program used to perform the numerical integration is given at the end of this appendix (Table E.1). It should be stressed that the integration constant, I_1, was not calculated explicitly in the numerical solution; a range of values for a were used to generate values of x_0, $\bar{x}$ and hence f_p, noting that each value of a relates to a specific value of x_0 and hence exchanger geometry. The advantage of this approach, as opposed to solving specific cases, is that a convenient global relationship for f_p can be obtained.

It was discovered that f_p could be fitted accurately (within ± 2%) by the following explicit relationships:

$$\begin{aligned} f_p &= \tfrac{1}{2} && (x_0 \leq 1.25) \\ f_p &= 0.133 + 0.45/x_0 && (1.25 < x_0 < 2.25) \\ f_p &= \ln(2)/x_0 && (x_0 \geq 2.25) \end{aligned} \qquad \text{(E.18)}$$

Equation (E.18) has an important advantage over Wills' implicit relationship (apart from being the correct solution) since it requires no iterative procedure and is therefore more convenient for use in computer design methods.

Table E.1: Numerical Integration Program

```
10 REM DATE 10/10/84
20 REM NAME:DRAFT
25 OPEN3,4
26 PRINT#3,"  A                    X0                  XBAR"
27 PRINT#3,"-----------------------------------------"
30 REM NUMERICAL EVALUATION OF THE
31 REM PENETRATION EQ. GIVING X0 &
32 REM XBAR FOR A RANGE OF THE
33 REM CONSTANT A.
40 DIM Z(2),X(2)
50 REM GIVE A IT'S CONSTANT VALUE
54 REM*******************************
55 REM USE A RANGE OF VALUES FOR A
56 REM AND HENCE A RANGE OF VALUES
57 REM FOR THE INTEGRATION CONSTANT
58 REM I1.
59 REM*******************************
60 A=0
62 FOR J=1 TO 100
63 A=A+0.1
94 REM*****************
95 REM  Z AT X=0,M=1
96 REM*****************
100 Z(1)=(1+A↑3)↑(1/3)
104 REM*****************
105 REM Z AT X=FP/Y,M=0.5
106 REM*****************
110 Z(2)=(.50↑-3+A↑3)↑(1/3)
120 FOR B= 1 TO 2
140 IF B=2 THEN GOTO 160
150 GOTO 190
160 X(B)=(1/3)*SQR(3)*(π/2)
165 REM*****************
170 REM    X0=H/Y
175 REM*****************
180 X0=X(2)-X(1)
190 Z=Z(B)
204 REM*****************************
205 REM X(B) IS THE VALUE OF THE
206 REM INTEGRAL AT Z(1) & Z(2)
207 REM*****************************
208 S=.5*LOG((Z-A)↑3/(Z↑3-A↑3))
210 T=SQR(3)*ATN((2*Z+A)/(SQR(3)*A))
220 X(B)=(S+T)/3
224 REM*****************
225 REM    X1=FP/Y
226 REM*****************
230 X1=X(2)-X(1)
240 NEXT
250 X0=.001*INT((X0*1000)+0.5)
260 X1=.001*INT((X1*1000)+0.5)
265 A=.1*INT((A*10)+.1)
270 PRINT#3,A,X0,X1
280 NEXT
290 STOP
300 END
```

APPENDIX F

ESTIMATION OF ERRORS

F.1 Introduction

In the main text pressure drop measurements have generally been presented in non-dimensionalised form as a function of Reynolds number. In order to estimate the maximum possible errors in each of the two non-dimensionalised groups, the errors in the parameters constituting these groups must be calculated first.

The crossflow measurements are considered for the purpose of illustrating the method used (Topping (1962)). The errors in the window data are quoted.

F.2 Mass Flowrate

A check on the calibration of the flowmeter (Appendix D) showed a possible error, in general, of approximately ± 1% in the mass flowrate. In addition, errors in reading the flowmeter gauge, due to small fluctuations, were estimated to contribute a further ± 1% uncertainty in the flowrate. The total maximum error assumed in the mass flowrate was, therefore, ± 2%.

F.3 Physical Properties

The shellside fluid temperature was measured with a platinum resistance thermometer, which had an accuracy of ± 0.1°C.

Errors in the fluid density were assumed to be negligible.

Possible maximum errors in the fluid viscosity were estimated from Rogers and Mayhew (1980) as ± 0.5%.

F.4 Flow Area

The crossflow area was defined as

$$\overline{A}_c^m = \frac{C_w}{P_y} W B_s \qquad (F.1)$$

The minimum gap per transverse pitch, W, can be expressed as $2 (P_t - D_o)$. Whilst both P_t and D_o have finite standard errors individually, it has been assumed that in a large tube bundle these errors are negligible due to self cancellation. The error in the transverse pitch, P_y, has likewise been assumed to be negligible viewing the bundle as a whole.

Therefore, the possible errors in the crossflow area derived primarily from the errors in the average crossflow width, C_w, and the baffle spacing, B_s. C_w is essentially a function of the shell inside diameter, which was machined to a tolerance of ± 0.1 mm. Likewise the spacer tubes, which control the baffle spacing, were machined to a tolerance of ± 0.1 mm. Clearly, the error in the crossflow area varies with baffle spacing.

The standard error in the area $(\delta \overline{A}_c^m)$ can be expressed as

$$\delta \overline{A}_c^m = \left[\left(\frac{\partial \overline{A}_c^m}{\partial C_w} \right)^2 (\delta C_w)^2 + \left(\frac{\partial \overline{A}_c^m}{\partial B_s} \right)^2 (\delta B_s)^2 \right]^{1/2} \qquad (F.2)$$

The resulting standard errors in the crossflow area, calculated from Equations (F.1) and (F.2) are shown in Table F.1.

Table F.1: Estimated Standard Errors in the Crossflow Area

Baffle Spacing (mm)	Standard Error $(\delta \overline{A}_c^m)$ (± %)
86.4	0.15
112	0.12
158	0.10

F.5 Pressure Drop

The Deltapi pressure transducer had an accuracy of ± 0.2% of full-scale deflection (660_0 N/m²), giving a possible error of 13 N/m² in each measurement.

F.6 Normalised Pressure Drop

Crossflow pressure drops were normalised (non-dimensionalised) using the following relationship:

$$\bar{n}_c = \frac{2\,\Delta p_c\,\rho}{N_c\,(\dot{M}_c/\bar{A}_c^m)^2} \qquad (F.3)$$

Therefore, the maximum standard error in $\bar{n}_c$ ($\delta\bar{n}_c$) can be expressed as

$$\delta\bar{n}_c = \left[\left(\frac{\partial\bar{n}_c}{\partial\Delta p_c}\right)^2 (\delta\Delta p_c)^2 + \left(\frac{\partial\bar{n}_c}{\partial\bar{A}_c^m}\right)^2 (\delta\bar{A}_c^m)^2 + \left(\frac{\partial\bar{n}_c}{\partial\dot{M}_c}\right)^2 (\delta\dot{M}_c)^2 \right]^{1/2} \qquad (F.4)$$

Since the error in $\bar{n}_c$ varies with the measured pressure drop, two extreme cases have been considered: highest and lowest measured pressure drop, which correspond to highest and lowest shellside mass flowrate respectively.

The resulting standard errors in $\bar{n}_c$, calculated from Equations (F.3) and (F.4) are shown in Table F.2.

Table F.2: Estimated Standard Errors in the Normalised Crossflow Pressure Drop

Baffle Spacing (mm)	Pressure Drop (magnitude)	Standard Error ($\delta\bar{n}_c$) (±%)
86.4	Largest	3
	Smallest	4
112	Largest	3
	Smallest	10
158	Largest	4
	Smallest	5

The equivalent standard errors for the window normalised pressure drops are given in Table F.3.

Table F.3: Estimated Standard Errors in the Normalised Window Pressure Drop

Baffle Spacing (mm)	Pressure Drop (magnitude)	Standard Error (δn_w) (±%)
86.4	Largest	4
	Smallest	5
112	Largest	5
	Smallest	6
158	Largest	5
	Smallest	9

F.7 Reynolds Number

The crossflow Reynolds number was defined as

$$\overline{Re}_c^m = \frac{\dot{M}_c \, (P_t - D_o)}{\overline{A}_c^m \, \eta} \qquad (F.5)$$

The standard error in the Reynolds number ($\delta\overline{Re}_c^m$) can be expressed as

$$\delta\overline{Re}_c^m = \left[\left(\frac{\partial \overline{Re}_c^m}{\partial M_c}\right)^2 (\delta M_c)^2 + \left(\frac{\partial \overline{Re}_c^m}{\partial \overline{A}_c^m}\right)^2 (\delta \overline{A}_c^m) + \left(\frac{\partial \overline{Re}_c^m}{\partial \eta}\right)^2 (\delta \eta)^2 \right]^{1/2} \qquad (F.6)$$

Differentiating Equation (F.5) and substituting into Equation (F.6) along with the geometric variables, gave the standard errors in Reynolds number as ±2% throughout the range of flowrates studied. The window Reynolds number was also shown to have a standard error of ±2%.

APPENDIX G

ESTIMATION OF CROSSFLOW AND WINDOW FLOW FRACTIONS

G.1 Introduction

The pressure drop measurements obtained in the current investigation, for leakage and non-leakage configurations, were used to estimate crossflow and window flow fractions. The method is described in detail below and the calculations illustrated using crossflow pressure drops measured in the large baffle spacing (B_s = 158).

G.2 Method

Definitions of crossflow Reynolds numbers, for both leakage and non-leakage data are:

$$Re_1 = \frac{\dot{M}_T \, (P_t - D_o)}{A_1 \, \eta_1} \qquad (G.1)$$

$$Re_2 = \frac{\dot{M}_C \, (P_t - D_o)}{A_2 \, \eta_2} \qquad (G.2)$$

where subscripts 1 and 2 denote leakage and non-leakage respectively.

Dividing Equation (G.2) by (G.1) and rearranging gives

$$x_c = \frac{\dot{M}_C}{\dot{M}_T} = \left(\frac{Re_2}{Re_1}\right) \left(\frac{A_2}{A_1}\right) \left(\frac{\eta_2}{\eta_1}\right) \qquad (G.3)$$

where x_c is the crossflow fraction in the leakage case.

By comparing the leakage and non-leakage Reynolds number, at a given pressure drop, x_c can be established. This was achieved as follows:

1) The non-leakage crossflow pressure drops were fitted empirically as a function of Reynolds number (Re_2, Equation (G.2)):

$$\Delta p_2 = 9.082 \times 10^{-4} (Re_2)^{1.91} \qquad (G.4)$$

Equation (G.4) fitted the data to within ±4%.

2) The pressure drop obtained in the leakage configuration (with Reynolds number Re_1) were substituted into Equation (G.4) to establish the Reynolds number in the non-leakage case (Re_2). Then both Re_1 and Re_2 were substituted into Equation (G.3), along with the geometric parameters and physical properties, to calculate x_c.

G.3 Sample Calculation

The leakage and non-leakage pressure drops are shown in Figure G.1, along with Equation (G.4). The data point ringed in Figure G.1 is used to illustrate the calculation.

Data

Leakage crossflow pressure drop	$- \Delta p_1 = 760$ N/m²
Leakage crossflow Reynolds number	$- Re_1 = 1829$
Leakage crossflow area	$- A_1 = 0.01350$ m²
Non-leakage crossflow area	$- A_2 = 0.01336$ m²
Fluid viscosity in leakage tests	$- \eta_1 = 1.002 \times 10^{-3}$ Ns/m²
Fluid viscosity in non-leakage tests	$- \eta_2 = 1.014 \times 10^{-3}$ Ns/m²

To estimate the non-leakage Reynolds number (Re_2) at the leakage crossflow pressure drop, Δp_1 is substituted into Equation (G.4). On rearranging Re_2 is calculated to be 1260 (see Figure G.1). Inserting Re_2, along with the flow areas and viscosities into Equation (G.3) gives

$$x_c = \frac{\dot{M}_c}{\dot{M}_T} = 0.69 \qquad (G.5)$$

The derived crossflow fractions, for each of the three baffle spacings, are shown in Table 9.2.

An identical method was used in the estimation of window flow fractions, these are shown in Table 9.4.

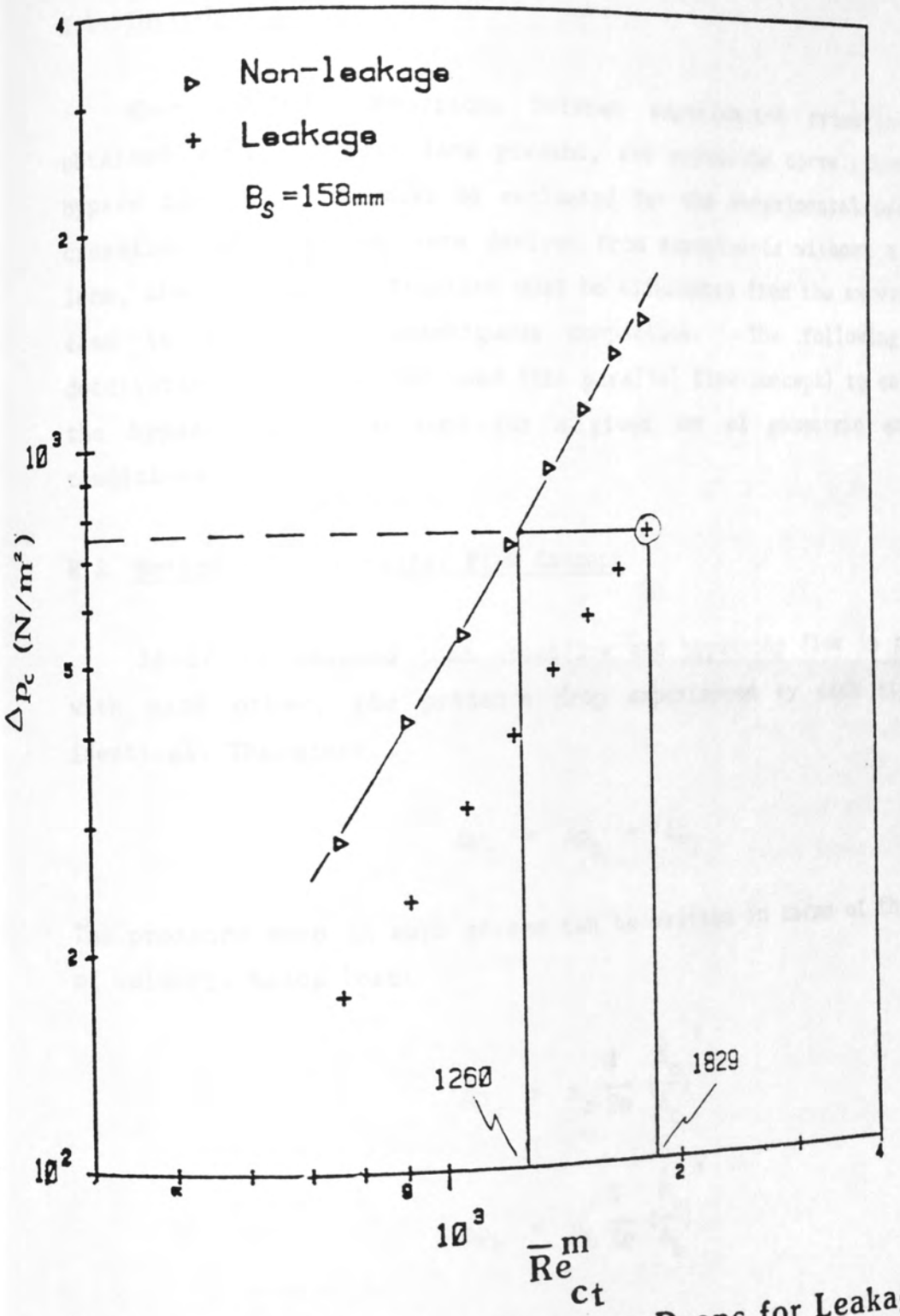

Figure G.1: Crossflow Pressure Drops for Leakage and Non-Leakage as a function of Reynolds Number. Data Obtained Using B_s=158mm.

APPENDIX H

ESTIMATION OF BYPASS FLOW FRACTIONS

H.1 Introduction

When making comparisons between experimental crossflow data obtained with a bypass lane present, and crossflow correlations, the bypass flow fraction must be evaluated for the experimental case: the crossflow correlations were derived from experiments without a bypass lane, the bypass flow fraction must be eliminated from the experimental case to enable an unambiguous comparison. The following is a description of the method used (the parallel flow concept) to calculate the bypass flow fractions for a given set of geometric and flow conditions.

H.2 Method - The Parallel Flow Concept

If it is assumed that crossflow and bypassing flow in parallel with each other, the pressure drop experienced by each stream is identical. Therefore,

$$\Delta p_c = \Delta p_b = \Delta p_T \tag{H.1}$$

The pressure drop in each stream can be written in terms of the number of velocity heads lost:

$$\Delta p_c = n_c \frac{1}{2\rho} \left(\frac{\dot{M}_c}{A_c}\right)^2 \tag{H.2}$$

$$\Delta p_b = n_b \frac{1}{2\rho} \left(\frac{\dot{M}_b}{A_b}\right)^2 \tag{H.3}$$

Equating Equations (H.2) and (H.3) gives

$$n_c \left(\frac{\dot{M}_c}{A_c}\right)^2 = n_b \left(\frac{\dot{M}_b}{A_b}\right)^2 \tag{H.4}$$

Both crossflow and bypassing can be related to the total flowrate, $\dot{M}_T$:

$$\dot{M}_c = x_c \dot{M}_T \tag{H.5}$$

$$\dot{M}_b = (1-x_c) \dot{M}_T \tag{H.6}$$

where x_c is the crossflow fraction.

Substituting Equations (H.5) and (H.6) into (H.4) yields the following:

$$n_c \left(\frac{\dot{M}_T x_c}{A_c}\right)^2 = n_b \left(\frac{\dot{M}_T (1-x_c)}{A_b}\right)^2 \tag{H.7}$$

On rearrangement and elimination of M_T the following expression for the fraction of crossflow is obtained:

$$x_c = \left(\left(\frac{n_b}{n_c}\right)^{1/2} \cdot \frac{A_c}{A_b} + 1\right)^{-1} \tag{H.8}$$

Clearly if the number of velocity heads lost in each flow path (n_c and n_b) are known, the fraction of crossflow and hence bypassing can be established. However, since n_c and n_b are functions of flowrate, an iterative procedure is required.

H.3 Iterative Solution Procedure

The following iterative scheme was used to establish the flow distribution:

1) Estimate the fraction of crossflow x_c and hence obtain an estimate of the bypass flow fraction $(1-x_c)$.

2) Calculate both crossflow and bypass characteristic flow areas, A_c and A_b.

3) Calculate both crossflow and bypass Reynolds numbers and hence the number of velocity heads lost in each stream, n_c and n_b.

4) Calculate the crossflow pressure drop from Equation (H.2) and compare with the value obtained from the previous loop. If the two values are the same, to within the required accuracy, the pressure drops in each stream are balanced. The calculation is terminated with x_c and $(1-x_c)$ satisfying Equation (H.7). If the pressure drops do not agree then continue to the next step.

5) Re-calculate x_c using Equation (H.8) and return to step 3.

APPENDIX I

COMPARISON BETWEEN EXPERIMENTAL WINDOW PRESSURE DROP DATA AND THE WINDOW MODEL OF WILLS (1984)

I.1 Introduction

The window model of Wills (1984) has been used to predict the window pressure drop obtained from a number of investigations. These were Leighton (1955), Macbeth (1973) and the current results. Each set of data were obtained in cylindrical baffled geometries.

The window model consists of geometric and crossflow-in-the-window terms. The geometric terms are simple to calculate since they are a function of crossflow area at the baffle tip plane and window flow area only. The frictional term, however, is a function of the crossflow distance into the window, which is governed by the crossflow penetration model, and the change in crossflow area due to the shell curvature.

The method used for calculating the crossflow-in-the-window pressure drop, accounting for the variation of flow area, is described below and is based on that proposed by Moore (1974).

I.2 Method

To standardise the predicted values with those measured, the predicted pressure drop associated with crossflow-in-the-window must be subtracted from the total crossflow pressure drop and added to the predicted window pressure drop. This operation would be a simple matter for a rectangular geometry since the crossflow-in-the-window pressure drop would be a linear proportion (based on the ratio of penetration distance to total crossflow path length) of the total crossflow pressure drop. However, all of the data under consideration were

obtained from cylindrical baffled models, introducing a further complication due to the variation in crossflow area. Moore (1974) tackled this problem by calculating the total crossflow pressure drop based on an average crossflow area (see Section 2.1.4), expressed in terms of the minimum centre-line flow area:

$$\Delta p_c = \frac{f_c^{\,m} \, D_t^{\,2}}{2 \rho P_x} \left(\frac{\dot{M}_c}{A_c}\right)^2 \int_0^B \frac{db}{\left(\frac{D_t}{2}\right)^2 - b^2} \qquad (I.1)$$

where B is the extent of crossflow from the shell centre line, which is equal to half the crossflow length, $L_c/2$.

The pressure drop associated with crossflow-in-the-window can be expressed as

$$\Delta p_{cw} = \Delta p_{c1} - \Delta p_{c2} \qquad (I.2)$$

where Δp_{c1} and Δp_{c2} are the crossflow pressure drops associated with the total crossflow path length (including crossflow-in-the-window) and the overlap region respectively.

Equations for both Δp_{c1} and Δp_{c2} can be obtained by integrating Equation (I.1) for the following two cases:

1) The crossflow region extends into the window region a distance defined by the penetration model. Therefore,

$$B_1 = (1 - 2 B_c (1-f_p)) D_t/2 \qquad (I.3)$$

where B_c is the baffle cut expressed as a fraction of the shell diameter and f_p is the penetration distance into the window expressed as a fraction of window height.

2) The crossflow path length is defined equal to the baffle overlap region. Therefore,

$$B_2 = (1 - 2 B_c) D_t/2 \qquad (I.4)$$

Integrating Equation (I.1) for the two cases and inserting into Equation (I.2) yields the following relationship:

$$\Delta p_{cw} = \frac{\zeta\, f_c^{\,m}\, D_t}{2\,\rho\, P_x} \left(\frac{\dot{M}_c}{A_c}\right)^2 \ln\left[\frac{2 - 2B_c\,(1-f_p)}{2B_c\,(1-f_p)}\right] \qquad (I.5)$$

where

$$\zeta = \frac{\ln\left[\dfrac{2 - 2B_c\,(1-f_p)}{2B_c\,(1-f_p)}\right] - \ln\left[\dfrac{2 - 2B_c}{2B_c}\right]}{\ln\left[\dfrac{2 - 2B_c\,(1-f_p)}{2B_c\,(1-f_p)}\right]} \qquad (I.6)$$

which can be written simply as

$$\Delta p_{cw} = \zeta\, \Delta p_{cl} \qquad (I.7)$$

Thus ζ is the fraction of the total crossflow pressure drop calculated by Moore (as used in the current version of TASC) associated with crossflow-in-the-window.

The values of f_p and ζ have been evaluated, for each geometric configuration under consideration, using both the Wills' (1984) penetration model and the new model, presented in Chapter 8. These values are given in Table I.1.

I.3 Closing Remarks

The integral given in Equation (I.1) is a standard form which can yield different solutions depending on the relative values of $D_t/2$ and b:

$$\int \frac{db}{\left(\frac{D_t}{2}\right)^2 - b^2} = \begin{cases} \left(\frac{D_t}{2}\right)^{-2} \tan^{-1}\left(\frac{2b}{D_t}\right) & \left(\frac{D_t}{2}\right)^2 > b^2 \\ (D_t)^{-1} \ln\left[\frac{D_t/2 + b}{D_t/2 - b}\right] & \end{cases} \qquad (I.8)$$

$$= \begin{cases} \left(\frac{D_t}{2}\right)^{-1} \coth^{-1}\left(\frac{2b}{D_t}\right) & b^2 > \left(\frac{D_t}{2}\right)^2 \\ (D_t)^{-1} \ln\left[\frac{b - D_t/2}{b + D_t/2}\right] & \end{cases} \quad \text{(I.9)}$$

Clearly, the solution given in Equation (I.9) can never arise since the crossflow path length cannot exceed the shell inside diameter. Equation (I.8) was, therefore, used throughout the analysis.

Table I.1: Values of the Fractional Penetration (f_p) and Fraction of Crossflow Pressure Drop in the Window Region (ζ) Using the Model of Wills (1984) and the Model Presented in This Work

Geometry		Wills (1984)		New Model (Current Work)	
Baffle cut, (-)	Baffle spacing (mm)	f_{pw} (-)	ζ_w (-)	f_{pm} (-)	ζ_m (-)
Leighton (1955)					
0.187	65.5	0.285	0.214	0.500	0.353
Macbeth (1973)					
0.184	48.5	0.307	0.225	0.500	0.349
"	97.0	0.386	0.277	0.500	0.349
0.250	48.5	0.266	0.264	0.426	0.385
"	97.0	0.355	0.333	0.500	0.435
0.375	48.5	0.211	0.411	0.322	0.525
"	97.0	0.305	0.510	0.500	0.652
Current Work					
0.250	86.4	0.234	0.237	0.361	0.338
"	84.8	0.232	0.236	0.356	0.334
"	112.0	0.270	0.267	0.434	0.391
"	110.4	0.268	0.266	0.430	0.388
"	158.0	0.316	0.304	0.500	0.435
"	156.4	0.314	0.302	0.500	0.435

APPENDIX J

PROCEDURE FOR DETECTING CROSSFLOW-LEAKAGE INTERACTION (WILLS (1984))

J.1 Introduction

Shell-and-tube heat exchanger design methods are built up from a number of empirical correlations and simple one-dimensional models. These correlations derive from isolated shellside flow phenomena (for example crossflow relationships derive from single pass rectangular bundles). Clearly, in a practical heat exchanger the components of pressure loss are not isolated from one another. Therefore, bringing together information from isolated phenomena could possibly lead to errors in predicted pressure drops if flow interactions are significant.

Wills (1984) suggested that the most significant interaction between flow streams was likely to be shown by the tube-baffle leakage mixing with the crossflow. He used one data set obtained by Macbeth (1973) (both leakage and non-leakage) and showed that the leakage crossflow pressure drops were considerably larger than could be expected from a non-leakage situation, for the same absolute flowrates. The method he adopted to detect so called 'crossflow leakage interaction' has been applied to the current data and the results are presented in Figure 9.7. The proposed method and sample calculation for the smallest baffle spacing (86.4 mm) is given below.

J.2 Method

The steps required in the calculation were as follows

(i) The window pressure drop data were fitted empirically against the window flowrate for the non-leakage geometry. Clearly, the window flowrate equals the total shellside flowrate in the absence of leakage. The resultant relationship was

$$\Delta p_w = 34.75 \, (\dot{M}_w)^{1.967} \qquad \text{(J.1)}$$

where Δp_w and $\dot{M}_w$ are window pressure drop and mass flowrate respectively. Equation (J.1) predicts all of the non-leakage window data to within ± 5%.

(ii) The crossflow pressure drops were fitted empirically against the crossflow flowrate (also equals total flowrate) for the non-leakage geometry. The resultant relationship was

$$\Delta p_c = 77.8 \, (\dot{M}_c)^{1.803} \qquad \text{(J.2)}$$

where Δp_c and $\dot{M}_c$ are crossflow pressure drop and mass flowrate respectively. Equation (J.2) predicts all of the crossflow data to within ± 3%.

(iii) Assuming that the window pressure drop, in the leakage case, depends only on the flowrate emerging from the crossflow (see Section J.6), Equation (J.1) can be used to estimate the crossflow flowrate for the leakage geometry. Using the estimated crossflow flowrate in Equation (J.2) yields an estimate of the non-leakage crossflow pressure drop. This may be compared with the experimental value of crossflow pressure drop when leakage is present.

J.3 Sample Calculation

The calculated point chosen to illustrate the procedure adopted is ringed on the plot shown in Figure 9.21. The relevant data required is

Baffle spacing	86.4 mm
Mass flowrate	6.89 kg/s
Fluid Temperature	23°C
Measured Pressure	
Non-leakage Crossflow	855 N/m²
Non-leakage Window	635 N/m²

J.4 Estimation of Crossflow Flowrate for the Leakage Geometry

The crossflow flowrate is estimated by substituting the measured leakage window pressure drop into Equation (J.1). Clearly, this assumes that the crossflow flowrate equals the window flowrate which is not strictly true for the leakage geometry (see J.5):

$$\dot{M}_w = \left(\frac{\Delta p_w}{34.75}\right)^{0.5084}$$

$$= 4.38 \text{ kg/s}$$

therefore,

$$\dot{M}_c = 4.38 \text{ kg/s}$$

J.5 Estimation of Equivalent Non-Leakage Crossflow Pressure Drop

The equivalent non-leakage crossflow pressure drop is estimated by substituting the crossflow flowrate, calculated in Section J.3, into Equation (J.2).

$$\Delta p_c = 77.8 \left(\dot{M}_c\right)^{1.803}$$

$$= 1114 \text{ N/m}^2$$

This value (ordinate) is compared with the measured crossflow pressure drop for the leakage geometry (abscisa) in Figure 9.21. The Figures show no indication of crossflow-leakage interaction.

J.6 Assumptions

In order to calculate the crossflow flowrate from the window pressure drop in the leakage case, an important assumption is necessary: the baffle leakage in the window is neither significant in magnitude nor in its contribution to the window pressure drop. Wills estimated from Macbeth's data that the effect of leakage in the window was insignificantly small (contributing approximately 3% towards the window pressure drop). Moreover, if such effects were larger the significance of the apparent leakage interaction would be enhanced.